

APPLICATION OF THE MUONIUM SPIN ROTATION TECHNIQUE TO
A STUDY OF THE GAS PHASE CHEMICAL KINETICS OF MUONIUM
REACTIONS WITH THE HALOGENS AND HYDROGEN HALIDES

by

DAVID MICHAEL GARNER

A THESIS SUBMITTED IN PARTIAL FULFILLMENT OF
THE REQUIREMENTS FOR THE DEGREE OF
DOCTOR OF PHILOSOPHY

in

THE FACULTY OF GRADUATE STUDIES
(Department of Chemistry)

We accept this thesis as conforming
to the required standard

THE UNIVERSITY OF BRITISH COLUMBIA
June, 1979

© David Michael Garner, 1979

In presenting this thesis in partial fulfilment of the requirements for an advanced degree at the University of British Columbia, I agree that the Library shall make it freely available for reference and study.

I further agree that permission for extensive copying of this thesis for scholarly purposes may be granted by the Head of my Department or by his representatives. It is understood that copying or publication of this thesis for financial gain shall not be allowed without my written permission.

Department of Chemistry

The University of British Columbia
2075 Wesbrook Place
Vancouver, Canada
V6T 1W5

Date 24 September, 1979

ABSTRACT

Muonium (Mu) is the atom formed by an electron bound to a positive muon "nucleus" (charge:+1, spin:1/2, lifetime: 2.2 μ s). Since muons are 207 times as massive as electrons, the reduced mass of Mu is 0.996 that of the hydrogen atom, and the Bohr radii and ionization potentials of Mu and H are essentially the same. Therefore, the chemical behaviour of the Mu atom is that of a light H isotope ($m_{\text{Mu}} = 1/9 m_{\text{H}}$) with a greatly enhanced sensitivity to H isotope effects.

Mu reaction rates are measured by a method called "Muonium Spin Rotation" (MSR) which resembles conventional resonance techniques such as NMR or ESR in that it monitors the characteristic Larmor precession of the Mu atom. However, unlike NMR or ESR, the MSR method does not detect the Mu Larmor precession by resonant power absorption, but rather through the peculiar spin dependent radioactive decay of the muon itself. The theoretical basis for the application of the MSR technique to the measurement of muonium reaction rates is derived. An extensive discussion is given to the practical aspects of the experimental implementation of the MSR technique.

Rate constants and activation energies are reported for the gas phase reactions: $\text{Mu} + \text{F}_2 \rightarrow \text{MuF} + \text{F}$ and $\text{Mu} + \text{Cl}_2 \rightarrow \text{MuCl} + \text{Cl}$ between 300 and 400K, and room temperature rate constants are reported for the reactions: $\text{Mu} + \text{Br}_2 \rightarrow \text{MuBr} + \text{Br}$ and $\text{Mu} + \text{HX} \rightleftharpoons \frac{\text{MuH} + \text{X}}{\text{MuX} + \text{H}}$, X = Cl, Br, I. While in most of these systems Mu reacts considerably faster than the heavier H isotopes, attention is focussed on hydrogen isotope effects in the $\text{Mu} + \text{F}_2$ and $\text{Mu} + \text{Cl}_2$ reactions. This discussion is based

on the extensive theoretical investigations of Connor et al., which show the $\text{Mu} + \text{F}_2$ reaction to be dominated by quantum mechanical tunnelling at room temperature. Experimentally, quantum tunnelling manifests itself in this reaction by producing two dramatic isotope effects at 300K: (1) the bimolecular rate constant for the Mu reaction (1.4×10^{10} l/mole-s) is at least six times that for the analogous H atom reaction, and (2) the apparent Arrhenius activation energy of this Mu reaction (0.9 kcal/mole) is less than half of that for $\text{H} + \text{F}_2$. In contrast, the $\text{Mu} + \text{Cl}_2$ reaction does not show any such strong isotope effects at 300K: (1) the bimolecular rate constant for $\text{Mu} + \text{Cl}_2$ (5.1×10^{10} l/mole-s) is no more than four times that of the analogous H reaction, and (2) the apparent activation energies for both Mu and H reactions are the same (1.4 kcal/mole). Preliminary calculations of Connor et al. on $\text{Mu} + \text{Cl}_2$ suggest that classical "wall reflection" partially offsets any rate enhancement due to quantum tunnelling. Quantitative isotope effects cannot be defined for the $\text{Mu} + \text{Br}_2$ and $\text{Mu} + \text{HX}$ reactions and their hydrogen isotopic analogues because of the absence of sufficient experimental and theoretical data; these reactions are discussed in terms of the general theory of isotope effects.

Table of Contents

Chapter I - Introduction	1
A Positive Muons and the μ^+ SR Method	1
B Muonium and the MSR Method	10
C Muonium Chemistry - An Historical Background	15
D Organization of the Dissertation	20
Chapter II - Experimental Details	23
A TRIUMF and the M20 Muon Beam Line	23
B The Gas Target, Counters, and Magnetic Field	32
C Data Acquisition	37
D Data Analysis	49
Chapter III - Theoretical Background	58
A Introduction	58
B Potential Energy Surfaces	60
(i) Semi-Empirical Potential Energy Surfaces	60
(ii) Contour Plots of the Potential Energy Surface for the Reaction $A + BC \rightarrow AB + C$	65
(iii) Potential Energy Surfaces for the Reactions: $Y + X_2 \rightarrow YX + X$, $Y = \text{Mu, H, D, T}$; $X = \text{F, Cl, Br}$	73
C Energy	82
(i) Classical Trajectories	83
(ii) Quasiclassical and Quantum Mechanical Trajectories	87
(iii) Transition State Theory	90
(iv) Reaction Enthalpy	92
(v) Reaction Activation Energy	94
(vi) Potential Energy Surfaces for the Reactions: $Y + HX \begin{matrix} \nearrow YX + H \\ \searrow YH + X \end{matrix}$, $Y = \text{Mu, H, D, T}$; $X = \text{Cl, Br, I}$	97
D Trajectory Calculations	109
E Transition State Theory	118
F Tunnelling	122
Chapter IV - Experimental Results and Their Interpretation	127
A $\text{Mu} + \text{F}_2 \rightarrow \text{MuF} + \text{F}$	129
B $\text{Mu} + \text{Cl}_2 \rightarrow \text{MuCl} + \text{Cl}$	157
C $\text{Mu} + \text{Br}_2 \rightarrow \text{MuBr} + \text{Br}$	171
D $\text{Mu} + \text{HCl} \begin{matrix} \rightarrow \text{MuCl} + \text{H} \\ \searrow \text{MuH} + \text{Cl} \end{matrix}$	178
E $\text{Mu} + \text{HBr} \begin{matrix} \rightarrow \text{MuBr} + \text{H} \\ \searrow \text{MuH} + \text{Br} \end{matrix}$	185
F $\text{Mu} + \text{HI} \begin{matrix} \rightarrow \text{MuI} + \text{H} \\ \searrow \text{MuH} + \text{I} \end{matrix}$	190
Chapter V - Summary and Conclusions	194
A Summary	194
B Past Perspective	195
C Future Perspective	198
D Closing Remarks	201

Table of Contents (Cont'd)

Literature Cited	203
Chapter I	203
Chapter II	206
Chapter III	207
Chapter IV	212
Chapter V	216
Appendix I	217
Appendix II	218
Appendix III	219
Appendix I - The Time Evolution of the μ^+ Spin Polarization in Muonium in a Transverse Magnetic Field	220
A State Vectors	220
B Time Evolution of the $M\mu$ States	223
C Time Evolution of the μ^+ Spin Polarization in $M\mu$	228
D Experimental Implications of $\langle \hat{P}_\mu(t) \rangle$	230
(i) Very Weak Fields (≤ 10 gauss) - the Standard MSR Signal	231
(ii) Intermediate Fields ($10 \leq B \leq 150$ gauss) - Two Frequency Muonium	234
(iii) High Fields (≥ 150 gauss)	236
Appendix II - The Effect of Chemical Reaction on the Muon Polarization	239
A General	239
B Generation of a Coherent Diamagnetic Muon Background: $\lambda \rightarrow 15 \mu s^{-1}$, $B \geq 10$ gauss	242
Appendix III - Data Acquisition with High Current Muon Beams: Theory and Practice	250
A The Optimal Good Event Rate	250
B Spectral Distortions due to Muon Pile-up	253
(i) Pre- μ_i Muons and τ_μ : 100% Decay Positron Detection Efficiency	257
(ii) Pre- μ_i Muons and τ_μ : ϵ Decay Positron Detection Efficiency	261
(iii) Pre- μ_i Muons and the MSR Signal: ϵ Decay Positron Detection Efficiency	269
(iv) Post- μ_i Muons and τ_μ : 100% Decay Positron Detection Efficiency	278
(v) Post- μ_i Muons and τ_μ : ϵ Decay Positron Detection Efficiency	280
(vi) Post- μ_i Muons and the MSR Signal: ϵ Decay Positron Detection Efficiency	284
C The MSR Data Acquisition System	294
(i) The Electronic Logic	294
(ii) The Microprogrammed Branch Driver	298

List of Figures

Chapter I

1	Energy spectrum of positrons from muon decay and the energy dependence of the asymmetry parameter	5
2	A typical μ^+ SR time histogram	9
3	A typical MSR time histogram	13
4	The MSR signal	16

Chapter II

5	The TRIUMF Cyclotron and experimental facilities (1977)	24
6	The M20 beamline (detail)	27
7	The gas phase MSR target apparatus	33
8	Nitrogen versus argon as moderator gases	36
9	MSR data acquisition logic (simplified)	39
10	The spectral distortion due to "early" second μ rejection	45

Chapter III

11	A potential contour map for the exothermic collinear $A + BC \rightarrow AB + C$ reaction	61
12	Potential energy surface for the $Y + F_2$ reaction	71
13	Potential energy surfaces for the collinear $Y + F_2$ reaction plotted in mass weighted coordinates	74
14	The bottleneck effect	77
15	Mass weighted potential energy surface for the collinear $Mu + F_2$ reaction	86
16	Potential surfaces for the collinear $H + HCl \rightarrow H_2 + Cl$ reaction	100
17	Isotope effects in transition state vibrations from mass variations of atom Y for the reaction $Y + AB \rightarrow YA + B$	123
18	Tunnelling transmission coefficients for the truncated Bell parabola and the Eckart barrier	126

Chapter IV

19	The effect of temperature on the $Mu + F_2$ MSR relaxation rates	132
20	Experimental Arrhenius plots for $Y + F_2$ reactions, $Y = Mu, H$	133
21	Collinear quantum and quasiclassical total reaction probabilities for $Y + F_2 (v=0,1)$	142
22	Integrand of the quantum collinear rate constant at 300 and 900K for $Y + F_2 (v=0)$	144
23	Integrand for the collinear quantum and quasiclassical rate constant at 300K for $Y + F_2 (v=1)$	145
24	Non-reactive quasiclassical trajectories for $Mu + F_2 (v=0)$ on the mass weighted LEPS surface	147
25	Arrhenius plots for the collinear quantum, quasiclassical, and transition state theory rate constants for $Y + F_2$	151
26	Comparison of quantum and tunnelling corrected transition state theory reaction probabilities for $Y + F_2 (v=0)$	153

List of Figures (Cont'd)

Chapter IV (Cont'd)

27	Comparison of quantum and transition state theory Arrhenius plots for the collinear $\text{Mu} + \text{F}_2$ ($v=0,1$)	154
28	Collinear quantum relative population distributions of product vibrational states for $\text{Y} + \text{F}_2$ ($v=0$)	156
29	The effect of temperature on the $\text{Mu} + \text{Cl}_2$ MSR relaxation rates	159
30	Experimental Arrhenius plots for $\text{Y} + \text{Cl}_2$ reactions, $\text{Y} = \text{Mu}, \text{H}, \text{D}$	160
31	Tunnelling corrected transition state theory Arrhenius plots for collinear $\text{Y} + \text{F}_2$ and $\text{Y} + \text{Cl}_2$	169
32	MSR relaxation rates as a function of Br_2 concentration in argon moderator at 295K	173
33	MSR relaxation rates as a function of HCl concentration in N_2 moderator at 295K	180
34	The MSR signals in pure N_2 versus pure HCl at 295K	181
35	MSR relaxation rates as a function of HI concentration in argon and N_2 moderator at 295K	192

Chapter V

36	MSR signals in pure argon and in Br_2 in argon at 1.8 gauss and 295K; data obtained at LBL	196
----	---	-----

Appendix I

I-1	Breit-Rabi diagram of the energy eigenstates of muonium in a magnetic field	226
I-2	The time evolution of the μ^+ spin polarization in a 100 gauss transverse magnetic field	235
I-3	"Two frequency precession" of the muon in muonium in fused quartz at 95 gauss	237

Appendix II

II-1	The effect of chemical reaction on the muonium signal	241
II-2	The linear dependence of the relaxation rate of the muonium signal on reagent concentration	243
II-3	The generation of a coherent diamagnetic muon background signal by fast chemical reactions of muonium	247
II-4	The dependence of the amplitude of the "residual muon polarization" on muonium reaction rate at 7.5 gauss	248

Appendix III

III-1	The net good event rate as a function of beam current for various muon decay gates	252
III-2	The effects of pre- μ_i muons on the apparent muon lifetime with $\epsilon = 100\%$.	262
III-3	Logarithmic plot of Figure III-2	263
III-4	The effects of pre- μ_i muons on the apparent muon lifetime with $\epsilon = 10\%$	267
III-5	Logarithmic plots of Figure III-4	268
III-6	The effects of pre- μ_i muons on the MSR signal with $\epsilon = 10\%$	273

List of Figures (Cont'd)

Appendix III (Cont'd)

III-7	The effects of pre- μ_i muons on the MSR signal with $\epsilon = 10\%$ (detail)	274
III-8	The origins of the lifetime distortions due to pre- μ_i muons	276
III-9	A possible example of the effect of pre- μ_i muons	277
III-10	The effects of post- μ_i muons on the apparent muon lifetime with $\epsilon = 100\%$	281
III-11	Logarithmic plots of Figure III-10	282
III-12	The effects of post- μ_i muons on the apparent muon lifetime with $\epsilon = 10\%$	285
III-13	Logarithmic plots of Figure III-12	286
III-14	The effects of post- μ_i muons on the MSR signal with $\epsilon = 10\%$	288
III-15	The effects of post- μ_i muons on the MSR signal with $\epsilon = 10\%$ (detail)	289
III-16	The origins of lifetime distortions due to post- μ_i muons	292
III-17	Relaxation effects in the MSR signal due to muon pile-up	293
III-18	The TRIUMF MSR data acquisition logic (detail)	295
III-19	Pulse timing and event identification for the logic of Figure III-18	297
III-20	Flow diagram of the TRIUMF MBD programme	307

List of Tables

Chapter I	
I	Properties of positive muons 2
II	Properties of muonium 11
Chapter II	
III	Nominal forward and backward μ^+ momenta and velocities as a function of decaying π^+ momentum 28
Chapter III	
IV	Energy definitions for the $Y + F_2$ reactions, $Y = \text{Mu, H}$ 93
V	Bond dissociation energies, zero point energies, and reaction enthalpies 95
Chapter IV	
VI	Summary of the experimental rate parameters for Mu and H reactions in the gas phase 128
VII	MSR relaxation rates for the reaction $\text{Mu} + \text{F}_2 \rightarrow \text{MuF} + \text{F}$ 131
VIII	Calculated rate constants for the collinear $Y + \text{F}_2 \rightarrow \text{YF} + \text{F}$ reactions 136
IX	Calculated rate constant ratios for the collinear $Y + \text{F}_2 \rightarrow \text{YF} + \text{F}$ reactions 137
X	Calculated activation energies for the collinear $Y + \text{F}_2 \rightarrow \text{YF} + \text{F}$ reactions 138
XI	MSR relaxation rates for the reaction $\text{Mu} + \text{Cl}_2 \rightarrow \text{MuCl} + \text{Cl}$ 158
XII	Experimental rate parameters for the reactions $Y + \text{Cl}_2 \rightarrow \text{YCl} + \text{Cl}$, $Y = \text{Mu, H, D}$ 162
XIII	MSR relaxation rates for the reaction $\text{Mu} + \text{Br}_2 \rightarrow \text{MuBr} + \text{Br}$ 172
XIV	MSR relaxation rates for the total $\text{Mu} + \text{HCl}$ reaction at 295K 179
XV	MSR relaxation rates for the total $\text{Mu} + \text{HBr}$ reaction at 295K 186
XIV	Experimental reaction rate parameters for $Y + Y'\text{Br} \rightarrow Y\text{Y}' + \text{Br}$ $\rightarrow Y\text{Br} + Y'$, $Y = \text{Mu, H, and D}$ 187
XVII	MSR relaxation rates for the total $\text{Mu} + \text{HI}$ reaction at 295K 191
Appendix I	
I-1	Values of magnetic field dependent variables in equations I(8) and I(12) 232

Acknowledgement

It is a pleasure to acknowledge the support of my research director, Dr. Don Fleming, who is always more of a "colleague" than a "director." His advice, always given with his characteristic enthusiasm, is usually accompanied by a patient respect for my independence.

Research at a meson factory is only possible with the efforts of an enormous number of people - unfortunately it is only possible to mention a few. In learning the "ropes" of experimental nuclear physics, it seems to me that my main teachers were Burt Pifer of the University of Arizona, Glen Marshall, Jess Brewer, and Professor John Warren, of the UBC Physics Department. A special acknowledgement should be given to Ryu Hayano of the University of Tokyo; the entire TRIUMF μ SR group is indebted to his genius in creating our exceedingly powerful data acquisition system which has helped advance μ SR into a new generation.

I also wish to thank my parents, which I have never before properly done, for encouraging and supporting my education, even after it became far removed from their experience. Finally, I thank Rosa Ho (who, quite unsuspectingly, became a muonium chemist herself, by marriage) for keeping me on course with her love and support whenever this thesis work fell into a state of crisis. As a muonium chemist she is more of a "director" than a "colleague."

CHAPTER I - INTRODUCTION

A Positive Muons and the μ^+ SR Method

The muon is an unstable elementary particle that was first observed as a component of cosmic rays [Anderson (37), Street (37)] and which is now artificially produced with high energy particle accelerators. Some of the properties of positive muons (μ^+) are summarized in Table I and include: unit charge, spin $\frac{1}{2}$, and a mean lifetime of 2.2 μ s.

Muons are decay products of pions, which, in turn, are produced in the nuclear interactions that take place when a nucleus is bombarded with high energy particles such as protons. Typical nuclei used for pion production at accelerators are copper and beryllium, and the minimum proton kinetic energy required for pion production in such a nucleus is about 145 MeV, the threshold energy. Positive pions (π^+) decay with a mean lifetime of 26 ns in the parity violating process [Bjorken (64)]:



which is exoergic by about 34 MeV and produces 4.1 MeV μ^+ .

The muon neutrino, ν_{μ} , is a spin $\frac{1}{2}$ particle with zero rest mass and 100% negative helicity. The helicity operator is defined as the dot product of the spin and momentum direction $\hat{h} = \vec{\sigma} \cdot \frac{\vec{p}}{|\vec{p}|}$, and has eigenvalues of +1 (positive

helicity) in which the spin is parallel to the momentum, and -1 (negative helicity) in which the spin is antiparallel to the momentum. In order to conserve linear and angular momentum, the muon formed in pion (spin 0) decay comes off in the

TABLE I: PROPERTIES OF POSITIVE MUONS

CHARGE: +1

SPIN: $\frac{1}{2}$

MASS: $105.6596 \text{ MeV}/c^2 = 206.7685 m_e$
 $= 0.1126 m_p$
 $= 0.7570 m_\pi$

MAGNETIC MOMENT: $4.49048 \times 10^{-23} \text{ erg G}^{-1}$
 $= 3.18334 \mu_p$
 $= 0.004836 \mu_e$

g-FACTOR: $2.0023318 = 1.000006 g_e$

MEAN LIFETIME: $2.1971 \mu\text{s}$

GYROMAGNETIC RATIO, $\frac{\gamma_\mu}{2\pi}$: $13.5544 \text{ kHz G}^{-1}$

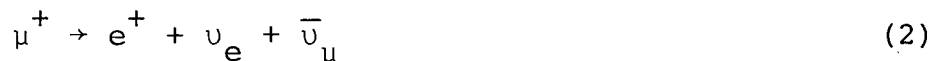
COMPTON WAVELENGTH, λ : $1.86758 \text{ fm} = \frac{\hbar}{m_\mu c}$

CHARGE RADIUS: $<0.01 \text{ fm}$

direction opposite to the neutrino with 100% negative helicity as well. This decay process is spatially isotropic in the rest frame of the pion. That parity is violated in pion decay is seen from the fact that under parity, the axial vector $\vec{\sigma}$ is unchanged, while the polar vector \vec{p} becomes $-\vec{p}$ and thus \hat{h} , a pseudoscalar, becomes $-\hat{h}$. In practical terms, the muon helicity created with the particle's birth can be translated into the design of μ^+ beams in which the muons have a net longitudinal spin polarization. A more detailed discussion of muon beams is given in Chapter II.

When high energy muons interact with matter, they thermalize primarily by ionization processes in about 10^{-9} s and retain their spin polarization [Hughes (66), Weissenberg (67), Brewer (75)]. In metals [Brewer (75), Grebinnik (76)] and gases such as He with large ionization potentials [Stambaugh (74)], μ^+ thermalize as "free" μ^+ ions; in many other materials, μ^+ end up chemically bound in diamagnetic environments. The spins of such muons will precess in a transverse magnetic field at a frequency which is proportional to the μ^+ gyro-magnetic ratio, $\frac{\gamma_{\mu}}{2\pi} = 13.55$ kHz/gauss. Because muon beams have a longitudinal spin polarization, all of the muons thermalize with the same initial phase with respect to spin precession in a transverse magnetic field.

The unstable μ^+ decays by another parity violating process:



where ν_e is an electron neutrino with negative helicity, $\bar{\nu}_{\mu}$

is a muon antineutrino with positive helicity, and e^+ is a positron with positive helicity. Weak interaction theory predicts that the three-body decay of the μ^+ is spatially anisotropic with respect to positron emission, which is preferentially along the direction of the μ^+ spin. This qualitative behavior was first confirmed experimentally by Garwin (57). The theoretical positron decay spectrum is given by the expression [Sachs (75)]:

$$\begin{aligned} \frac{dR(w, \theta)}{dw d\Omega} &= \frac{w^2}{2\pi} \{ (3-2w) - P(1-2w)\cos\theta \} \\ &= \frac{C}{2\pi} \{ 1 + D\cos\theta \} \end{aligned}$$

where $w = E/E_{\text{Max}}$ is the positron energy in units of the maximal possible energy, $E_{\text{Max}} = \frac{1}{2}m_{\mu} = 52.8 \text{ MeV}$, θ is the angle between the spin of the decaying muon and its positron trajectory, and P is the degree of spin polarization of the decaying muons. The positron energy spectrum and the asymmetry parameter, D , for $P=1$ are shown in Figure 1.

In practice, the positrons are detected with an efficiency $\epsilon(w)$ which is not constant over their energy range. The observed probability distribution then becomes [Brewer (75), Weissenberg (67)]

$$\begin{aligned} \frac{dR}{d\Omega} &= \int_0^1 \frac{dR(w, \theta)}{dw d\Omega} \epsilon(w) dw \\ &= \frac{1}{4\pi} \bar{\epsilon} (1 + \bar{A}\cos\theta) \end{aligned}$$

If positrons of all energies were detected with the same efficiency, the observed average asymmetry, \bar{A} , would be $\frac{1}{3} P$. In practice, the detection efficiency of low energy

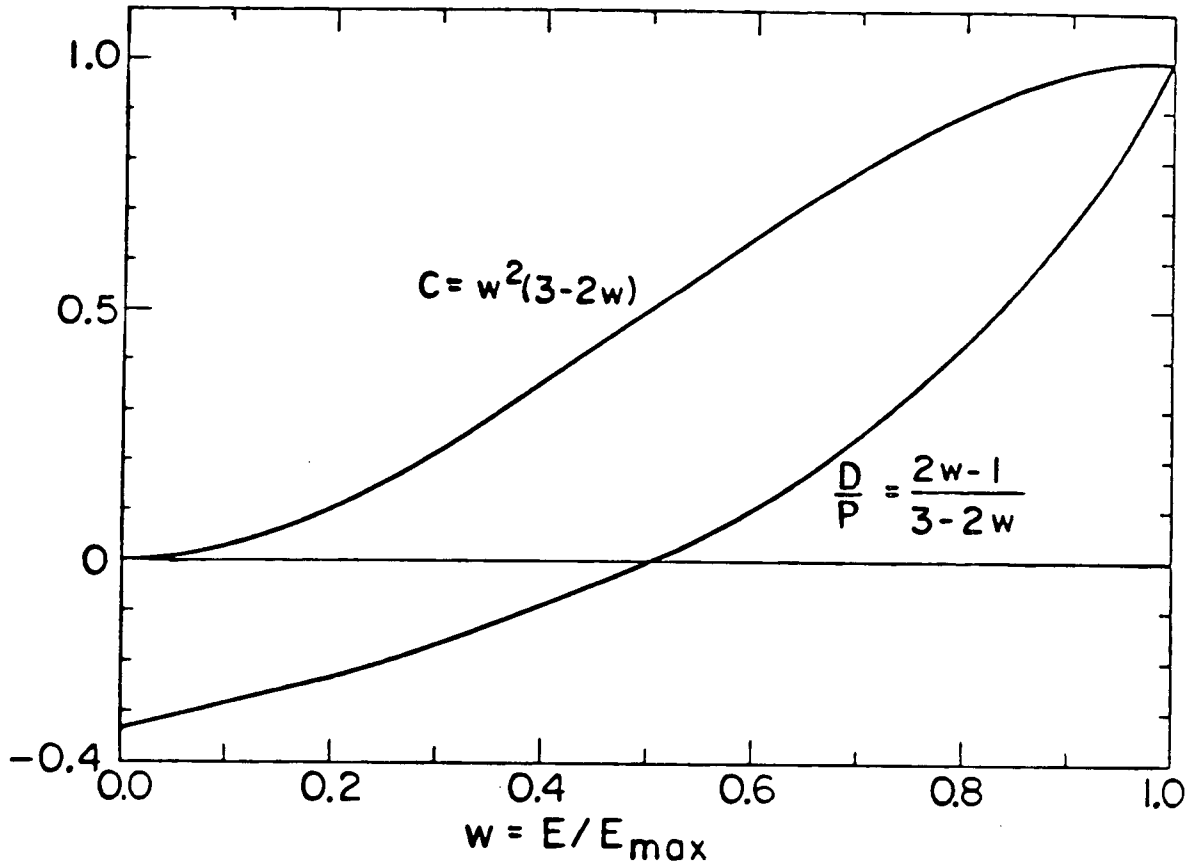


FIGURE 1: Energy spectrum of positrons from muon decay (upper curve) and energy dependence of the asymmetry parameter for 100% beam polarization ($P=1$; lower curve). The energy is given as a fraction of the maximal possible energy, $E_{\max} = 52.8$ MeV.

e^+ is reduced and the lowest energy e^+ are absorbed by matter before reaching the detectors resulting in an observed \bar{A} larger than $\frac{1}{3} P$. This effect is offset, however, by the reduction in P due to kinematic depolarization (real muon beams are not 100% polarized) and due to averaging over finite detector solid angle. In most muon experiments, the beam polarization, positron detection efficiency and solid angle corrections are not explicitly known and the resultant effective muon asymmetry, A_μ , is treated empirically in the expression:

$$R(\theta) \approx 1 + A_\mu \cos\theta \quad (3)$$

Since the average decay positron energy is about 35 MeV, corresponding to a radiation length of $15 \text{ g} \cdot \text{cm}^{-2}$ in Pb, most positrons are observable even if the muon decay occurs deep inside a substantial target.

The time differential measurement of the asymmetric decay of a spin polarized ensemble of positive muons precessing in a transverse magnetic field forms the basis of the μ^+ SR technique. The acronym, μ^+ SR, stands for "muon spin rotation" and was coined to draw attention to the strong resemblance in information content that this method bears to the familiar resonance techniques of NMR and ESR. Except in special variations such as the stroboscopic method [Schenck (76)], μ^+ SR examines one muon at a time using counting techniques common to experimental nuclear physics. The phrase "muon ensemble" in the present discussion, then, refers to an ensemble in time rather than in space.

In a μ^+ SR experiment, a longitudinally spin polarized

μ^+ passes from the beam channel through a plastic scintillator counter array and thermalizes in a target material of interest. The counters are arranged to identify muons which stop in the target; when such an event occurs, an electronic pulse is generated which starts some kind of high precision clock. The muon precesses in the target at a frequency $\omega_\mu = \gamma_\mu B$ where γ_μ is its gyromagnetic ratio and B is the transverse magnetic field experienced by the μ^+ . Noting that $\theta = \omega_\mu t$, the positron decay spectrum (3) becomes:

$$R(t) = 1 + A_\mu \cos \omega_\mu t$$

The beam polarization ensures that all muons have the same initial precession phase. A transverse magnetic field of from 50 gauss to several kgauss is externally applied in the case of non-magnetic targets; for ferromagnetic targets, a substantial transverse magnetic field may be intrinsic to the material, in which case the muon precession frequency is a direct measure of the internal field at the μ^+ in that magnetic material [Nishida (77)]. A positron counter array placed in the plane of muon precession at an angle ϕ to the initial muon beam monitors the μ^+ decay and generates an electronic pulse to stop the clock previously started by the muon entering the target. The measured time interval is incrementally binned in a time histogram, the clock is reset, and the process is repeated, typically $10^6 - 10^7$ times.

Since μ^+ decay is spatially asymmetric, the probability of detecting the positron from muon decay rises and falls as the precessing μ^+ spin swings past the fixed e^+ detectors. Because the solid angle subtended by the positron

counters is small, most muon decays are not detected, in which case the clock is reset after some arbitrary "time out" period of several muon lifetimes. The resultant μ^+ SR time histogram has the form:

$$N(\phi, t) = N_0 e^{-t/\tau_\mu} \{1 + A_\mu(t) \cos(\omega_\mu t + \phi)\} + Bg \quad (4)$$

where N is the number of counts in a histogram time bin, N_0 is a normalization factor, τ_μ is the μ^+ lifetime of 2.2 μ s, $A_\mu(t)$ is the muon asymmetry which is usually time dependent, ω_μ is the muon precession frequency, and Bg is a time independent background due to accidental events. A typical μ^+ SR time spectrum is shown in Figure 2; its most dominant features are the exponential muon lifetime upon which is superimposed the oscillating asymmetrical muon decay. The asymmetry, $A_\mu(t)$, often decays with time due to spin dephasing phenomena identical to T_2 relaxation in NMR and commonly has the form:

$$A_\mu(t) = A_\mu e^{-\lambda t} \quad (5)$$

where $\lambda = 1/T_2$. An example of such a relaxation mechanism is μ^+ spin dephasing due to local fluctuations in the internal magnetic field experienced by a μ^+ diffusing between different interstitial sites in a ferromagnetic crystal of Fe [Nishida (77)].

μ^+ SR is a passive non-resonance analogue of proton NMR in which the special properties of the muons are responsible for signal generation, eliminating the requirement for conventional power absorption detection. All of the information contained in NMR spectra transformed into the time domain is, in principle, contained in μ^+ SR spectra. Of course, the time

μ^+ SR: μ^+ IN ALUMINIUM. 69 GAUSS

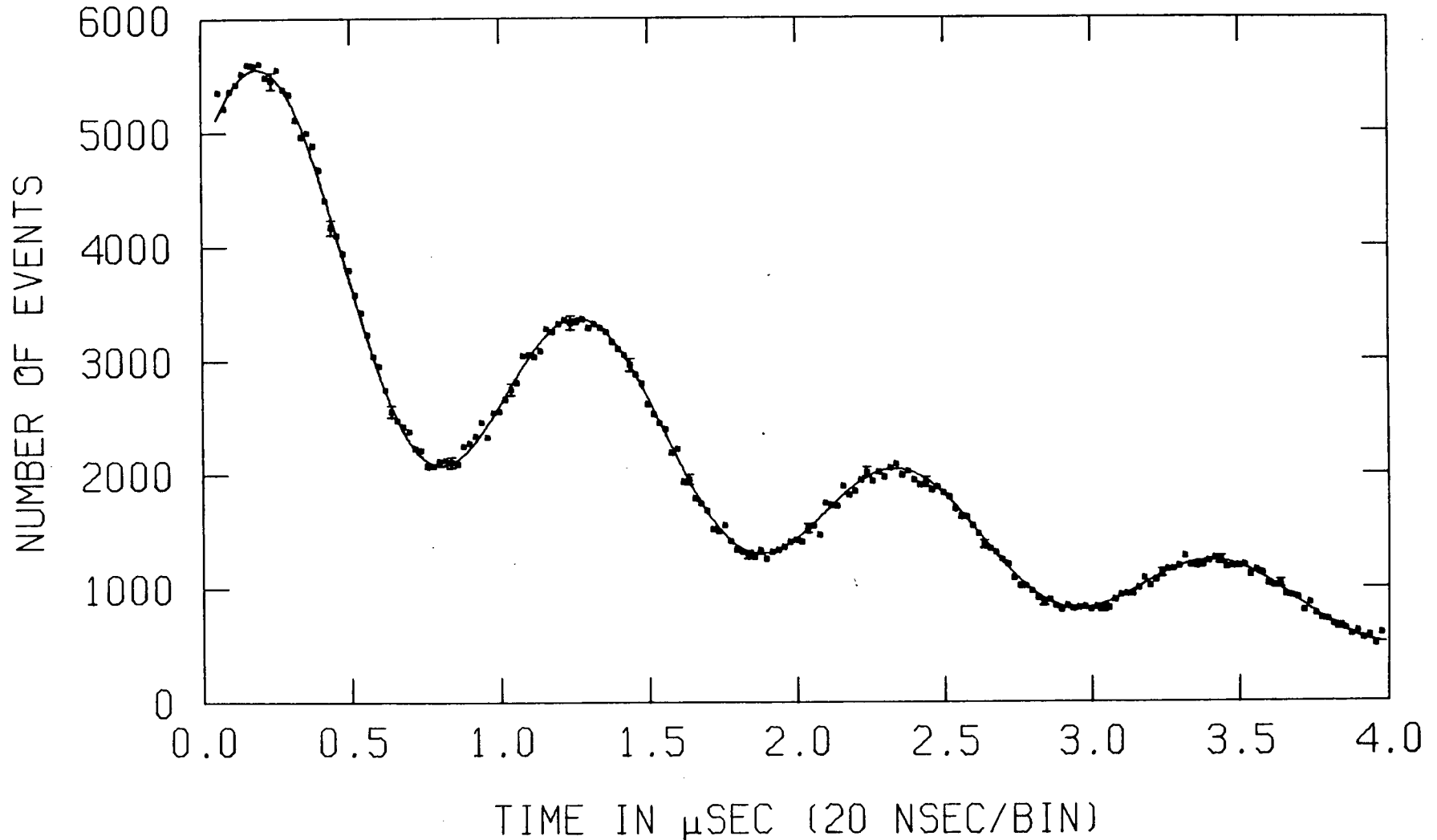


FIGURE 2: A typical μ^+ SR time histogram (data points) and χ^2 -minimum fit to equation (4). The error bars (on every 10th point) are due to counting statistics only. The histogram contains about 5×10^5 events. The μ^+ asymmetry is about 35% and $\lambda = 0.03 \mu\text{s}^{-1}$.

scale of phenomena detectable by μ^+ SR is fixed by the μ^+ lifetime. The μ^+ SR method has a number of potential advantages over NMR; one muon at a time is present in the sample thereby eliminating interferences due to interaction of the μ^+ with themselves; the μ^+ SR signal is measurable from within bulk magnetic materials while the r.f. required for NMR will only penetrate the skin of the sample; the μ^+ is a simple point charge without a complicating structure; and, in crystals, μ^+ probe the interstitial region while NMR is often constrained to examination of the lattice sites themselves.

B Muonium and the MSR Method

In most gases, liquids and non-metallic solids, the μ^+ captures an electron from the medium during the final stages of its thermalization process to form the hydrogen-like atom, muonium (Mu) [Hughes (66), Mobley (67), Brewer (75), Fleming (79)]. Some of the properties of Mu are given in Table II. Since the muon is 207 times as massive as the electron, the reduced mass of Mu is 0.996 that of H and consequently the Bohr radius and ionization potentials of H and Mu are essentially the same. Mu, therefore, behaves chemically like a light isotope of H [Goldanskii (71), Brewer (75), Jean (78)] with a mass $\frac{1}{9}$ that of normal H. This substantial mass difference potentially makes Mu an exceptionally sensitive probe of isotope effects in chemical reactions of H.

In muonium, the μ^+ spin is not only coupled to an external magnetic field but also to the electron spin via the hyperfine interaction. Since the muons are polarized while the

TABLE II: PROPERTIES OF MUONIUM

MASS: $207.8 m_e$

$0.1131 m_H$

REDUCED MASS: $0.9956 \mu_H$

FIRST BOHR RADIUS, $(a_0)_{\text{Mu}}$: $0.5315 \times 10^{-8} \text{ cm}$

$$= 1.0044 (a_0)_H$$

FIRST IONIZATION POTENTIAL: 13.54 eV

$$= 0.9956 \text{ I.P.}_H$$

THERMAL DEBROGLIE WAVELENGTH (300K): $2.979 \times 10^{-8} \text{ cm}$

$$= 2.967 \lambda_H$$

$$= \frac{h}{\sqrt{2\pi k_B T m}}$$

HYPERFINE FREQUENCY, ω_0 : $2.8044 \times 10^{10} \text{ rad s}^{-1}$

MEAN THERMAL VELOCITY (300K): $0.75 \times 10^6 \text{ cm s}^{-1}$

$$= 2.97 \bar{v}_H$$

$$= \left(\frac{8k_B T}{\pi m} \right)^{1/2}$$

captured electrons are unpolarized, the initial spin states of Mu are 50% $|\alpha_{\mu}\alpha_e\rangle$ and 50% $|\alpha_{\mu}\beta_e\rangle$, where the muon polarization direction is the quantization axis. In finite transverse magnetic field, the time evolution of the μ^+ spin polarization in Mu is quite complicated; the detailed calculation is given in Appendix I. The upshot of this calculation in the weak transverse magnetic field limit (< 10 gauss) is, however, simple: μ^+ in half of the Mu ensemble ($|\alpha_{\mu}\alpha_e\rangle$) precess at the muonium Larmor frequency, $\omega_{Mu} = 103 \omega_{\mu}$, in the sense opposite to "free" μ^+ precession; μ^+ in the other half of the Mu ensemble ($|\alpha_{\mu}\beta_e\rangle$) oscillate at the hyperfine frequency, $\omega_o = 2.8 \times 10^{10}$ rad s⁻¹. Since the experimental time resolution is about 1 nanosecond, the hyperfine oscillation is not observable and this half of the Mu ensemble appears to be totally depolarized.

Monitoring the time evolution of the μ^+ spin in Mu in weak transverse magnetic field via the asymmetric μ^+ decay forms the basis of the MSR method for studying muonium. The MSR acronym stands for "muonium spin rotation" and the method is identical with μ^+ SR with the exceptions that the μ^+ precession frequency in Mu is 103 times that for "free" μ^+ and that the μ^+ asymmetry in Mu is reduced by half. Figure 3 shows a typical MSR spectrum which has essentially the same appearance as a μ^+ SR spectrum in a magnetic field 103 times stronger. In practice, MSR histograms have the form:

$$N(\phi, t) = N_0 e^{-t/\tau_{\mu}} \{ 1 + A_{Mu}(t) \cos(\omega_{Mu} t + \phi_{Mu}) + A_{\mu} \cos(\omega_{\mu} t - \phi_{\mu}) \} + Bg \quad (6)$$

where ω_{Mu} and ω_{μ} are the muonium and muon precession frequencies,

MSR: MU IN 780 TORR N₂ AT 6.9 GAUSS

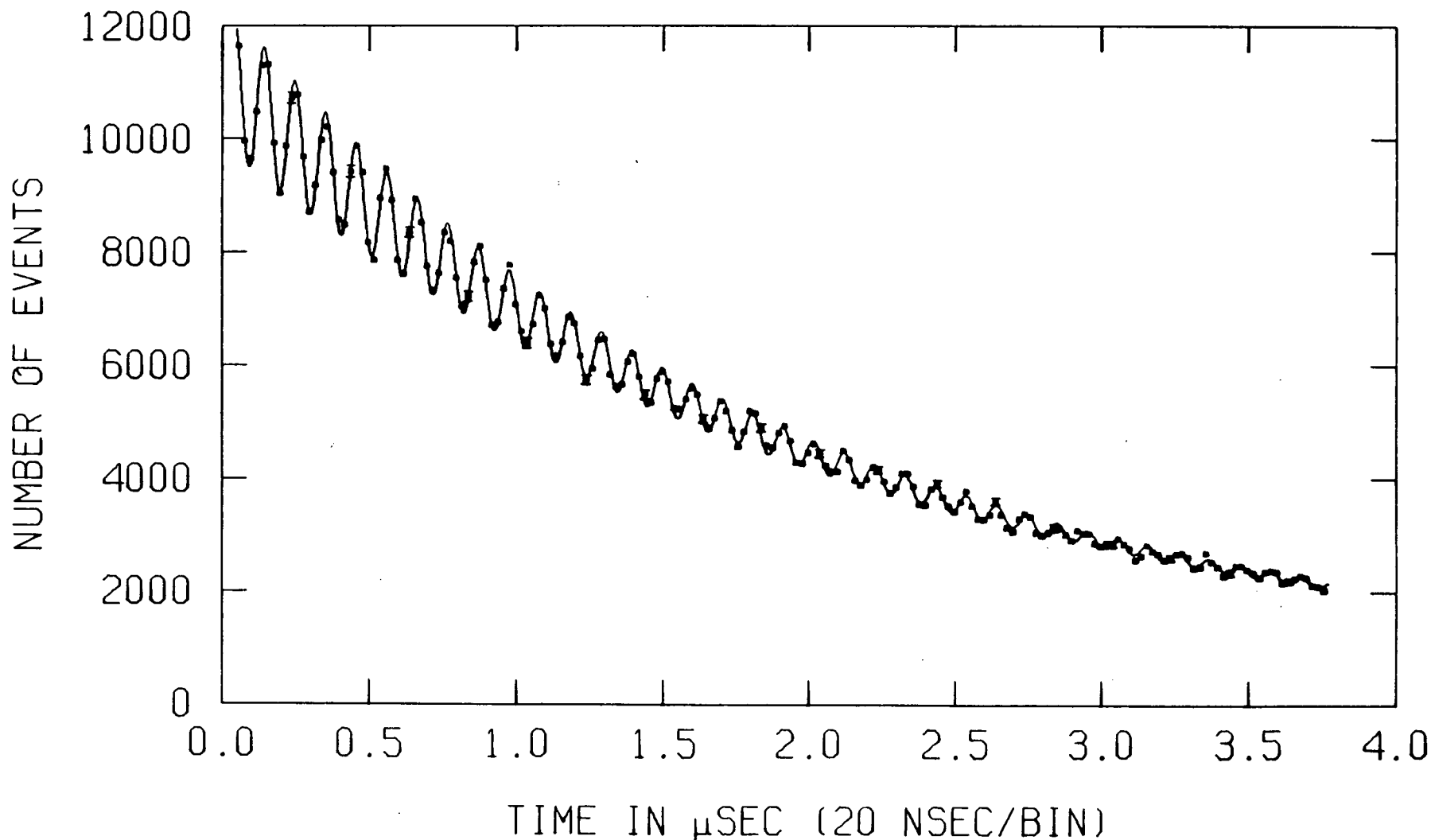


FIGURE 3: A typical MSR time histogram (data points) and χ^2 -minimum fit to equation (6). The histogram contains about 10^6 events and the error bars are due to counting statistics only. The Mu asymmetry is about 11% and the background μ^+ asymmetry is about 5.5%.

ϕ_{Mu} and ϕ_{μ} are the initial muonium and muon phases, while $A_{\text{Mu}}(t)$ and A_{μ} are the muonium and muon asymmetries. The "free" muon precession term may come from several sources: Mu formation in some materials is incomplete; in gas targets, muons may scatter into the walls of the gas vessel where they may not form Mu; muonium atoms may react chemically on the very short time scale of less than one hyperfine period of 0.225 ns. (probably by epithermal reaction) in which case the hyperfine interaction is broken, resulting in coherent precession of the polarized μ^+ ensemble residing in diamagnetic environments. In muonium experiments, the asymmetry of the free μ^+ term is usually independent of time while the muonium asymmetry generally has a form similar to equation (5):

$$A_{\text{Mu}}(t) = A_{\text{Mu}} e^{-\lambda t} \quad (7)$$

The muonium relaxation rate, λ , is due to effects such as pressure broadening in gases, chemical reaction and magnetic field inhomogeneity. The effects of chemical reactions are discussed in some detail in Appendix II. Finally, it should be noted that the phases, ϕ_{Mu} and ϕ_{μ} , have opposite signs to account for the fact that the free μ^+ and μ^+ in Mu precess in opposite directions. In condensed media with a well defined μ^+ stopping region, the magnitudes of ϕ_{Mu} and ϕ_{μ} are the same; however, in low pressure gases, the μ^+ stopping region is smeared out enough that significant differences in the magnitudes of ϕ_{Mu} and ϕ_{μ} may appear.

Throughout this thesis, reference will be made to the MSR "signal," $S(\phi, t)$, which is defined as:

$$S(\phi, t) = A_{\text{Mu}} e^{-\lambda t} \cos(\omega_{\text{Mu}} t + \phi_{\text{Mu}}) + A_{\mu} \cos(\omega_{\mu} t - \phi_{\mu}) \quad (8)$$

Figure 4 shows the MSR signal corresponding to the time histogram of Figure 3. The slow free muon precession appears as an approximately linear background at the weak magnetic fields used in MSR.

C Muonium Chemistry - An Historical Background

Muonium formation was first proposed as an explanation for the observation that the "residual muon polarization" (see Appendix II) is not the same in all condensed media [Swanson (58)]. Nosov and Yakovleva (63) and Ivanter and Smilga (68) derived a detailed model for muon depolarization phenomena in solids. Firsov and Byakov (65) attempted to relate the residual polarization to Mu chemistry in liquids with a model in terms of which the later results of Babaev (66) were misinterpreted. In 1969, Ivanter and Smilga (69) extended the formalism to correctly treat Mu chemistry in liquids for simple reactive systems.

The first extensive experimental study of thermal Mu reactions was by Brewer (72) who applied a modified form of the muonium mechanism of Ivanter and Smilga to the measurement of bimolecular rate constants of simple Mu reactions in liquids. These experiments, conducted at the 184" Cyclotron at the Lawrence Berkeley Laboratory (LBL), grew out of an experiment to determine the muon's magnetic moment precisely [Hague (70)] which required small corrections due to chemical effects. Brewer also found it necessary to extend the model to include epithermal reactions of Mu as well as reactions in which

MSR: MU IN 780 TORR N₂ AT 6.9 GAUSS

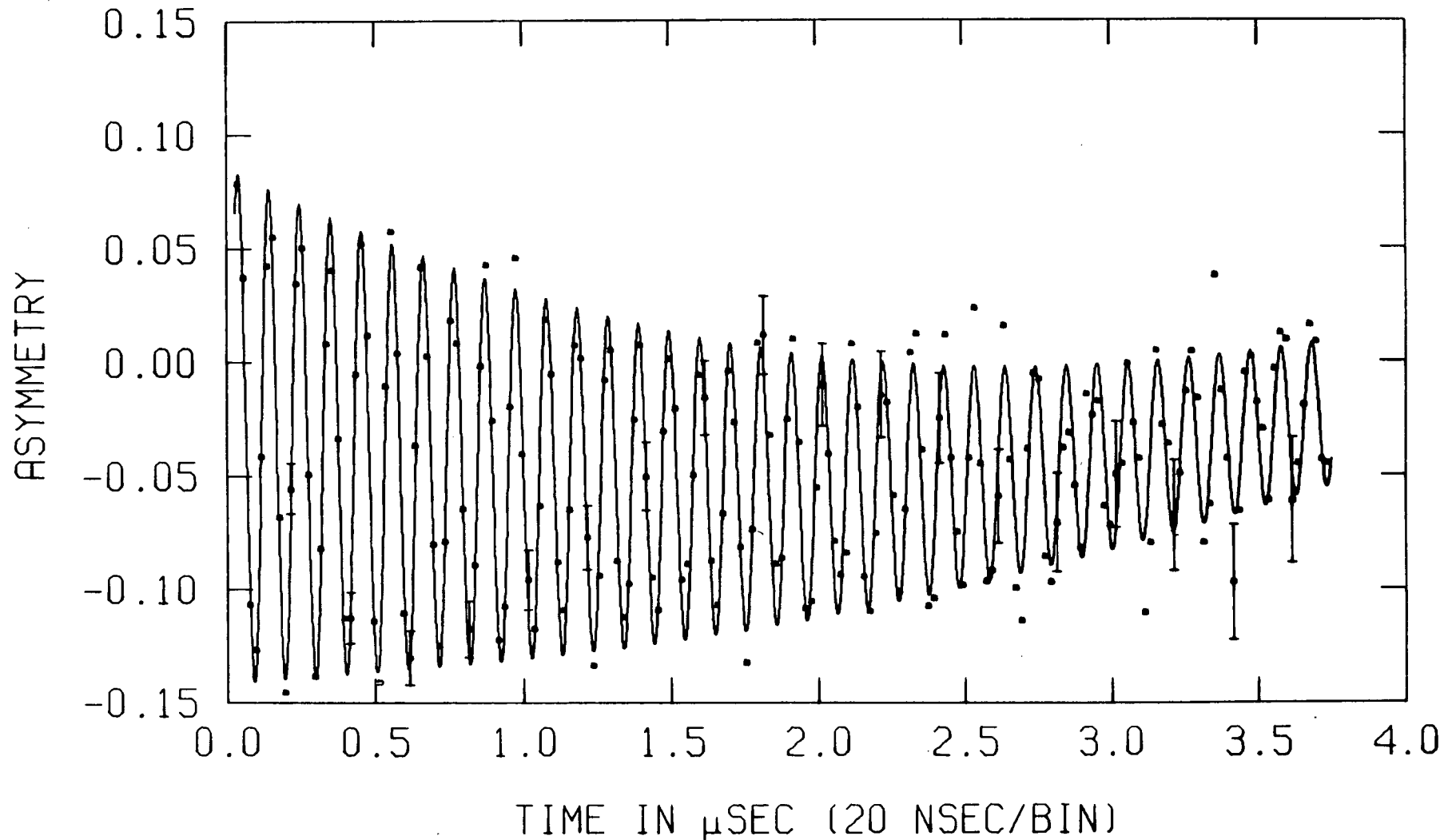


FIGURE 4: The MSR signal, $S(\phi, t)$, corresponding to the histogram shown in Figure 3. The line is a χ^2 -minimum fit to equation (8). The rapid oscillations are due to μ^+ precession in Mu, while the slowly curving drift is due to "free" μ^+ precession.

transient muonic radicals are formed. Although Brewer's work established the foundations of experimental Mu chemistry, it suffered from a number of serious shortcomings, the most notable of which was the failure to detect muonium in liquids directly by the MSR method. Muonium reactions were measured by the indirect residual polarization method described in Appendix II using μ^+ SR techniques. With this method, details of the reaction mechanisms had to be inferred and the rate constants obtained were largely model dependent. In reactions involving several rate processes, such as those due to intermediate radical formation, the extracted rate constants were highly correlated and of questionable absolute accuracy [Percival 1-(76), Percival (77)]. While this indirect method has been substantially replaced with more direct methods described below, Brewer's pioneering work provided a valuable preliminary insight into the details of muonium chemistry in liquids. For example, in spite of tentative results suggesting the possibility of direct detection of muonic radicals in condensed media [Kent (77), Bucci (78)]¹, Brewer's work still provides the most convincing demonstration of the importance of such radicals in liquid phase reactions of Mu [Brewer (73)]. Although the subject of some contention [Percival (78)], the residual polarization method might well prove to be the one most amenable to the study of epithermal Mu reactions in liquids.

¹During preparation of this thesis, the direct observation of several muonic radicals was confirmed at SIN [Roduner¹ (78)].

The study of muonium chemistry in liquids is complicated by several processes such as solvolysis and "spur" reactions [see, for example, Gold (78)]. From the viewpoint of understanding elementary chemical rate processes, the gas phase provides a physical context which is more theoretically tractable than the liquid phase. The only gas phase Mu chemistry studies prior to the work in this thesis were a series of experiments conducted by Mobley et al. [Mobley (66), 1-(67), 2-(67)] in argon gas at high pressure (40 atmospheres) at the Nevis Laboratory at Columbia University. A variety of techniques including direct observation of Mu by the MSR method were employed to examine the interactions of Mu with O_2 , C_2H_4 and CH_3Cl and a number of other reagents. Unfortunately, the conventional muon beam available to Mobley was of such high momentum that very high pressure gas targets were required to thermalize a useful fraction of the beam. At 40 atmospheres, three body processes play an important role in the chemical reactions; it is preferable to use low pressure gas targets at about 1 atmosphere to measure bimolecular Mu reaction rates.

Motivated by a proposal to measure the conversion of muonium (μ^+e^-) to antimuonium (μ^-e^+) [see, for example, Lederman (77)] which requires the production of thermal Mu in vacuum, a group from the University of Arizona designed a new kind of low momentum muon beam line at the 184" Cyclotron at LBL [Pifer (76)]. Some of the details of this new "surface" muon beam (sometimes called an "Arizona" muon beam) are given in Chapter II. In collaboration with the Arizona group, this thesis work was started at their surface muon facility at

LBL during 1974-75 when the first low pressure gas phase Mu bimolecular reaction rate constant was determined by the MSR technique, for the $\text{Mu} + \text{Br}_2$ reaction at 295 K in 1 atmosphere of Ar [Fleming (76)]. The collaboration with the Arizona group was continued until July, 1975, when support for physics experiments at the 184" Cyclotron ceased and the machine became a dedicated medical facility. It is, perhaps, an historical footnote to remark that the $\text{Mu} + \text{Cl}_2$ reaction rate measurement [Fleming (77)] was the last non-medical experiment executed on that machine.

A major technological advance in the study of muon physics and chemistry in recent years is the development of a new generation of a very high current "intermediate" energy particle accelerators, the so-called "meson factories". These machines produce meson beams with intensities that are two or more orders of magnitude greater than those previously available. At present, there are three such facilities operational in the world: the Schweizerisches Institut für Nuklearforschung (SIN) near Zürich, the Clinton P. Anderson Meson Physics Facility (LAMPF) at Los Alamos, and the Tri-University Meson Facility (TRIUMF) in Vancouver. In 1976, gas phase Mu reaction rate measurements at low pressure were first performed at TRIUMF on the M20 μ^+ SR Facility operating in surface muon mode. Although surface muon beam lines required for low pressure gas phase targets are currently being commissioned at LAMPF and under construction at SIN, at present TRIUMF is the only meson factory with an operational facility of this kind. Recently, another surface muon facility (using

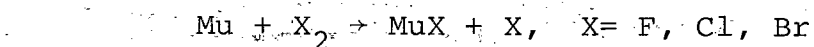
the beam components from the original Arizona beam line at Berkeley) was de-commissioned at the 600 MeV synchrocyclotron of the Space Radiation Effects Laboratory (SREL) in Virginia.

With the advent of meson factories came a number of advances in Mu chemistry, among the most important of which was the direct observation of Mu in water by the MSR technique at SIN [Percival 2-(76)]. This discovery, recently confirmed at TRIUMF [Jean 1-(78)], has largely rendered obsolete the residual polarization method used by Brewer in the study of thermal chemical reactions of Mu in the liquid phase and placed liquid Mu chemistry on the firmer experimental footing previously enjoyed only by gas phase studies. It should be remarked that liquid phase MSR signals are much weaker than gas phase signals. To date, the SIN group have applied MSR to the study of a number of chemical reactions in a variety of liquid media [Percival (77), Roduner 2-(78)].

Further impetus was given to gas phase Mu chemistry when the first detailed theoretical calculation of a Mu reaction rate was performed by a group in Europe [Connor 1-(77)] for the reaction: $\text{Mu} + \text{F}_2 \rightarrow \text{MuF} + \text{F}$. Considerable attention will be given to this and subsequent calculations in Chapter IV.

D Organization of the Dissertation

This thesis reports the first measurements of Mu reaction rates in low pressure gases (~1 atmosphere), for the reactions:



and



at 295K. In addition, activation energies are reported for the F_2 and Cl_2 reactions between 300 and 400K.

As detailed in Chapters III and IV, the motivation for this study is twofold: (1) as a light isotope of H, Mu provides a remarkably sensitive probe of mass effects in H atom reactions, and (2) unlike the techniques of H atom chemistry, MSR is literally a one-atom-at-a-time method, unencumbered by interactions of the Mu atoms with themselves. With sufficient understanding of the first point, it may be possible to exploit the second point to obtain accurate values of H atom reaction rates for systems where they are not measurable by other methods.

This thesis is composed of three main parts. Chapter II describes how the MSR technique is applied to the measurement of gas phase chemical reaction rates. Included are descriptions of the surface muon beam, gas target apparatus, counting procedures, electronic logic and data acquisition, and methods of data analysis.

Chapter III presents a brief general theoretical discussion of gas phase reactions of Mu as an H isotope. Mu and H are compared in terms of the kinetic isotope effect; possible implications of differing energy dispositions in the transition state and among reaction products of Mu and H reactions are discussed; and, finally, some dynamical isotope

effects are examined with particular attention to quantum mechanical tunnelling.

In Chapter IV, the experimental gas phase Mu reaction rate measurements are compared with experimental values for the analogous H atom reactions and with theoretical predictions.

CHAPTER II - EXPERIMENTAL DETAILS

It was mentioned in Chapter I that the first of the experiments described in this thesis were conducted at the 184" Cyclotron at Berkeley; details of those experiments are not given here but may be found in several references [Pifer (76), Fleming (76), Fleming 1-(77)]. Like most technologies, MSR methods are constantly evolving. Rather than attempting to provide a history of MSR development at LBL and TRIUMF, this Chapter will only describe the "state of the art" techniques as practiced at TRIUMF in 1978. Some specific suggestions for future improvements, particularly in the electronic logic system, are included.

A. TRIUMF and the M20 Muon Beam Line

The TRIUMF Annual Reports 1972-76 are a good source for detailed information on the many TRIUMF facilities; only a few central points are given here. The TRIUMF cyclotron and experimental areas are shown in Figure 5. TRIUMF is a sector-focussed H^- cyclotron that delivers protons of continuously variable energy ranging from 185-520 MeV at maximum design currents of 100 μA at 500 MeV and 450 μA at 450 MeV. Most of the experiments described in this thesis were conducted with a 5-10 μA proton beam at 500 MeV. One of the most attractive features of the TRIUMF cyclotron from the viewpoint of MSR is its 100% macroscopic duty cycle: seen on a macroscopic time scale (as short as microseconds), the proton beam appears to be a continuous current without a time

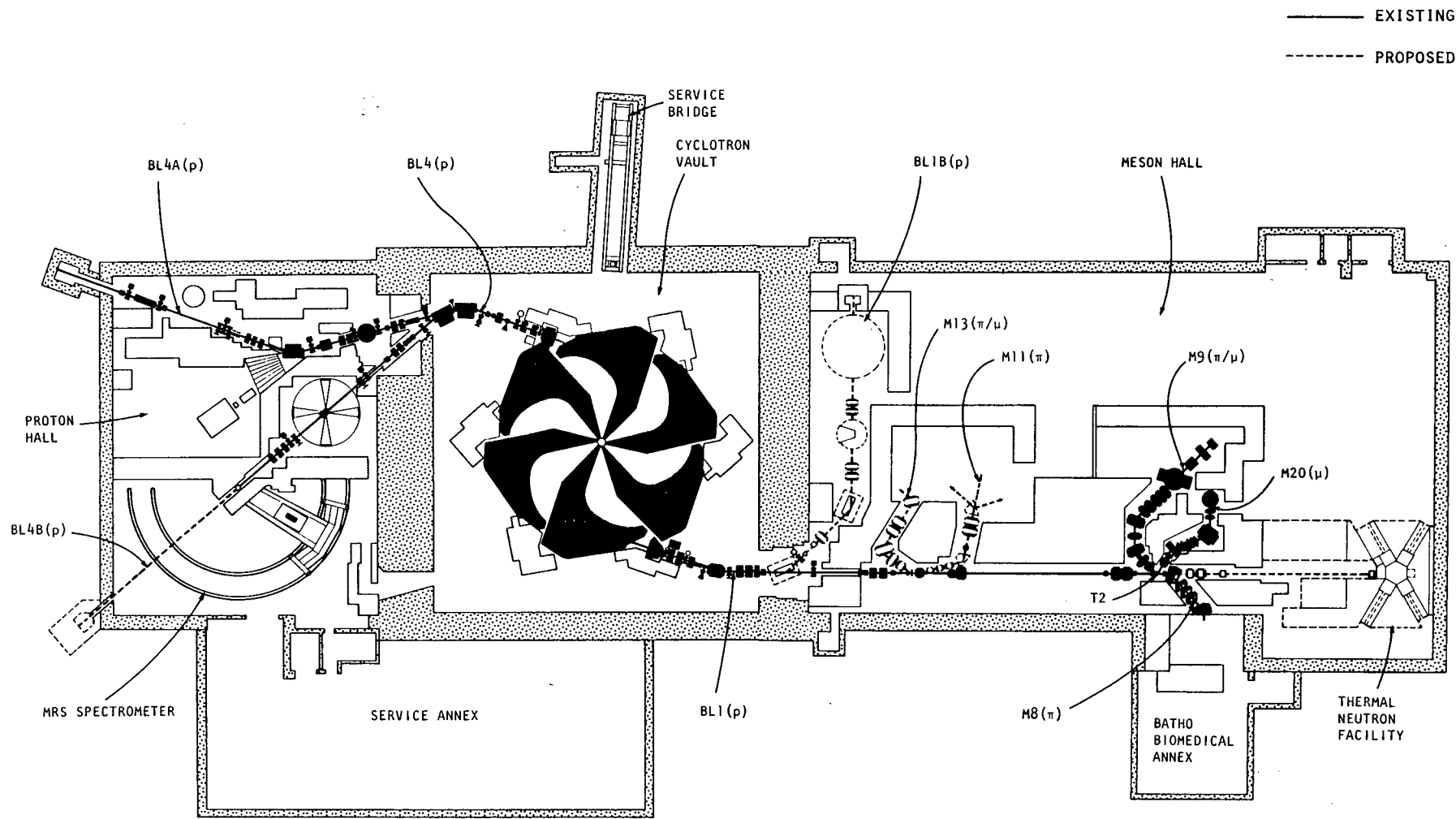


FIGURE 5: The TRIUMF Cyclotron and experimental facilities (1977).

structure. The microscopic duty cycle is a 5 nanosecond burst of protons every 43 ns. The MSR method requires that at most one muon be in the target at a time. Thus, the instantaneous muon stopping rate in the target has an absolute upper limit of the order of $10^5 \mu^+ s^{-1}$ (the inverse of a few muon lifetimes). At pulsed beam facilities such as LAMPF, which has a 6% duty cycle (a 500 μs burst every 8 ms), the maximum allowable average counting rate is decreased by exactly the duty factor of the machine. This limitation occasionally can be side-stepped by the use of special multiple muon techniques such as the stroboscopic method [Schenck (76)], but the severe restrictions placed on the experiments that use this method greatly limit its applicability. Even with its 100% duty cycle, the intense beams available at TRIUMF are capable of implanting more than one muon in a target at a time; a detailed discussion of this problem of muon "pile-up" is given in Section C and Appendix III.

A proton beam, extracted from the cyclotron by stripping the electrons from the H^- ions, passes down beamline-1 (BL-1) in the "meson hall" and strikes a pion production target, T2. The target used in this work consists of a water-cooled beryllium strip, 10 cm long in the beam direction, and 5mm by 15 mm in cross section; pions are produced here via nuclear reactions such as: ${}^9\text{Be}(p, \pi^+) {}^{10}\text{Be}$. Three secondary beamlines simultaneously extract mesons (π or μ) produced at T2: M8, primarily intended for use in π^- cancer therapy; M9, a

"stopped" π^\pm or μ^\pm beamline used for a variety of experiments (the modifier "stopped" indicates that the π or μ beam is of sufficiently low energy to stop in small experimental targets, in contrast to π or μ beams used for scattering experiments); and M20, a stopped μ^\pm beamline which is essentially dedicated to μ^+ SR. The experiments described in this thesis were performed on M20 which generally operates parasitically, delivering muons whenever there is beam on T2.

M20 (shown in Figure 6) transports a muon beam in vacuum to the experimental target in one of three operating modes: "conventional," "cloud" or "surface" muon mode. In conventional mode, positive pions produced from T2 at 55° to the proton beam are collected into M20 by the quadrupole doublet Q1-Q2 and then momentum selected ($\frac{\Delta p}{p} \approx 20\%$, $p \leq 170$ MeV/c) by the first bending magnet, B1 ("Patty-Jane"). Of course, B1 also charge selects particles since neutrals (γ, π^0, n) pass straight through B1 and negative particles are bent out of the beamline. Some fraction of the π^+ ($\tau_\pi = 26$ ns) decay in flight between B1 and B2 ("Cal-Tech") in quadrupoles Q3-Q7 (the "straight section"). Seen in the pion rest frame, π^+ decay is spatially isotropic and the μ^+ formed have a momentum of 29.8 MeV/c. Thus μ^+ that are formed in the momentum direction of the pion beam ("forward" muons) have ≤ 29.8 MeV/c more momentum than that selected by B1 and μ^+ that are formed opposite to the momentum direction of the pion beam ("backward" muons) have ≥ 29.8 MeV/c less momentum than that selected by B1. Nominal forward and backward μ^+ momenta are given as a function of decaying π^+ momentum in Table III.

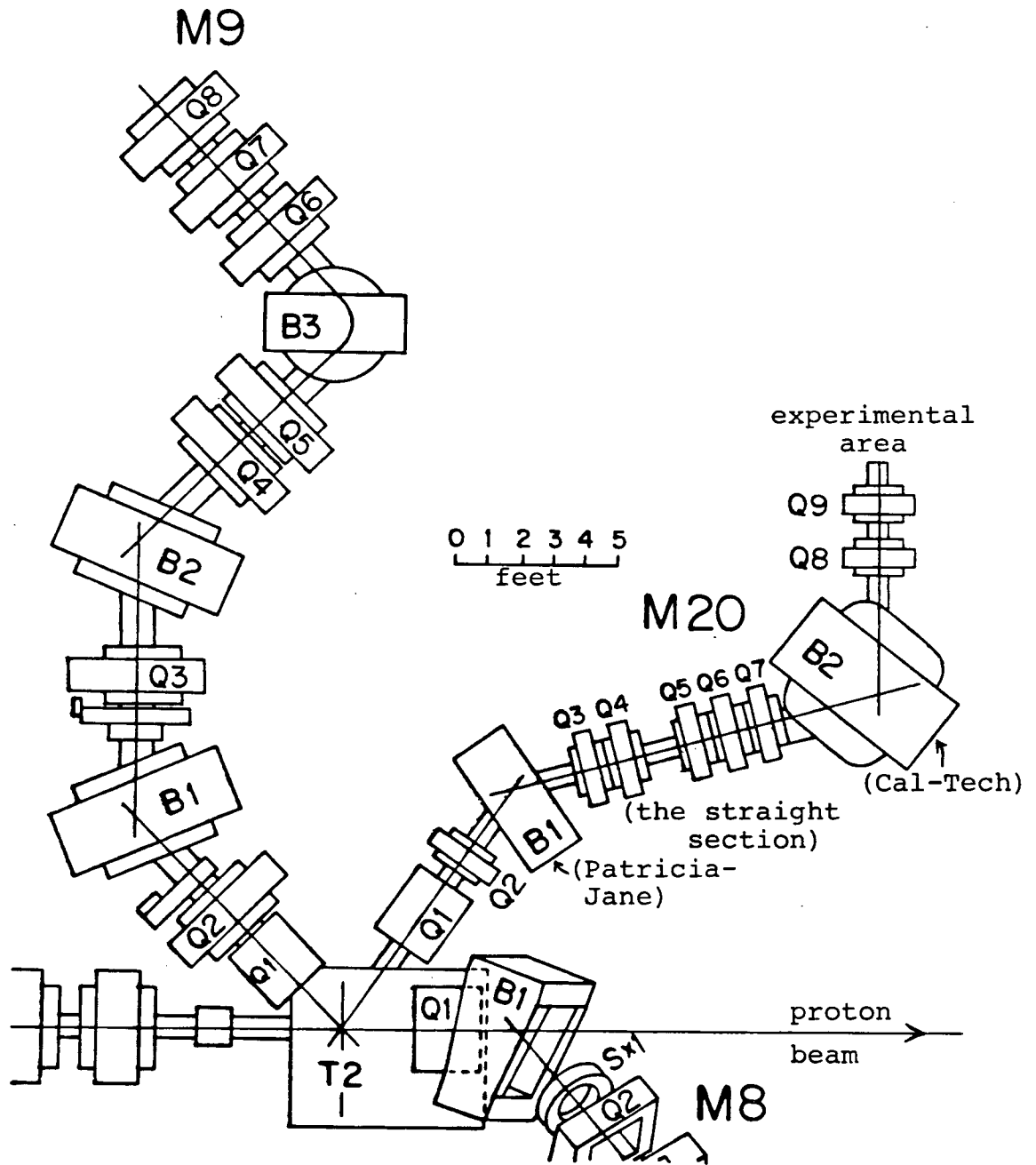


FIGURE 6: The M20 beamline (detail).

TABLE III: NOMINAL FORWARD AND BACKWARD μ^+ MOMENTA AND VELOCITIES[†]
AS A FUNCTION OF DECAYING π^+ MOMENTUM

Pions		Forward Muons		Backward Muons	
$\bar{p}_\pi + (\text{MeV}/c)$	β_{π^+}	$\bar{p}_\mu + (\text{MeV}/c)$	β_{μ^+}	$\bar{p}_\mu + (\text{MeV}/c)$	β_{μ^+}
170	0.77	180.6	0.86	86.7	0.63
160	0.75	171.2	0.85	80.5	0.60
150	0.73	161.8	0.84	74.2	0.57
140	0.71	152.4	0.82	67.9	0.54
130	0.68	143.0	0.80	61.5	0.50
120	0.65	133.7	0.78	55.1	0.46
110	0.62	124.5	0.76	48.5	0.42
100	0.58	115.4	0.74	42.0	0.37
90	0.54	106.3	0.71	35.3	0.32
80	0.50	97.3	0.68	28.5	0.26
70	0.45	88.5	0.64	21.7	0.20
60	0.39	79.7	0.60	14.7	0.14
50	0.34	71.0	0.56	7.6	0.07
40	0.27	62.5	0.51	0.4	0.00
30	0.21	54.1	0.45	-7.0	-0.07
20	0.14	45.9	0.40	-14.4	-0.13
10	0.07	37.8	0.34	-22.1	-0.20
0	0.00	29.8*	0.27	-29.8	-0.27

[†] \bar{p} and β are given with respect to the π^+ beam direction with

$$\beta = \frac{\bar{v}}{c}$$

* "surface" or "Arizona" muons

Notice that the momentum separation between μ^+ and π^+ is excellent for backward μ^+ but rather poor for forward μ^+ . The second bending magnet, B2, is tuned to momentum select either forward or backward muons from the other particles in the beam (e^+ , π^+ , μ^+ , p^+). The resultant high momentum polarized μ^+ beam is delivered to the μ^+ SR apparatus at the end of the beamline through the last quadrupole doublet, Q8-Q9.

In "cloud" muon mode, high momentum (<170 MeV/c) μ^+ produced from the "cloud" of pions decaying in flight between T2 and B1 are collected and transported through M20 with B1 and B2 both set at the same momentum-selecting fields. The essential difference between conventional and cloud muon modes, then, is that in the former case, muons are produced from pions decaying in flight after the first bending magnet, while in the latter case, muons come from π^+ decaying before the first bending magnet near T2. In general, cloud muon mode produces higher fluxes of μ^+ by a factor of as much as 4 but with a lower polarization than conventional forward muon mode (50-60% polarization compared to 70-80%) and with much worse contamination with protons, pions and positrons. When M20 is tuned for backward conventional muons, the flux is lower by about a factor of 10 compared to forward muons but beam contamination is lower by several orders of magnitude (see Table III).

In practice, with proton currents of $<10\mu\text{A}$, beam quality is often sacrificed for flux by operating M20 in cloud muon mode, yielding about $10^4 \mu^+ \text{s}^{-1}$ over a 10 cm x 10 cm area per

μ A of protons. The beam delivered in this mode is contaminated with positrons and pions in a 100:3:1 ratio to muons; there is also some contamination from forward scattered protons from T2. μ^+ SR experiments utilizing cloud muons are complicated by the necessity to work around this contamination. Since all particles delivered by the beamline are of the same momentum distribution, the slower, more massive protons and pions may be eliminated by differential absorption in degrader placed upstream of the μ^+ SR target. Positrons are separated from muons logically, rather than physically, by placing a veto counter downstream of the muon target; the positrons are sufficiently energetic to pass through the target in which most of the muons stop. None of these methods are completely successful in removing beam contamination resulting in the appearance of various background signals in the μ^+ SR time spectrum. In addition to these drawbacks, cloud or conventional muons are unsatisfactory for gas phase targets since their high momentum and concomitant long range require a high pressure stopping target [Mobley 2-(67)].

Surface or Arizona muon mode [Pifer (76)] is similar to cloud muon mode inasmuch as muons are collected by M20 directly from T2. The difference is that surface muons come from pions that decay at rest on the surface of the pion production target (see Table III) whereas cloud muons come from pions decaying in flight between T2 and B1. Since cloud muons include both forward and backward muons, the beam polarization is low; virtually all surface muons, however, arise from π^+ decaying in the forward direction, giving them a very high polarization

(>95%). Surface muons are nearly monoenergetic (4.1MeV) with a nominal momentum of 29.8MeV/c corresponding to a range of only 148 mg cm^{-2} of CH_2 or about 130 cm in argon gas at one atmosphere. Contamination of the surface muon beam with pions and protons is negligible. The velocity of 30 MeV/c pions is about $0.2c$ corresponding to a beamline transit time of 160 ns or 6 pion lifetimes; thus only about 0.3% of the small number of pions initially produced at 30 MeV/c survive to reach the end of the beamline. Protons at 30 MeV/c have insufficient range to penetrate the thin (0.05 mm Mylar) beamline vacuum window. However, as in other modes of operation, there are about 100 times more positrons than muons in the surface muon beam. Fortunately, the positrons can be logically distinguished from μ^+ by pulse height discrimination, as described in Section C below [Marshall (76)] which eliminates the complication of a positron veto counter requirement. Unfortunately, this tidy, logical removal of the contamination requires physical placement of the counters used to monitor positrons from muon decay at 90° to the beam to prevent their saturation by beam positrons; for many experiments, this restriction is prohibitive. In the near future, some of the M20 positron contamination will be removed by adding a very thin degrader in the straight section. This will reduce the μ^+ momentum much more than the positron momentum, so that by tuning Cal-Tech to the lower μ^+ momentum, the positron contamination will be considerably reduced. The disadvantage of this simple separation technique is that it sacrifices both μ^+ flux and range, the latter being

at a premium for surface muons. However, it should be possible to partially compensate for this loss by redesigning the surface μ^+ SR targets to incorporate fewer and thinner windows. At present, M20 delivers about 6×10^3 surface $\mu^+ s^{-1}$ over a 10 cm x 10 cm area per μA of 500 MeV protons incident on the 10 cm Be target of T2.

B. The Gas Target, Counters and Magnetic Field

The gas target and counter configuration are illustrated in Figure 7. The gas target vessel is an aluminum cylinder 75 cm in length with a 25 cm inner diameter. One end of the gas can is fitted with a thin (0.13 - 0.25 mm Mylar) window 20 cm in diameter which is capable of supporting a vacuum of 5×10^{-6} torr or an absolute pressure of ≈ 2.5 atmospheres. The volume of the target vessel is 36.65 ± 0.34 l at an absolute pressure of 800 torr, accounting for the volume displacement caused by pressure distortion of the Mylar window. The other end of the aluminum cylinder is closed with a flange housing pressure gauges and a stainless steel vacuum rack. The gas can is wrapped in heating tape and insulation providing the target with an operational temperature range from ~ 300 to ~ 400 K. The temperature is monitored with a copper-constantan thermocouple which is placed to probe the muon stopping region; the temperature variation across the diameter of the vessel is less than 2K. Cooling coils are mounted at both ends of the vessel to accelerate stabilization of the target temperature. This rudimentary target system will be redesigned in the near future to allow a much wider working temperature range and

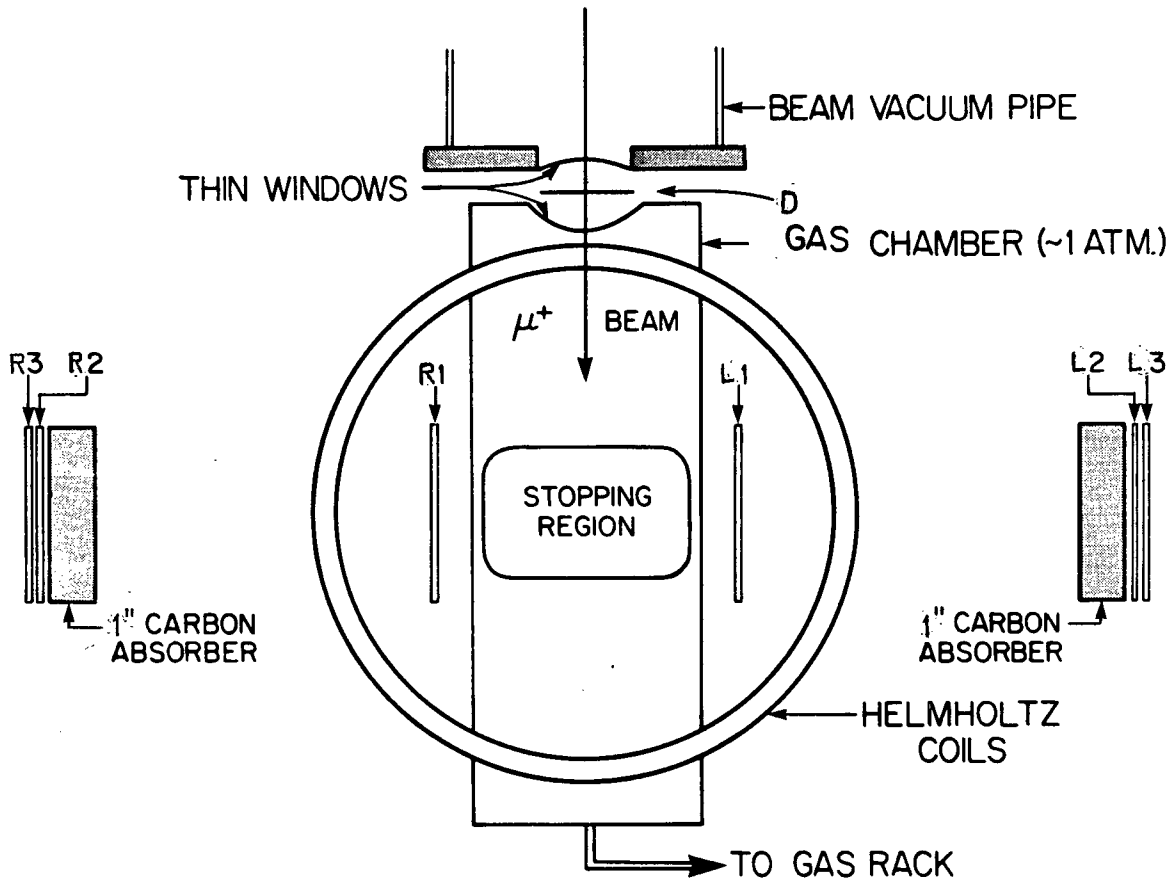


FIGURE 7: The gas phase MSR target apparatus (top view). The counter telescopes are designated left and right according to the convention: muon's eye view.

somewhat larger pressure range.

The gas target vessel is mounted on a portable cart between dual Helmholtz coils driven by a current regulated Hewlett-Packard Harrison 6268A power supply. These coils provide a variable magnetic field from ~ 1 to 75 gauss which is homogeneous to better than 0.1% over a volume of 400 cm^3 .

A single thin (40 mg cm^{-2}) $10 \text{ cm} \times 10 \text{ cm}$ NE102 plastic scintillator [Marshall (76)] serves as a beam defining and μ - stop timing counter. Two positron telescopes are placed at $\pm 90^\circ$ to both the beam direction and the transverse magnetic field. Each telescope consists of one $20 \text{ cm} \times 20 \text{ cm} \times 0.6 \text{ cm}$ (closest to the target) and two $20 \text{ cm} \times 40 \text{ cm} \times 0.6 \text{ cm}$ plastic scintillators, as shown in Figure 7, which normally operate with 1" of graphite degrader between the first and second counters. This degrader serves to reduce scattered beam positron background and to absorb low energy positrons from muon decay, thereby enhancing the empirical muon asymmetry (see Figure 1). The "left" and "right" positron telescopes are designated by the mnemonic convention: muon's eye view.

The gas phase targets consist of chemically inert moderator gas containing small concentrations of the reagent of interest. The moderator gas serves not only to thermalize the incoming muons, but also to provide the ionization processes etc. for the formation of Mu [Stambaugh (74)]. In the earlier experiments, Ar was employed as the moderator gas; recently, N_2 has been used because it has been found to

be about 1.5 times more efficient than Ar at producing Mu without causing a significantly different background Mu relaxation, λ_0 (see Appendix II), as illustrated in Figure 8. Furthermore, N_2 has a lower muon stopping density than Ar, thereby providing a longer muon range that affords greater flexibility in the design of windows and counters for optimizing the location of the muon stopping region with respect to the positron counters. The experimental operating pressure is usually chosen to be about 780 torr in order to reduce possible O_2 leakage into the reaction vessel. In N_2 at this pressure, the residual range of surface muons, which have been degraded by passing through the thin counter and two windows, is about 30 ± 5 cm at 300K. At higher temperatures, this operating pressure is maintained; the subsequent lower density of the gas target is compensated for by using a thicker window (required for high temperatures) and additional sheets of Mylar degrader. A muon range curve is taken at each temperature to ensure optimal location of the muon stopping region. Occasionally, the reaction rate of Mu with a reagent is sufficiently slow (eg. HCl) that such large concentrations of that reagent are required that it must then also serve as the moderator. In recent experiments, the high purity moderator gases are further purified by passing them through activated charcoal or a Dow Chemical G.C. carrier purifier, reducing O_2 contamination to less than 1 ppm. This results in a reduced background Mu relaxation rate, λ_0 , although the effect is not dramatic.

Measured concentrations of reactant gas are added to

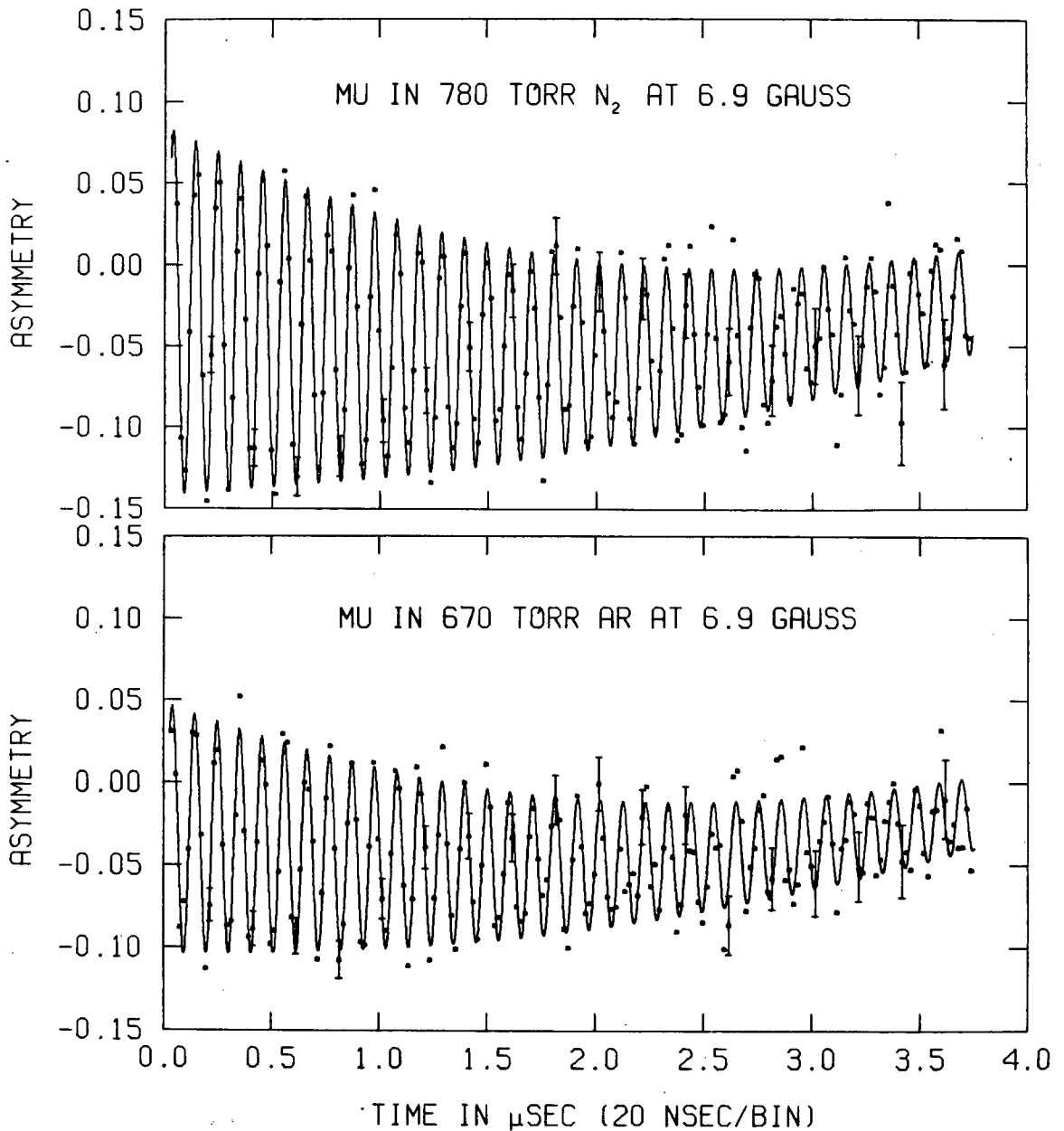


FIGURE 8: Nitrogen versus argon as moderator gases. Both spectra were taken under identical conditions, except that the gas pressures were chosen to optimize the location of the muon stopping region. In nitrogen (top), the muonium signal amplitude is 11.4 ± 0.3 % with a relaxation rate of $0.34 \pm 0.02 \mu\text{s}^{-1}$. In argon (bottom), the muonium signal amplitude is 7.6 ± 0.2 % with a relaxation rate of $0.33 \pm 0.03 \mu\text{s}^{-1}$.

the reaction vessel by filling a small bulb of known volume to a measured pressure, then flushing it into the evacuated target can with moderator. In this way, concentrations of reactant may be conveniently varied from 10^{15} - 10^{19} molecules cm^{-3} (10^{-6} - 10^{-2} M). Reagents which are condensed at S.T.P., such as bromine, are introduced by filling the bulb with the equilibrium vapour pressure at a known temperature, as described in Fleming (76). At each temperature, the gas vessel is "conditioned" with 300 torr of reactant for about 1 hour before any experiments are run. This ensures that sufficient quantities of reagents like F_2 have enough time to form inert compounds on the surfaces of any components of the target vessel that are chemically reactive with that reagent. Interestingly, the Mylar window has proven to be inert even to 300 torr of F_2 at 400K. In order to verify the inertness of the target vessel surfaces to very reactive chemicals like F_2 , the reagent concentrations are varied randomly from one Mu rate measurement to the next. Since reactions with metal surfaces tend to follow -1 order kinetics [Frost (61)], it should be possible to identify any ongoing interference reactions from the systematics of the Mu rate measurements. This serves to check the validity of the implicit assumption that the concentration of reagent remains constant during the experimental runs which typically take 1 to 2 hours each.

C. Data Acquisition

Before describing the data acquisition system, it is useful, perhaps, to reiterate the essential features of an

MSR experiment. Upon leaving the beamline, a muon passes through a counter (designated 'D' in Figure 7) which generates a start pulse for a high precision clock. Within $\sim 10^{-9}$ seconds of reaching the stopping region of the target, the muon thermalizes as Mu and precesses in a weak transverse magnetic field. At some later time (up to several microseconds) the muon decays, emitting a positron preferentially along its spin direction at the moment of decay. If the spin vector of the muon happens to point toward the positron telescope when it decays, there is a high probability that the decay positron will be detected, generating a stop pulse for the clock. The resulting time interval is incrementally binned in a histogram, the clock is reset and the entire process is repeated $10^6 - 10^7$ times. Should no decay positron be detected during some adjustable "time-out" period of several muon lifetimes, the clock is automatically reset.

A simplified diagram of the TRIUMF MSR data acquisition system is shown in Figure 9 (taken from [Marshall (76)]). Pulses from the counters at the top of the diagram (corresponding to those in Figure 7) are time adjusted by variable delays (denoted δ in the diagram) before being input to discriminators where "real" signals are distinguished from noise. The thin 'D' counter used for detecting surface muons also serves to discriminate muons from positrons: at 30 MeV/c, positrons travel essentially at c and are minimum ionizing, depositing very little energy in the thin counter, in contrast to the slower muons travelling at $< 0.3c$ which are many times more ionizing. By adjusting the voltage on the D counter

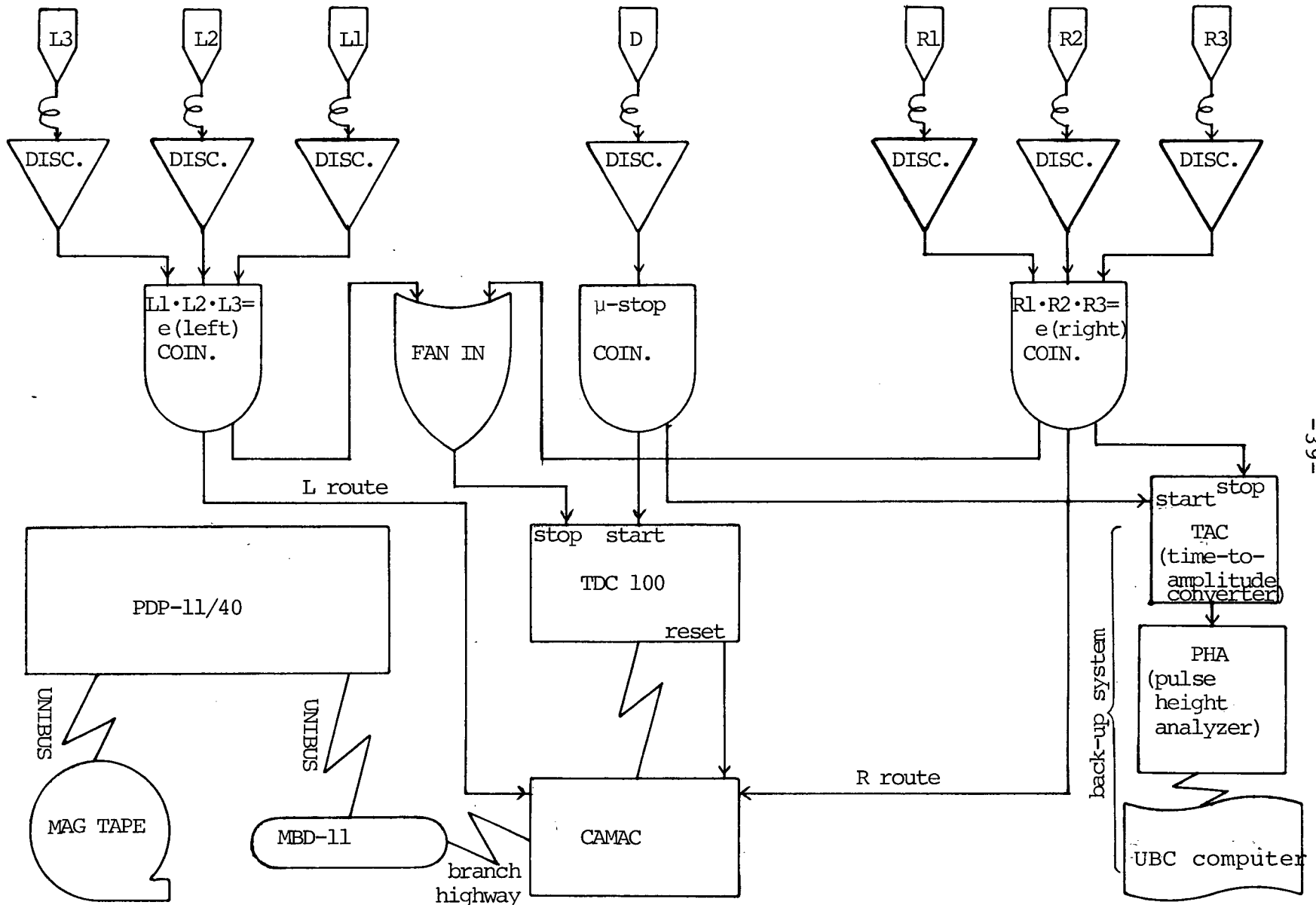


FIGURE 9: MSR data acquisition logic (simplified).

photomultiplier, positron signals can be made to form a band with a pulse height of ~ 50 mV, while muon signals form a band with pulse heights of 300 - 400 mV. Adjustment of the D discriminator threshold to greater than 50 mV effectively makes the muon "trigger" transparent to positrons while retaining a high efficiency ($>95\%$) for muons. The muon pulses are input to the start of an E.G. & G. Model TDC-100 time-to-digital converter, which has a nominal time resolution of 0.125 ns and an adjustable range from 4 μ s to 34 ms. The TDC-100 also activates a fast "time-out" reset if no stop pulse is accepted during the pre-selectable time range.

Discriminated pulses from the left and right positron telescopes are input into separate coincidence units (logical "and's") which identify positrons by the Boolean logical expressions: $e_L^+ = L_1 \cdot L_2 \cdot L_3$ or $e_R^+ = R_1 \cdot R_2 \cdot R_3$. The threefold coincidence requirement ensures that accepted events correspond to positrons that pass through all three counters and the carbon degrader. This defines the acceptance solid angle and eliminates low energy positrons from the muon decay, thereby enhancing the empirical μ^+ asymmetry; more importantly, the degrader absorbs scattered positrons from the beam, thereby reducing background which has the time structure of the TRIUMF cyclotron (23.3 MHz). Accepted positron events are logically "or-ed" from the left and right telescopes with a "fan-in" unit and input to the stop of the TDC. Simultaneous with stopping the clock, the left or right positron pulses set a telescope identification bit in a pattern recognition unit mounted in the CAMAC computer-logic interface.

Upon completion of the digitization, the TDC writes the measured time interval into a CAMAC input register which generates a "look-at-me" (LAM) signal to activate the Bi-Ra Microprogrammed Branch Driver (MBD-11, Model 2) which services the data stored in CAMAC. The MBD is a fast micro computer which is interfaced via UNIBUS to the main data acquisition computer (a Digital Equipment Corporation PDP-11/40) and controls the CAMAC crate(s) via a Branch Highway. Although under the ultimate control of the main computer, the MBD's operation is functionally independent of and simultaneous with that of the PDP-11, thereby relieving the latter from time-consuming data acquisition tasks, liberating it for more sophisticated on-line data analysis. The MBD reads the CAMAC data and resets the electronics in preparation for acceptance of a new event. The MBD identifies the positron telescope that generated the event, and performs the necessary shifting, subtracting and base-addition functions required to increment the address in the PDP memory representing the histogram bin corresponding to the measured time interval. Thus separate left and right histograms are collected simultaneously, each normally consisting of 2000 bins of 2 ns each, giving a total range of 4 μ s. The system is capable of supporting almost any number of histograms of any size with a maximum time resolution of 0.125 ns. However, at present the time-resolution of the counters is about 1.5 ns.

The data acquisition hardware and software is interfaced to the experimenter through the PDP-11 computer, executing a sophisticated programme written primarily by R.S. Hayano of

the University of Tokyo [Hayano 1-(76), Hayano 2-(76)] with help from J.H. Brewer of U.B.C. This data acquisition programme will support several independent experiments running simultaneously and is completely flexible with respect to the number, size and time resolution of histograms required for each experiment. Many experiment-monitoring features are built-in, including provision to display all or part of any histogram on a graphics terminal under light pen control. The programme provides a high level of data protection by regularly updating histogrammed data on permanent disk files; a powerful "crash recovery" facility minimizes data loss due to computer problems. Many levels of redundancy ensure continued data acquisition capability in the face of non-pathological hardware failure - for example, breakdown of a disk drive, the graphics terminal, or other control terminal will not cripple the computer's data taking functions. Several on-line analysis routines such as fast fourier transforms (FFT) are available for monitoring an experiment. At present, the PDP-11 does not support data analysis programmes of sufficient capability to perform "final" data analysis, although implementation of such programmes will be made in the near future. Until then, data is written on a 9-track magnetic tape and analyzed off-line on the UBC computer center IBM 370/168 Michigan Terminal System (MTS) as described in the next Section.

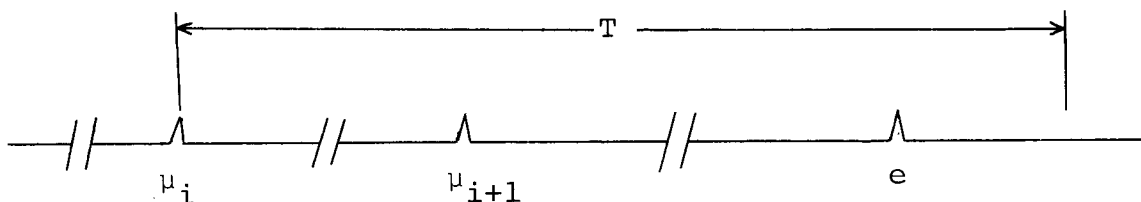
The foregoing description of the MSR data acquisition system is a simplified overview; the serious problem of "muon pile-up" has been ignored and only superficial treatment has been given to the intertwined data processing relationships

between the electronic logic, MBD and PDP. The qualitative problems of muon pile-up and hardware-independent solutions are identified below. A numerical assessment of these problems as a function of muon beam current is left to Appendix III, which also provides a detailed description of the MSR data acquisition system.

In the following discussion, it is convenient to define a fixed muon decay gate or maximum muon life expectancy time range, T , which in practice is set to a few muon lifetimes. A muon entering the target at the onset of this time interval is assumed to have decayed by the expiration of T , corresponding to the TDC "time-out" period mentioned above. For instance, if an experimenter sets $T = 4\tau_{\mu}$, then the assumption that the muon has decayed during T is good to better than 2%.

Following the entry of a muon, μ_i , that opens the T -gate and starts the TDC, a second "pile-up" muon, μ_{i+1} , may enter the target before the expiration of T and before any decay positron is detected. When such an event sequence occurs, an ambiguity is created since there is no way to identify which muon is associated with any subsequently detected decay positron. Since there is a high probability that any decay positron detected during T will belong to μ_{i+1} rather than to μ_i , the time correlation between a μ and its decay e is lost if this positron is allowed to stop the clock. Acceptance of these events at sufficiently high muon beam currents will result in a time histogram containing a reduced MSR signal and a distorted background. To zeroth

order, it is necessary to logically reject this event sequence (called "early second μ " events) represented schematically by:



where time moves from left to right and $//$ indicates some arbitrary time.

Rejection of early second μ events is not, however, a complete solution to the problem of multiple muons. In fact, a linear distortion of the time spectrum (with a negative slope) is generated at sufficiently large μ -stop rates when only early second μ are rejected, as illustrated in Figure 10. This comes from the fact that, given a constant beam current with muons arriving at times given by a Poisson distribution (see Appendix III), there is a higher probability that an event will be rejected due to an early second μ if μ_i decays at late times than if it decays at early times. There is simply a greater opportunity for an early second muon to enter the target if the first muon survives a long time before decaying. It should be noted that the presence of μ_{i+1} in the target merely creates an ambiguity in the association of any detected e with its decaying μ ; sometimes the detected e does correspond to μ_i . That is, some early second μ events are "good" events in the sense that the decay e that stopped the

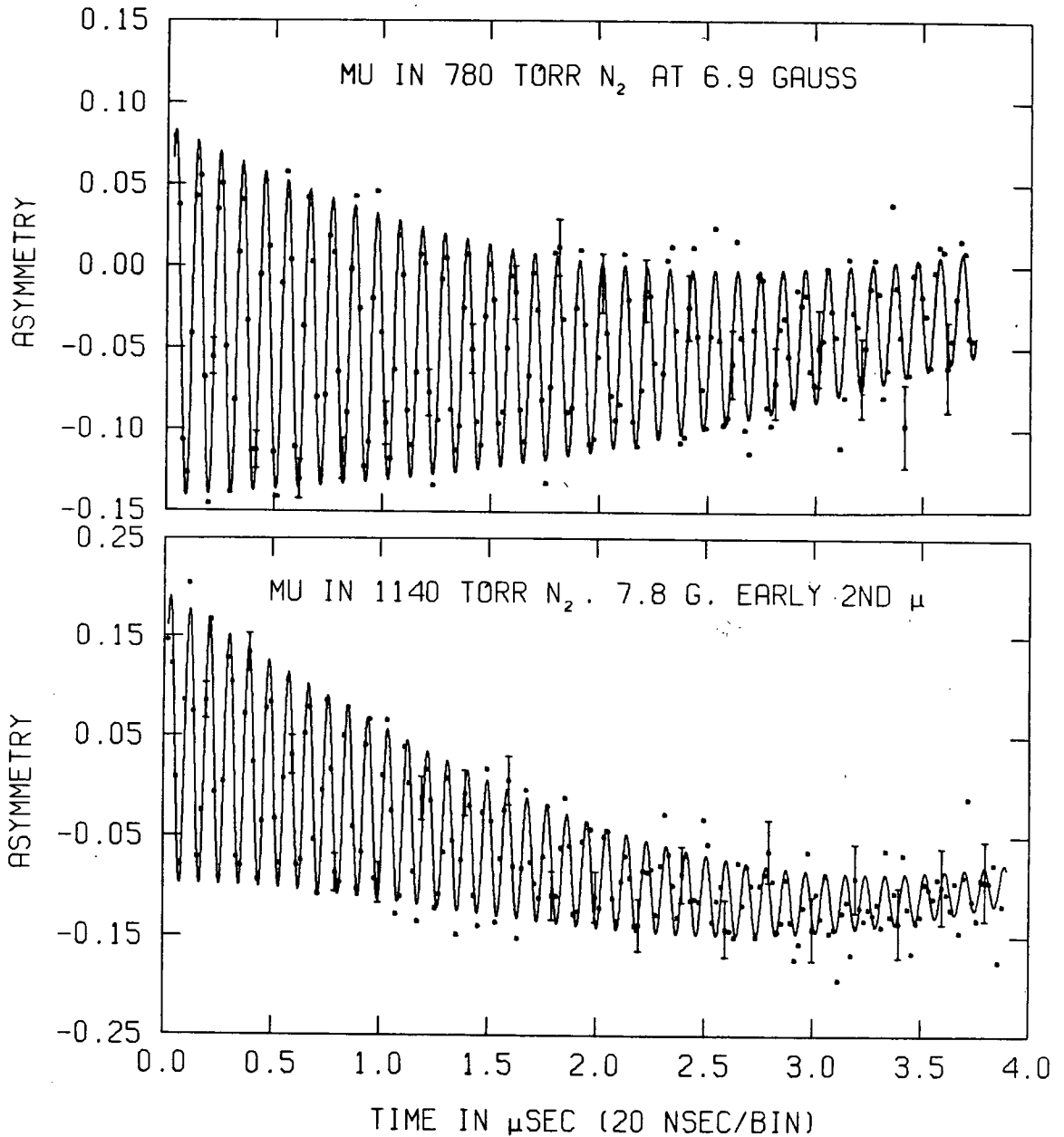
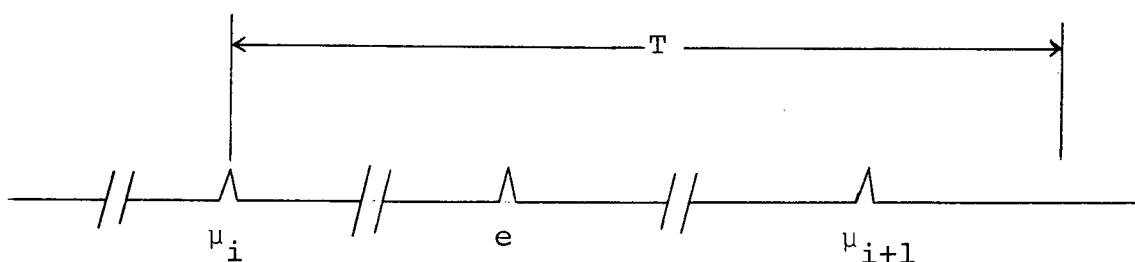


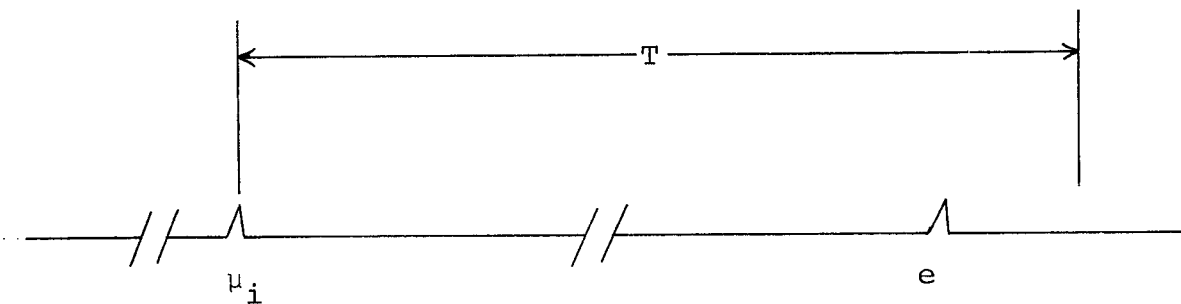
FIGURE 10: The spectral distortion due to "early" second μ rejection: the top spectrum has both "early" and "late" (i.e. "post- μ_1 ") second μ rejection, while the bottom spectrum has "early" second μ rejection only, giving rise to a large background distortion with a negative slope. It should be noted that the asymmetry scales are different for the two spectra.

clock corresponds to μ_i , the muon that started the clock, even though they are not identifiable as such. Another way of looking at the artificial distortion, then, is that because there is much time available for an early second μ to enter the target and cause rejection of an event if μ_i decays at late times, the efficiency of event acceptance (that is, the number of "good" events accepted relative to the total number of good events) is small at late times; conversely, if μ_i decays at early times, early second μ have little opportunity to lower the efficiency of event acceptance. The result is that the normalization of equation (6) (Chapter I) decreases with time. If fitting procedures assume time independence of the normalization, its artificial time dependence expresses itself in an erroneously small apparent muon lifetime and an artificially large apparent muonium relaxation rate.

It is, therefore, essential that a constant fraction of events per histogram time increment be rejected in order to avoid generation of the artificial backgrounds described above. This is accomplished by not only rejecting early second μ events, but also rejecting what are called "late second μ " events; that is, events in which μ_{i+1} enters the target before the expiration of T , but after a decay positron is detected:



Thus, an accepted event is one in which no second μ arrives during T:

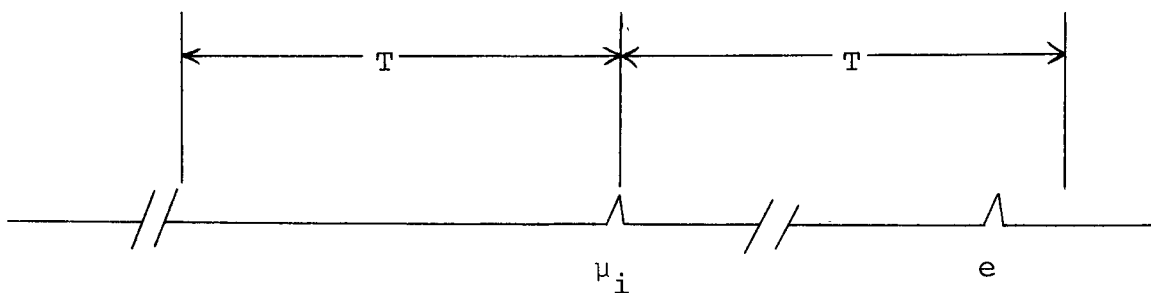


Higher order corrections for multiple particle events can be made, but the rejection of early and late second μ (collectively called "post- μ_i second μ ") is the most important, both in terms of absolute numbers (which are muon rate dependent) but also in terms of the spectral distortions introduced by failure to reject these events (see Appendix III).

One higher order correction comes from consideration of the time interval preceding the entry of μ_i into the target. In the foregoing discussion, it was assumed that, upon entry, μ_i is the only muon resident in the target; but this may not be the case. Even with post- μ_i second μ rejection, there are two situations in which a muon may already be resident in the target when μ_i enters. (1) If μ_{i-2} was the previous T-gate opening muon and μ_{i-1} was an early or late second μ , then after the T-gate has closed it may be assumed that μ_{i-2} has decayed, but μ_{i-1} may still be present when μ_i opens the next T-gate. (2) Whenever there is an accepted event, there is an intrinsic electronics "deadtime" during which time-digitization occurs and the event is transferred to the histogram. During this deadtime, the experiment is

effectively "turned off" and all event monitoring is suppressed (reasons for this are detailed in Appendix III; this is a general feature of the logic whenever more than one electronics module, such as the TDC and pattern recognition unit, must be read and reset by the computer. To preserve the integrity of the next event, it is essential that all such modules be available for new data at exactly the same time).

Consequently, when the experiment is "turned on" again at some arbitrary later time, the logic is unaware of the presence of any muons in the target. To correctly deal with muon pile-up, the only acceptable events are those where no muon enters the target during a time T either before or after μ_i entered the target:



However, it is shown in Appendix III that "pre- μ_i " multiple muon events are several orders of magnitude less frequent than "post- μ_i " multiple muon events. Furthermore, while such muons do lower the apparent Mu asymmetry, they distort the histogram less significantly than post- μ_i multiple muon events.

Another higher order correction can be made for events with more than one positron detected during T after μ_i enters the target, creating an obvious ambiguity. Possible sources of "extra" e include accidental counts (possibly related to beam contamination and therefore beam current dependent) or e

from muons that happen to survive T (in the example above where $T = 4 \tau_{\mu}$, 2% of the muons survive T). If the positron telescopes are properly shielded against accidentals from the beam, multiple- e events are extremely rare and can be ignored for all but the most precise work. The most significant distortion introduced in the histogram by multiple- e is likely to be the microscopic time structure of the cyclotron beam.

The experiments described in this thesis employed "post- μ_1 " multiple muon rejection and multiple- e rejection only. "Pre- μ_1 " multiple muon rejection will be incorporated into the data acquisition logic at higher beam currents.

A final high event rate consideration of relevance to very high precision work is associated with counter response characteristics [Hague (70)]. Counter photomultipliers have a minimum recovery time of about 20 ns. Signals produced by a photomultiplier which is not fully recovered are reduced in amplitude and may be rejected by discriminators. This may be prevented by additional gating to ensure that the events of interest were counted by fully recovered photomultipliers. This consideration is an argument for improving the beam quality of M20 to ensure that the severe positron contamination does not distort μ^+ signals from the D counter.

D. Data Analysis

Figures often beguile me, particularly when I have the arranging of them myself. The remark attributed

to Disraeli would apply - "There are three kinds of lies - lies, damned lies, and statistics."

Mark Twain's Autobiography
(Vol. I, p. 246).

Most data analysis is presently performed off-line on the IBM 370/168 using multiparameter chisquared minimization performed by a powerful, general minimization routine called MINUIT [James (71)] that was adapted from the Control Data Corporation (CDC) 7600 computer library at the European Organization for Nuclear Research (CERN), in Geneva. MINUIT is an easy-to-use programme with enough flexibility to allow the user to devise a wide variety of fitting strategies; only a few of its capabilities are mentioned here. Two minimization algorithms are normally used: the simplex method of Nelder and Mead [Nelder (67)] and a variation of the Davidon (68) variable metric method called MIGRAD. The latter method, which is particularly efficient given a good set of initial parameter guesses, requires first partial derivatives of the function being minimized; these may be provided analytically by the user or may be calculated numerically by MINUIT. MINUIT will accomodate up to 50 variable parameters, any number of which may be FIXEd at any time and RESTOREd at any later time. Parameters may be constrained to any physically meaningful numerical range. Covariance matrices and correlation coefficients are calculated by MINUIT, either as an estimate generated by MIGRAD or from the so-called hessian matrix, which is exact for a Gaussian parent distribution. Detailed non-symmetric error estimates of parameters for non-parabolic minima may be calculated by a search

method called MINOS. A number of checks for the presence of local minima are also made by MINUIT.

The gas phase Mu data analysis in this thesis has been performed in three stages: raw histograms are analyzed to extract pseudo-first order rate constants; the linear dependence of these pseudo-first order rate constants on reactant concentration yields bimolecular rate constants at a given temperature; and, finally Arrhenius fits of the temperature dependent bimolecular rate constants provide values of activation energies and pre-exponential factors.

Raw histograms are fitted to a model of the basic form of equation (6), Chapter I:

$$N(\phi, t) = N_0 e^{-t/\tau_\mu} [1 + A_{\text{Mu}} e^{-\lambda t} \cos(\gamma_{\text{Mu}} Bt + \phi_{\text{Mu}}) + A_\mu \cos(\gamma_\mu Bt - \phi_\mu)] + Bg$$

where t is the independent variable, and eight unknown parameters are sought: N_0 , A_{Mu} , λ , B , ϕ_{Mu} , A_μ , ϕ_μ , and Bg with $\gamma_{\text{Mu}} B = \omega_-$ as defined in Appendix I, and $\gamma_\mu B = \omega_\mu$. Of these, λ is the parameter of central interest, although A_{Mu} and A_μ provide information about fast epithermal Mu reactions (see Appendix II, Section B). As explained in Chapter I, experience has shown that ϕ_{Mu} and ϕ_μ cannot be assumed to be equal, possibly because some fraction of the "free" μ^+ signal comes from muons stopped in the walls of the gas target vessel which are geometrically inequivalent to the ensemble of Mu stopped in the gas. In all cases, the muon lifetime is assumed to be fixed at 2.1971 μs . This assumption is physically valid since μ^+ lifetimes are

independent of their environment to at least a few parts per million [Sachs (75)]; practically, the validity of this assumption depends very strongly upon the integrity of the multiple muon rejection logic described in the preceding section. The empirical value of A_{Mu} normally ranges between 10% and 15% and A_{μ} is generally less than 5%, depending upon the stopping medium and detailed counter configuration; conveniently measurable values of λ range between $0.1 \mu\text{s}^{-1}$ and $15 \mu\text{s}^{-1}$.

Left and right histograms are analyzed independently, yielding two redundant values of λ at each reagent concentration. The time bin corresponding to "time zero" is estimated to a precision of about 2 ns by performing a brief measurement of the time required for beam positrons to scatter between the 'D' counter and positron telescopes. To accomplish this, the photomultiplier voltage on the 'D' counter is increased, thereby increasing the positron pulse height above the 'D' discriminator threshold, and the positron telescope threefold coincidence requirement is reduced to the single counter closest to the target, which always defines the timing of the coincidence output. Each 2000 bin histogram of 2 ns bins is normally rebinned to 4 or 8 ns/bin depending upon the Mu precession frequency, resulting in an effective histogram size of about 1000 or 500 bins containing about 10^6 events (some of the original bins are eliminated because they precede $t=0$). Valid data is normally contained in the histograms within about $t = 10$ ns after time zero, but careful adjustment of the logic timing can reduce this to about $t = 3$ ns. In contrast,

it may be noted that experiments requiring a positron veto seldom contain valid data before $t = 25$ ns, and often not before $t = 100$ ns, due to the width of the anti-coincidence requirement. An eight parameter fit to a 450 bin histogram by MINUIT consumes about 2 to 25 seconds of CPU time, depending on the quality of the initial guesses to the parameters.

The familiar definition of χ^2 is given by

$$\chi^2(\underline{x}) = \sum_{k=1}^K \left(\frac{Y_k - T_k(\underline{x})}{\sigma_k} \right)^2 \quad (9)$$

where $\underline{x} = x_i$, $i = 1, n$, are the variable parameters, K is the number of data points, Y_k and σ_k^2 are the measured values and their variances and $T_k(\underline{x})$ are the values predicted by the model. Since counting statistics generally follow a Poisson distribution, the variance σ_k^2 is just Y_k for large Y_k , the number of events per fitted time bin. For histogram analysis, the definition of χ^2 is modified to

$$\chi^2(\underline{x}) = \sum_{k=1}^K \frac{(Y_k - T_k(\underline{x}))^2}{T_k(\underline{x})} \quad (10)$$

where $\sigma_k^2 = Y_k$ is replaced by $\sigma_k^2 = T_k(\underline{x})$. This modification in weighting is made to eliminate extraordinary weighting of unusually low points and can be seen as follows: consider a situation in which one datum is unusually high and another is correspondingly low; definition (9) provides the high point with a smaller weighting factor $(\frac{1}{\sigma_k})^2$ than the low point thereby biasing the fit to the lower point; definition (10) weights both points equally. For most histograms, model (10) provides

a χ^2 per degree of freedom of $0.95 \leq \chi^2 \leq 1.05$.

Individual pseudo-first order rate constants from left and right counter telescopes are simultaneously fitted to equation II(2), Appendix II:

$$\lambda = k[X] + \lambda_0$$

to yield the bimolecular rate constant, k . λ is determined for at least five concentrations of X including $[X] = 0$. The true definition of χ^2 from (9) above is used for these fits, but in this case σ_k is given from the errors in λ calculated by MINUIT. More experimental data is accumulated in histograms with fast relaxations in order to reduce the relative uncertainty in the determination of λ . Plots of λ versus $[X]$ in this thesis show weight averaged λ 's from left and right telescopes for graphical clarity, but the fitted lines correspond to simultaneously fitted left and right values of λ .

For temperature dependent k 's, fits are made to the familiar expression:

$$k = Ae^{-E_a/RT} \quad (11)$$

where E_a , the Arrhenius activation energy, and A , the pre-exponential factor, are the parameters of interest. Again, the true definition of χ^2 from (9) is used for fits of the logarithmic form of (11):

$$\ln k = -E_a/RT + \ln A \quad (12)$$

Cvetanovic and Singleton (77) have pointed out that the proper

weighting factors of the k 's in equation (12) must be obtained by the iterative procedure

$$w_i' = \frac{k_i^* (k_i - k_i^*)}{\ln(k_i/k_i^*)} w_i \quad (13)$$

where $w_i' = \left(\frac{1}{\sigma_i^2}\right)'$ is the exact statistical weight for an experimental $\ln k_i$ in (12), $w_i = \left(\frac{1}{\sigma_i^2}\right)$ is the statistical weight of an experimental k_i in (11), and k_i^* is the best fit prediction of k_i . Since k_i^* are unknown, w_i' are obtained by iteration of current MINUIT values of k_i^* .

Most of the gas phase Mu measurements reported in this thesis have been taken at a magnetic field of 7 to 8 gauss. Fields greater than 10 gauss are complicated by the beat frequency (see Appendix I), $\Omega = \left(\omega_+^2 + \frac{\omega_0^2}{4}\right)^{1/2} - \frac{\omega_0}{2} \approx \frac{\omega_+^2}{\omega_0}$. At 10 gauss, the envelope of $\cos \Omega t$ ($\Omega = 2.8 \times 10^5 \text{ s}^{-1}$) reduces A_{Mu} to $0.4 A_{\text{Mu}}$ after $4 \mu\text{s}$, a typical experimental time range. When fitted to equation (6), this leads to an apparent relaxation rate of $0.2 \mu\text{s}^{-1}$ for a stable, long-lived Mu signal. This bogus "relaxation" rate increases as the square of the applied field and has the appearance of a Gaussian relaxation. In principle, a fitting function can be devised to include the beat without introducing any new parameters since Ω depends only on known constants and B , which is a parameter anyway. However, inclusion of this complication to the fitting function increases computational cost and the beat is highly correlated to A_{μ} and λ at low fields. Clearly, these factors are not prohibitive, but they are easily avoidable complications.

Failure to account for the beat envelope using model (6) as the fitting function will generate a systematic error reducing k . This arises since, at 10 gauss for example, a non-relaxing signal will appear to relax at $\sim 0.2 \mu\text{s}^{-1}$ while a fast relaxing signal ($\lambda = 15 \mu\text{s}^{-1}$, say) is unaffected by the $\cos\Omega t$ envelope which is almost flat near $t = 0$. Thus, the systematic error introduced to λ decreases with increasing reagent concentration.

For fast relaxations, higher fields are preferable, in principle, for reasons illustrated in the figures of Appendix II and also because a large number of oscillations in the short-lived Mu signal produce more reliable fits to the field and phases. It would then seem to be optimal to increase B as a function of λ . There is a serious practical objection to this proposal, however, in that relaxation rates of 10 - 15 μs^{-1} are generally difficult to fit. It is often necessary to FIX several parameters in order to reduce model (6) to a function that is sensitive to the data and λ . The important candidates for FIXing are B and A_{Mu} which requires accurate foreknowledge of these parameters. In practice, it is not reasonable to precisely calibrate the magnetic field produced in the Helmholtz coils as a function of electric current because non-reproducible background contributions to B fluctuate over time periods of days, making constant recalibration necessary. These unreproducible contributions to B can be traced to such events as movement of the TRIUMF 50 ton crane over the experimental area, changes in magnetic field settings of beam line components in adjacent beamlines, and constant re-stacking of steel and iron neutron shielding

around adjacent experiments. Such effects constructively or destructively add significant, though homogeneous, components to the experimental magnetic field. Fortunately, the experimental field is generally constant over the time during which a series of concentrations of a reactant are examined. Without calibration, it is impossible to set B reproducibly to better than a few percent. Experience has shown that fitted values of weak fields from experimental data taken over 24 - 48 hours are constant within a standard deviation of less than 1%, giving a more accurate measure of the field than calibration would give. In the near future, the field will be stabilized by a continuous monitor in a feedback loop, which will allow reliable and consistent field settings.

The fitting procedure adopted is to first fit B (in the 7-8 G range) for a series of runs at low reagent concentration and then to FIX this value of the field to fit the fast relaxation runs.

CHAPTER III - THEORETICAL BACKGROUND

A Introduction

The initial motivation for undertaking the experimental study of the chemical reaction rates of Mu was to examine the behaviour of Mu as a light isotope of hydrogen (see Chapter I, Section B). It was hoped that the substantial mass difference between Mu and H would provide an exacting test of modern calculations of H atom reaction kinetics, particularly with respect to quantum mechanical effects such as tunnelling [Fleming (76)]. It was expected that comparison of both theoretical and experimental results for reactions of Mu with those of the other H isotopes might not only lead to improved theoretical methods for treating H atom reactions, but it might also provide new information about such computational tools as potential energy surfaces. It is shown in this Chapter and the next that many of these objectives have already reached a high level of realization. In the course of studying Mu reaction kinetics, a second motivation for the experiments became clear; this is discussed in Chapter IV.

The selection of chemical systems for study, namely Mu with the halogen and hydrogen halide families, was based partly on the considerable theoretical and experimental interest in the H analogue reactions, and partly on the experimental compatibility of these reagents with the MSR method: gas phase targets at about 1 atmosphere may be readily prepared with a wide range of reactant concentrations; and the reactions are sufficiently fast at or near room temperature to consume Mu

during its 2.2 μs lifetime. As noted in Chapter I, the experiments have been confined to the measurement of thermally averaged rate constants and activation energies. Modern state-to-state techniques employing lasers, atomic beams, and infrared chemiluminescence are not yet available to Mu studies.

It would be inappropriate to attempt to present a comprehensive review of the theory of chemical kinetics in this thesis which is essentially experimental in content (indeed, the pace of development of chemical reaction rate theory is so frenetic that such a review would be impossible). On the other hand, the debut of gas phase Mu reaction rate data has sparked considerable theoretical activity, notably by Connor, Jakubetz, Manz, and Laganà who have performed quantum mechanical (QMT) [Connor 1-(77), 1-(78), 1-(79)], quasiclassical (QCT) [Connor 1-(79)], and classical (CT) [Jakubetz (79)] trajectory calculations, as well as transition state theory (TST) [Connor 1-(79)] Jakubetz 1-(78), (79)] calculations on the reactions of Mu, H, D, and T with F_2 and who are presently performing similar calculations on the Cl_2 reactions; other authors have done state-to-state calculations of Mu reaction rates which are of less direct relevance to the present experimental work (see eg. [Fischer 1,2-(77), Korsch (78)]). Since most of the experimental results of this thesis are interpreted in terms of the calculations of Connor et al. (Chapter IV), one of the aims of the present Chapter is to outline their various theoretical approaches. The primary aim of this Chapter though, is to explore some qualitative predictions of the reaction rates of Mu versus H based both on the calculations mentioned above and

on selected considerations from the theory of chemical kinetics.

B Potential Energy Surfaces

Most chemists likely have at least some familiarity with the notions of a potential energy surface and an associated reaction path. These concepts are illustrated in Figure 11. The determination of a potential energy surface to describe the interatomic potentials of the reacting atoms is the starting point for all trajectory calculations [Johnston(66), Laidler (65)], and, to a lesser extent, it is a requirement for TST calculations as well. Depending on the details of the specific calculation, TST may not require the complete potential surface, but only the minimum energy path for the reaction. Before considering particular potential energy surfaces for the reactions studied in this thesis, a few comments should be made about such surfaces in general.

(i) Semi-Empirical Potential Energy Surfaces

In principle, it should be possible to determine potential energy surfaces from ab initio methods involving the solution of the Schrödinger equation, perhaps with the aid of approximations based on various quantum mechanical criteria [Laidler (65), Jakubetz 1-(78)]. Unfortunately, it is still impossible to perform such calculations with sufficient accuracy to be of general use to reaction kinetics [Van Hook (70), Jakubetz 1-(78)], with the possible exception of the $H + H_2$ system (see eg. [Liu (78)]). In the face of this obstacle, it is customary to

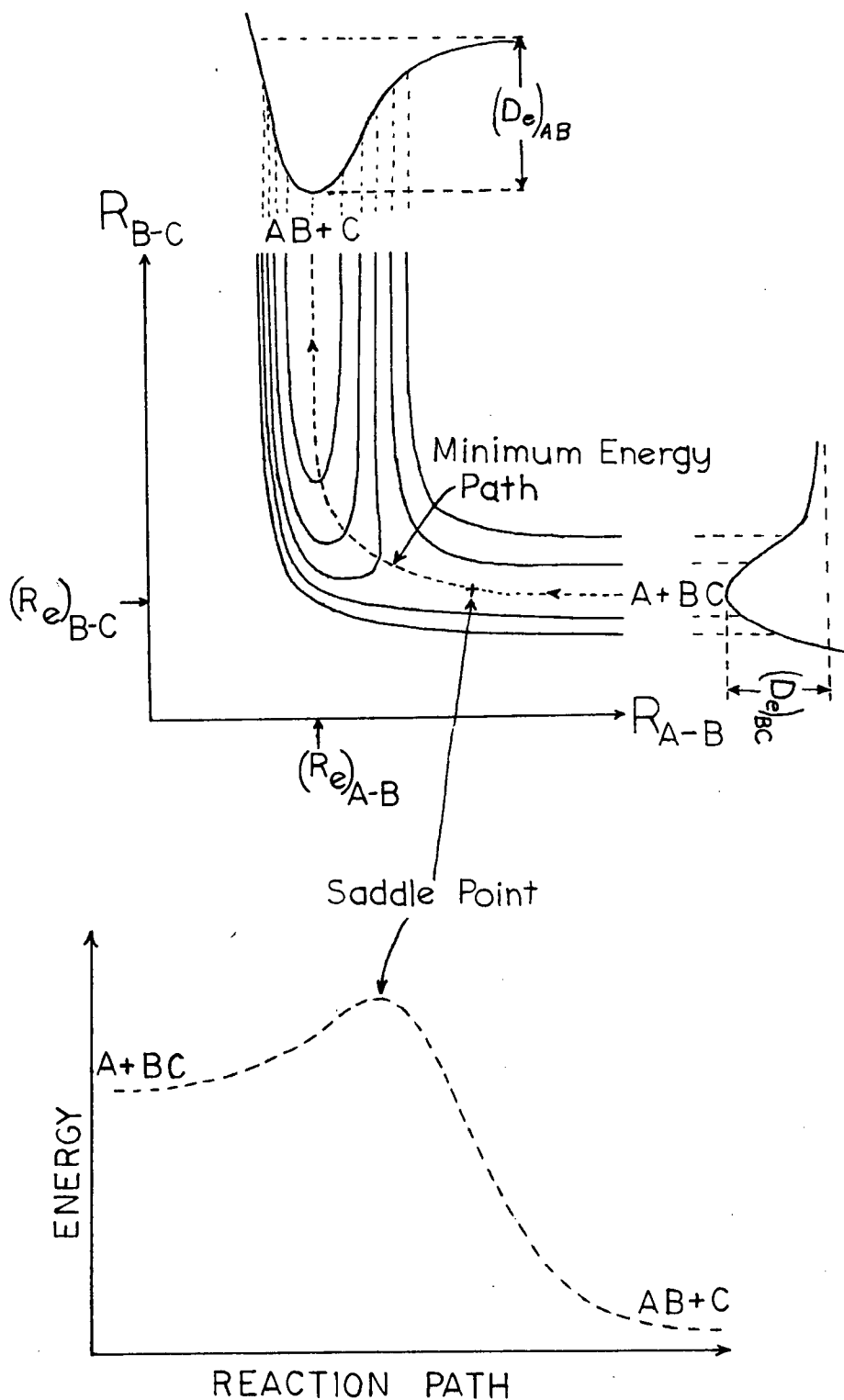


FIGURE 11: A potential contour map for the exothermic collinear $A + BC \rightarrow AB + C$ reaction. The minimum energy path through the saddle point (+) is denoted by the dashed line. The entrance valley depth is $-D_e(BC)$ measured from the valley floor, and the exit valley depth is $-D_e(AB)$. The saddle point is above the valleys, but below the plateau.

employ so-called "semi-empirical" potential energy surfaces (although, the degree of empiricism actually employed often blurs any distinction between "semi-empirical" and "wholly" empirical methods) which are distinguished from ab initio surfaces by the fact that parameters are left for adjustment based not on theoretical grounds, but rather on a posteriori experimental results [Laidler (65)]. The use of a semi-empirical surface necessarily removes some (but certainly not all or even most) of the predictive utility of the theory. Indeed, many reviewers (see eg. [Johnston (66), Laidler (65), Thompson (76)]) have pointed out that while the accuracy of a kinetic calculation depends rather directly on the accuracy of the potential energy surface, many qualitative predictions can and have been made from consideration of inaccurate or even completely hypothetical potential energy surfaces (eg. [Kuntz (65), Polanyi (69), Mok (69), Polanyi (78)]). In this way, chemical kinetic theory and experiments take on an explicit symbiotic relationship in a "bootstrap" procedure whereby experiments serve not only to test the accuracy of the calculations, but also to adjust the parameters of the potential energy surface, which, in turn, leads to improved calculations.

Probably the most commonly used semi-empirical methods of determining a potential energy surface are variations of the method due to London, Eyring, Polanyi and Sato (LEPS). A good discussion of the development of semi-empirical potential energy surfaces is given in Laidler and Polanyi (65). The surfaces considered in this thesis are all essentially variations of the LEPS surface. The LEPS method is a modification

of the Heitler-London approximation for the electronic energy of H_2 using the (unnormalized) wavefunction

$$\psi = \psi_A(1)\psi_B(2) \pm \psi_B(1)\psi_A(2)$$

which has H-H interaction eigenvalues of

$$V(r) = \frac{Q_A \pm J_A}{1 \pm S_A^2} \quad (14)$$

where Q_A , J_A , and S_A are the Coulomb, exchange, and overlap integrals which are functions of r , the internuclear separation. In equation (14), the plus sign refers to the singlet (bound) state and the minus sign refers to the triplet (repulsive) state. It may be noted that J is negative and $|J| > Q$ near r_e , the equilibrium internuclear separation. London, Eyring, and Polanyi extended this treatment to the H_3 system, to give a potential energy expression

$$V(r_{AB}, r_{BC}, r_{AC}) = Q_{AB} + Q_{BC} + Q_{AC} \pm \left[\frac{1}{2} (J_{AB} - J_{BC})^2 + \frac{1}{2} (J_{BC} - J_{AC})^2 + \frac{1}{2} (J_{AC} - J_{AB})^2 \right]^{1/2} \quad (15)$$

where they identified the singlet state with the Morse functions of the diatomic pairs:

$$Q_{ij} + J_{ij} = {}^1V(\Delta r_{ij}) = {}^1D_{ij} (e^{-2\beta_{ij}\Delta r_{ij}} - 2e^{-\beta_{ij}\Delta r_{ij}}) \quad (16)$$

where ${}^1D_{ij}$ and β_{ij} are constants obtained spectroscopically and $\Delta r_{ij} = r_{ij} - r_e$ with i, j referring to appropriate combinations of the atomic labels A, B, and C. ${}^1D_{ij}$ is related to β_{ij} by $\beta_{ij} = \pi v_0 \left(\frac{2\mu}{{}^1D_{ij}} \right)^{1/2}$ where v_0 is a fundamental vibrational

frequency and μ is the reduced mass of the diatomic pair. The LEP treatment neglects the overlap integral S^2 , and assumes a constant fraction of coulombic binding energy $\left(\frac{Q_A}{Q_A + J_A} \right)$

independent of r . The Sato modification [Sato (55)] of equation (16) is:

$$V(r_{AB}, r_{BC}, r_{AC}) = \frac{1}{1 + S^2} [Q_{AB} + Q_{BC} + Q_{AC} \pm \{ \frac{1}{2}(J_{AB} - J_{BC})^2 + \frac{1}{2}(J_{BC} - J_{AC})^2 + \frac{1}{2}(J_{AC} - J_{AB})^2 \}^{1/2}] \quad (17)$$

where the triplet (anti-bonding) state is identified with a modified Morse function (anti-Morse or Sato-Morse):

$$\frac{Q_{ij} - J_{ij}}{(1 - S^2)} = {}^3V(\Delta r_{ij}) = \frac{{}^1D_{ij}}{2} (e^{-2\beta_{ij}\Delta r_{ij}} + 2e^{-\beta_{ij}\Delta r_{ij}}) \quad (18)$$

and the singlet state (equation (16)) becomes:

$$\frac{Q_{ij} + J_{ij}}{(1 + S^2)} = {}^1V(\Delta r_{ij}) = {}^1D_{ij} (e^{-2\beta_{ij}\Delta r_{ij}} - 2e^{-\beta_{ij}\Delta r_{ij}}) \quad (19)$$

The overlap integral in the LEPS formulation (equation (17)) is left as an adjustable parameter ($\Delta \equiv S^2$ is called the Sato parameter) which is normally found to be much smaller than the true overlap integral. It should be noted that the Sato modification set S^2 constant over all internuclear separations and independent of atomic labels. Most authors use empirical variations of the LEPS formulation such as: replacement of the constant S^2 with S_{ij}^2 terms for each atomic pair [Kuntz (66), Jonathan (72)] which may or may not be dependent upon the internuclear distance (Jonathan et al. examined both cases, Kuntz et al. used S_{ij}^2 independent of r_{ij}); empirical adjustment of the triplet anti-Morse function (equation (18)) by forms which replace $\frac{{}^1D_{ij}}{2}$ by an adjustable ${}^3D_{ij}$ ([Jonathan (72)] also examined this); or replacement of the anti-Morse function by, for example:

$$\begin{aligned}
 {}^3V_{ij}(\Delta r_{ij}) &= {}^3D_{ij}(e^{-2\beta_{ij}\Delta r_{ij}} + 2e^{-\beta_{ij}\Delta r_{ij}}) \text{ for } r_{ij} \leq r^* \\
 &= C(r_{ij} + A)e^{-\sigma r_{ij}} \text{ for } r_{ij} \geq r^*
 \end{aligned}$$

where 3D , B , C , A , σ , and r^* are adjustable parameters ([White (73)]; in fact, White used an empirical valence bond variation of the LEP surface).

Clearly, all LEPS formulations mentioned require experimental input. LEPS surfaces are usually "optimized" by adjusting the variable parameters until some type of trajectory calculations performed on the surface reproduce a set of experimental results. For example, Jonathan et al. (72), tailored the LEPS surface for the reaction $H + F_2 \rightarrow HF + F$ such that three dimensional quasiclassical trajectory calculations (see Section D below) give an HF vibrational energy distribution, reaction activation energy, rate constant and reaction enthalpy in agreement with experiment. Clearly, this procedure is not likely to converge to a unique "correct" surface; it is only hoped that it produces a useful surface.

(ii) Contour Plots of the Potential Energy Surface for the Reaction $A + BC \rightarrow AB + C$

In this Section, it is shown how contour plots, such as in Figure 11, provide the basis for setting up a conceptually and computationally simple picture of the atom-diatom collision process. For the three atom $A + BC$ system, the interatomic potential energy is a function of the positions of the three nuclei and therefore a function of nine coordinates. However, it is only the relative motion of the nuclei within their

center of mass frame that is of relevance to the collision since translation or rotation of the three atoms together as a rigid body will not affect this interatomic potential. Thus, the interatomic potential energy is a function of three coordinates: r_{AB} , r_{BC} , and r_{AC} or, more commonly, r_{AB} , r_{BC} , and θ_{ABC} , the ABC bond angle. Consequently, contour plots of the potential energy function must be drawn with respect to two coordinates, with the third coordinate fixed. Usually, such contour plots show the potential energy as a function of r_{AB} and r_{BC} (as in Figure 11) with θ_{ABC} fixed; in fact, most commonly, θ_{ABC} is fixed at 180° describing the collinear configuration of the three atoms. There are at least two good reasons why the collinear potential surface is the one most often considered: firstly, as discussed in Section D below, the degree of complexity of trajectory calculations increases tremendously from the collinear to the coplanar to the three dimensional cases, not only because of the need to consider more surfaces, but also because of the increased number of internal degrees of freedom of the system with the corresponding increase in the number of reaction channels available (more product vibrational and rotational states are included); and, secondly, the simpler collinear calculations often (but by no means always) provide a reasonably accurate description of the reaction, partly because it is usually the case that the collinear reaction geometry is the energetically favored one. In fact, Jonathan et al. (72) have pointed out that an energetically favored collinear configuration seems to be a general feature of LEPS surfaces; however, this general-

ization does not in itself imply that the collinear configuration will necessarily dominate the reaction dynamics because it neglects other topological features of the potential surface as well as the role played by multi-dimensional internal energy modes of the target molecule, which may be available for promoting reaction.

The chemical reaction $A + BC \rightarrow AB + C$ is envisioned as the movement of a representative mass point (the features of which are detailed below) along the potential energy surface through the reactant valley, across the saddle point, and finally exiting along the product valley. This notion that the electronic potential energy surface mediates the motion of the nuclei of the atoms is an implicit statement of the Born-Oppenheimer (BO) approximation: the electronic energy of the atoms is separable from their nuclear energy. This approximation, sometimes called the low kinetic energy approximation [Schatz (77), Levine (74)], is valid for most atoms at normal temperatures, where nuclear velocities are much less than the electron velocities. Since the mean velocity of an ensemble of atoms at a given temperature is inversely proportional to the square root of their masses (see Section D below), it is expected that the BO approximation will break down at lower temperatures for Mu than for H. To date, the BO approximation has always been invoked in calculations of the reactions of Mu, although its validity in these cases has not yet been examined [Jakubetz 1-(78)]; a discussion of the validity of the BO approximation with application to, among others, the $H + HD$ reaction is given by Bardo and Wolfsberg (78) who find it to be

accurate to within a few percent in the cases studied. Correlated with the BO approximation is the assumption of electronic adiabaticity [Nikitin (74)]: the system remains in the ground electronic state throughout the reactive collision. Besides depending on the collision time, this assumption depends upon the electron angular momentum and the correlation of electronic states [Smith (77)]. The assumption of electronic adiabaticity is the standard procedure for both trajectory and TST treatments of the reactions considered in this thesis; the practical consequence of this assumption is that only ground state potential energy surfaces need be considered. The final, and, from the point of view of this thesis, most important consequence of the BO approximation is that the potential energy surface is invariant to isotopic substitution [Van Hook (70), Nikitin (74)]; that is, identical potential energy surfaces are applicable to reactions of Mu, H, D and T.

It has already been stated that reactive atom-diatom collisions can be pictured as the transmission of some kind of particle across the barrier of a potential energy surface. Levine and Bernstein (72) call this picture the "analogue" formulation of the problem and it is necessary to determine the identity of these particles moving on the potential surface. To this end, it is useful to consider the freshman physics problem of the collision of two structureless billiard balls. Although this problem is treated correctly by separately solving the equations of motion for each ball, in some ways it is more useful to consider the equivalent problem in which the

motion of the center of mass itself is partitioned from the relative motion within the center of mass frame. This procedure simplifies both the problem and the interpretation of its solution by eliminating the motion of the center of mass which is extraneous to the collision itself. For example, one finds that the system kinetic energy in the center of mass frame is given by

$$E_{\text{trans}} = \frac{1}{2}\mu v_r^2 \quad (20)$$

where v_r is the relative velocity of the two balls and μ is their reduced mass. Equation (20) is remarkable in that it looks just like an equation of motion for a single particle of mass μ . Given this interpretation, some of the properties of the two body collision are described by the analogue equations of motion of a single representative point with some effective mass. The use of a potential energy contour plot to describe the atom-diatom collision is a generalization of this procedure to three bodies. Points along the reaction path on the potential energy surface describe the configuration of the three atoms at various stages of collision. Instead of solving the equations of motion for all three atoms (which is occasionally done), the reactive collision is described by solving the equations of motion of a single representative mass point moving along the potential energy surface, situated in the center of mass frame.

The problem now arises as to what effective mass to assign to this representative point. To illustrate this problem, consider the collinear LEPS potential energy surface

due to Jonathan et al. (72) shown in Figure 12 for the reaction $Y + F_2 \rightarrow YF + F$, $Y = Mu, H, D, T$ (adapted from [Connor 1-(78)]).

As the representative point moves along the reactant valley towards the potential saddle on a line parallel to the r_{YF} axis, its motion simply describes a two body collision as in equation (20) with H (say) as one body, and F_2 as the other.

Thus, the effective mass is $\mu_{H,F_2} = \frac{m_H(m_F + m_F)}{m_H + m_F + m_F} \approx 1$ amu, and

the relative translational kinetic energy is given by

$E_{trans} = \frac{1}{2}\mu_{H,F_2} \dot{r}_{HF}^2$, where $\dot{r} \equiv \frac{dr}{dt}$. On the other hand, after

reaction, the representative point moves along the product valley away from the saddle point on a line parallel to the

r_{FF} axis, thereby describing another two body system, this time

of HF and F. Here the effective mass is $\mu_{HF,F} = \frac{(m_H + m_F)m_F}{m_H + m_F + m_F}$

≈ 9 amu and the relative translational kinetic energy is given

by $E_{trans} = \frac{1}{2}\mu_{HF,F} \dot{r}_{FF}^2$. In general, it can be shown that the

effective mass of the representative point is a function of the direction of its motion along the potential energy surface (an excellent discussion of this subject is found in Johnston (66)),

varying continuously from 1 to 9 amu in the present example as

the slope of its trajectory varies from 0 to ∞ . When the

vibrational motion of the target F_2 and product HF are taken

into account, trajectories of the representative point are

oscillatory so that their effective masses are also oscillatory,

thereby making this analogue picture both computationally and

conceptually complicated.

This complication is removed by representing the potential energy surface with a mass weighted coordinate system (for

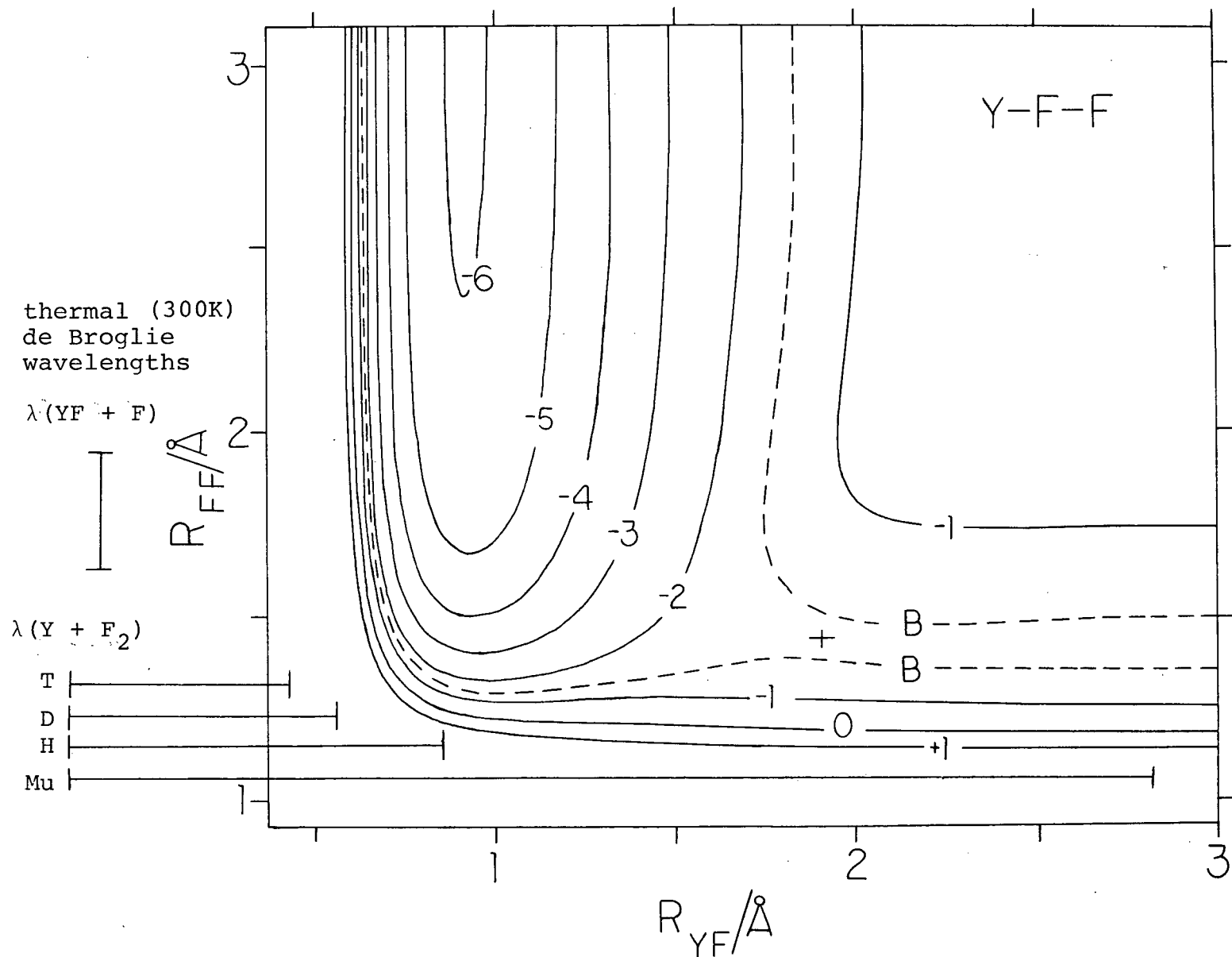


FIGURE 12: Potential energy surface for $Y + F_2$ due to Jonathan (72), adapted from Connor 1- (78). Solid contours are labelled in eV from the F_2 dissociation limit. Dashed contour, B, is at $E_{trans}^{OC} = 0.087$ eV, the quasiclassical threshold.

a derivation, see Johnston (66)). For the collinear configuration of atoms A, B, and C, it may be shown that the kinetic energy in the center of mass frame is given by:

$$E_{\text{trans}} = \frac{1}{2M} [m_A (m_B + m_C) \dot{r}_{AB}^2 + 2m_A m_C \dot{r}_{AB} \dot{r}_{BC} + m_C (m_A + m_B) \dot{r}_{BC}^2] \quad (21)$$

where $M = m_A + m_B + m_C$. The first and last terms have been previewed in the above discussions of pure A-BC and pure AB-C motion. The middle cross-product term provides the continuous variation between the two motional extremes and anticipates that any new coordinate system, q_{AB} and q_{BC} , that diagonalizes equation (21) will be skewed with respect to the cartesian r_{AB} and r_{BC} . In general, there may be more than one coordinate transform that diagonalizes the kinetic energy [Johnston (66)]; for the collinear case, a common mass weighted coordinate transformation is [Marcus (77)]:

$$\begin{aligned} r_{AB} &= q_{AB} - q_{BC} \operatorname{ctn}\alpha \\ r_{BC} &= s q_{BC} \operatorname{csc}\alpha \end{aligned} \quad (22)$$

where $s = \left(\frac{m_A (m_B + m_C)}{m_C (m_A + m_B)} \right)^{1/2}$ and $\operatorname{csc}\alpha = \left(\frac{m_A m_C}{(m_A + m_B)(m_B + m_C)} \right)^{1/2}$,

and α is the skewing angle. Equations (22) give the kinetic energy expression:

$$E_{\text{trans}} = \frac{1}{2} \mu_{A,BC} (\dot{q}_{AB}^2 + \dot{q}_{BC}^2)$$

and define the constant effective mass of the representative point as $\mu_{A,BC}$. For other than the collinear configuration, different but similar expressions to equations (22) are required to diagonalize the kinetic energy (see eg. [Gatz (66)]). With the transformation of the potential energy surface into a

mass weighted coordinate system, the atom-diatom collision can be completely understood classically in terms of the trajectory of a ball rolling along a physical surface under the influence of gravity. Although the foregoing discussion explicitly refers to trajectories, it is also applicable to TST calculations which can be viewed as a statistical treatment of trajectories not requiring their individual calculation (there are also statistical dynamical theories [Connor 1-(76)]).

(iii) Potential Energy Surfaces For the Reactions: $Y + X_2 \rightarrow YX + X$, $Y = \text{Mu, H, D, T}$; $X = \text{F, Cl, Br, I}$

While invariance of a potential energy surface under isotopic substitution is a consequence of the BO approximation, the above discussion clearly shows that the effective potential energy surface (i.e. mass weighted) displays no such invariance. This is illustrated in the mass weighted LEPS surface for the $Y + F_2 \rightarrow YF + F$, $Y = \text{Mu, H, D, T}$, reaction shown in Figure 13 (adapted from [Connor 1-(78)]), corresponding to the LEPS surface of Figure 12. In this Figure, the mass weighting scheme used is [Connor (75)]:

$$\begin{aligned}
 q_{YF} &= \left(\frac{\mu_{Y,F_2}}{\mu_{F_2}} \right)^{1/2} (r_{YF} + 0.5 r_{FF}) \\
 &= \left(\frac{\mu_{Y,F_2}}{\mu_{F_2}} \right)^{1/2} R_{Y,F_2}
 \end{aligned} \tag{23}$$

$$q_{F_2} = r_{F_2}$$

where R_{Y,F_2} is the distance from Y to the center of mass of F_2 , and the skewing angle α is given by:

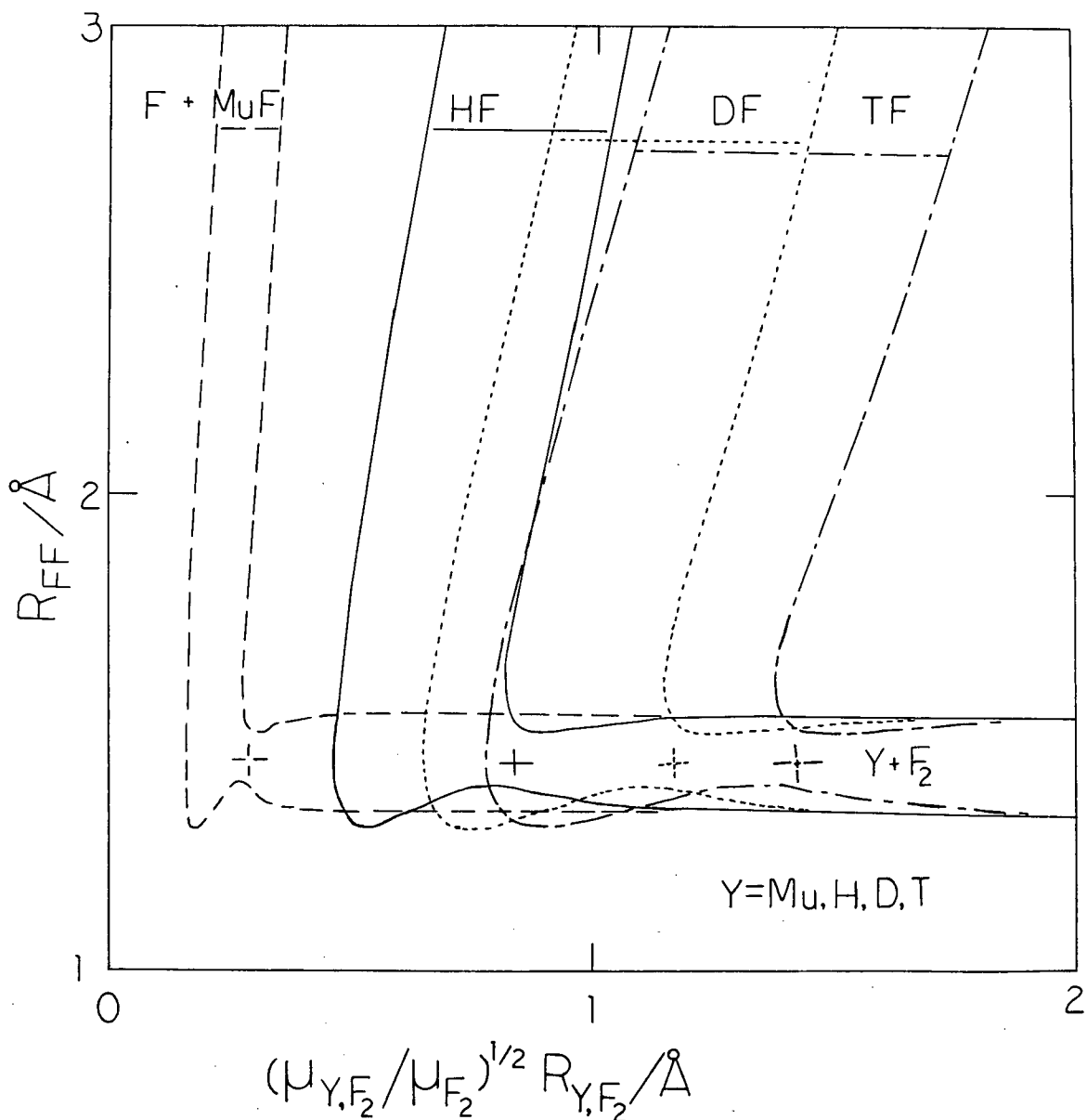


FIGURE 13: Potential energy surfaces of Jonathan (72) for the collinear $Y + F_2$ reaction, plotted in mass weighted coordinates, adapted from Connor 1-(78). The mass weighting scheme is described in the text. The single contours are for $E_{\text{trans}} = 0.087 \text{ eV} (2.01 \text{ kcal/mole})$ (contour B of Figure 12). Saddle points are indicated by crosses.

$$\tan\alpha = \left(\frac{m_Y + 2m_F}{m_Y} \right)^{1/2}$$

In this mass weighting scheme, the kinetic energy in the center of mass frame is given by:

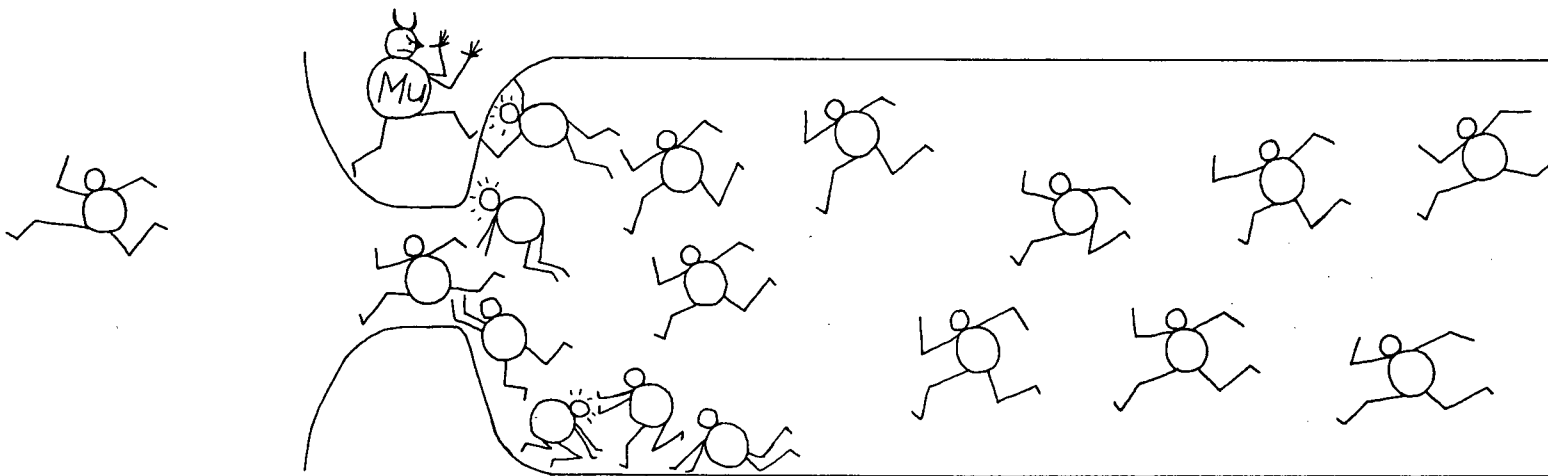
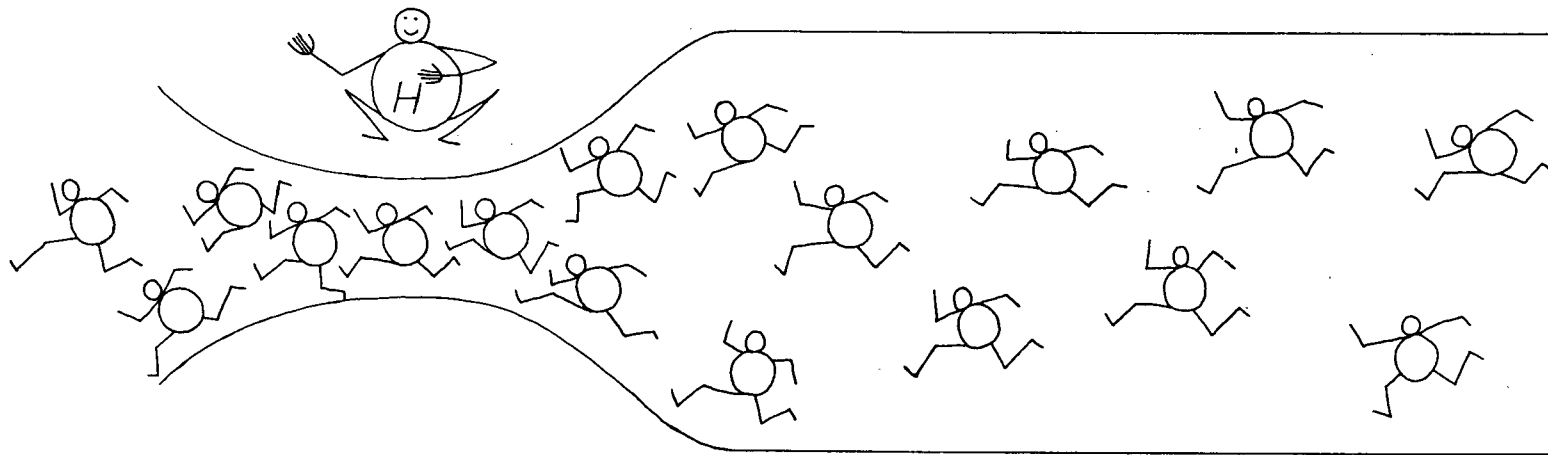
$$E_{\text{trans}} = \frac{1}{2}(\mu_{F_2}) (\dot{q}_{YF}^2 + \dot{q}_{FF}^2)$$

with an effective mass of μ_{F_2} for the representative point for all isotopic forms of Y. The single contours shown in Figure 13 correspond to a relative translational kinetic energy, $E_{\text{trans}} = 2.01$ kcal/mole (or the equivalent potential energy relative to zero as defined in Section C below), which is approximately the classical threshold for the reaction. The skewing angles of the Mu, H, D, and T surfaces are 86.9, 80.9, 77.4, and 74.9 degrees respectively. Besides showing that the skewing angle approaches 90° as the isotopic mass decreases, Figure 13 shows a pronounced contraction of the exit valley and a sharp constriction (or "bottleneck") in the entrance valley near the saddle point for the lighter isotope. Another feature of this surface to note is that the potential energy barrier or saddle point is "early"; that is, it is located along the entrance valley for all isotopic variations of the reaction.

Although the LEPS surfaces for the reactions of H isotopes with Cl_2 , Br_2 and I_2 are not as well known as those for the F_2 reaction [Jakubetz 1-(78), Connor 2-(77)], it is expected that their topological features should be similar to the F_2 surface [Bauer 1-(78), Pattengill (76), Blais (74)] with two notable exceptions: (1) while the collinear reactive geometry is strongly favored for the F_2 and Cl_2 reactions [Jakubetz 1-(78),

Polanyi (75)], this is probably not the case for the Br_2 and I_2 reactions [Baybutt (78), Bauer 1-(78), Blais (74)]; and (2), the existence of a static potential energy barrier (saddle point on the potential energy surface) is not clearly established for the Br_2 and I_2 reactions [White (73), Baybutt (78), Blais (74)]. For the sake of argument, in the following discussion, it is assumed that the LEPS surfaces for the halogen homologous series are similar, with potential energy barriers decreasing in the order $\text{Cl} > \text{Br} > \text{I}$ (the F_2 reaction has an anomalously smaller barrier than the Cl_2 reaction [Pattengill (76), Anlauf (72)]); furthermore, it is assumed that the Mok-Polanyi [Mok (69)] correlation holds: the potential energy barrier moves to consecutively earlier positions as the barrier height decreases in a series of exothermic reactions.

Within the assumptions made above, it seems clear that the mass weighted LEPS surfaces for the H isotope reactions with the halogen series should display the same essential behaviour as that shown in Figure 13, from which a number of generalizations can be made concerning the reaction dynamics. A substantial "bottleneck effect," whimsically illustrated in Figure 14 (adapted from Connor 2-(77)), was predicted by Manz (76) on the basis of Figure 13 before being verified by detailed trajectory calculations. This effect suggests that classical contributions to the reaction probability favor the heavy H isotopes for which the motion of the representative points through the bottleneck displays essentially laminar flow in contrast to the turbulent flow exhibited in the Mu reaction.



$F + YF$ \leftarrow ----- $Y + F_2$

The bottle-neck effect

FIGURE 14: Adapted from Connor 2-(77).

On this basis, it is predicted that classically the reaction probability will follow the order $T > D > H > \text{Mu}$. Similarly, the contraction of the product valley in the Mu case presents a greater probability for classical non-reactive "back-reflection" of the representative points off the strongly repulsive wall in the product valley directly opposite the saddle point, corresponding to high energy collisions; that is, the contracted product valley makes it much more difficult for the reaction to "turn the corner" in the Mu case than for the other H isotopes. This effect, which has been theoretically verified [Connor 2-(78)], again suggests a reaction probability order of $T > D > H > \text{Mu}$, since the classical Mu reaction probability (or cross section) will fall off at lower energies in the high temperature regime than for the other H isotopes. A much less important but correlated effect is that due to the skewing angle of the potential surface: the smaller the skewing angle, the less prone to back-reflection is the reaction. Again, this favors the order $T > D > H > \text{Mu}$.

The existence of an "early" potential energy barrier has a number of implications. From the point of view of this thesis, perhaps the most important implication of this topological feature is the fact that the representative point crosses the potential barrier while it is still on a trajectory that is more or less parallel to the r_{YX} axis. As shown in Part (ii) above, this means that the effective mass of the representative point, on either the unweighted surface or on the surface that is mass weighted according to equations (22), is μ_{Y,X_2} , which is essentially equal to the H isotopic mass

(alternatively, in the Connor mass weighting scheme of equation (23) in which the effective mass of the representative point is the same for all H isotopes, the width of the energy barrier is proportional to $(\mu_{Y,X_2})^{1/2}$). Consequently, the full mass effect of H isotopic substitution is utilized in barrier penetration (quantum mechanical tunnelling) [Jakubetz 1-(78)]. This would not be the case if the potential energy surface had a symmetrically placed or late barrier. From these considerations, it is expected that the Mu reaction will be subject to much greater tunnelling than the other H isotopes, tending to order the quantum mechanical reaction probabilities in the low temperature regime $\text{Mu} > \text{H} > \text{D} > \text{T}$. Furthermore, shown to scale on the left of Figure 12 are the thermal de Broglie wavelengths ($\lambda = \frac{h}{(2\pi k_B T \mu)^{1/2}}$) of the effective masses of the representative points μ_{Y,F_2} , corresponding to Y-F₂ motion, and $\mu_{XF,F}$ (\approx constant for all Y), corresponding to YF-F motion¹; substitution of X = Cl, Br, or I for F does not affect the μ_{Y,X_2} wavelength, but further contracts the $\mu_{YX,X}$ wavelength. As a rough rule, if the thermal de Broglie wavelength of a particle

¹Strictly speaking, the representative point slows down as it encounters the potential energy barrier so that its de Broglie wavelength is a function of its coordinates on the potential energy surface. Denoting q_r as a general reaction coordinate, the de Broglie wavelength of the representative point is given by $\lambda(q_r) = \frac{h}{(2\mu[E_{\text{trans}} - V(q_r)])^{1/2}}$, where μ is its effective mass, E_{trans} is the initial relative translational kinetic energy, and $V(q_r)$ is the height of the potential surface at q_r above the asymptotic reactant valley [Nikitin (74)]. Consequently, the thermal de Broglie wavelengths shown in Figure 12 are minimum thermal averages. This point does not fundamentally affect the arguments made above.

is shorter than the width of a barrier, tunnelling is minimal; conversely, if its thermal de Broglie wavelength is longer than the barrier width, tunnelling is expected to be important [Nikitin (74)]. These considerations suggest that quantum mechanical reaction probabilities may be accurately estimated by applying some sort of one dimensional barrier penetration correction to classical or TST calculations [Jakubetz (79)] without the need to consider such complications as alternate tunnelling paths ("corner cutting") (see eg. [Marcus (78), Johnston (61)]).²

Another implication of the early potential barrier concerns the final state vibrational energy distributions of the reaction products (rotational energy transfer cannot take place in collinear collisions). Although final state distributions are as yet experimentally inaccessible to Mu studies, they are of sufficient theoretical interest to warrant a brief discussion. For exothermic reactions, late potential energy barriers are associated with repulsive energy release in which the reaction exoergicity is released as the reacting atoms separate; early potential energy barriers are often associated with mixed energy release, that is, part of it is attractive (released as the projectile atom approaches the target molecule), and part of it is repulsive. Although the collinear LEPS surfaces for the F_2 and Cl_2 reactions are known to be predominantly repulsive

²Actually the barriers to tunnelling considered in most trajectory or TST calculations are not identical to the static barriers described by the potential energy surface. Nevertheless, the present discussion is valid because the location and shape (but not height) of these barriers are essentially the same as the static potential energy barriers. This point is discussed in Section C below.

[Polanyi (75), Pattengill (76), Wilkins (75)], it is not clear if this is the case for the Br_2 and I_2 surfaces [Polanyi (75), Blais (74), Baybutt (78)]. In any case, a corollary of the Mok-Polanyi correlation is expected to hold: "in a homologous series in which a falling barrier is not accompanied by an increase in exothermicity, the increase in attractive energy release will be accompanied by a decrease in repulsive energy release [Mok (69)]." Roughly speaking, the attractive part of a mixed energy release is transformed into vibrational energy of the products, while the repulsive part is transformed into translational kinetic energy of the products [Polanyi (72)]. Since the skewing angles of the $\text{Y} + \text{X}_2$ potential energy surfaces are approximately the same, it is expected that as X changes from F to I, the increase in attractive energy release will be accompanied by an increase in the vibrational energy of the products [Wilkins (75)]. On the other hand, as Y varies from T to Mu, the product energy distributions should display the "light atom anomaly [Polanyi (75)]:" on repulsive surfaces, when the mass of the attacking atom is much less than those of the target molecule, less reaction exoergicity is channelled into product vibrational energy as the mass of the attacking atom decreases. This may be pictured as an inertial effect in which the rapid release of the reaction exoergicity on the dominant repulsive part of the surface imparts such momentum to the separating heavy atoms (B-C) that the relatively insignificant momentum of the light attacking atom (A) is overwhelmed. On the other hand, if A were of a comparable mass to the atoms of the target molecule, it would have such inertia that when

the repulsive reaction exoergicity slammed B into it, the result would be a vibrationally excited A-B molecule.

Since the dynamics of the reactions of H isotopes with the hydrogen halides are probably influenced more by the disposition of energy among internal molecular modes than by the topology of the potential energy surfaces, the discussion of H-HX LEPS surfaces is deferred until the next Section where these energy effects are taken into account.

C Energy

To this point, H isotope effects have been discussed on the basis of intuitive predictions of the behaviour of trajectories of a representative point encountering characteristic topological features of electronically adiabatic potential energy surfaces. Besides the potential energy surface and the translational kinetic energy of the representative point, reference has been made to other energies such as the reaction activation energy and enthalpy, classical threshold energy, and internal energy of the target and product molecules. The task of this Section is to define these forms of energy and interpret their roles in the reaction process. Finally, some of these ideas are applied in a discussion of H isotope - hydrogen halide reactions.

Energy definitions used in conjunction with potential energy surfaces depend upon the choice of an arbitrary reference point of zero energy for which, unfortunately, there is no single convention. For example, in Figure 12, all of the contours of the LEPS surface are drawn with respect to

zero defined as the dissociation limit of F_2 , except for the dashed contour representing a potential energy equivalent to the relative translational kinetic energy of the classical threshold, which is drawn with respect to a different zero as defined below. This confusion is further aggravated by the fact that various authors often use the same name to refer to different energies. For example, in a discussion of the reactions of $Y + F_2 \rightarrow YF + F$, $Y = Mu, H, D, T$, what Connor et al.¹(79) call the "barrier height" is quoted with values of both 2.35 and 1.08 kcal/mole, the former referring to the height of the saddle point relative to the bottom of the asymptotic reactant valley, while the latter refers to this value less the zero point vibrational energy of the F_2 molecule. This multiplicity of definitions has its genesis in the multitude of approaches to the calculation of reaction kinetics; for example, classical trajectory calculations apply a different meaning to the "barrier height" than quasiclassical or quantum mechanical trajectory calculations. Clearly, there is a need for considerable care in defining the various energy terms.

(i) Classical Trajectories

The picture of a ball rolling along the minimum energy path of the potential energy surface corresponds to a purely classical trajectory in which the internal vibrational and rotational energies of the target molecule are initially zero. In this case, it is useful to consider the potential barrier height, denoted here as E_b^{Cl} and defined as the elevation of the

saddle point above the bottom of the asymptotic reactant valley. Within the BO approximation, E_b^{Cl} is the same for all isotopic variants of the H atom reactions. Since there is no internal energy in the target molecule at the onset of collision in this picture, the relative translational kinetic energy of the representative point is the only energy available to propel it over the potential barrier to bring about reaction. Therefore, the relative translational kinetic energy, E_{trans}^{Cl} , is also measured with respect to zero taken as the bottom of the asymptotic reactant valley. It is useful to picture the relationship between the kinetic energy of the representative point and the potential energy surface in terms of an airplane flying through the valley at a constant altitude measured from the asymptotic minimum of the reactant valley. In this picture, the height of the plane above the valley floor corresponds to the kinetic energy of the representative point, and it is clear that if the altitude of the airplane does not exceed the elevation of the saddle point, a non-reactive crash will occur. The utility of this pedantic analogy will become evident in the later discussion of quasiclassical and quantum mechanical trajectories.

Closely related to the potential energy barrier height is the notion of a classical threshold energy, denoted E_T^{Cl} and defined as the minimum translational kinetic energy of the representative point required for reaction. In terms of the purely classical picture discussed in the previous paragraph, it might seem that the threshold energy is identical to the potential barrier height, but this is generally not the case.

To understand the difference, it must be noted that although the classical picture under consideration assumes that initially the target molecule possesses no internal energy, it does not prohibit the transfer of collisional kinetic energy into internal energy of the target molecule. As implied in the discussions in Section B on back-reflection and the light atom anomaly, inertia will cause the trajectory of the representative point to deviate from the minimum energy path as it attempts to "turn the corner" of the potential energy surface [Nikitin (74)]. Not even in the case of early barriers can it be assumed that the saddle point is collinear with the incident minimum energy path, as illustrated in Figure 15 for the $\text{Mu} + \text{F}_2 \rightarrow \text{MuF} + \text{F}$ reaction (adapted from Connor 1-(77)). Consequently, the representative point generally attempts to cross the potential barrier at a point other than the minimum barrier height. For surfaces with symmetrically placed, or late barriers, the representative point will possess a relatively large component of velocity perpendicular to the minimum energy path as it attempts to cross the barrier, corresponding to conversion of some of the initial translational kinetic energy into vibrational energy of the reacting species. In short, threshold energies are dynamical quantities while energy barriers are static. From these considerations of the classical trajectory, it can be seen that the classical threshold energy must be greater than or equal to the potential energy barrier height. In the case of quasiclassical trajectories, it may happen that the reaction threshold energy is less than E_b^{Cl} , as discussed later in this Section.

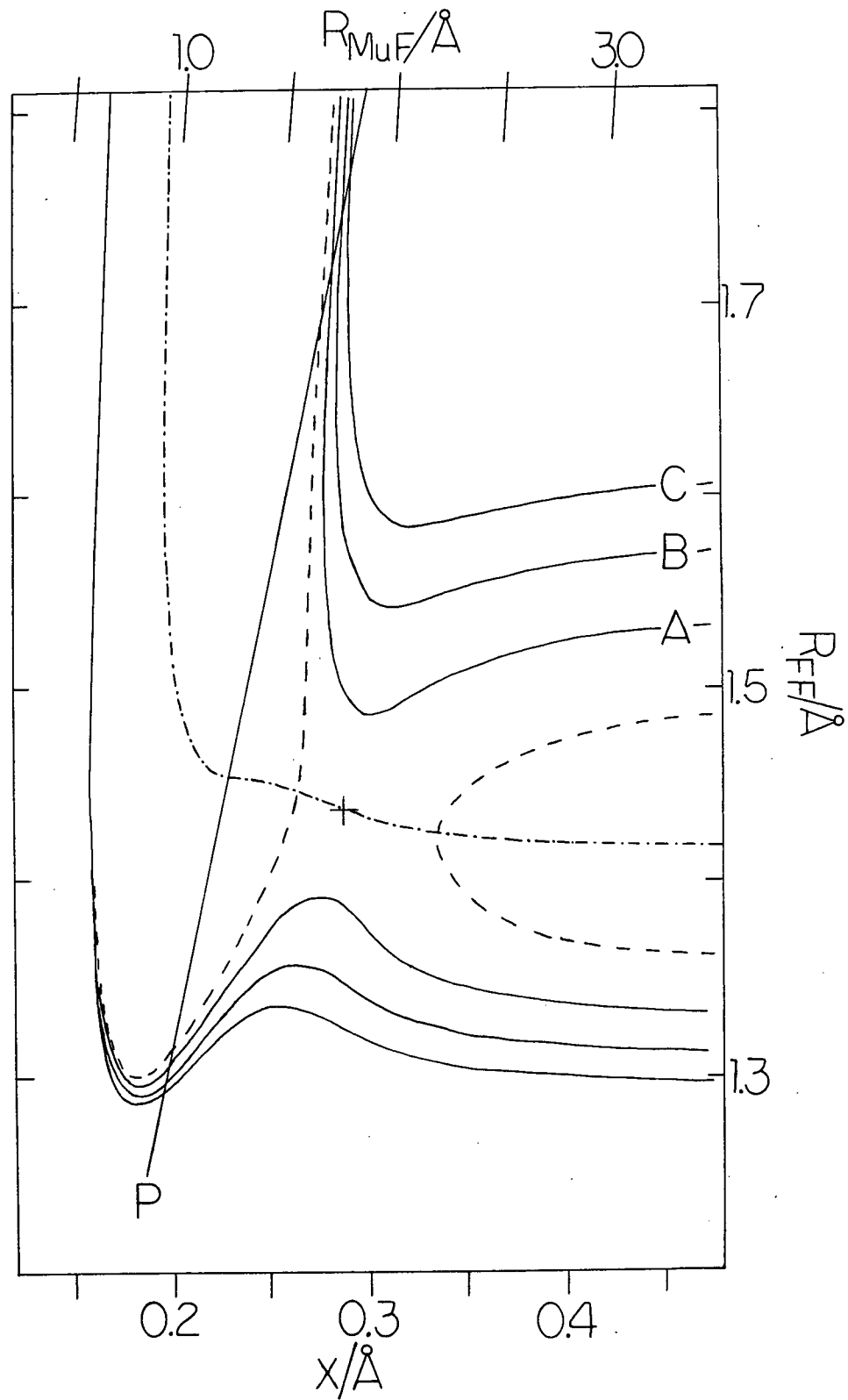


FIGURE 15: Mass weighted potential energy surface for the collinear $\text{Mu} + \text{F}_2$ reaction, adapted from Connor 1-(77); x is defined in the text. The dash-dot line is the minimum energy path. The dashed lines indicate contours where the reactant and product translational energy is zero. Contours A, B, and C are at $E_{\text{OC}}^{\text{trans}} = 0.08, 0.16, \text{ and } 0.24$ eV. Line P is the "line of no return" mentioned in Chapter IV.

For surfaces possessing early barriers, it is expected that threshold energies for the various H isotopes will be similar (but not identical) to each other due to the relatively mild distortions of the reactant valley under the transformation to mass weighted coordinates (eg. Figure 13). As discussed in the previous Section, H isotope reactions with the halogens display a "bottleneck" effect which tends to order $E_T^{Cl} : \text{Mu} > \text{H} > \text{D} > \text{T}$.

It should be noted that the commonly used phrase, "the classical threshold energy of the reaction," implying the existence of a unique value, often represents a misuse of the language. Certainly, in the case of purely classical trajectories, there is a unique threshold energy for each surface. However, multidimensional trajectory calculations must be performed on several surfaces, each with its own threshold energy. Thus, while one may speak of the classical threshold energy for a one dimensional trajectory, three dimensional trajectories have a range of threshold energies over the various ABC bond angles and impact parameters (that is, the minimum distance between the approach trajectory and the center of mass of the target molecule). The notion of a single reaction threshold energy is even less precise in the case of quasiclassical trajectories, discussed next.

(ii) Quasiclassical and Quantum Mechanical Trajectories

Although it was shown in the previous Section that classical trajectories provide a qualitatively useful picture of the dynamics of a reaction, it is unrealistic to ignore the

initial internal vibrational and rotational energy of the target molecule. In principle, all of the vibrational energy of the target molecule is available to promote reaction since the B-C stretch in the reaction $A + BC \rightarrow AB + C$ corresponds to the reaction coordinate along the product valley. Quasi-classical trajectory calculations are formulated such that before any interaction of the collision partners occurs, the internal states of the target molecule are described by quantum mechanical probability density functions; but once the trajectory begins, all of the motion is classical [Thompson (76)]. Of course, quantum mechanical trajectory calculations involve quantum state distributions throughout the reaction. A more detailed discussion of the various types of trajectories is given in Section D.

For QCT and QMT calculations, it is customary to define a number of energies relative to zero taken as the height of the vibrational energy of the target molecule (denoted E_v) above the bottom of the asymptotic reactant valley, thereby assuming that all of this vibrational energy is available for reaction. For example, this zero energy is shown as the dashed contour in Figure 15 for the reaction $Mu + F_2 \rightarrow MuF + F$ with F_2 in the $v = 0$ state. Based on this energy zero, the physical barrier height, E_b^{phys} , is defined as

$$E_b^{\text{phys}} = E_b^{\text{Cl}} - E_v \quad (24)$$

It may be noted that all of these quantities are invariant under isotopic substitution of the projectile atom. E_b^{phys} serves as the boundary that differentiates dynamical tunnelling from static tunnelling as discussed in Section F below. Since

all of the vibrational energy of the target molecule may be available to promote reaction, the translational kinetic energy of the representative point is also measured relative to this zero contour and is denoted $E_{\text{trans}}^{\text{QC}}$. In terms of the picture of an airplane flying up the reactant valley, this new zero energy corresponds to a flooded valley with a shoreline corresponding to the dashed contour of Figure 15, for example. The initial translational kinetic energy of the representative point is equivalent to the altitude of the airplane above sea level, and if this altitude does not exceed the elevation of the physical barrier, a non-reactive crash will occur. For the reaction of Mu with F_2 in the $v = 1$ state, $E_1 > E_b^{\text{Cl}}$ so there is no physical barrier to reaction.

For QCT, it is also common to define a threshold energy, E_T^{QC} , corresponding to the minimum translational kinetic energy required for reaction. While the notion of a threshold energy has little meaning in terms of QMT calculations, the quasiclassical threshold energy is useful for partitioning QMT results into classically allowed and purely quantum mechanical processes, as discussed in Section F below. For the same reasons mentioned in the case of classical threshold energies, quasiclassical threshold energies must be greater than or equal to the physical barrier height, E_b^{phys} . However, because any amount of the vibrational energy of the target molecule, E_v , may be available to promote reaction, the quasiclassical threshold energy may not only be greater than or equal to, but also less than the potential barrier height, E_b^{Cl} [Nikitin (74)]. A good discussion of the origins and interpretation of quasi-

classical threshold energies is given in Porter et al. (73). A major problem in defining quasiclassical thresholds for even a single surface is the fact that the reaction probability is not only energy dependent but it also depends on the phase of oscillation of the target molecule. Quasiclassical threshold definitions are obtained by some kind of averaging process (such as Monte Carlo averaging) over the oscillator phase; however, different procedures result in slightly different threshold energies [Connor 1-(76)]. As in the discussion of classical thresholds above, the mass distortions of the effective potential energy surfaces for H isotope - halogen reactions suggest that the quasiclassical threshold energies are also ordered $\text{Mu} > \text{H} > \text{D} > \text{T}$.

(iii) Transition State Theory

While TST calculations may be based on the potential energy barrier, E_b^{Cl} [Persky (77), Jakubetz (79)], it is more common to make the assumption of vibrational adiabaticity (VA): "the reactant vibrations (except for the one that becomes the reaction coordinate) evolve smoothly into those of the activated complex, and finally into those of the product, without any change in vibrational quantum numbers [Weston (72)]." Of course, the amount of vibrational energy is not constant because the vibrational force constants (or curvature of the potential surface) change during the progress of the reaction. For the reaction $\text{A} + \text{BC} \rightarrow \text{AB} + \text{C}$, the VA barrier heights are defined as [Connor 1-(79), Jakubetz (79)]:

$$E_V^{\text{VA}}(\text{A}) = E_b^{\text{Cl}} + E_V^\ddagger(\text{A}) - E_V \quad (25)$$

where $E_V^\ddagger(A)$ is the energy of the bound normal mode(s) of $(ABC)^\ddagger$ and E_b^{Cl} and E_V have been defined above. The double dagger refers to the transition state. The values of E_V^\ddagger and hence E_V^{VA} depend on the H isotopic mass and are ordered: $Mu > H > D > T$, predicting an inverse isotope effect for all isotopic H atom reactions which orders the reaction rates: $T > D > H > Mu$ (this is often referred to as the "secondary isotope effect" [Nikitin (74), Van Hook (70)]). In many cases, such as $Y + X_2 \rightarrow YX + X$, $Y = Mu, H, D, T$; $X = F, Cl$; the presence of Y in the transition state weakens the X-X bond without complete compensation from the formation of the Y-X bond [Jakubetz (79), Connor 1-(79)] with two results: (1) $E_V \gtrsim E_V^\ddagger(Y)$ and thus $E_V^{VA}(Y) \lesssim E_b^{Cl}$ and (2) due to vibrational anharmonicity, higher energy vibrational states are more closely spaced than lower ones so that $E_0^\ddagger(Y) - E_0 > E_1^\ddagger(Y) - E_1$ and thus $E_0^{VA}(Y) > E_1^{VA}(Y)$. Linear transition state triatomics have four normal modes of vibration: two bound bending modes, the bound symmetric stretch corresponding to motion along a line perpendicular to the reaction path at the saddle point, and the unbound asymmetric stretch corresponding to motion along the reaction path itself (this mode has an imaginary frequency). For the collinear reaction, the symmetric stretch is the only bound normal mode, uniquely defining $E_V^\ddagger(A)$.

In general, the assumption of vibrational adiabaticity is approximately valid at normal temperatures [Levine (74)]. In the particular cases of H isotope reactions with halogens, the early barriers are expected to favor the VA assumption because the transition state corresponds to an only slightly perturbed

target molecule [Connor 1-(79), Jakubetz (79)]. Although quasiclassical trajectory calculations do not assume vibrational adiabaticity (allowing a continuous energy transfer between the vibrational and translational modes in either direction), the preceding arguments on the expected validity of VA provide the basis for making the "first guess" prediction that the quasiclassical thresholds, E_T^{QC} , for these reactions will be very similar to the VA barrier heights.

Table IV compares the values of the energy definitions made so far for the collinear reaction $Y + F_2 \rightarrow YF + F$, $Y = Mu, H$, based on the LEPS surface due to Jonathan et al. (72).

(iv) Reaction Enthalpy

Thermodynamic reaction enthalpies are calculated with Hess's Law by summing the heats of formation of reactants and products under isothermal standard state conditions at 298K, ΔH_{298}^0 . The results are averaged over Maxwell-Boltzmann internal energy state distributions at 298K and also include any contributions due to physical state changes (heats of vaporization, solidification, etc.). From the viewpoint of calculations of the rates of isolated atom-diatom reactions, it is more useful to consider reaction enthalpies as the difference between the bond dissociation energies, D_0 , of the product and reactant molecules. The bond dissociation energy is defined by $D_0 = D_e - E_0$, where D_e is the equilibrium dissociation energy (depth of the Morse potential), and E_0 is the zero point energy (ZPE). Since this definition of reac-

TABLE IV: ENERGY[†] DEFINITIONS FOR THE COLLINEAR Y + F₂ REACTION
Y = Mu, H, FOR THE LEPS SURFACE OF JONATHAN (72)

	Mu	H
CLASSICAL BARRIER HEIGHT, E_b^{Cl}	2.35	2.35
PHYSICAL BARRIER HEIGHT, E_b^{phys}	1.08	1.08
QUASICLASSICAL THRESHOLD ENERGY, E_T^{QC} [§]	1.80	2.06
ZERO POINT ENERGY OF F ₂ , $E_0(F_2)$	1.27	1.27
ZERO POINT ENERGY OF ACTIVATED COMPLEX, $E_0^\ddagger(YFF)$	1.20	1.12
VIBRATIONALLY ADIABATIC BARRIER HEIGHT, E_0^{VA}	2.28	2.20
E_1^{VA}	2.15	1.91

[†] kcal/mole, taken from Connor (79)

[§] the origin of the lower value of E_T^{QC} for Mu is explained in Chapter IV, p. 148.

tion enthalpy is based on ZPE's, it corresponds to the Maxwell-Boltzmann population at 0K and is often denoted ΔH_0^0 [Wolfrum (77), Douglas (76)]. ΔH_0^0 is also independent of physical state changes.

The bond dissociation energies, ZPE's, and reaction enthalpies of the molecules and reactions studied in this thesis are summarized in Table V. This table shows that some of the reactions of Mu with the hydrogen halides are endothermic; some implications of this are discussed below in this Section. In general, because of the larger ZPE of products containing lighter H isotopes, the exothermicity of H isotope reactions based on ΔH_0^0 are ordered: T > D > H > Mu.

(v) Reaction Activation Energy

Although a general discussion of trajectory methods is left to the next Section, it is useful at this point to anticipate one of the major concepts common to those methods, in order to derive the Tolman interpretation of the activation energy (following [Levine (74)]). All trajectory calculations provide values of some form of reaction rate constant that is a function of the relative translational kinetic energy of the colliding species. In order to calculate thermally averaged rate constants from these results, it is necessary to compute an integral of the following general form:

$$k(T) = \int_0^{\infty} \frac{e^{-E/k_B T}}{Q} k(E) dE \quad (26)$$

where $e^{-E/k_B T}$ is the Boltzmann weighting factor and Q is the partition function which normalizes the result. Partition

TABLE V: BOND DISSOCIATION ENERGIES, ZERO POINT ENERGIES, AND REACTION ENTHALPIES[†]

reactant molecule	D_e	E_0	product molecule	D_e	E_0	ΔH_0^0
F ₂	37.59	1.27	MuF	141.13	16.61	-88.2
			HF	141.13	5.78	-99.0
			DF	141.13	4.25	-100.6
			TF	141.13	3.56	-101.2
Cl ₂	57.88	0.81	MuCl	106.43	12.24	-37.1
			HCl	106.43	4.27	-45.1
			DCl	106.43	3.07	-46.3
			TCl	106.43	2.52	-46.8
Br ₂	45.92	0.46	MuBr	90.36	10.92	-34.0
			HBr	90.36	3.79	-41.1
			DBr	90.36	2.68	-42.2
			TBr	90.36	2.20	-42.8
HCl	106.43	4.27	MuH (MuCl)	109.46 (106.43)	13.53 (12.24)	+6.2 (+7.9)
			HH (HCl)	109.46 (106.43)	6.23 (4.47)	-1.1 (0.0)
			DH (DCl)	109.46 (106.43)	5.38 (3.04)	-1.9 (-1.2)
			TH (TCl)	109.46 (106.43)	5.07 (2.52)	-2.2 (-1.8)
HBr	90.36	3.79	MuH (MuBr)	109.46 (90.36)	13.53 (10.92)	-9.4 (+7.1)
			HH (HBr)	109.46 (90.36)	6.23 (3.79)	-16.7 (0.0)
			DH (DBr)	109.46 (90.36)	5.38 (2.68)	-17.5 (-1.1)
			TH (TBr)	109.46 (90.36)	5.07 (2.20)	-17.8 (-1.7)
HI	73.66	3.27	MuH (MuI)	109.46 (73.66)	13.53 (9.52)	-25.5 (+6.3)
			HH (HI)	109.46 (73.66)	6.23 (3.27)	-32.8 (0.0)
			DH (DI)	109.46 (73.66)	5.38 (2.33)	-33.7 (-0.9)
			TH (TI)	109.46 (73.66)	5.07 (1.91)	-34.0 (-1.4)

[†] all values are in kcal/mole calculated from spectroscopic data from G. Herzberg, Spectra of Diatomic Molecules, 2nd ed., Van Nostrand, Princeton, 1950.

functions have the general form

$$Q = \sum_i e^{-\epsilon_i/k_B T} \quad (27)$$

where ϵ_i is the energy of the i th state. On the other hand, the Arrhenius activation energy expression, $k(T) = A e^{-E_a/k_B T}$, is a measure of the rate of change of the rate coefficient as a function of inverse temperature. Assuming temperature independence of the pre-exponential factor (which is, in fact, weakly temperature dependent), this may be re-written:

$$E_a = \frac{-k_B d[\ln k(T)]}{d\left(\frac{1}{T}\right)} \quad (28)$$

Substitution of equation (26) into (28) yields:

$$E_a = \frac{\int_0^\infty E e^{-E/k_B T} k(E) dE}{\int_0^\infty e^{-E/k_B T} k(E) dE} - \left(\frac{k_B d[\ln Q(T)]}{d\left(\frac{1}{T}\right)} \right) \quad (29)$$

The first term of this expression is clearly an average energy and it is interpreted as the average energy of those collisions which result in reaction, $\langle E^* \rangle$. Differentiation of the second term of equation (29) followed by substitution of equation (27) yields:

$$\frac{k_B T^2 d[Q(T)]}{Q(T)} = \frac{\sum_i \epsilon_i e^{-\epsilon_i/k_B T}}{\sum_i e^{-\epsilon_i/k_B T}}$$

which is just the average energy of the reactants, $\langle E \rangle$. Thus, equation (29) is simply:

$$E_a = \langle E^* \rangle - \langle E \rangle \quad (30)$$

that is, the activation energy is just the difference between the average energy of those collisions that actually result in reaction and the average energy of all collisions. This

conceptually useful result is due to R. C. Tolman (27). The process of quantum mechanical tunnelling reduces $\langle E^* \rangle$ from the value it would have classically, thereby lowering E_a . In the high temperature regime, the relative contribution of tunnelling to the reaction rate is diminished from that of the low temperature regime since a higher fraction of collisions are energetically capable of reacting classically. These considerations predict that the tunnelling process will manifest itself experimentally in terms of the temperature dependence of equation (30): E_a will decrease with decreasing temperature. Similarly, it has already been mentioned that Mu is expected to tunnel more easily than H in reactions with halogens due to the smaller effective mass of the representative point. Thus, in the same temperature range (fixed $\langle E \rangle$), one expects to find experimental values of E_a to be reduced for the Mu reactions. Other dynamical effects besides tunnelling may contribute to $\langle E^* \rangle$; for example, all of the classical dynamical effects discussed so far in the H isotope - halogen reactions tend to raise $\langle E^* \rangle$ for the Mu reaction, thereby possibly offsetting any tunnelling effects. These considerations clearly show that activation energies are not just energy averages but also dynamical averages.

(vi) Potential Energy Surfaces for the Reactions $Y + HX \rightarrow YH + X$
 $Y = \text{Mu, H, D, T}; X = \text{Cl, Br, I.}$

Before considering specific potential energy surfaces for the hydrogen - hydrogen halide (HX) reactions, it should be noted that this seemingly simple substitution of the X_2 mole-

cule by an HX molecule greatly complicates both the experimental and theoretical studies of this series of reactions. Testimony to this is the vast amount of conflicting literature published in the past twenty years on these reactions; as an example, a good summary of the theoretical and experimental debate on the $H + HCl$ reaction may be found in [Bauer 2-(78), Weston (79)]. The $Y + HX$ systems have two reaction channels: hydrogen abstraction ($Y + HX \rightarrow YH + X$) and hydrogen exchange ($Y + HX \rightarrow YX + H$), each with its own potential energy surfaces. Experimentally, this means that rate data for the individual reaction channels must probably be obtained via measurements of product formation rather than reactant depletion. Since the MSR method is of the latter variety, it has so far only been possible to measure the total μ reaction rates ($k_{abs} + k_{exc}$) and, in fact, only the room temperature reaction rates have been measured to date. In principle, it may be possible to determine the Arrhenius parameters for the individual reaction channels of μ by simply measuring the temperature dependence of the total reaction rates in the usual way. If both the μ exchange and abstraction reactions display Arrhenius straight-line behaviour over a wide temperature range (which, in view of the results discussed in Chapter IV, might not be the case, and, in fact it is not clear that even H displays this behaviour [Bauer 2-(78); Clyne (66)]), and if the activation energies for the two reaction channels are substantially different (this is probably true; see eg. [Bauer 2-(78)]), then the Arrhenius plot for the total reaction could show a break with the high activation energy reaction described by the high

temperature part of the plot and the low activation energy reaction described by the low energy part.

Reactions of HF are not considered in this thesis because it is expected that the reaction rates of Mu with HF are so slow that they are immeasurable by the MSR technique.

Accurate experimentally optimized LEPS surfaces do not exist for either the exchange or abstraction reactions of H isotopes with the hydrogen halides because many of the experimental results are "equivocal or contradictory [McDonald (75)]." Two topologically different surfaces have been recently considered for the abstraction reactions (Figure 16 shows the $H + HCl \rightarrow H_2 + Cl$ examples): (1) the simple LEPS surface shown at the top of the Figure (adapted from [Persky (78)]), optimized for the reverse reaction: $H_2 + Cl \rightarrow HCl + H$ which has an early barrier to H abstraction and the same essential features as the H isotope - halogen surfaces (Figure 12), and (2) the valence bond modified LEP surface mentioned in Section B, shown at the bottom of the Figure (adapted from [Porter (73)]; also optimized for the reverse reaction) which, besides having an early barrier to H abstraction, shows shallow potential wells in both the reactant and product valleys. Although three dimensional QCT calculations performed on the Persky surface are in very good agreement with experimental results of $Cl + H_2$ versus $Cl + D_2$ isotope effects and the absolute rate constant for the $Cl + H_2$ reaction [Persky (78)], and, although a truly accurate surface will provide the basis for accurate descriptions of a chemical reaction in both directions, surfaces that have been optimized with respect to a

thermal (300K)
de Broglie wavelengths

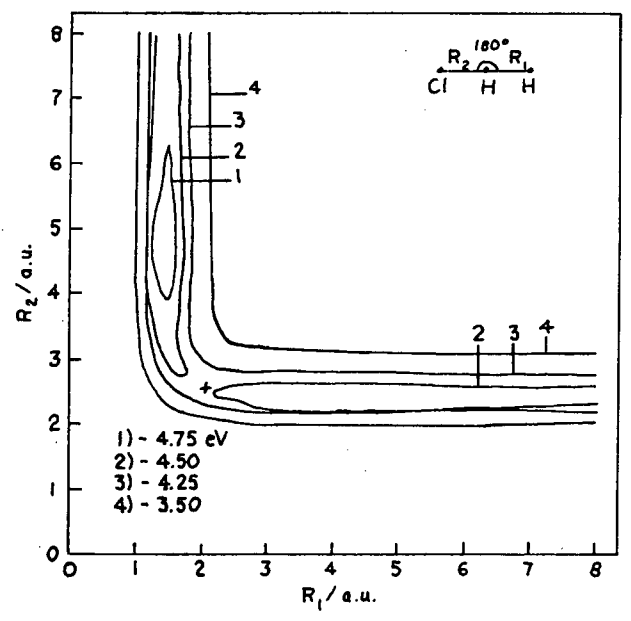
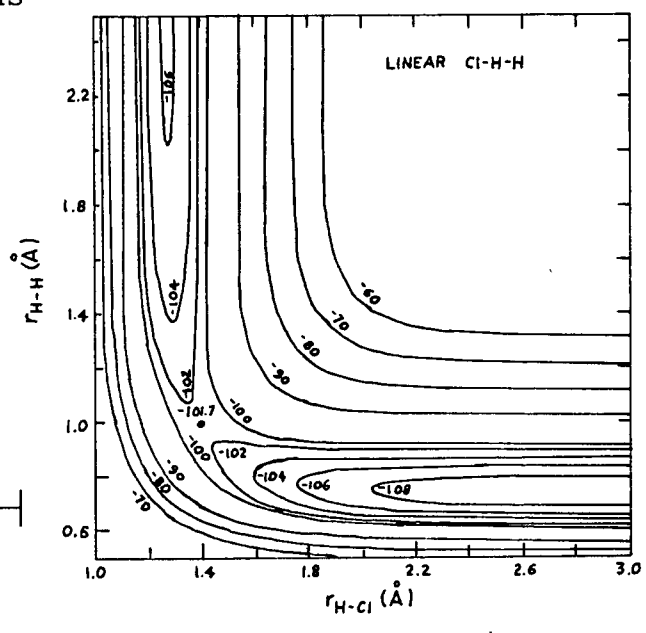
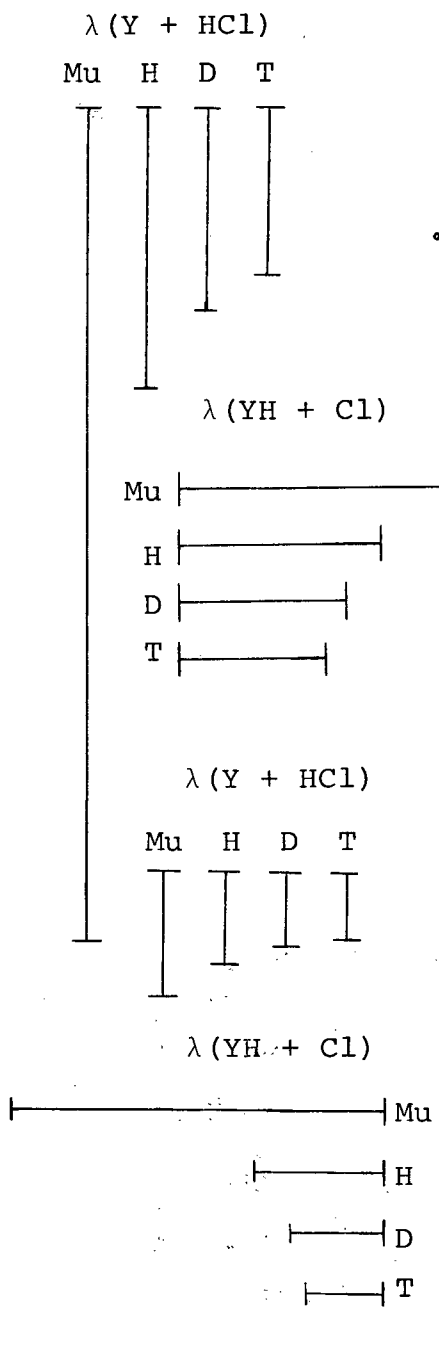


FIGURE 16: Potential surfaces for the collinear $H + HCl \rightarrow H_2 + Cl$ reaction, adapted from Persky (78) (top) and Porter (73) (bottom). Note that the Persky surface is drawn reversed from the other contour plots shown in this thesis; it has its reactant valley at the top and its product valley at the right. The Persky surface contours are labelled in kcal/mole relative to the dissociation limit of H_2 . The 300K thermal de Broglie wavelengths of the representative points on trajectories parallel to the axes are shown at the left of each surface.

reaction in one direction must be viewed with caution when applied to the reverse reaction [Heidner (76)]. In fact, a general failing of LEPS surfaces is "that semi-empirical surface parameters obtained by calibration on one reaction are often not transferrable to another reaction involving the same atoms [White (73)];" (in his paper, White discusses some successful exceptions to this generalization). This problem sometimes appears as a general constraint in the consideration of H isotope exchange versus abstraction reactions with the hydrogen halides, although many authors simply treat each reaction channel independently of the other (eg. [Klein (78)]).

Porter et al. predict that the abstraction reaction surfaces for the linear configuration possess wells corresponding to weakly stable H_2-X and $H-HX$, $X = Cl, Br, I$, with depths ranging from 1-4 kcal/mole. Furthermore, they have found that some of these minima are sufficiently deep to accomodate one or more vibrational levels for the H, D, or T isotopic variations of the complexes and that these complexes should be stable enough to permit isolation at low temperatures. However, there is not yet any experimental evidence available to support these predictions. On the other hand, experimental data exists to suggest that HX_2 species have been isolated [Noble (68), Bondybey (71), Noble (72)] and Porter et al. found that by using their parameters for the H_2-X surfaces, they can construct $H-X_2$ surfaces that qualitatively agree with these experimental observations. From this fact, the credibility of the presence of wells in the H_2-X surfaces might be inferred. However, a number of counter-arguments on the question of the

existence of stable H-X₂ species are given in Bauer et al. 2-(78) and references therein.

If the existence of potential wells like those of the Porter surface is assumed, it is interesting to speculate on what effect they would have on the reactions. It is expected that the Mok-Polanyi correlation holds for this series of reactions [Porter (73)]: as X changes from Cl to I, the barrier height decreases and moves to progressively earlier positions. Unfortunately, the barrier heights for these reactions are not well known, but they appear to be about twice as high as those for the corresponding Y + X₂ reactions and range from about 5 kcal/mole for H + HCl to about 0.5 kcal/mole for H + HI [Klein (78), Persky (77), White (73), Bauer 2-(78)]. Consequently, for the H + HCl and H + HBr reactions at least, reactive collisions require such energy that it is unlikely that either the reactants or products will be trapped or even much affected by the wells, unless an extremely efficient energy transfer mechanism exists. For the H + HI system, relatively long-lived complexes may exist even for reactive collisions. In that case, the reaction would no longer be "direct" [Levine (74)] with a collision time shorter than one vibrational period ($\sim 10^{-13}$ s), but would be "compound" or "complex", with very complicated trajectories. Similarly, low temperature (low relative velocity) non-reactive collisions of H with HX, X = Cl, Br, I, may be expected to be of a compound nature, rather than direct. This has interesting implications for the measurements of Mu reaction rates with HX molecules with the MSR method. Direct non-reactive collisions of Mu with target

molecules are not expected to cause much depolarization of the muon because the interaction times are short, typically $\lesssim 10^{-14}$ s, compared to the hyperfine frequency of Mu, $\lesssim 10^{-10}$ s⁻¹; the fact that a long-lived Mu signal is observed in N₂ is experimental evidence of this. On the other hand, compound non-reactive collisions may be sufficiently intimate that the muon will be efficiently depolarized by the quasi-stable muonic radical formed in the collision. From these considerations, one might expect Mu reactions to display apparent inverse Arrhenius behaviour at low temperatures where the relative numbers of truly reactive collisions are few; as the temperature is lowered, the efficiency of non-reactive depolarization of the muon increases, thereby increasing the apparent Mu reaction rate. In this way, the MSR method may present an experimental means of testing the existence of potential wells in these reaction surfaces. One final consideration on this subject is the large ZPE of Mu-containing molecular bonds: since the wells are relatively shallow, they may not be capable of supporting any bound vibrational states of the muonic complex molecules, in which case the complexes would not be long-lived. A detailed consideration of the potential wells is required to clarify this question.

Besides having wells, the Porter surfaces differ from Persky's surface by the fact that their valleys possess bottlenecks near the saddle point, particularly in the H-HBr and H-HI surfaces [Porter (73)]. Other than these differences, the main topological features of the two types of surfaces are similar. The reaction dynamics for abstraction

are dominated by the collinear reaction for both surfaces [Klein (78), Thompson (75)], mainly because the barrier increases by a factor of about six as the H-H-Y bond angle changes from 180° to 90° . Although these surfaces possess early barriers, they are not as early as the corresponding Y-X₂ surface barriers, so that the saddle points are more displaced from the line along the reactant approach valley. The relative "lateness" of the barriers suggest that the classical thresholds, E_T^{Cl} , will be substantially greater than the potential barrier heights, E_b^{Cl} , and that the quasiclassical thresholds, E_T^{OC} , will be substantially greater than the physical barrier heights, E_b^{phys} . Furthermore, the activated complexes of Y-HX are expected to have relatively strong Y-H and H-X bonds, unlike the Y-X₂ activated complexes which are just slightly perturbed X₂ molecules. This effect, combined with the relatively large ZPE's of Y-H molecular bonds, suggest that $E_V^\ddagger(Y) \gtrsim E_V$, so that: (1) $E_V^{VA}(Y) \gtrsim E_b^{Cl}$ and (2) $E_0^{VA}(Y) \lesssim E_1^{VA}(Y)$, opposite to the Y-X₂ case. These considerations, plus the relative heights of the potential barriers, suggest that the abstraction reactions, Y + HX, will be slower than the corresponding Y + X₂ reactions. Although the assumption of vibrational adiabaticity is not likely to be as valid for the Y + HX abstraction reactions as for the Y-X₂ reactions because of their barrier locations, if the VA barrier heights are taken as "first guesses" of the quasiclassical thresholds, then it is expected that the inverse isotope effect that orders the reaction rates T > D > H > Mu will be much more severe for the Y + HX abstraction reactions. The VA barriers also suggest

that vibrational excitation of the target molecules will be less effective in promoting the abstraction reactions than in the halogen molecule reactions; this prediction has been experimentally confirmed [Wolfrum (77), Arnoldi (76)]. It may also be expected that the relatively large vibrational non-adiabaticity of the abstraction reactions causes VA-TST to overestimate the effective barrier height, thereby making its predicted reaction rates erroneously small.

The displacement of the saddle points from the reactant approach valleys also has a number of effects on the tunnelling process. It is less likely that a single one dimensional barrier penetration correction applied to QCT or TST calculations of $Y + HX$ abstraction will provide an accurate approximation of the QMT results as in the case of $Y + X_2$ reactions because: the effective mass of the representative point changes during the tunnelling process; there is no obvious single tunnelling path or barrier due to the inertial effects that cause the representative point to deviate from the minimum reaction path; and "corner cutting" tunnelling paths are likely to be important [Marcus (77), Johnston (61)]. The last point is readily appreciated when it is noted that the skewing angles of the mass weighted coordinate system for the linear $Y-HCl$ surfaces are 71.6° , 45.8° , 36.4° , and 31.4° for $Y = Mu, H, D,$ and T respectively; skewing angles for $Y-HBr$ and $Y-HI$ surfaces are quite similar. Consequently, corner cutting tunnelling path lengths are ordered $Mu > H > D > T$, partially offsetting the tunnelling advantage Mu enjoys due to the effective mass of the representative point, $\mu_{Y,HX}$ (equations (22)). Figure 16

shows the thermal de Broglie wavelengths of the representative points for the isotopic variants of H corresponding to motion parallel to the unweighted surface axes. The particular mass combinations for Y + HX abstraction do not contract the product path de Broglie wavelengths as much as in the case of Y + X₂ reactions (c.f. Figure 12). Since the representative point crosses the potential barrier on a trajectory that is between the asymptotic reactant and product trajectories, Mu holds a smaller tunnelling advantage in these reactions than in the Y + X₂ reactions. Thus, while tunnelling still orders the reaction rates Mu > H > D > T, tunnelling is not expected to greatly favor Mu over the other H isotopes in these reactions. The ΔH_0^0 endothermicity of the Mu + HCl abstraction reaction (Table 5) due to the ZPE of Mu-H also restricts Mu tunnelling by rendering a substantial part of the barrier inaccessible as a tunnelling path.

It has already been stated that the Mok-Polanyi relation holds for the Y-HX abstraction reactions and thus it is expected that as X changes from Cl to I, more reaction energy is transferred into product vibration. However, the light atom anomaly is not expected to operate strongly on these reactions since the reaction exoergicity slams an H atom into an atom of comparable mass, resulting in a vibrationally excited product. Thus, it is expected that a much greater fraction of the reaction energy appears as product vibration in the Y-HX abstraction reactions than in the Y-X₂ reactions. The light atom anomaly still predicts that the products of the Mu + HX abstraction will have less reaction energy channelled into

vibration than is the case in the H + HX reactions.

The potential energy surfaces for the Y + HX hydrogen exchange reactions are much more poorly known than those for the hydrogen abstraction reactions. For the H + HCl exchange reaction, for example, proposed surfaces range from those with symmetrically placed potential wells (instead of barriers) of 5-9 kcal/mole, to those with potential barriers of 15-25 kcal/mole ([Bauer 2-(78)] and the references therein). The LEPS formulation has been declared "too inflexible" to model these potential surfaces [Valencich (77)]. Consequently, it is of little use to consider any specific examples of exchange reaction surfaces. Nonetheless, it is possible to comment on some of the gross topological features of the surfaces for these reactions. The bulk of the post-1970 theoretical and experimental papers on these reactions agree that Y + HX exchange reactions possess potential barriers, rather than wells, in the symmetrical Y-X-H configuration [Klein (78), Bauer 2-(78), Endo (76), Botschwina (77), Dunning (77), Wolfrum (77), Valencich (77)], and several of these authors believe that the exchange barriers exceed the corresponding abstraction barriers [Bauer 2-(78), Endo (76), Botschwina (77), Dunning (77), Wolfrum (77)]. Unlike the abstraction reaction surfaces, the exchange reaction surfaces do not seem to be very sensitive to the bond angle [Klein (78), Thompson (75)], and, in fact, Klein and Veltman's (78) LEPS surface slightly favors a bond angle of 90° over the collinear surface. It has also been suggested that the exchange reaction surfaces possess potential wells in the product and reac-

tant valleys similar to those proposed for the abstraction reaction surfaces [Thompson (75)].

All collinear exchange reaction potential surfaces are perfectly symmetrical about a line drawn through the origin and saddle point at 45° to each axis. If it is assumed that the exchange reaction surfaces possess barriers rather than wells, then the saddle point corresponds to a complex with equally strong Y-X and X-H bonds and all of the energy threshold and barrier relations predicted in the abstraction reactions will also hold for the exchange reactions, except that the inequality relations may be even stronger. Although surfaces with symmetrically placed barriers are expected to be prone to "corner cutting" tunnelling paths [Marcus (78), Johnston (61)], the strong effect due to the sharp skewing angles for the mass weighted abstraction surfaces is absent in the exchange surfaces where the skewing angles for Y + ClH, for example, are: 89.5° , 88.4° , 87.8° , and 87.3° for Mu, H, D and T respectively. The importance of tunnelling is, however, diminished for Mu + XH exchange because of the endothermicity of the reactions (see Table 5) which restricts tunnelling to the top part of the barriers.

Without knowledge of the potential energy barriers, it is impossible to predict which reaction channel is faster: hydrogen atom abstraction or exchange. Most experimental evidence suggests that abstraction is faster than exchange at ordinary temperatures, but that the reverse is true at high temperatures ($>2000\text{K}$) [Endo (76), Bauer 2-(78)]; these results have been interpreted as evidence that hydrogen exchange has

an unusually small steric factor [Thompson (75)] or that exchange has a much higher activation energy than abstraction [Endo (76), Bauer 2-(78)]. A dynamical argument has been proposed to explain these experimental observations [Bauer 2-(78), Klein (78)]. At room temperature, the most populated rotational states of hydrogen halide molecules are 2 or 3 corresponding to rotational frequencies of about $2 \times 10^{12} \text{ s}^{-1}$. Since the HX center of mass is almost coincident with the X nucleus, to a slowly approaching atom, the HX molecule looks like a sphere with an H atom "crust" covering the larger X atom. Consequently, the collision takes place in the abstraction reaction configuration: Y-H-X. As the relative velocity of the collision partners increases, this rotational screening of the halogen atom diminishes, increasing the opportunity for the exchange reaction configuration to occur: Y-X-H. This effect has not been predicted in three dimensional QCT calculations [Thompson (75), White (73)] which show little sensitivity to the target molecule rotational states; statistical phase space calculations, however, are in qualitative agreement with this effect [Truhlar (69)]. If it is assumed that this effect is important, then it is expected that the branching ratios for abstraction to exchange are smaller for Mu reactions than for other H isotope reactions at the same temperatures, since the mean velocity of the lighter Mu atom is three times that of H.

D Trajectory Calculations

The first objective of all trajectory calculations, is

to determine the state-to-state reaction probabilities as a function of the relative translational kinetic energy or velocity of the colliding species. These probabilities are denoted $P_{s' \leftarrow s}(E_{\text{trans}})$, where s' refers to product molecule states and s refers to reactant molecule states. The number and type of quantum states included in s and s' depends on the dimensionality of the calculations and the level of approximation to which the calculations are carried out. As mentioned in Section B, collinear collisions are direct "knock out" processes where the attacking atom approaches the center of mass of the target molecule end on. For such a collision, the rotational states of the target molecule are ignored and there is no collisional orbital angular momentum transferred since the impact parameter, $b = 0$. Furthermore, it has already been noted that the bending vibrations of the activated complex are also ignored in collinear collisions. These considerations, plus the fact that trajectories need only be performed on the one potential energy surface corresponding to a bond angle of 180° , indicates that collinear state-to-state reaction probabilities may be determined with relative ease. Two dimensional (coplanar) trajectory calculations include the collinear case as well as trajectories on all surfaces corresponding to bond angles ranging from 0° to 180° . All in-plane rotations and vibrations are included in the target, product, and activated complex molecules. Because the impact parameters are not constrained to zero, orbital angular momentum transfer may occur. All internal states and impact parameters are included in three dimensional calculations, thereby requiring

the sampling of a continuum of possible trajectories.

State-to-state reaction probabilities are given by [Persky (77)]:

$$P_{s' \leftarrow s}(E_{\text{trans}}) = \frac{N_{s' \leftarrow s}^R(E_{\text{trans}})}{N_s(E_{\text{trans}})}$$

where $N_{s' \leftarrow s}^R$ is the number of reactive state-to-state trajectories at a given energy and N_s is the total number of trajectories calculated at that energy for initial state, s . For three dimensional trajectory calculations, it is common to define a total reaction cross section [Persky (77), White (73)]:

$$\sigma_{s' \leftarrow s}(E_{\text{trans}}) = \pi b_{\text{Max}}^2(E_{\text{trans}}) P_{s' \leftarrow s}(E_{\text{trans}}) \quad (31)$$

where b_{Max} is the largest impact parameter that yields an appreciable reaction probability; in order to compare the calculations with experimental atomic and molecular beam data, it is useful to define a differential cross section [Persky (77)]:

$$\frac{d\sigma_{s' \leftarrow s}(E_{\text{trans}})}{d\Omega} = \frac{\pi b_{\text{Max}}^2 N_{s' \leftarrow s}^R(E_{\text{trans}}, \theta)}{2\pi \sin\theta N_s(E_{\text{trans}}) \Delta\theta} \quad (32)$$

where $N_{s' \leftarrow s}^R(E_{\text{trans}}, \theta)$ is the number of reactive collisions with scattering angle between θ and $\theta + \Delta\theta$, and $d\Omega$ is an increment of solid angle. Of course, three dimensional trajectory cross sections have the units of area and differential cross sections have the units of area/solid angle. Occasionally, so-called "cross sections" are defined for coplanar calculations [Baer (76)] analogous to equations (31) and (32):

$$\sigma_{s' \leftarrow s}(E_{\text{trans}}) = 2b_{\text{Max}}(E_{\text{trans}}) P_{s' \leftarrow s}(E_{\text{trans}}) \quad (33)$$

and

$$\frac{d\sigma_{s' \leftarrow s}(E_{\text{trans}})}{d\Omega} = \frac{2b_{\text{Max}} N_{s' \leftarrow s}^R(E_{\text{trans}}, \theta)}{2N_s(E_{\text{trans}}) \Delta\theta} \quad (34)$$

These "cross sections" have units of length and length/unit angle respectively.

State-to-state reaction probabilities or cross sections are often summed over all final states, s' , to give a total reaction cross section of an initial state, s [Connor 1-(78)]:

$$\sigma_s^t(E_{\text{trans}}) = \sum_{s'} \sigma_{s' \leftarrow s}(E_{\text{trans}})$$

Equation (26) (Section C) gives a general integral for converting energy dependent rate constants to thermally averaged rate constants; particular integral expressions equivalent to equation (26) are [Eliason (59), Connor 1-(78), Weston (72)]:

$$(1D) \quad k_s(T) = \left(\frac{1}{2\pi\mu k_B T}\right)^{1/2} \int_0^\infty P_s^t(E_{\text{trans}}) e^{-E_{\text{trans}}/k_B T} dE_{\text{trans}} \quad (35)$$

$$(2D) \quad k_s(T) = \left(\frac{2}{\mu}\right)^{1/2} \frac{1}{k_B T} \int_0^\infty \sigma_s^t(E_{\text{trans}}) E_{\text{trans}}^{1/2} e^{-E_{\text{trans}}/k_B T} dE_{\text{trans}} \quad (36)$$

$$(3D) \quad k_s(T) = \left(\frac{1}{\pi\mu}\right)^{1/2} \left(\frac{2}{k_B T}\right)^{3/2} \int_0^\infty \sigma_s^t(E_{\text{trans}}) E_{\text{trans}} e^{-E_{\text{trans}}/k_B T} \cdot dE_{\text{trans}} \quad (37)$$

where μ is the reduced mass of the reactants and $k_s(T)$ is an initial state thermal reaction rate constant with units of $\text{cm molecule}^{-1} \text{s}^{-1}$, $\text{cm}^2 \text{molecule}^{-1} \text{s}^{-1}$, and $\text{cm}^3 \text{molecule}^{-1} \text{s}^{-1}$ for the one, two, and three dimensional cases respectively.

Finally, total thermal reaction rate constants are obtained by averaging $k_s(T)$ over the Boltzmann distribution of initial states, s :

$$k(T) = \sum_s f_s(T) k_s(T) \quad (38)$$

where $f_s(T)$ is the fraction of target molecules in state s given by:

$$f_s(T) = \frac{g_s e^{-\epsilon_s/k_B T}}{\sum_s g_s e^{-\epsilon_s/k_B T}}$$

where g_s is a degeneracy factor and ϵ_s is the energy of state, s [Weston (72)]. An important feature of equations (35) - (37) is that the thermal rate constants are functions of the temperature independent reactant reduced mass term, $\mu^{-1/2}$, regardless of the trajectory dimensionality. For reactions of H isotopes with relatively heavy molecules (M.W. ≥ 35 amu), this mass factor predicts that $k_{\text{Mu}}:k_{\text{H}}:k_{\text{D}}:k_{\text{T}} \approx 2.9:1.0:0.72:0.59$ [Connor 1-(78)]. This isotope effect may be simply interpreted as the mass dependence of the mean relative velocity of the reacting species, $\bar{v} = \left(\frac{8k_B T}{\pi \mu} \right)^{1/2}$ [Weston (72)] and is often called the "trivial" isotope effect [Fleming (76), Fleming 1-(77), Jakubetz 1-(78)] because it is not dependent on the reaction dynamics; all dynamical information about the reaction, as well as the effects of the mass weighting of the potential energy surface, are contained in the reaction cross section.

State-to-state reaction probabilities are artificial constructs in the cases of classical and quasiclassical trajectory calculations which, by definition, have access to a continuous rather than quantal range of energy transfer. In both cases, the final state energies are related to quantum states by some arbitrary binning procedure which assigns a range of final state energies extending above and below a given

quantum energy state to that state [Thompson (76)]. It may be recalled (Section C) that in the case of purely classical trajectories, the target molecules initially possess no internal energy (in violation of the zero point energy) while in the case of quasiclassical trajectories, the target molecule initially possesses proper quanta of internal energy.

Classical and quasiclassical trajectories are often calculated by solving Lagrange's or Hamilton's equations of motion. Lagrange's equations are given by [Messiah (58)]

$$\frac{d}{dt} \left(\frac{\partial L}{\partial \dot{q}_r} \right) - \frac{\partial L}{\partial q_r} = 0 \quad (r = 1, 2, \dots, R)$$

with the Lagrangian function given by

$$L(q_1, q_2, \dots, q_R, \dot{q}_1, \dot{q}_2, \dots, \dot{q}_R; t) = T(\dot{q}_1, \dot{q}_2, \dots, \dot{q}_R) - V(q_1, q_2, \dots, q_R)$$

where q_r are generalized coordinates, T is the kinetic energy and V is the potential energy of the system. The classical Hamiltonian function which spans the $2R$ dimensional coordinate and momentum space (phase space) is given by [Messiah (58)]:

$$H(q_1, \dots, q_R, p_1, \dots, p_R; t) = \sum_{r=1}^R \dot{q}_r \frac{\partial L}{\partial \dot{q}_r} - L = T(p_1, \dots, p_R) + V(q_1, \dots, q_R)$$

and the equations of motion are given by

$$\dot{q}_r = \frac{\partial H}{\partial p_r} \quad ; \quad \dot{p}_r = -\frac{\partial H}{\partial q_r} \quad (r = 1, 2, \dots, R)$$

In principle, these equations of motion can be solved exactly to obtain the completely deterministic classical trajectories. Statistically averaged reaction probabilities must be obtained by multiple integration over collision variables such as impact

parameter, molecular orientation and vibrational phase. Generally, it is difficult to determine the functional form of the reaction probability dependence on these collision variables which is required to perform this integration. Consequently, statistical averaging is often accomplished by a procedure such as Monte Carlo integration which determines the reaction probability from a statistically significant sample of trajectories computed from values of the collision variables selected randomly from a weighted distribution. This procedure, which normally requires the calculation of several thousand trajectories, has the physically appealing feature "that it simulates the random process by which collisions in the laboratory actually occur [Thompson (76)]." QCT calculations are often called "Monte Carlo" calculations (eg. [Blais (74)]) or simply "classical" calculations to distinguish them from quantum mechanical treatments.

The conventional quantum mechanical approach to atom-diatom reaction trajectories is to solve Schrödinger's equation, $H\Psi = E\Psi$, $H = T + V$, to evaluate the scattering matrix (S-matrix) elements which lead directly to the quantized reaction probabilities, $P_{S' \leftarrow S} = |S_{S' \leftarrow S}|^2$ [Manz (75)]. This procedure, which is almost always carried out by approximation methods, only gives the net result of the collision in terms of a reaction probability, since the entire potential is inserted into Schrödinger's equation and only the asymptotic reactant and product wavefunctions are determined while the interaction region is treated like a "black box." Classical variables such as the phase of the harmonic oscillator appear in ampli-

tudes of probability functions quantum mechanically and may give rise to such purely quantum mechanical effects as wave interference.

Although the quantum mechanical treatment may represent an exact formulation of the reaction problem, in general, only approximate solutions can be found for it, whereas the approximate classical formulation of the reaction can usually be solved exactly. From the viewpoint of understanding the reaction dynamics in detail, classical results provide a valuable insight. For example, it is not possible to distinguish purely quantum mechanical effects such as tunnelling from classical effects on the basis of quantum mechanical results alone (this point is discussed further in Section F). More importantly, classical trajectories are totally deterministic and provide a detailed picture of the reactive or non-reactive scattering processes; because S-matrix quantum mechanical results do not really define any trajectories, the effect of specific topological features on the potential cannot be determined directly.

A number of methods have been devised to obtain more dynamical information from quantum mechanical calculations. One approach is to monitor the S-matrix as the potential energy function is changed to indirectly infer the effects of various potential features. A more direct approach is to calculate the flow of the quantum mechanical probability distributions through the interaction region (so-called "streamlines," the quantum analogue of classical trajectories) by formulating the reaction as a quantum hydrodynamics problem (see eg. [Hirsch-

felder (76)]). Another approach is an ingenious modification of the conventional S-matrix calculations known as the "state path sum method [Manz (74), (75)]." This method is briefly described here since it was employed by Connor et al. 1-(78), 1-(77) in their quantum mechanical calculations of the Mu reaction rates. Normal S-matrix calculations can be thought of as dividing the potential energy surface into three regions: the asymptotic reactant and product regions, separated by the interaction region of the potential. At the boundary between the reactant and interaction regions, the quantum state probability distributions are known; the solution of the Schrödinger equation gives the corresponding quantum state probability distributions at the boundary of the interaction and product regions, the connection being made via the "black box" S-matrix. With the state path sum method, the interaction region is subdivided into an arbitrary number of sectors and an S-matrix is calculated for each. As a result, virtual quantum state probability distributions are known at each sector boundary of the interaction region of the potential surface. Consequently, if, for example, a particular collision has a low net reaction probability, it is possible to determine which part of the potential energy surface is responsible for this result. A "state path" is a complete line connecting an asymptotic reactant state, s , to an asymptotic product state, s' , through the various sectors of the interaction region. Manz has devised algorithms for sectoring the interaction region and identifying the dominant state paths.

E Transition State Theory

No attempt is made to derive TST in this Section; it merely examines TST predictions for H isotope effects. As normally formulated [Johnston (66), Weston (72), Kuppermann (79)], the TST expression for the rate constant of the reaction $Y + AB \rightarrow YA + B$ is:

$$k = \Gamma_t \frac{k_B T}{h} \frac{Q^\ddagger}{Q_Y Q_{AB}} e^{-E^{VA}/k_B T} \quad (39)$$

where Γ_t is a tunnelling correction factor, h is Planck's constant, Q^\ddagger , Q_Y , and Q_{AB} are the products of the translational, vibrational, electronic, and rotational partition functions of the activated complex and reactants respectively, and E^{VA} is an energy barrier, taken as the VA barrier in this treatment (Section (C), Part (iii), and equation (25)). Kuppermann (79) has shown that equation (39) applies to both the collinear and three dimensional reactions when the appropriate partition functions and VA barriers are used. Equation (39) only assumes the existence of thermal equilibrium among the reactants (implicit in the definition of a thermal reaction rate constant), vibrational adiabaticity, and the absence of effects due to the curvature of the reaction path [Kuppermann (79)].

Since the target molecule is the same for H isotope reactions of the type, $Y + AB \rightarrow YA + B$, the rate constant ratios for the Y and Y' isotopic reactions do not include Q_{AB} partition functions:

$$\frac{k}{k'} = \frac{\Gamma_t}{\Gamma'_t} \left(\frac{Q_{Y'}}{Q_Y} \right)_{\text{trans}} \left(\frac{Q^\ddagger}{Q'^\ddagger} \right)_{\text{rot}} \left(\frac{Q^\ddagger}{Q'^\ddagger} \right)_{\text{vib}} \left(\frac{Q^\ddagger}{Q'^\ddagger} \right)_{\text{trans}} \cdot e^{-[E^\ddagger(Y) - E^\ddagger(Y')]/k_B T} \quad (40)$$

where the electronic partition functions are assumed to cancel due to the BO approximation. For a non-linear YAB molecule the three dimensional translational and rotational partition functions are given by [Van Hook (70)]:

$$Q_{\text{trans}} = (2\pi M k_B T)^{3/2} V/h^3 \quad (41)$$

$$Q_{\text{rot}} = \left(\frac{8\pi^2}{s}\right) (8\pi^3 I_A I_B I_C)^{1/2} \left(\frac{k_B T}{h^2}\right)^{3/2} \quad (42)$$

where M is the molecular mass, V is the container volume, I_A , I_B and I_C are the moments of inertia of the molecule about its three principal axes, and s is a symmetry factor. The quantized harmonic oscillator vibrational partition functions are given by [Frost (61)]:

$$Q_{\text{vib}} = \prod_i^{\text{internal modes}} (1 - e^{-h\nu_i/k_B T})^{-1} \quad (43)$$

where ν_i is a normal mode vibrational frequency. Substituting equations (41) to (43) into (40) and expanding the VA barrier term yields:

$$\frac{k}{k'} = \frac{\Gamma_t}{\Gamma'_t} \left(\frac{m_{Y'}}{m_Y}\right)^{3/2} \left(\frac{M^\ddagger}{M'^\ddagger}\right)^{3/2} \left(\frac{I_A I_B I_C}{I'_A I'_B I'_C}\right)^{1/2} \cdot \left(\prod_i \frac{1 - e^{-h\nu_i^\ddagger(Y')/k_B T}}{1 - e^{-h\nu_i^\ddagger(Y)/k_B T}}\right) e^{-\frac{h}{2k_B T} \sum_i [\nu_i^\ddagger(Y) - \nu_i^\ddagger(Y')]} \quad (44)$$

where m_Y and $m_{Y'}$ are the atomic masses of the Y and Y' isotopes, M and M' are the molecular masses of the activated complexes and ν_i^\ddagger are the bound normal vibrational energies of the activated complexes (the unbound vibration corresponding to the reaction coordinate is excluded). This expression may be further simplified by substitution of the Redlich-Teller

product theorem [Johnston (66), Van Hook (70)]:

$$\left(\frac{M}{M'}\right)^{3/2} \cdot \left(\frac{I_A I_B I_C}{I'_A I'_B I'_C}\right)^{1/2} = \prod_i \left(\frac{m_i}{m'_i}\right)^{3/2} \prod_i^{3n-6} \frac{v_i}{v'_i} \quad (45)$$

where m_i are the masses of the atoms comprising the molecule of mass M , to yield:

$$\frac{k}{k'} = \frac{\Gamma_t}{\Gamma'_t} \frac{v^\ddagger(Y)}{v^\ddagger(Y')} \prod_i^{3n-7} \frac{v_i^\ddagger(Y)}{v_i^\ddagger(Y')} \frac{1 - e^{-hv_i^\ddagger(Y')/k_B T}}{1 - e^{-hv_i^\ddagger(Y)/k_B T}} \cdot e^{-\frac{h}{2k_B T} \sum_i^{3n-7} [v_i^\ddagger(Y) - v_i^\ddagger(Y')]}$$

where the imaginary (unbound) frequencies, v_i^\ddagger , corresponding to the reaction coordinate, have been factored out. Denoting $u_i^\ddagger = \frac{hv_i^\ddagger}{k_B T}$, the last three factors in (46) may be combined to give

$$\frac{k}{k'} = \frac{\Gamma_t}{\Gamma'_t} \frac{v^\ddagger(Y)}{v^\ddagger(Y')} \prod_i^{3n-7} \frac{\left(\frac{u_i^\ddagger(Y)}{2}\right) \sinh\left(\frac{u_i^\ddagger(Y')}{2}\right)}{\sinh\left(\frac{u_i^\ddagger(Y)}{2}\right) \left(\frac{u_i^\ddagger(Y')}{2}\right)} \quad (46)$$

Noting that the isotopic frequency ratios are related to the isotopic masses according to [Weston (72), Nikitin (74), Karplus (70)],

$$\frac{v(Y)}{v(Y')} = \left(\frac{\mu(Y')}{\mu(Y)}\right)^{1/2}$$

the rate constant ratio becomes

$$\frac{k}{k'} = \frac{\Gamma_t}{\Gamma'_t} \left(\frac{\mu^*(Y')}{\mu^*(Y)}\right)^{1/2} \prod_i^{3n-7} \frac{\left(\frac{u_i^\ddagger(Y)}{2}\right) \sinh\left(\frac{u_i^\ddagger(Y')}{2}\right)}{\sinh\left(\frac{u_i^\ddagger(Y)}{2}\right) \left(\frac{u_i^\ddagger(Y')}{2}\right)} \quad (47)$$

where μ^* denotes the effective masses possessed by the representative point on the barrier-crossing trajectory.

Equation (47) contains a number of interesting terms.

Unlike the temperature independent term of collision theory (Section D) which only depends on the reduced mass of the reactants, the TST temperature independent term, $\left(\frac{\mu_Y^*}{\mu_Y}\right)^{1/2}$, depends on the effective mass of the representative point as it crosses the potential barrier; that is, it depends on the location of the potential barrier. In this sense, the TST temperature independent term contains dynamical information, in contrast to the corresponding collision theory term. In the limiting case of a very early barrier (such as in the $Y + F_2$ reactions), this term does predict $\frac{k_{Mu}}{k_H} \approx 2.9$, in accord with the collision theory result; this temperature independent mass effect is often called the "primary" isotope effect [Nikitin (74)]. It is customary to denote $\Gamma_v \equiv \frac{u/2}{\sinh(u/2)}$ to indicate the quantum nature of the vibrational partition functions [Johnston (66)]. In the limit of low vibrational frequencies and high temperatures [Johnston (66), Weston (72)]

$$\Gamma_v = \frac{u/2}{\sinh(u/2)} \approx (1 + \frac{u^2}{24} + \frac{u^4}{1920} + \frac{u^6}{7!2^6} + \dots)^{-1}$$

and $\lim_{u \rightarrow 0} \Gamma_v = 1$

Conversely, in the limit of low temperature and high frequencies,

$$\Gamma_v \approx u e^{-u/2}$$

and $\lim_{u \rightarrow \infty} \Gamma_v = 0$

Clearly, the exponential dependence of Γ_v on u indicates that if the isotopic substitution of Mu results in a substantial increase in u^\ddagger , there will be a very strong reduction in

$\Gamma_{\text{V}}^{\ddagger}(\text{Mu})/\Gamma_{\text{V}}^{\ddagger}(\text{H})$. In general, if the barrier is early, the activated complex corresponds to a very slightly perturbed target molecule with symmetric stretch vibrations that display a very weak dependence on isotopic substitution, and thus $\Gamma_{\text{V}}^{\ddagger}(\text{Mu})/\Gamma_{\text{V}}^{\ddagger}(\text{H}) \rightarrow 1$; conversely, as the barrier becomes progressively later, the values of u^{\ddagger} increase and take on strong isotopic dependences, and thus $\Gamma_{\text{V}}^{\ddagger}(\text{Mu})/\Gamma_{\text{V}}^{\ddagger}(\text{H}) \rightarrow 0$. Stretching vibrations are usually stronger than bending vibrations [Johnston (66)] and thus they might be expected to have a stronger influence on $\Gamma_{\text{V}}^{\ddagger}(\text{Mu})/\Gamma_{\text{V}}^{\ddagger}(\text{H})$; Figure 17 shows this to be the case. The Figure plots $\Gamma_{\text{V}}^{\ddagger}/\Gamma_{\text{V}}^{\ddagger}$, as a function of the percent of u/u' (i.e. u corresponds to a lighter isotope than u') for various values of u' . From the Figure, it is clear that a small increase in u over u' for a strong stretching vibration (typically $>300 \text{ cm}^{-1}$ for an early barrier) reduces $\Gamma_{\text{V}}^{\ddagger}/\Gamma_{\text{V}}^{\ddagger}$, more than a large increase in u/u' for a weak bending vibration (typically $<50 \text{ cm}^{-1}$ for an early barrier). Isotope effects due to $\Gamma_{\text{V}}^{\ddagger}/\Gamma_{\text{V}}^{\ddagger}$ are referred to as "secondary" isotope effects [Nikitin (74)].

F Tunnelling

There are two definitions of tunnelling applicable to chemical reactions [Connor 1-(76)]. The first is the standard "static" or "energetic" definition associated with barrier penetration; the model of nuclear alpha decay is one of the more celebrated examples. In a chemical reaction, static tunnelling occurs when there is a non-zero reaction probability despite the fact that the total energy of the colliding species (i.e. the relative translational kinetic

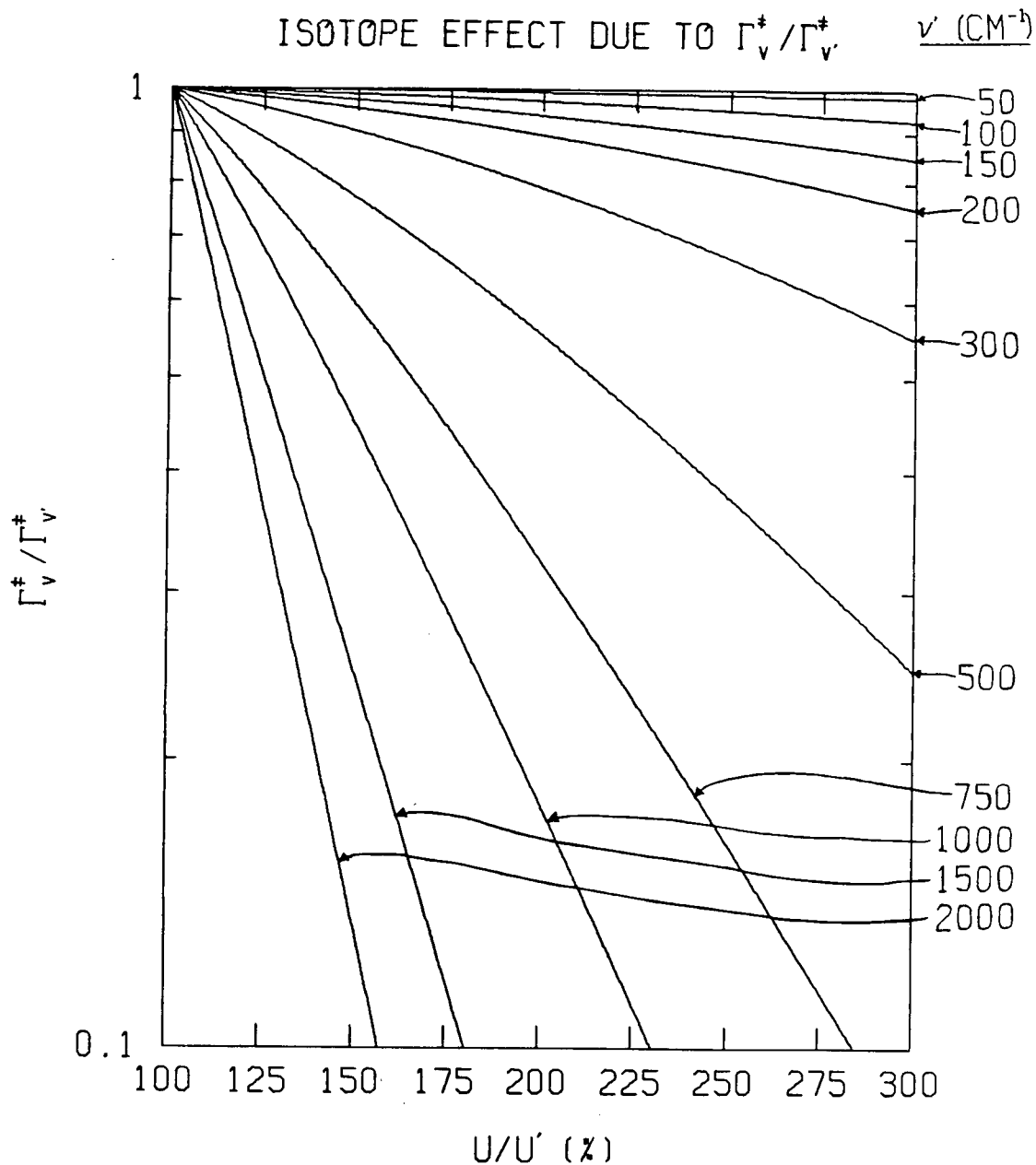


FIGURE 17: Isotope effects in transition state vibrations from mass variations of atom Y for the reaction $Y + AB \rightarrow YA + B$. $\Gamma_v^*/\Gamma_v^\ddagger$ is plotted as a function of the percent increase in the isotope-dependent vibrational frequency of ν over ν' for the various values of ν' indicated on the right. It is assumed that the frequencies of ν and ν' correspond to transition state molecules containing light and heavy isotopes of atom Y respectively, at 300K.

energy plus the internal vibrational energy of the target molecule) is less than the potential barrier height. In terms of the energy definitions of Section C, the physical barrier height, E_b^{phys} , defined by equation (24), is the static tunnelling barrier; reactive collisions with less relative translational kinetic energy than E_b^{phys} occur by static tunnelling. As discussed in the next Chapter, although Mu reactions show an appreciable amount of static tunnelling, this form of tunnelling is relatively unimportant at normal temperatures ($>200\text{K}$) [Connor 1-(77), 1-(76)]. The second form of tunnelling is "dynamic." This refers to reactive collisions that are energetically allowed and which do occur quantum mechanically but which are classically forbidden, not because of energy, but because of the reaction dynamics. According to the definitions of Section C, the quasiclassical threshold energy, E_T^{QC} , is the dynamic tunnelling barrier; reactive collisions with less relative translational kinetic energy than E_T^{QC} but more than E_b^{phys} occur by dynamic tunnelling. Dynamic tunnelling is by far the most dominant form of tunnelling in chemical reactions [Connor 1-(76)].

In Section C it was noted that quasiclassical threshold energies are difficult to define precisely because of Monte Carlo averaging; thus, dynamic tunnelling may be somewhat ambiguous since it is defined in terms of E_T^{QC} . It is simply noted here that Connor 1-(76) has shown that tunnelling may be unambiguously defined in terms of complex-valued classical trajectories arising from semiclassical scattering theory.

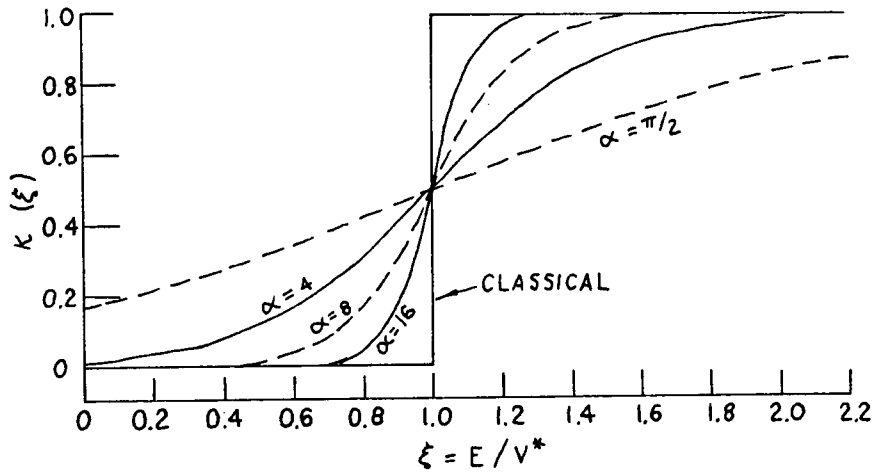
The tunnelling correction term, Γ_t , applied to TST

(c.f. equation (39)) is normally calculated as a quantum barrier penetration coefficient for a mathematically one dimensional barrier [Johnston (66), Jakubetz (79)].

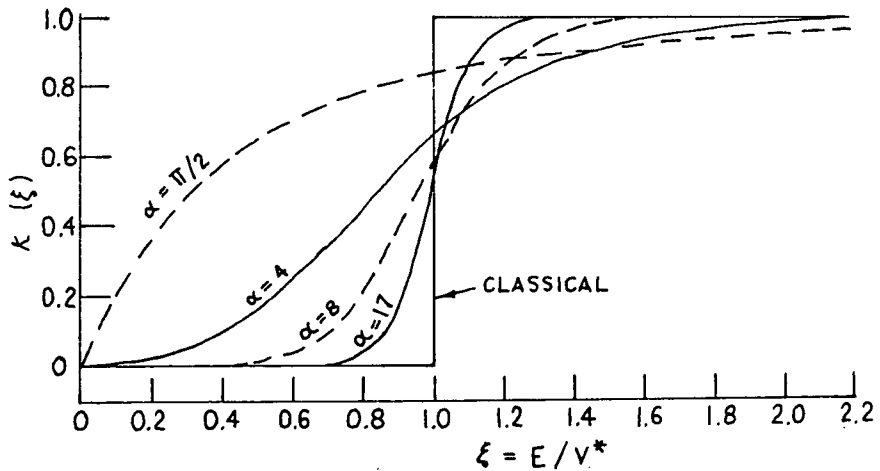
Johnston (66) notes that this approach may be "better chemical engineering than natural philosophy;" nonetheless, this attractively simple quantum correction to the classical rate expression is often remarkably successful. Three one dimensional barrier penetration correction models are most commonly used for Γ_t . The first order Wigner correction

[Johnston (66), Nikitin (74)] is $\Gamma_t = 1 + \frac{h|v^*|^2}{24k_B T}$, where $|v^*| = \frac{1}{2\pi} \left(\frac{|F^*|}{\mu} \right)^{1/2}$ is the imaginary frequency corresponding to the reaction coordinate and $|F^*| = \left| \frac{d^2V(q)}{dq^2} \right|$ is the force constant

(curvature) of the potential surface at the saddle point; this first order correction is valid for $\frac{h|v^*|}{k_B T} \ll 1$. While the Wigner expansion may be applied to any shape of one dimensional barrier, exact tunnelling corrections have been worked out for two stylized reaction barriers [Johnston (66)]: the truncated, inverted parabola, calculated by R. P. Bell; and the barrier due to C. Eckart. The Eckart barrier, the most realistic of the two since it has a smooth, continuous base unlike the truncated parabola, may be symmetrical, corresponding to a thermoneutral reaction, or unsymmetrical, corresponding to an exothermic reaction. The parameterization of the Bell and Eckart barriers and the analytical forms of the transmission coefficients may be found in Johnston (66) or Jakubetz (79). Figure 18 (adapted from Johnston (66)) compares the transmission probabilities for the two barriers as a function of energy at various values of the barrier height.



(a)



(b)

FIGURE 18: Tunnelling transmission coefficients as a function of energy normalized to the barrier height for the truncated Bell parabola (top) and Eckart barrier (bottom), adapted from Johnston (61). The α parameter describes the shape of the barrier: large $\alpha \rightarrow$ high, wide barrier; small $\alpha \rightarrow$ short, narrow barrier. Johnston has noted that the Bell transmission coefficients are symmetrical to inversion about $\kappa = 0.5$, $\xi = 1$. Furthermore, because of the Bell truncation, κ does not approach zero at $\xi = 0$ for low values of α . It is also noted that quantum mechanical reflection as well as penetration occurs with these barriers.

CHAPTER IV - EXPERIMENTAL RESULTS AND THEIR INTERPRETATION

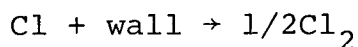
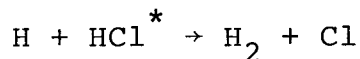
In this Chapter, the experimental results for each Mu reaction are reported and compared with recent experimental results for the analogous H atom reactions and with theoretical predictions, where available; Table VI summarizes the results. For some reactions, several H atom reaction rate parameters are reported with rate constants varying by factors of three or more and activation energies varying by 50%. This underscores the fact that "the wealth of data on bimolecular reactions that involve free radicals or atoms is more testimony to the growing awareness of the importance of these intermediates in kinetic systems and the frequency of their occurrence than to the great accuracy of the results [Benson (60)]." The relatively poor knowledge of gas phase H atom reaction rates available today is due to two experimental limitations: (1) until about a decade ago, there were few techniques available to measure gas phase H atom reaction rates directly, either by monitoring reactant depletion via some observable of H atoms or its reactant partner, or by monitoring product formation; rather, H atom reaction rates were indirectly inferred from a postulated reaction mechanism and associated "steady state" approximations, thereby making the results model dependent; (2) while the advent of modern techniques such as mass spectrometric fast flow sampling of product formation or ESR detection of H atoms in dilute gases has made rate measurements direct, it has not completely removed the systematic errors due to competitive reactions among the relatively large concentrations of highly reactive atomic and molecular species simultaneously present in the experimental

TABLE VI: SUMMARY OF THE REACTION RATE PARAMETERS FOR Mu AND H IN THE GAS PHASE

Reaction	E_a (kcal/mole)	Muonium $k(295K)^\dagger$	E_a (kcal/mole)	Hydrogen $k(295K)^\dagger$	$\frac{k_{Mu}}{k_H}(295)$	ref.
$Y+F_2 \rightarrow YF+F$	0.92 ± 0.23	1.4 ± 0.1	2.4 ± 0.2	0.20 ± 0.05	6.8 ± 1.5	Dodonov (70)
			2.2 ± 0.1	0.09 ± 0.01	14.6 ± 1.6	Homann (77)
$Y+Cl_2 \rightarrow YCl+Cl$	1.36 ± 0.21	5.1 ± 0.2	1.8 ± 0.6	1.7 ± 0.6	2.9 ± 1.0	Dodonov (70)
			1.4 ± 0.2	0.41 ± 0.04	13 ± 1.2	Ambidge (76)
			1.20 ± 0.14	1.2 ± 0.1	4.4 ± 0.4	Wagner (76)
			1.14 ± 0.17	1.3 ± 0.1	4.1 ± 0.3	Bemand (77)
$Y+Br_2 \rightarrow YBr+Br$	—	24 ± 3	—	$2.2 \pm 1.5^*$	$11 \pm 8^*$	Fleming (76)
			$1.8 \pm 0.4^*$	$5.1 \pm 0.6^*$	$4.7 \pm 0.8^*$	Fass (70) + Endo (76)
$Y+HCl \rightarrow$ products	—	$<0.000034 \pm$ 0.000005	—	0.009 ± 0.004	<0.004 ± 0.002	Bott (76)
$Y+HCl \rightarrow YH + Cl$	—	—	$3.18 \pm 0.17^*$	0.0021^* ± 0.0002	$<0.016^*$ ± 0.003	Weston (79)
$Y+HBr \rightarrow$ products	—	0.91 ± 0.10	2.57 ± 0.11	0.21 ± 0.02	4.4 ± 0.6	Endo (76)
$Y+ HI \rightarrow$ products	—	2.53 ± 0.13	0.00 ± 0.25	0.11 ± 0.02	23 ± 4	Sullivan (62)
			$0.70 \pm 0.25^*$	$1.5 \pm 0.5^*$	$1.7 \pm 0.6^*$	Jones (73)

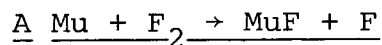
$^\dagger 10^{10}$ l/mole-s
* estimates only

apparatus. For example, the very fast reaction of $H + Cl_2 \rightarrow HCl^* + Cl$, where * denotes a vibrationally excited molecule, may be accompanied by the following side reactions [Wagner (76)]:



which consume additional H and Cl atoms and regenerate Cl_2 , thereby altering the reaction stoichiometry. To reduce these interferences, H atom kineticists are constantly striving (with considerable success) to perform rate measurements under more dilute conditions, but an impairing reduction in the observable signal inevitably accompanies these efforts.

In Chapter III, it was noted that the first motivation for undertaking the kinetic study of the reactions of Mu was to investigate isotope effects in H atom reactions. The second motivation for the study arises from the fact that MSR measurements are literally one-atom-at-a-time experiments which are not susceptible to the kinds of interferences that plague H atom measurements as outlined above. As a result, the MSR method might well provide the most accurate (isotopic) values of H atom reaction rates. This is not to say that MSR measurements are necessarily unambiguous - since the method simply measures the relaxation of the MSR signal, care must be taken in identifying the source of this relaxation which need not be chemical reaction (see Appendix II).



The MSR relaxation rates at various F_2 concentrations, measured in N_2 moderator between 295 and 383K, are listed in

Table VII. The influence of temperature on the reaction rates is illustrated in Figure 19 [adapted from Garner (78)] which plots the MSR relaxation rate data at 295 and 383K. The bimolecular rate constants determined by χ^2 minimum fits of the relaxation rate data to equation II(3) are also given in the Table and illustrated in the Arrhenius plot of Figure 20 [Garner (78)]. The χ^2 minimum fit of these data to the logarithmic Arrhenius expression (equation (12)) yields:

$$\log_{10}k(1/\text{mole-s}) = (10.83 \pm 0.20) - (200 \pm 50/T) , \quad (1\sigma)$$

with $k(300\text{K}) = (1.46 \pm 0.11) \times 10^{10}$ 1/mole-s and $E_a = (0.92 \pm 0.23)$ kcal/mole.

The experimental rate parameters of the reaction: $\text{H} + \text{F}_2 \rightarrow \text{HF} + \text{F}$ have been reviewed by Jones et al. (73) and Foon and Kaufman (75). These authors recommend the direct mass spectrometric probe measurements of a fast flow system by Albright et al. (69) and Dodonov et al. (70) from 294 to 565K which yielded $k(300) = (2.15 \pm 0.46) \times 10^9$ 1/mole-s with $E_a = 2.4 \pm 0.2$ kcal/mole and $\log_{10}A(1/\text{mole-s}) = (11.079 \pm 0.035)$. These results are in good agreement with the more recent EPR flow system measurements of Rabideau et al. (72) who determined $k(300\text{K}) = (2.5 \pm 0.2) \times 10^9$ 1/mole-s and estimated $E_a = 2.6$ kcal/mole, and with the earlier indirect results of Levy and Copeland (68) obtained by thermal, O_2 - inhibited $\text{H}_2 - \text{F}_2$ reaction, which gave $k(288\text{K}) = 1.8 \times 10^9$ 1/mole-s. However, the most recent measurement of this reaction rate is the flow system mass spectrometric determination from 224 to 493K by Homann et al. (77) which yielded $E_a = 2.2 \pm 0.1$ kcal/mole, $\log_{10}A(1/\text{mole-s}) = (10.6 \pm 0.1)$ and $k(300\text{K}) = (1.00 \pm 0.08) \times 10^9$ 1/mole-s. While the activation

TABLE VII: MSR RELAXATION RATES FOR THE REACTION $\text{Mu} + \text{F}_2 \rightarrow \text{MuF} + \text{F}$

Temperature (K)	Bimolecular Rate Constant $k(10^{10} \text{ M}^{-1} \text{ s}^{-1})$	$[\text{F}_2]$ (10^{-4} M)	Relaxation Rate $\lambda(\mu\text{s}^{-1})^\dagger$
295 \pm 2	1.42 \pm 0.07	0.0	0.68 \pm 0.06
		0.40 \pm 0.02	1.27 \pm 0.11
		0.69 \pm 0.04	1.63 \pm 0.12
		1.08 \pm 0.05	1.74 \pm 0.14
		1.23 \pm 0.03	2.18 \pm 0.23
		1.43 \pm 0.06	2.25 \pm 0.18
		1.93 \pm 0.04	3.56 \pm 0.34
		2.33 \pm 0.06	4.25 \pm 0.38
		2.98 \pm 0.07	5.66 \pm 0.47
327 \pm 3	1.63 \pm 0.10	0.0	0.64 \pm 0.04
		0.59 \pm 0.02	1.32 \pm 0.14
		1.16 \pm 0.03	2.73 \pm 0.41
		1.68 \pm 0.04	3.33 \pm 0.41
		2.11 \pm 0.05	3.55 \pm 0.47
		2.67 \pm 0.06	6.52 \pm 0.62
353 \pm 4	1.84 \pm 0.13	0.0	0.72 \pm 0.07
		0.48 \pm 0.02	1.55 \pm 0.08
		0.99 \pm 0.03	2.44 \pm 0.23
		1.40 \pm 0.03	3.53 \pm 0.42
		1.83 \pm 0.05	4.34 \pm 0.40
383 \pm 2	2.03 \pm 0.14	0.0	0.72 \pm 0.08
		0.91 \pm 0.02	2.41 \pm 0.31
		1.24 \pm 0.03	3.95 \pm 0.47
		1.82 \pm 0.05	4.16 \pm 0.42
		2.46 \pm 0.06	5.87 \pm 0.59

† Relaxation rates reported are weighted averages of the left and right positron telescope histograms.

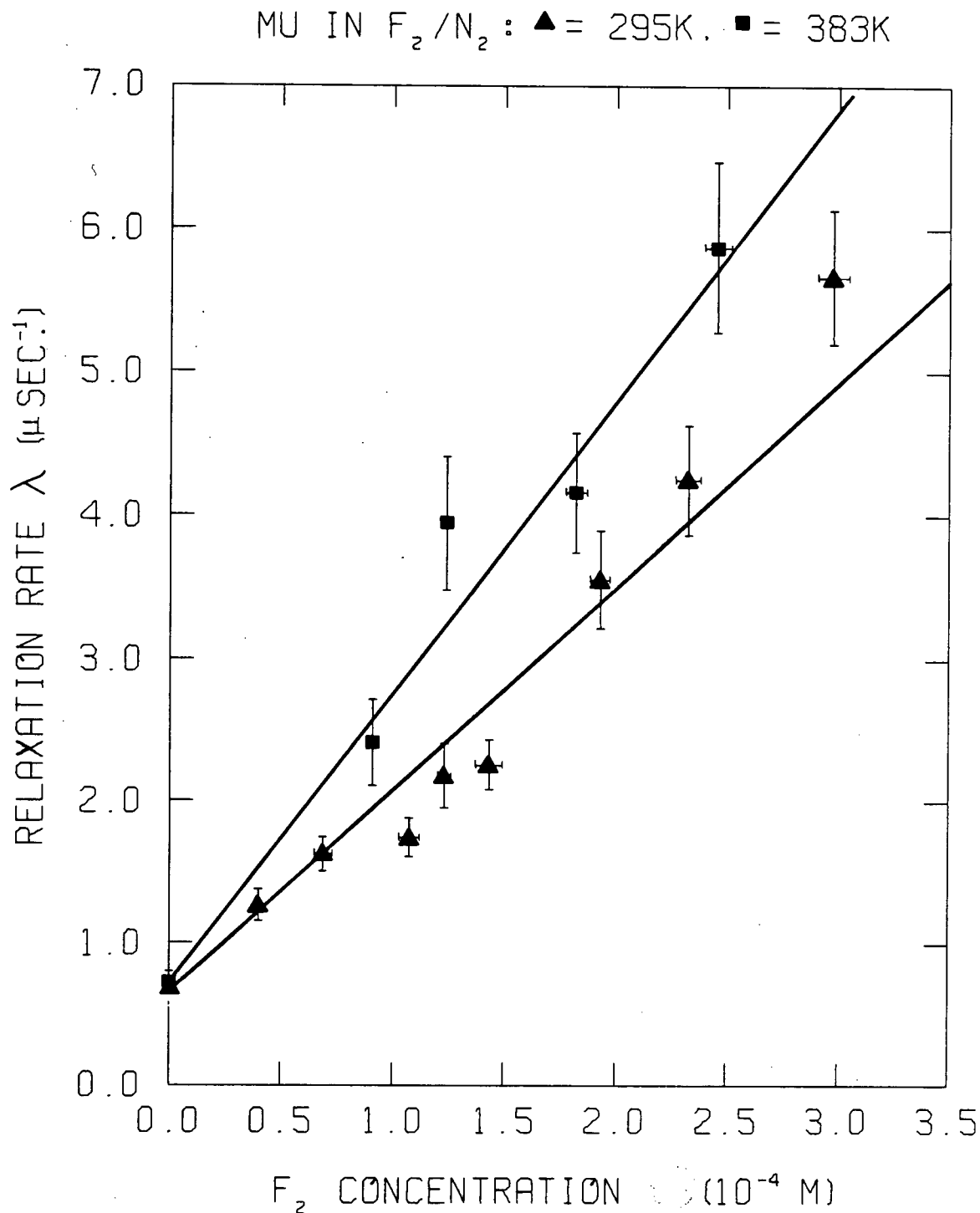


FIGURE 19: The effect of temperature on the Mu + F₂ MSR relaxation rates. The lines are χ^2 minimum fits of the data to equation II(3) corresponding to $k = (1.42 \pm 0.07) \times 10^{10}$ l/mole-s at 295 K (triangles) and $k = (2.03 \pm 0.14) \times 10^{10}$ l/mole-s at 383K (squares). Experimental points shown are weighted averages from the left and right telescope histograms.

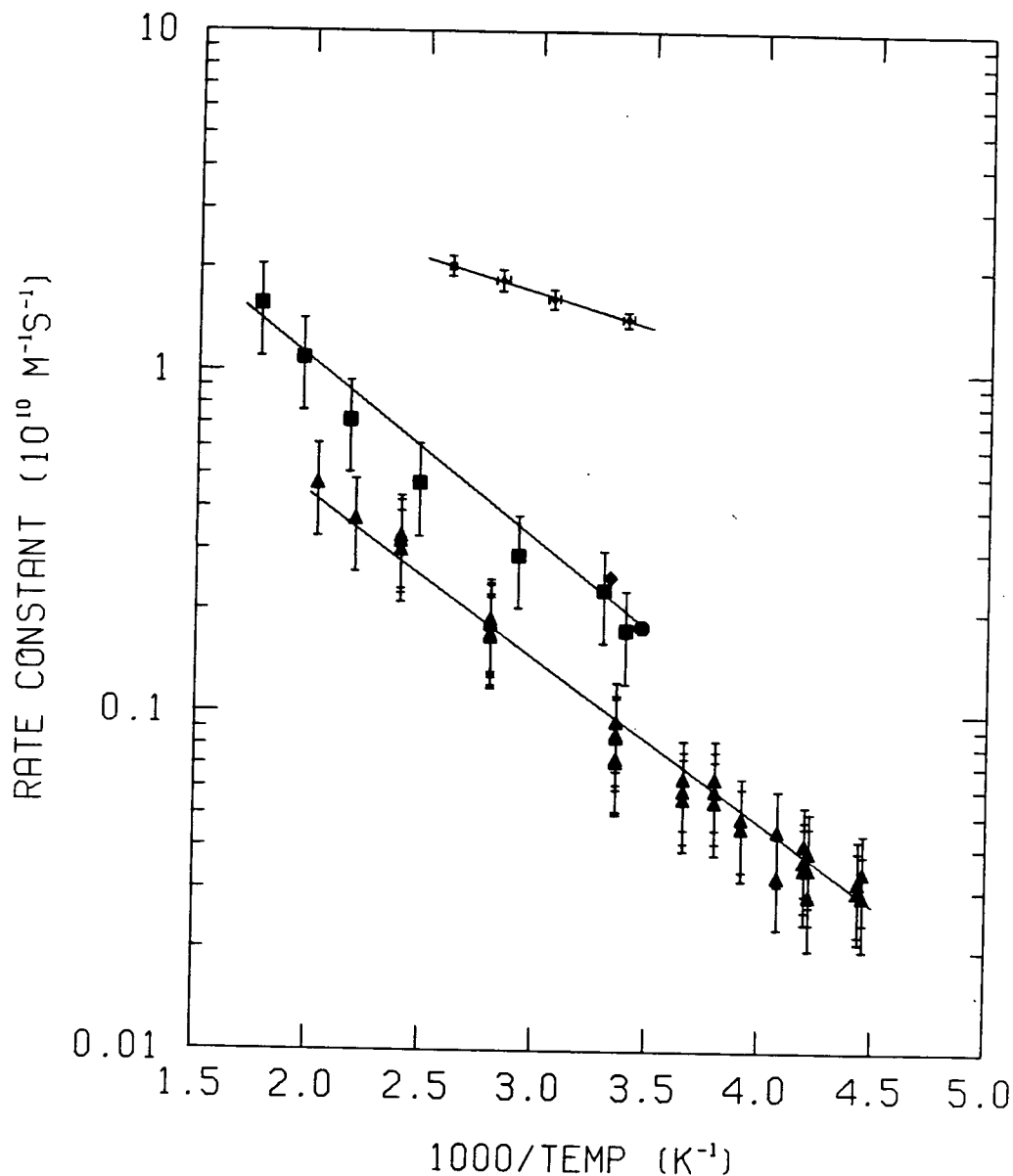


FIGURE 20: Experimental Arrhenius plot for the $Y + F_2$ reactions, $Y = \text{Mu}, \text{H}$. The Mu data is on the top line (this work). The H data is due to Rabideau(72) (diamond), Levy(68) (octagon), Dodonov(70) (squares), and Homann(77) (triangles). The error bars on the Mu data are statistical only; the error bars on the H data are estimates given by the authors which apparently include systematic errors.

energy is in agreement with the previous determinations, $k(300\text{K})$ is a factor of two smaller. Homann et al. (77) cite several possible reasons for this discrepancy. The experimental results for the H atom reaction from all of these authors are also shown in the Arrhenius plot of Figure 20.

Clearly, the activation energy for the Mu reaction with F_2 is less than half of that for the analogous H atom reaction at 300K, indicating that the average energy of reactive Mu collisions is much less than that of reactive H collisions, according to the Tolman interpretation of activation energy (see Chapter III, Section C). Furthermore, the Mu:H rate constant ratio is either $\frac{k_{\text{Mu}}}{k_{\text{H}}}(300\text{K}) = 6.8 \pm 1.5$, using the H atom results of Albright et al., or 14.6 ± 1.6 , using the results of Homann et al. Certainly, the Mu reaction at 300K is much faster than the H atom reaction; it is at least (2.3 ± 0.5) times faster than predicted by the temperature independent mass factor of 2.9. This extra rate enhancement must be due to dynamical effects, and, as discussed throughout Chapter III, the only such effect likely to enhance the rate of Mu reaction with F_2 is quantum tunnelling. The measured reduction in the Mu activation energy, relative to the H atom values, is also consistent with this tunnelling interpretation.

The only "stand alone" experimental indicator of the presence of tunnelling in thermally averaged reactions is curvature in Arrhenius plots (Chapter III, Section C, [Laidler (65)]), but this test is not unambiguous since the preexponential factor is also weakly temperature dependent. Besides, it is difficult to obtain sufficient experimental precision over a wide

enough temperature range to demonstrate significant Arrhenius plot curvature, particularly for reactions of gases [Laidler (65), Jakubetz (79)]. Consequently, the absence of curvature in the limited Mu data of Figure 20 is more likely a manifestation of the insufficient temperature range of the measurements than an indication of the absence of tunnelling. On the other hand, the H atom data of Albright et al. does show a slight curvature although it may not be significant given their estimated rate constant uncertainties of 25 to 30%. In any case, these data are suggestive of a tunnelling contribution to the H + F₂ reaction and give apparent activation energies of about 2.2 kcal/mole from 300 - 400K and 3.3 kcal/mole from 450 - 570K.

A number of QMT, QCT, and TST investigations have been performed on the reactions of H isotopes, including Mu, with F₂. The collinear modified LEPS surface of Jonathan et al. (72) (shown in Figure 12) has been used by Connor et al. to calculate exact collinear quantum mechanical trajectories by the state path sum method [Connor 1-(77), 1-(78), 1-(79)] collinear quasi-classical trajectories [Connor 2-(78), Connor 1-(79)] and collinear vibrationally adiabatic TST calculations [Connor 1-(79)]; Jakubetz 1-(78), (79) also used this surface to investigate tunnelling corrections to TST calculations. The collinear reaction rate constants, isotopic rate constant ratios, and apparent activation energies calculated by these authors for the reactions $Y + F_2(v = 0, 1) \rightarrow YF + F$, Y = Mu, H, D, T between 200 and 1100K are listed in Tables VIII, IX, and X respectively. The vibrational populations of F₂ at thermal equilibrium at 300, 550, and 900K are 98%, 89%, and 74% for v = 0, and 2%, 9%, and 19% for

TABLE VIII: CALCULATED RATE CONSTANTS FOR THE COLLINEAR Y + F₂ → YF + F REACTIONS

(a) $k_0(Y)$ (cm s ⁻¹ molecule ⁻¹)*				
T/K	Mu	H	D	T
Quantum [†]				
300	1.5(4)	2.3(3)	1.4(3)	1.1(3)
550	4.7(4)	1.3(4)	8.9(3)	7.3(3)
900	1.0(5)	3.4(4)	2.4(4)	2.0(4)
Quasiclassical [†]				
300	4.5(3)	1.6(3)	1.2(3)	9.8(2)
550	3.1(4)	1.2(4)	8.4(3)	7.0(3)
900	8.8(4)	3.2(4)	2.3(4)	1.9(4)
TST (no tunnelling) [†]				
300	4.1(3)	1.6(3)	1.2(3)	1.0(3)
550	3.1(4)	1.2(4)	8.5(3)	7.1(3)
900	9.1(4)	3.2(4)	2.4(4)	2.0(4)
TST (Eckart tunnelling correction) [§]				
300	1.6(4)	2.1(3)	1.4(3)	1.1(3)
550	5.0(4)	1.3(4)	8.9(3)	7.3(3)

(b) $k_1(Y)$ (cm s ⁻¹ molecule ⁻¹)*				
T/K	Mu	H	D	T
Quantum [†]				
300	1.9(4)	3.3(3)	2.2(3)	1.8(3)
550	5.5(4)	1.6(4)	1.2(4)	9.6(3)
900	1.1(5)	3.9(4)	2.8(4)	2.3(4)
Quasiclassical [†]				
300	7.2(3)	2.5(3)	1.9(3)	1.7(3)
550	3.6(4)	1.5(4)	1.1(4)	9.3(3)
900	8.7(4)	3.8(4)	2.8(4)	2.3(4)
TST (no tunnelling) [†]				
300	5.1(3)	2.6(3)	2.1(3)	1.8(3)
550	3.5(4)	1.5(4)	1.2(4)	9.9(3)
900	9.7(4)	3.8(4)	2.8(4)	2.4(4)
TST (Eckart tunnelling correction) [§]				
300	1.9(4)	3.3(3)	2.4(3)	2.0(3)
550	5.5(4)	1.6(4)	1.2(4)	1.0(4)

* Y = Mu, H, D, or T. The number in parenthesis indicates the power of 10 by which the entry should be multiplied.

[†] from Connor 1-(79)

[§] from Jakubetz (79)

TABLE IX: CALCULATED RATE CONSTANT RATIOS FOR THE COLLINEAR Y + F₂ → YF + F REACTIONS

(a) $k_0(Y)/k_0(H)^*$					(b) $k_1(Y)/k_1(H)^*$				
T/K	Mu	H	D	T	T/K	Mu	H	D	T
Quantum [†]					Quantum [†]				
300	6.6	1	0.63	0.50	300	5.7	1	0.68	0.55
550	3.7	1	0.69	0.56	550	3.4	1	0.71	0.59
900	3.1	1	0.70	0.58	900	2.9	1	0.72	0.60
Quasiclassical [†]					Quasiclassical [†]				
300	2.8	1	0.74	0.62	300	2.9	1	0.77	0.66
550	2.7	1	0.73	0.61	550	2.4	1	0.75	0.63
900	2.7	1	0.72	0.60	900	2.3	1	0.74	0.61
TST (no tunnelling) [†]					TST (no tunnelling) [†]				
300	2.6	1	0.75	0.63	300	2.0	1	0.81	0.71
550	2.7	1	0.74	0.61	550	2.3	1	0.76	0.65
900	2.8	1	0.73	0.61	900	2.6	1	0.74	0.63
TST (Eckart tunnelling correction) [§]					TST (Eckart tunnelling correction) [§]				
300	7.6	1	0.66	0.53	300	5.6	1	0.72	0.60
550	4.0	1	0.71	0.58	550	3.4	1	0.73	0.62
			Temperature Independent Factor.			2.9	1	0.72	0.59

* Y = Mu, H, D, or T.

† from Connor 1-(79)

§ from Jakubetz (79)

TABLE X: CALCULATED ACTIVATION ENERGIES FOR THE COLLINEAR Y + F₂ → YF + F REACTIONS

(a) E _a ⁽⁰⁾ (Y) (kcal mole ⁻¹)*					(b) E _a ⁽¹⁾ (Y) (kcal mole ⁻¹)*				
T/K	Mu	H	D	T	T/K	Mu	H	D	T
Quantum [†]					Quantum [†]				
300	1.2	2.1	2.3	2.3	300	1.1	1.9	2.0	2.0
550	1.9	2.5	2.6	2.6	550	1.8	2.3	2.3	2.3
900	2.6	2.9	3.0	3.0	900	2.4	2.7	2.7	2.7
Quasiclassical [†]					Quasiclassical [†]				
300	2.4	2.5	2.5	2.5	300	2.0	2.2	2.2	2.2
550	2.7	2.7	2.7	2.7	550	2.3	2.5	2.4	2.4
900	3.1	3.1	3.1	3.1	900	2.7	2.8	2.8	2.8
TST (no tunnelling) [†]					TST (no tunnelling) [†]				
300	2.6	2.5	2.5	2.5	300	2.5	2.2	2.1	2.1
550	2.8	2.7	2.7	2.7	550	2.7	2.5	2.4	2.3
900	3.2	3.1	3.1	3.1	900	3.0	2.8	2.7	2.7
TST (Eckart tunnelling correction) [§]					TST (Eckart tunnelling correction) [§]				
300	1.2	2.1	2.3	2.3	300	1.1	1.9	2.0	2.0
550	1.9	2.6	2.6	2.6	550	1.8	2.3	2.3	2.3

* Y = Mu, H, D, or T.

† from Connor 1-(79)

§ from Jakubetz (79)

for $v = 1$ respectively; consequently, $k_0(T)$ approximates $k(T)$ to better than 0.5% at 300K and better than 2.8% at 900K. It may be noted that the original QMT reaction probabilities for the Mu reaction [Connor 1-(77), Connor 1-(78)] were recalculated and found to be about 12% larger than first reported [Connor 1(79)]; the new results are thought to be accurate to better than 3%. It should also be noted that the quantum calculations for the Mu reactions were calculated by defining a "line of no return" on the potential surface such that the reaction is presumed to proceed once a given collision crosses this line; this procedure does not allow for reflection of the representative point from the repulsive product valley wall and therefore over-estimates the reaction probability for collisions at very high relative translational kinetic energy. However, QCT calculations show that this effect should not influence the rate constants in the temperature range below 1000K [Connor 2-(78), 1-(79)].

At 300K, the predicted collinear QMT activation energies for the Mu and H reactions, 1.2 and 2.1 kcal/mole respectively, are in good agreement with the experimental values, 0.9 ± 0.2 and 2.3 ± 0.2 kcal/mole respectively. Furthermore, at 300K, comparison of the predicted Mu:H rate constant ratio of 6.6 with the experimental values shows remarkable agreement with the value of 6.8 ± 1.5 obtained from k_H measured by Albright et al., but clear disagreement with the value of 14.6 ± 1.6 obtained from the results of Homann et al. That these collinear calculations apparently agree well with most of the experimental results is, in itself, an interesting fact. The quantitative agreement might well be fortuitous since: (1) "the successful

theoretical prediction of an energy of activation does not imply that the details of the theory are even qualitatively correct [Truhlar (78)]," and (2) despite the agreement between the predicted Mu:H rate constant ratio and the experimental value that uses the results of Albright et al., this cannot be interpreted as removing the ambiguity of the experimental rate constant ratios since the Jonathan et al. surface used in the calculations was optimized by quasiclassical trajectories which did not incorporate tunnelling, and may, therefore, be inaccurate [Connor 2-(78)]. On the other hand, there are a number of reasons to suppose that the collinear calculations do faithfully describe the reaction, at least qualitatively [Connor 1-(79), Jakubetz (79)]: (1) as mentioned in Chapter III, the collinear configuration is energetically favored for the Jonathan et al. surface, (2) three dimensional trajectory calculations show that the reaction is collinearly dominated due to the reaction dynamics [Polanyi (75)], and (3) because the saddle point is very early, the transition state is just a slight perturbation of the target molecule and thus the three dimensional bending vibrations of the transition triatomic should not greatly alter the collinear potential [Connor 1-(79)].

Like the experimental results, the QMT calculations are strongly suggestive of tunnelling in the Mu reaction. The quantum $k(Y)/k(H)$ rate constant ratios of Table IX for both the $F_2(v = 0)$ and $F_2(v = 1)$ reactions approach the limiting temperature independent mass factor ratios of 2.9:1.0:0.72:0.59 (see Chapter III, Section D, p. 113) as the temperature approaches 900K, indicating that the large dynamical effects that enhance

the room temperature Mu reaction cease to operate in the high temperature "classical" regime. The dramatic increase in the Mu reaction activation energy (Table X), which approaches an isotope independent value near 900K, is also consistent with tunnelling in the context of the Tolman interpretation of activation energy (Chapter III, p. 97).

A revealing indication of the dynamics of the $Y + F_2$ reactions is illustrated in Figure 21 (adapted from [Connor 1-(79)]) which compares the energy dependence of the total reaction probabilities, $P_S^t = \sum_{S'} P_{S'+S}^t$ (see Chapter III, Section D), for the quasiclassical and quantum mechanical trajectories. In both cases, at lower values of E_{trans}^{QC} , P_S^t is ordered $Mu > H > D > T$, while at higher values of E_{trans}^{QC} , P_S^t displays the opposite behaviour; the curves cross near $P_S^t = 0.5$. In the Figure, the physical barrier height, E_b^{phys} , for the $F_2(v = 0)$ reaction is indicated by an arrow at $E_{trans}^{QC} = 1.08$ kcal/mole (there is no physical barrier to the $F_2(v = 1)$ reaction). It may be recalled from Chapter III, Section F, that E_b^{phys} represents the "static" tunnelling barrier: collisions with less relative translational kinetic energy than E_b^{phys} are not allowed to react classically due to their energy deficit. From Figure 21, it is clear that only the Mu reaction displays considerable static tunnelling. It will also be recalled that the quasiclassical threshold energies, E_T^{QC} , represent the barriers to "dynamic" tunnelling: collisions with less relative translational kinetic energy than E_T^{QC} , but with more than E_b^{phys} , are classically forbidden, not because of the energy balance as in the "static" case, but because of the availability of energy, as governed by the reaction dynamics. The Figure

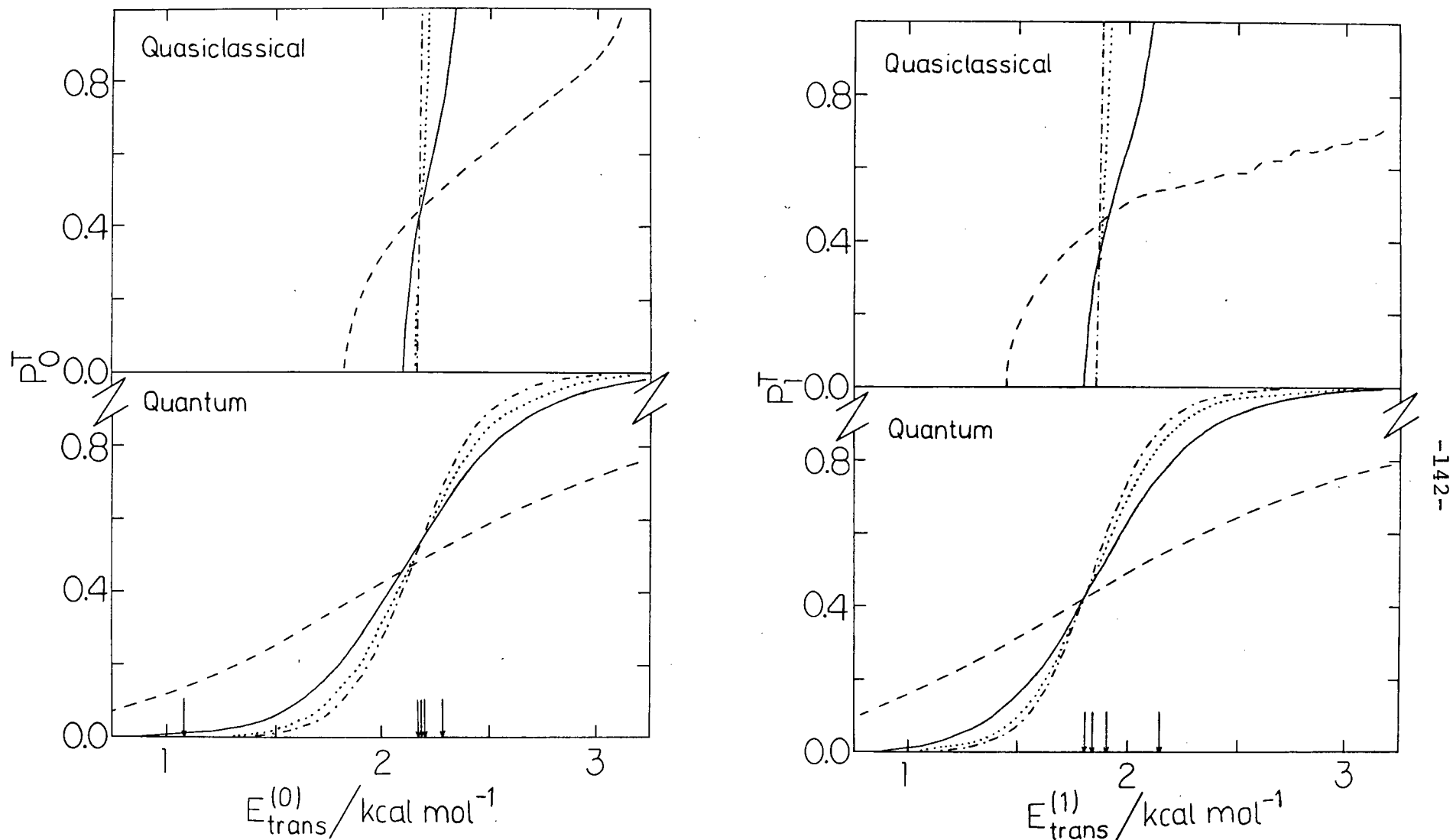


FIGURE 21: Collinear quantum and quasiclassical total reaction probabilities as a function of collision energy for $Y + F_2(v=0,1) \rightarrow YF + F$, $Y = \text{Mu}(\text{---})$, $\text{H}(\text{—})$, $\text{D}(\cdots)$, or $\text{T}(\text{-}\cdots\text{-})$, adapted from [Connor 1-(79)]. The significance of the arrows is described in the text.

clearly shows that all isotopic variants of the reaction display considerable dynamic tunnelling which is much more dominant than static tunnelling, even in the case of muonium.

The Boltzmann distribution must be considered in order to appreciate the importance of the tunnelling-enhanced reaction probability on the ensemble reaction process. Figure 22 plots the integrand of equation (35) ($P_s^t(E_{\text{trans}})e^{-E_{\text{trans}}/k_B T}$) as a function of E_{trans} for the quantum mechanical reaction probabilities at 300 and 900K for the $Y + F_2(v = 0)$ reaction (adapted from [Connor 1-(78)]). In the Figure, arrow A indicates the physical barrier height at 0.0472 eV (1.08 kcal/mole), arrow B, at 0.087 eV (2.01 kcal/mole), indicates the quasiclassical threshold for the H atom reaction (from [Jonathan (72)]), and arrow C indicates $k_B T$ at (a) 300K and (b) 900K. A comparison of arrow B with the quasiclassical thresholds of Figure 21 reveals that it is approximately the average of the quasiclassical thresholds for the isotopic variants of this reaction. For the sake of illustration, arrow B, the average E_T^{QC} , divides the "tunnelling" reaction region from the "classical" region. Thus, Figure 22 clearly demonstrates that the room temperature muonium reaction is dominated by tunnelling, which also contributes significantly to the room temperature H atom reaction, whereas, at 900K, classical processes dominate the reactions for all H isotopes. Figure 23 (adapted from [Connor 1-(79)]), a plot similar to Figure 22, compares the rate constant integrand for the quasiclassical and quantum mechanical reactions of the $F_2(v = 1)$ state at 300K. Once again if the average E_T^{QC} is taken as the line that approximately separates classical from tunnelling processes, it is seen that

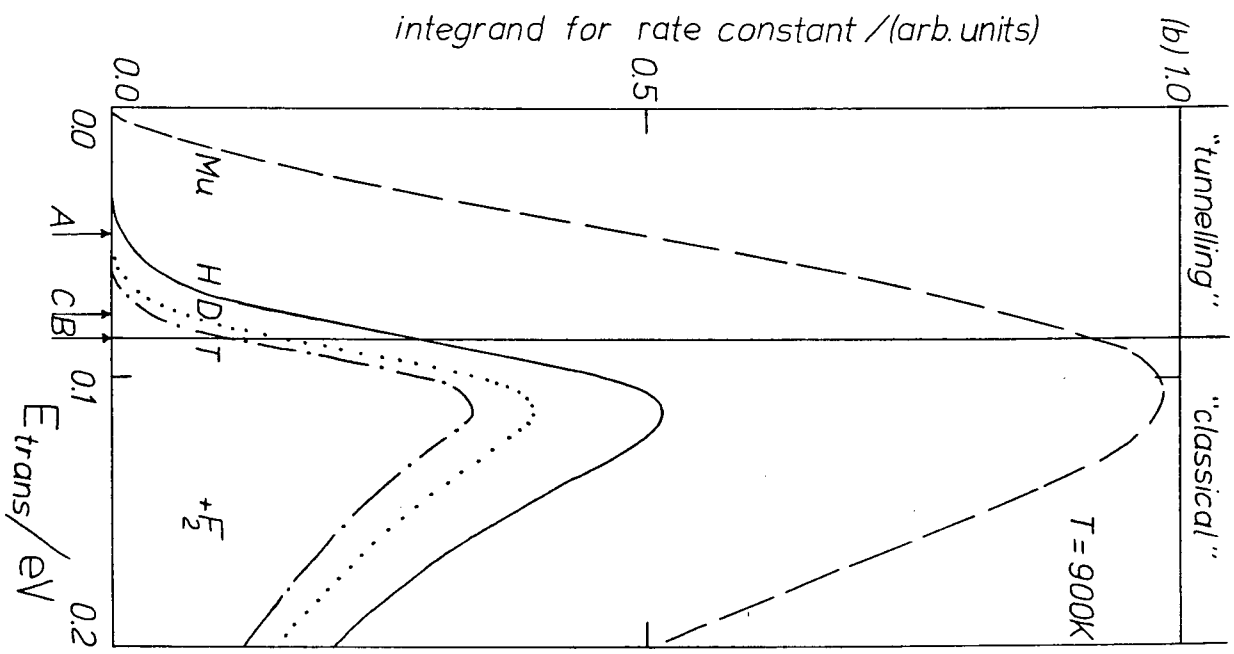
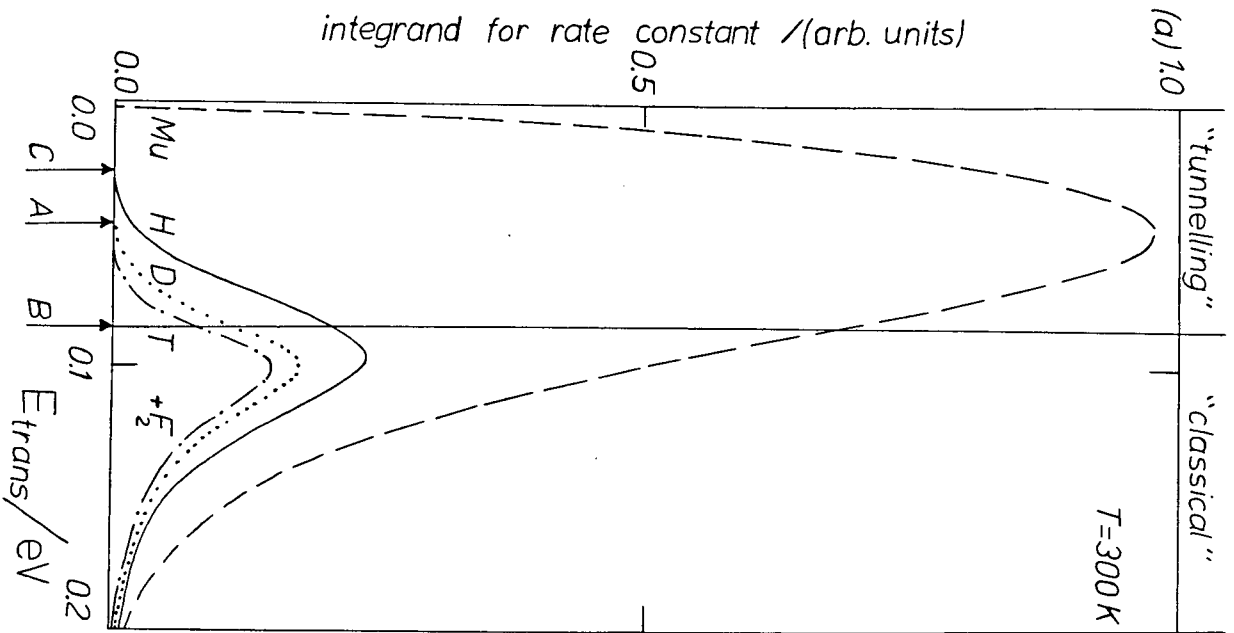


FIGURE 22: Integrand of the quantum collisional rate constant (a) $T = 300\text{K}$ (b) $T = 900\text{K}$, adapted from [Connor 1--(78)]. The text describes the significance of arrows A, B, and C.

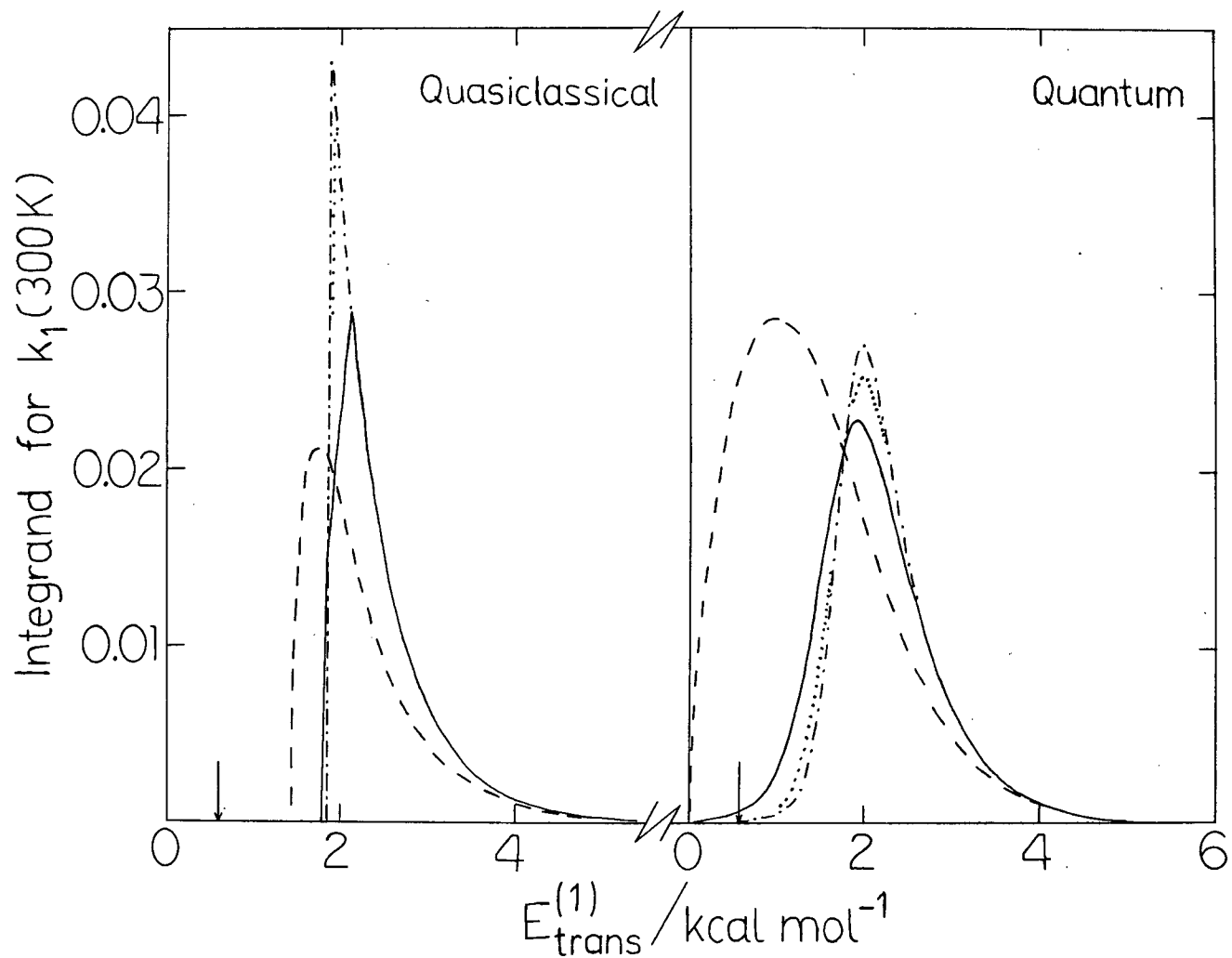


FIGURE 23: Integrand for the collinear quantum and quasiclassical rate constant $k_1(T)$ at 300K for the reaction: $Y + F_2(v=1) \rightarrow YF + F$, $Y = \text{Mu}(\text{---})$, $\text{H}(\text{—})$, $\text{D}(\cdots)$, and $\text{T}(\text{---})$, adapted from [Connor 1st(79)]. The arrows indicate $k_B T$ at 300K.

tunnelling completely dominates the muonium reaction at room temperature and contributes significantly to the H atom reaction rate as well.

The calculations of Connor et al. also reveal a great deal about the high temperature "classical" behaviour of the Y + F₂ reactions. Figure 21 shows that P_s^t for high energy collisions is ordered T>D>H>Mu for both the QCT and QMT calculations. From the discussion in Chapter III, Section B, p.76, this behaviour may be explained in terms of the classical "bottleneck" effect arising from the sharper constriction in the reaction valley for the lighter H isotopes. Verification of this effect is given in Figure 24 (adapted from [Connor 2-(78)]) which shows non-reactive quasiclassical trajectories at various collision energies on the mass weighted muonium potential energy surface with F₂ initially in the v = 0 state. The plot at E_{trans}^{QC} = 1.6 kcal/mole, which is greater than the physical barrier height, but less than the quasiclassical threshold, shows collisions at all vibrational phases of F₂ to be not only non-reactive, but also elastic since the vibrational frequency of F₂ is not altered by the collisions. The other plots are for values of E_{trans}^{QC} > E_T^{QC} and show ranges of vibrational phase for which the collisions are non-reactive; it may be noted that some of the non-reactive collisions are inelastic, particularly at high values of E_{trans}^{QC}. All four plots of Figure 24 show the quasiclassical non-reactivity of the Mu + F₂ collisions at moderately high energies to be due to the bottleneck effect. Figure 21 indicates the importance of this effect in the relatively slow rise of the quasiclassical P_s^t curves from 0.5 to 1 for the Mu

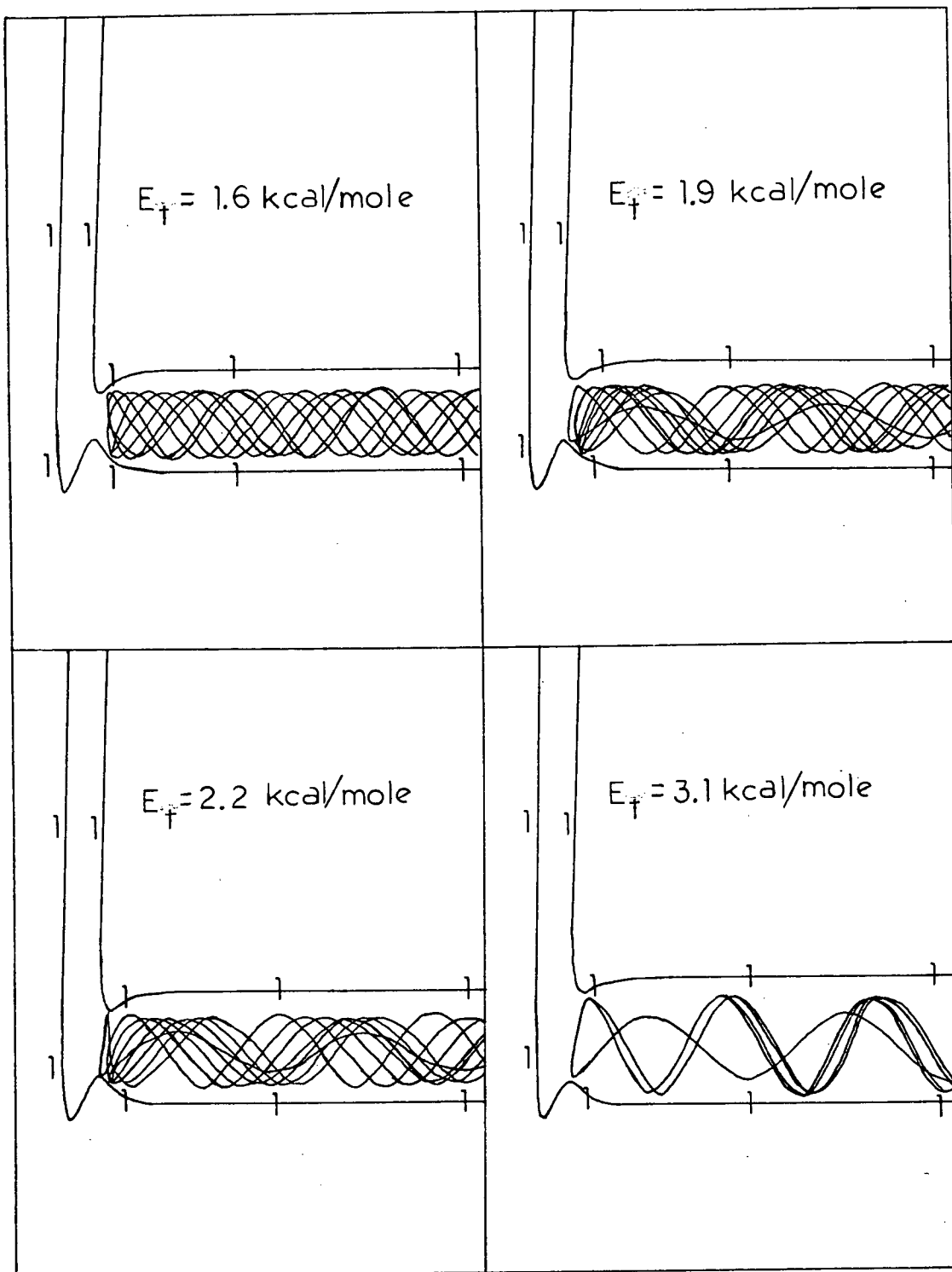


FIGURE 24: Non-reactive quasiclassical trajectories for the reaction: $\text{Mu} + \text{F}_2(v=0) \rightarrow \text{MuF} + \text{F}$ on the mass weighted LEPS potential energy surface of [Jonathan (72)], adapted from [Connor 2-(78)]. In the notation of the text, $E_t \equiv E_{\text{trans}}^{\text{OC}}$. The quasiclassical threshold energy for the reaction is 1.80 kcal/mole.

reaction, particularly for the $F_2(v=1)$ collisions for which P_S^t shows some structure. The origin of this structure is non-reactive back reflection of the representative point off the strongly repulsive wall of the product valley, as discussed in Chapter III, p. 78. The QCT calculations of Connor 2-(79) confirm that the onset of this effect occurs at lower collision energies for Mu than for the other H isotopes due to the extreme contraction of the mass weighted product valley for the lighter isotope. For the $v=0$ reaction, the onset of wall reflection occurs at $E_{trans}^{QC} = 7$ and 40 kcal/mole for Mu and H respectively. For $Mu + F_2(v=1)$, wall reflection begins at $E_{trans}^{QC} = 2$ kcal/mole, thereby competing with bottleneck reflection and giving rise to the observed P_S^t structure.

Arrows in Figure 21 indicate the vibrationally adiabatic barriers (see Chapter III, Section C) $E_0^{VA} = 2.28, 2.20, 2.17,$ and 2.16 kcal/mole and $E_1^{VA} = 2.15, 1.91, 1.84,$ and 1.80 kcal/mole for Mu, H, D, and T respectively. In discussing VA in the context of an early barrier, it was pointed out that when the VA assumption holds, E_V^{VA} gives good "first guess" values for the quasiclassical threshold energies. Figure 21 shows this to be an excellent approximation for the $Y + F_2$ reactions, with the exceptions of the muonium reaction and the fact that $E_V^{VA}(Y)$ have the opposite ordering to $E_T^{QC}(Y)$. In other words, the VA assumption, which has general validity for these reactions, is better for the heavier H isotopes than for the lighter ones. This may also be understood in terms of the bottleneck. Besides reflecting representative points non-reactively (the normal bottleneck effect), this constriction in the saddle point region

promotes vibrational non-adiabaticity by presenting a potential surface geometry that greatly perturbs the quasiclassical trajectories. For a restricted range of vibrational phases, the conversion of vibrational energy of the F_2 molecule to translational energy of the representative point may help propel the system to reaction, thereby reducing the quasiclassical threshold energy. Evidently, the sharper bottlenecks of the lighter H isotopes cause greater vibrational-translational energy transfer since they cause a more dramatic perturbation in the quasiclassical trajectory. Expressed in the jargon of molecular dynamics, the bottleneck encounter for the light isotope takes place in the "sudden" regime, while the heavy isotope encounter is in the "adiabatic" regime [Levine (74)].

The foregoing discussion of the general validity of the vibrational adiabaticity assumption suggests that simple TST calculations of the $Y + F_2$ reaction rates using a vibrationally adiabatic barrier should provide fairly accurate estimates of the quasiclassical reaction rates, with the possible exception of the muonium reaction. Indeed, Connor et al. (79) have found this to be the case. Tables VIII - X show the VA-TST rate constants, rate constant ratios, and activation energies for the H, D, and T reactions to be within 5% of the quasiclassical results in most cases; for muonium, the somewhat less spectacular agreement is typically in the 10 - 20% range, except for the case of the $F_2(v = 1)$ rate constant at 300K which differs by about 40%. Clearly, the easily calculated VA-TST rate constants are sufficiently accurate, in general, to be used as substitutes for the much more laborious quasiclassical rate constant calculations.

Thus, VA-TST may be used to economically optimize potential energy surfaces, not only for this reaction, but also for reactions of the same general type (i.e. exothermic, light-heavy-heavy atom reactions with early barriers that are dominated by the collinear reaction geometry).

Figure 25 (adapted from [Connor 1-(79)]) displays the TST, QCT, and QMT rate constants as Arrhenius plots (for H, D, and T, the TST results are essentially coincident with the QCT results and therefore are not shown). As expected, the quantum Arrhenius plots show noticeable curvature due to tunnelling, but it should be noted that the quasiclassical plots are also weakly curved. Although the curvature in the quantum Arrhenius plot for the Mu reaction is significant, it is not dramatic; if the theoretical plot proves to be physically accurate, then the experimental demonstration of the Arrhenius plot curvature, even for the case of the Mu reaction, will require that the experiment be conducted over a wide temperature range, $\sim 200 - 600\text{K}$ [Jakubetz (79)].

Having noted the relative success of collinear vibrationally adiabatic TST calculations in reproducing the quasiclassical rate constants for the $\text{Y} + \text{F}_2$ reaction and having noted the striking resemblance between the quantum mechanical reaction probability curves of Figure 21 with the one dimensional tunnelling transmission coefficients of Figure 18, Jakubetz 1-(78), (79) investigated the application of one dimensional tunnelling corrections to VA-TST calculations for the reactions: $\text{Y} + \text{F}_2$ and $\text{Y} + \text{Cl}_2$. Three tunnelling corrections were investigated: the Wigner correction, and corrections for the truncated Bell parabola and

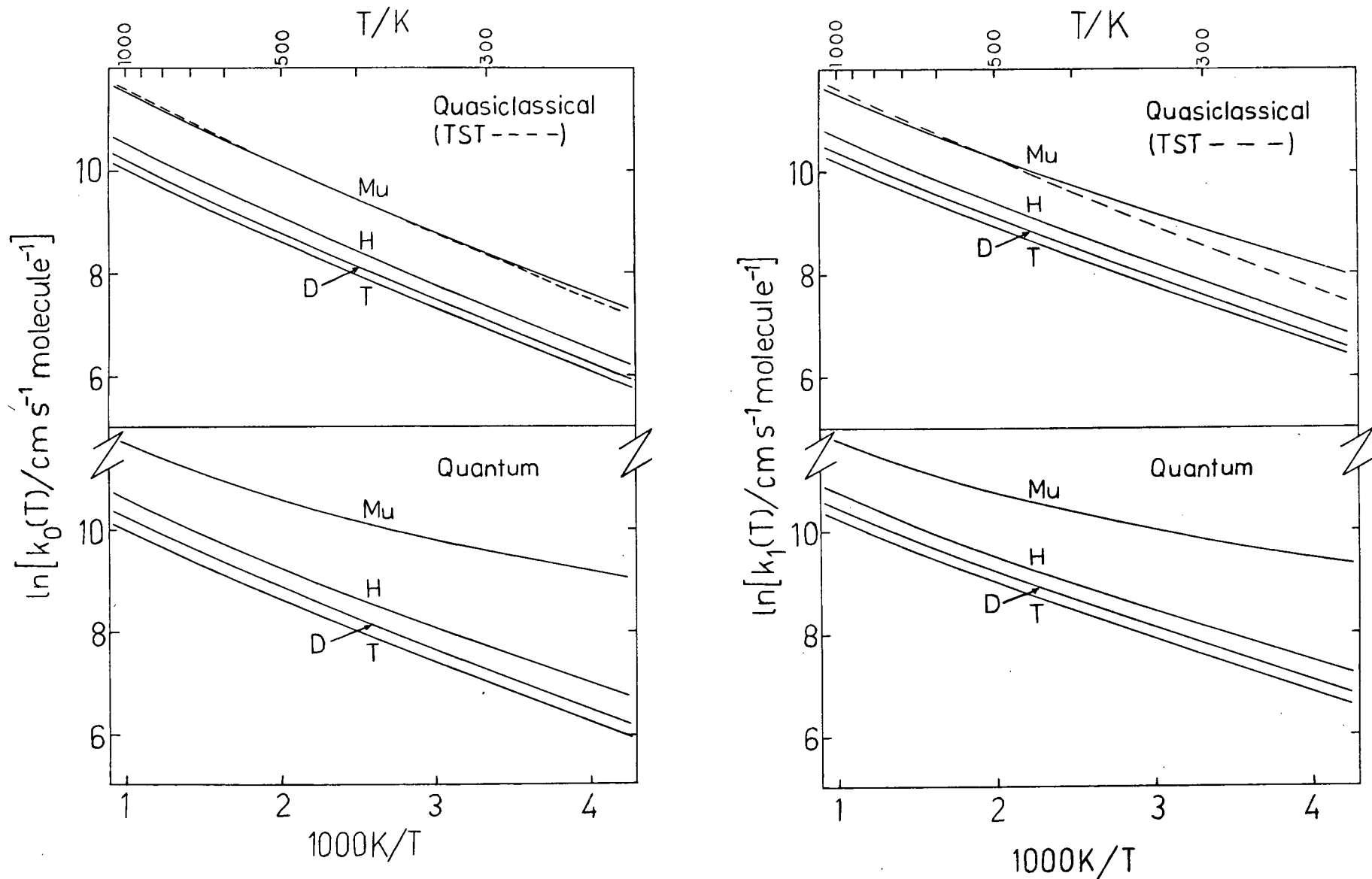
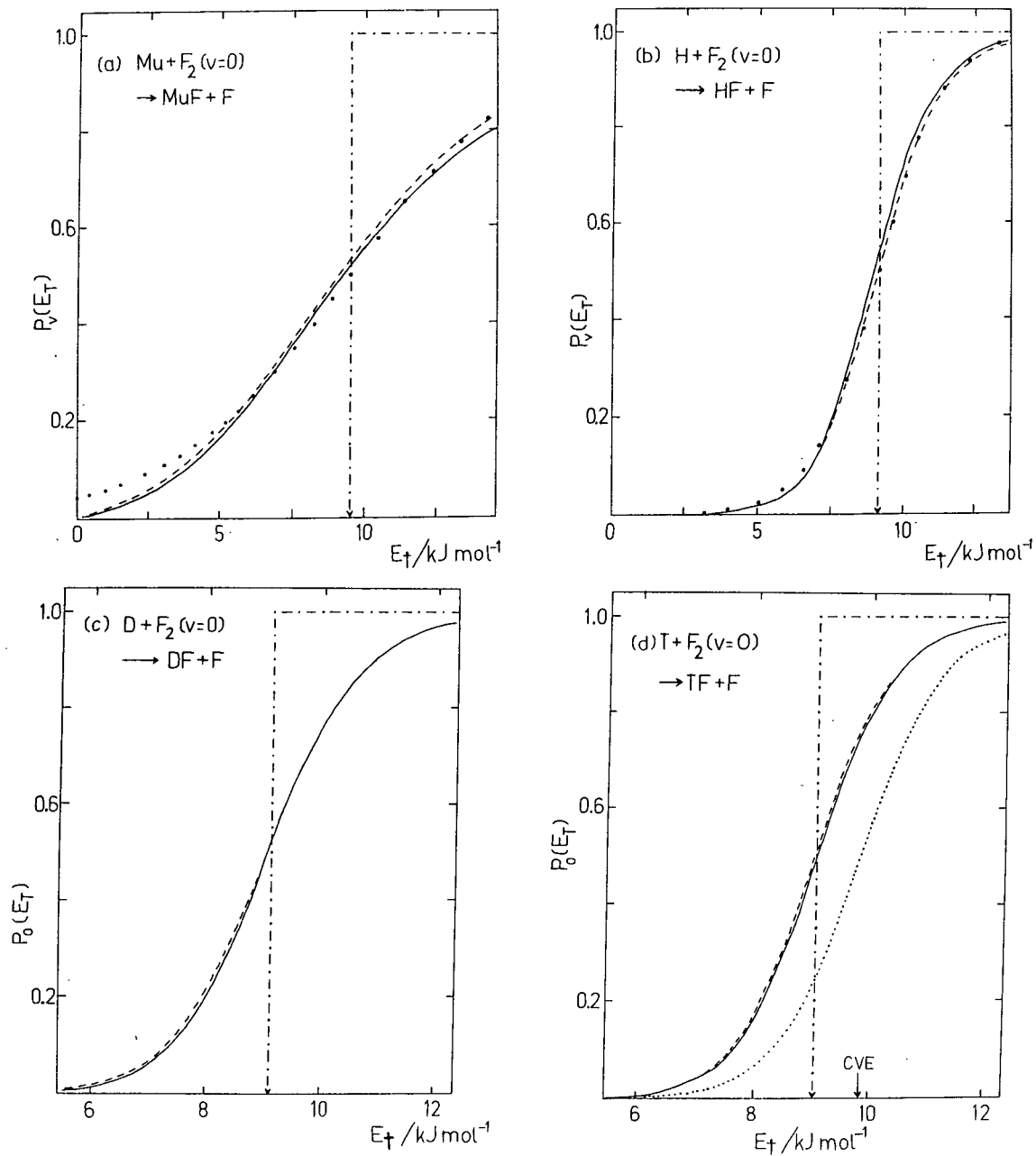


FIGURE 25: Arrhenius plots for the collinear quantum, quasiclassical, and transition state theory rate constants for the reaction: $Y + F_2 \rightarrow YF + F$, $Y = \text{Mu}, \text{H}, \text{D}, \text{and T}$, adapted from [Connor 1-(79)]. The TST results² for the H, D, and T isotopes are essentially coincident with the quasiclassical results, and therefore are not illustrated.

the unsymmetrical Eckart barriers (see Chapter III, Section F). Figure 26 (adapted from [Jakubetz (79)]) compares the F_2 ($v = 0$) total reaction probabilities resulting from the various tunneling corrections with the exact quantum mechanical results of Connor et al. and with uncorrected TST results for the $Y + F_2$ reactions. In all cases, the Eckart barrier-TST curves are in excellent agreement with the exact quantum results - the agreement is almost perfect for the D and T reactions. The Arrhenius plots of Figure 27 (adapted from [Jakubetz (79)]) show that the Bell and Eckart corrections provide essentially the same excellent agreement with the quantum results for the H, D, and T reactions; indeed, even the very much simpler Wigner correction (not shown in Figure 27) provides good "first guess" approximations to the quantum results for these reactions. However, Figure 27 also shows that this is not the case for the muonium reaction which is only well described by the Eckart correction. Jakubetz has pointed out that the failure of the Bell correction for Mu is due to the unrealistic truncation of the parabolic barrier which results in an over estimate of the low collision energy reaction probabilities (c.f. Figure 26). The general success of these tunnelling corrections can be largely attributed to the early barrier location in these reactions as discussed in Chapter III, p. 78. Figure 26(d) also shows an Eckart fit to the "conservation of vibrational energy" (CVE) barrier, which is just the classical barrier height, E_b^{Cl} , as defined on page 83; the failure of this barrier supports the assumption of vibrational adiabaticity.

The last point of discussion on the $Y + F_2$ reaction is

FIGURE 26: Comparison of quantum and transition state theory reaction probabilities for the reaction: $Y + F_2 \rightarrow YF + F$, $Y = \text{Mu, H, D, or T}$, adapted from [Jakubetz (79)]; quantum (—) [Connor 1-(78)]; tunnelling corrected Eckart barrier VA-TST (---), tunnelling corrected Bell barrier VA-TST (···), uncorrected VA-TST (·-·-); plot (d) also shows tunnelling corrected Eckart barrier CVE-TST (···). In the notation of the text, $E_t \equiv E_{\text{trans}}^{\text{OC}}$.



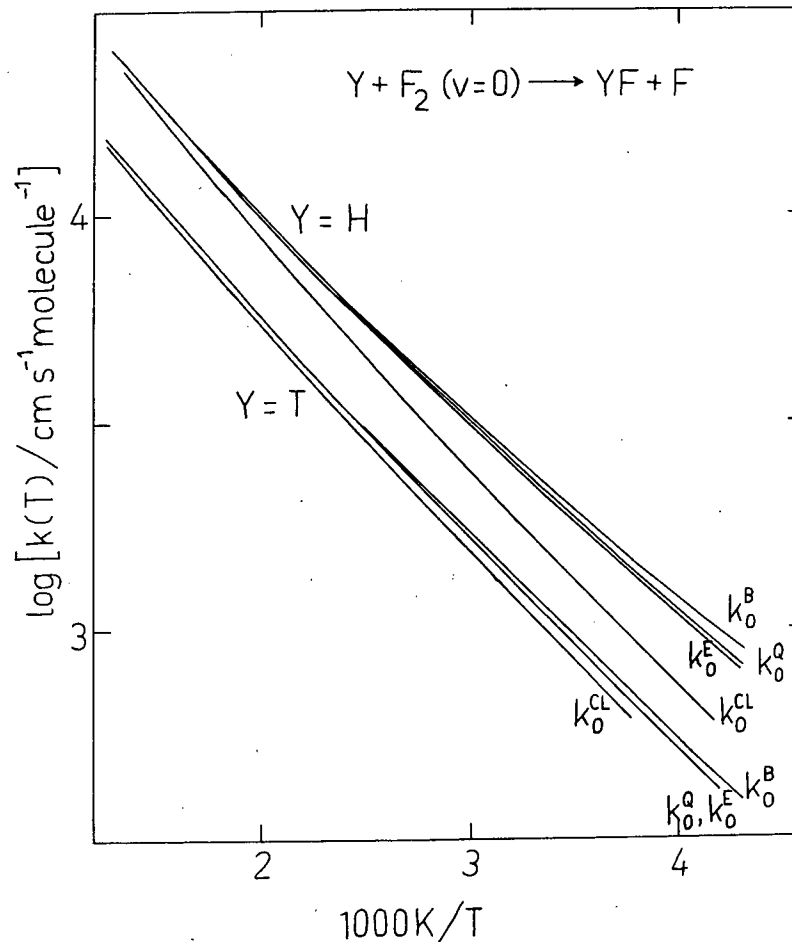
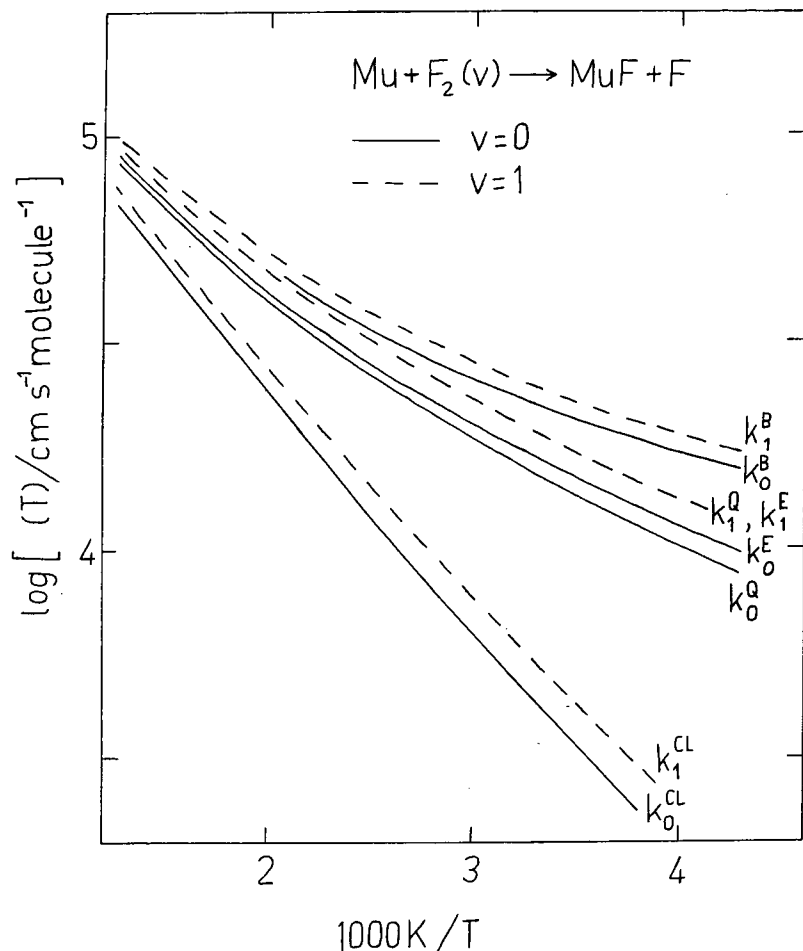


FIGURE 27: Comparison of quantum and transition state theory Arrhenius plots for collinear $\text{Mu} + \text{F}_2(v=0,1)$ (left) and $\text{H} + \text{F}_2(v=0)$ and $\text{T} + \text{F}_2(v=0)$ (right), adapted from [Jakubetz (79)]. Results shown are exact quantum (Q) [Connor 1-(78)], Eckart VA-TST (E), Bell VA-TST (B), and uncorrected VA-TST (CL). For the Mu reaction, k_0^Q and k_0^E coincide over the whole temperature range, while for the H and T reactions, k_0^Q and k_0^E coincide over the whole range.

the product vibrational state distribution. For the $Y + F_2$ reaction, Figure 28 (adapted from [Connor 1-(78)]) plots the calculated relative population distribution of product vibrational states, normalized to the most populated state, \hat{s}' , as a function of the fraction of product vibrational energy, $f_{s'} = E_{s'}/D_0$, where D_0 is the dissociation energy of YF and $E_{s'}$ is the energy of the s' level, both measured relative to $s' = 0$. The Figure shows the results at $E_{trans}^{QC} = 2.45$ kcal/mole, but the vibrational distributions are relatively insensitive to the collision energy [Connor 1-(78)]. The most populated level has the values $\hat{s}' = 1, 6, 9,$ and 12 for Mu, H, D, and T respectively; the H atom result is in agreement with the infrared chemilluminescence results of Jonathan et al. (72) and Polanyi et al. (72). From these calculations, the average fraction of one dimensional product vibrational energy, defined by $\langle f_{s'} \rangle = \sum_{s'=0}^t P_{s'+0}^t f_{s'}/P_0^t$, is 0.40, 0.58, 0.64, and 0.68 for Mu, H, D, and T respectively; again, the H atom results are in agreement with the corrected [Jakubetz 2-(78)] experimental values of 0.55 due to Jonathan et al. and 0.62 due to Polanyi et al. The order $Mu < H < D < T$ for $\langle f_{s'} \rangle$ is in qualitative agreement with the light atom anomaly (Chapter III, p. 81), in which less reaction exoergicity is transformed into product vibration as the mass of the attacking atom decreases. Fischer and Venzl (78) derived an analytic expression that succeeds well in calculating the product vibrational energy distribution for exothermic light-heavy-heavy atom reactions and which is sensitive to the interaction length (saddle point location) and the relative attractiveness of the potential energy surface (see Chapter III, p. 80). This expression may be used

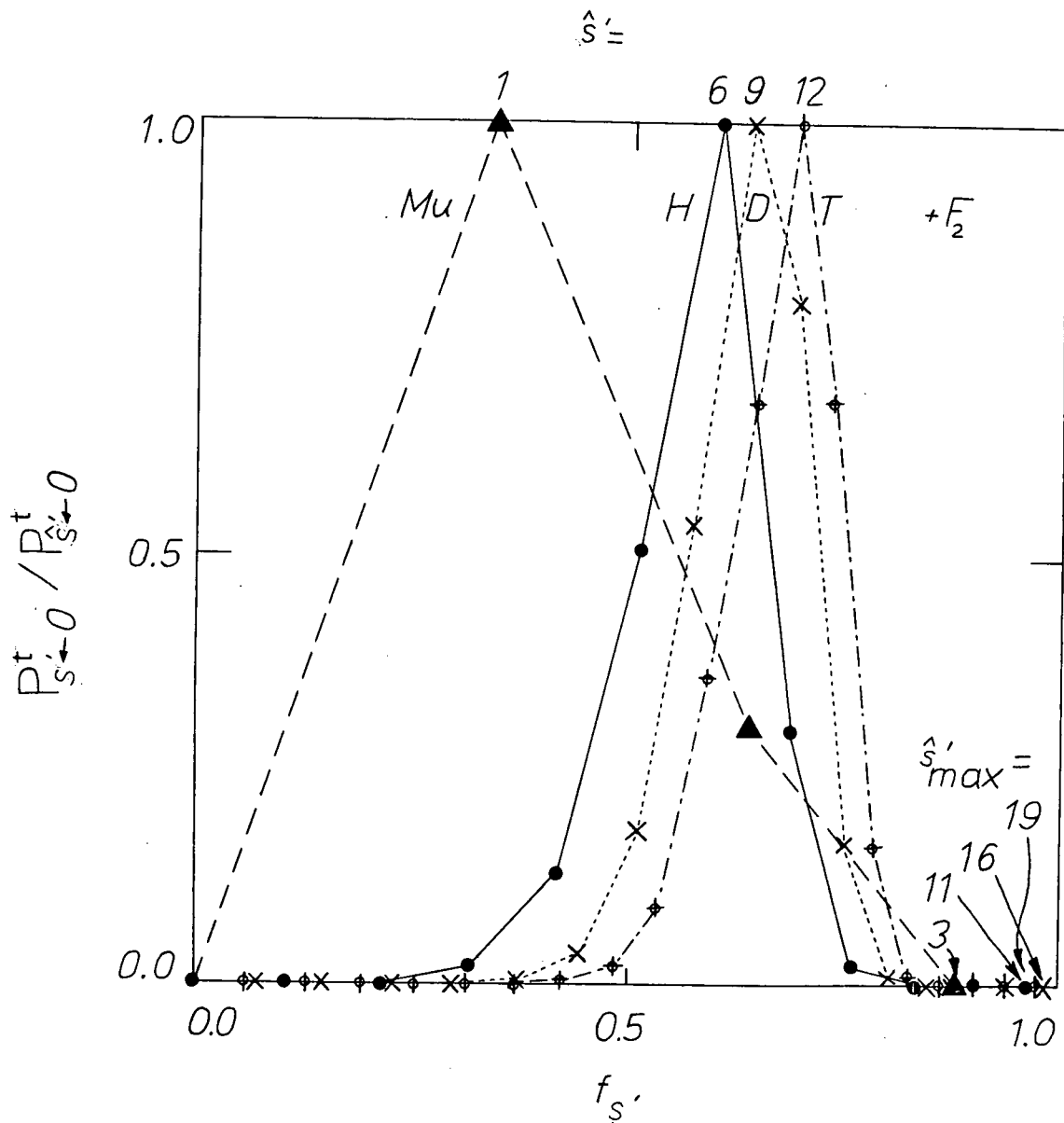
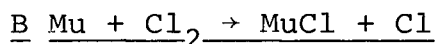


FIGURE 28: Collinear quantum mechanical relative population distribution of product vibrational states normalized to the most populated state \hat{s}' at $E_{trans} = 2.45$ kcal/mole for the $Y + F_2(v=0) \rightarrow YF + F$ reactions, $Y = Mu, H, D,$ and T , adapted from [Connor 1-(78)].

to economically narrow the parameter range for LEPS surfaces by fitting the experimental results for the vibrational distribution. Korsch (78) derived a similar, but simpler, expression which only requires a hand calculator to compute. Although it is not yet possible to experimentally measure product vibrational energy distributions for Mu reactions, the present work has indirectly aided in the development of the computational tools described above since it prompted the exact quantum mechanical calculations of these distributions which were then used as a critical test of the analytic expressions subsequently developed [Jakubetz 1-(78)].



The MSR relaxation rates at various Cl₂ concentrations, measured between 295 and 381K, are listed in Table XI. To illustrate the influence of temperature on the reaction rate, Figure 29 plots the MSR relaxation data obtained at 295 and 384K. The bimolecular rate constants, determined by χ^2 minimum fits of the relaxation rate data to equation II(3), are also listed in the Table and illustrated in the Arrhenius plot of Figure 30. The χ^2 minimum fit of these data to the logarithmic Arrhenius expression (equation (12)) yields:

$$\log_{10} k(1/\text{mole}\cdot\text{s}) = (11.72 \pm 0.14) - (300 \pm 50/T), \quad (1\sigma)$$

with $k(300\text{K}) = (5.29 \pm 0.14) \times 10^{10}$ 1/mole-s and $E_a = (1.36 \pm 0.21)$ kcal/mole. As indicated in the Table, the moderator for three of the rate constant measurements is argon, while N₂ is the moderator for the 370K measurements. Other than the MSR signal enhancement due to N₂ moderator (see Figure 8), no

TABLE XI: MSR RELAXATION RATES FOR THE REACTION: $\mu + \text{Cl}_2 \rightarrow \mu\text{Cl} + \text{Cl}$

Temperature (K) [Moderator gas]	Bimolecular		Relaxation Rate λ (μs^{-1}) [†]
	Rate Constant $k(10^{10} \text{ M}^{-1} \text{ s}^{-1})$	$[\text{Cl}_2]$ (10^{-5} M)	
295 ± 2 [Argon]	5.17 ± 0.24 * (5.45 ± 0.19)	0.0	0.13 ± 0.02 *
		0.98 ± 0.04	0.66 ± 0.12 *
		1.58 ± 0.05	1.45 ± 0.22 *
		1.80 ± 0.07	1.09 ± 0.03 *
		2.45 ± 0.08	1.65 ± 0.17 *
		3.12 ± 0.07	1.90 ± 0.03 *
		3.71 ± 0.11	2.36 ± 0.17 *
		4.90 ± 0.11	2.49 ± 0.27 *
		6.85 ± 0.15	3.07 ± 0.17 *
		(4.73 ± 0.56) **	0.29 ± 0.07 **
			1.09 ± 0.15 **
			2.32 ± 0.25 **
			3.03 ± 1.11 **
	336 ± 2 [Argon]	6.83 ± 0.59	0.0
2.23 ± 0.07			1.82 ± 0.19
3.84 ± 0.11			3.40 ± 0.40
370 ± 3 [Nitrogen]	7.27 ± 0.72	0.0	0.00 ± 0.23 §
		2.19 ± 0.07	1.58 ± 0.43 §
		3.40 ± 0.10	3.62 ± 0.77 §
		4.47 ± 0.13	3.64 ± 0.92 §
		5.81 ± 0.16	5.23 ± 1.05 §
		5.94 ± 0.16	3.83 ± 1.75 §
		6.79 ± 0.19	4.09 ± 0.91 §
381 ± 2 [Argon]	9.22 ± 0.65	0.0	0.47 ± 0.03
		0.74 ± 0.05	1.07 ± 0.09
		1.94 ± 0.07	2.21 ± 0.27
		6.69 ± 0.18	7.25 ± 0.64

† Relaxation rates reported are weighted averages of the left and right positron telescope histograms.

* Room temperature data obtained at LBL (1975).

** Room temperature data obtained at TRIUMF (1976).

§ MSR relaxation rates in left and right histograms differ systematically because of the use of a different geometry for each telescope resulting in different λ_0 's for left and right. Relaxation rates reported are weighted averages of $(\lambda - \lambda_0)$.

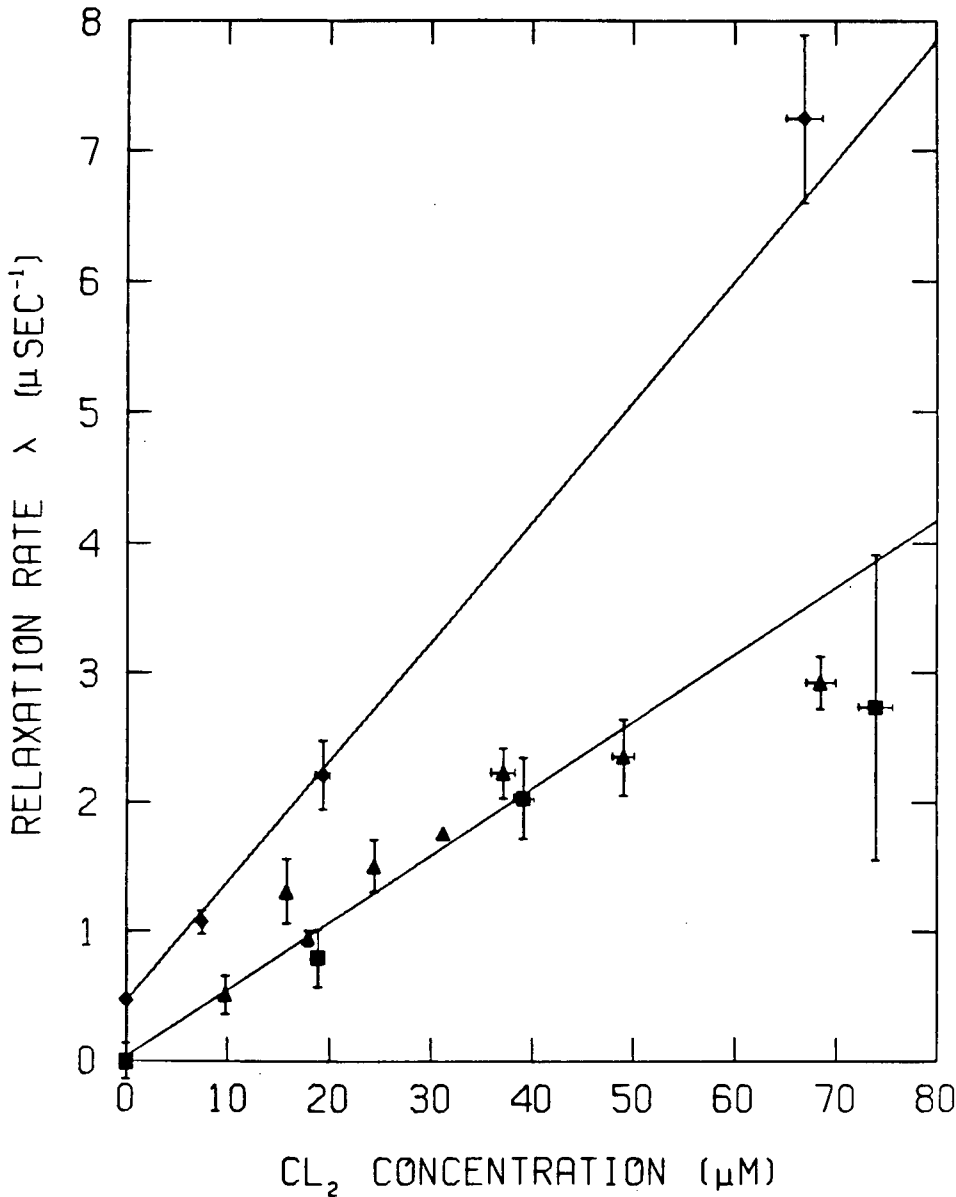


FIGURE 29: The effect of temperature on the $\text{Mu}_2 + \text{Cl}_2$ MSR relaxation rates. The lines are χ^2 minimum fits to the pseudo-first order kinetic expression of equation II(3) corresponding to $k = (5.17 + 0.24) \times 10^{10}$ l/mole-s at 295K (squares and triangles) and $k = (9.22 + 0.65) \times 10^{10}$ l/mole-s at 381 K (diamonds). The triangles represent data taken at LBL during 1975, while the squares and diamonds represent data taken at TRIUMF. The 295 K data represent $(\lambda - \lambda_0)$ in order to account for the different λ_0 's obtained at LBL and TRIUMF.

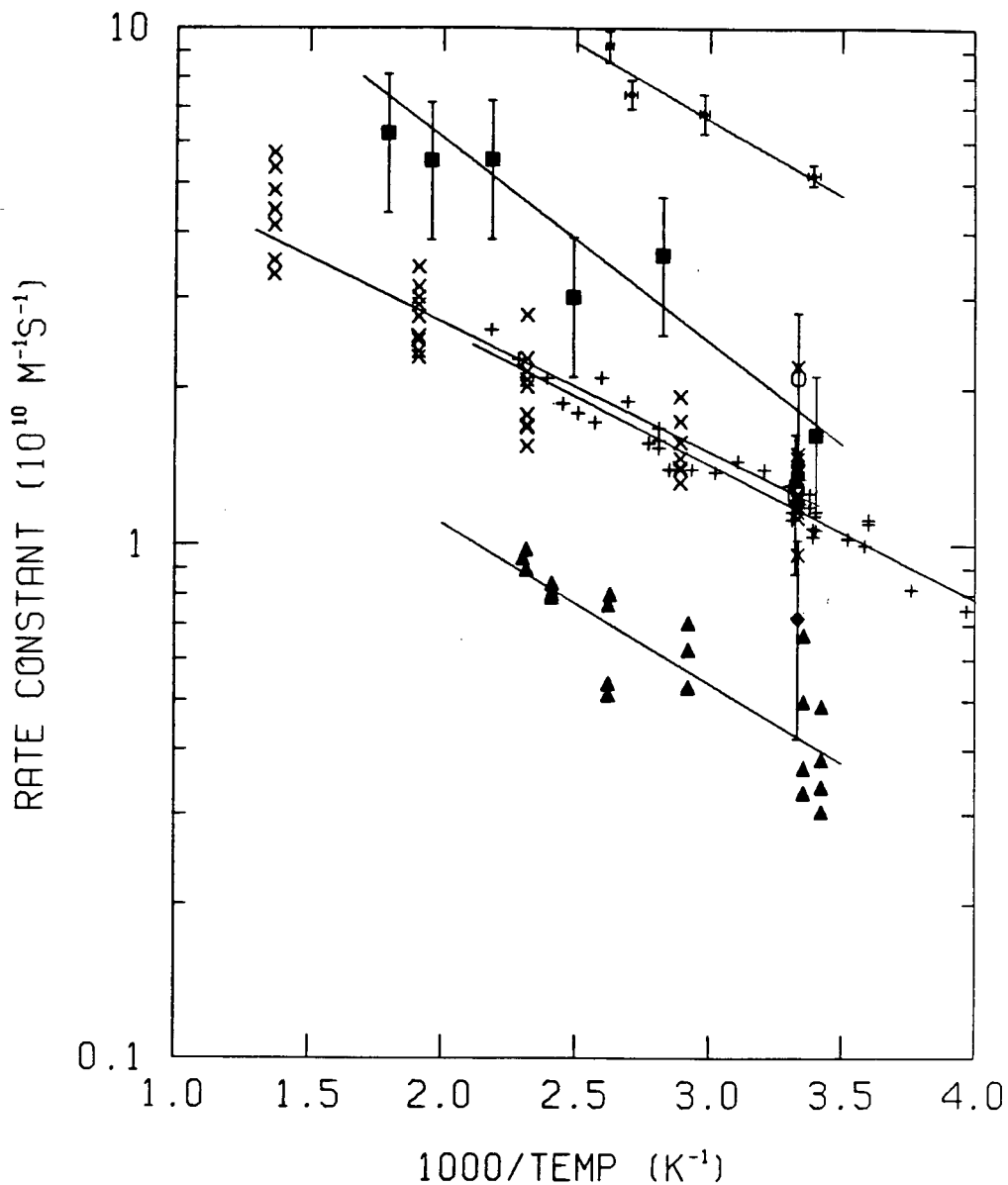


FIGURE 30: Experimental Arrhenius plot for the $Y + Cl_2$ reactions, $Y = Mu, H, D$. The Mu data is on the top line (this work). The H data is due to Stedman(70) (open octagon), Dodonov(70) (squares), Ambidge(76) (triangles), Wagner(76) (+), and Bemand(77) (x). The D datum is due to Stedman (70) (diamond). The error bars on the Mu data are statistical only.

moderator effects are detectable in the rate constant measurements. A χ^2 minimum fit to equation (12) using only the Ar moderator data yields $\log_{10} k(1/\text{mole-s}) = (11.78 \pm 0.14) - (320 \pm 50/T)$, consistent with the result reported above. As discussed in [Fleming 1-(77)], the 295 K reaction rate was measured both at LBL and TRIUMF using the same method but completely different equipment, yielding rate constants of (5.4 ± 0.2) and $(4.7 \pm 0.6) \times 10^{10}$ l/mole-s respectively. To date, this is the only measurement of the reproducibility of the MSR method in determining gas phase Mu reaction rates.

The $\text{H} + \text{Cl}_2 \rightarrow \text{HCl} + \text{Cl}$ reaction rate has been measured directly by several authors in the past 10 years; their results are compared with the Mu rates in Table XII and Figure 30. From the Table, the activation energies determined by the various investigators are in reasonable agreement; however, the rate constants and preexponential factors show some serious discrepancies. The two most recent results, due to Bemand et al. (77) and Wagner et al. (76), using Lyman- α fluorescence, are essentially identical to each other. The recent ESR measurements of Ambidge et al. (76), however, give a value of $k(300\text{K})$ a factor of three smaller and a value of A a factor of two smaller than the Lyman- α fluorescence results. Bemand et al. and Wagner et al. discuss the possible origins of the various experimental discrepancies and suggest that the ESR results of Ambidge et al. may be in error due to their use of a nearly equal H/Cl_2 stoichiometry which may lead to interferences due to Cl atom-wall reactions. In contrast, the Lyman- α fluorescence experiments used a Cl_2/H ratio varying from 5 - 15. The less sensitive, earlier mass spectrometric

TABLE XII: EXPERIMENTAL RATE PARAMETERS FOR THE REACTION: $Y + Cl_2 \rightarrow YCl + Cl$, $Y = Mu, H, D$

Isotope	Method	Temp (K)	E_a (kcal/mole)	$\log_{10} A$ ($M^{-1} s^{-1}$)	$k(300K)$ ($10^{10} M^{-1} s^{-1}$)	$\frac{k_{Mu}}{k_{H(D)}}(300K)$	reference
Mu	MSR	295 - 384	1.36 ± 0.21	11.72 ± 0.14	5.3 ± 0.1	—	present work
H	ms [†]	294 - 565	1.8 ± 0.3	11.57 ± 0.04	1.8 ± 0.6	2.9 ± 1.0	Albright (69)
H	ms [†]	300	—	—	2.1 ± 0.7	2.5 ± 0.8	Stedman (70)
H	ESR	292 - 434	1.4 ± 0.2	10.66 ± 0.11	0.42 ± 0.04	13 ± 1.2	Ambidge (76)
H	Lf [§]	252 - 458	1.20 ± 0.14	10.94 ± 0.08	1.2 ± 0.1	4.4 ± 0.4	Wagner (76)
H	Lf [§]	300 - 750	1.14 ± 0.17	10.93 ± 0.07	1.3 ± 0.1	4.1 ± 0.3	Bemand (77)
D	ms [†]	300	—	—	0.72 ± 0.30	7.4 ± 3.1	Stedman (70)

[†] mass spectrometric fast flow

[§] Lyman- α fluorescence

measurements agree with the Lyman- α fluorescence results within the experimental error. It may also be noted from Table XII that Stedman et al. (70) measured the $D + Cl_2$ reaction rate at 300K mass spectrometrically.

Despite the variation in the measured H atom reaction rate data, two points clearly emerge from their comparison with the Mu reaction rate parameters: (1) in all cases, the apparent activation energies are the same within the experimental uncertainties, and (2) compared with the mass spectrometric H atom reaction rate constants at 300K, there is no rate enhancement for the Mu reaction beyond the temperature independent mass factor of 2.9 (Chapter III, p 113), or, if compared with the Lyman- α fluorescence results at 300K, the rate constant is enhanced by a factor of only 1.48 ± 0.14 beyond the factor of 2.9. (As previously mentioned, the anomalously large Mu:H rate constant ratio due to Ambidge et al. (76) appears to be in error). Furthermore, the rate constant ratios, Mu:H:D at 300K, are $2.7 \pm 0.9:1.0:0.34 \pm 0.18$ using the mass spectrometric H atom rate constants, or $4.3 \pm 0.4:1.0:0.58 \pm 0.24$ using the Lyman- α fluorescence H atom rate constants; these may be compared with the temperature independent mass factors of 2.9:1.0:0.72.

Clearly, there is no experimental evidence to indicate that Mu exhibits a substantial tunnelling advantage over the other H isotopes when reacting with Cl_2 , in sharp contrast to the $Y + F_2$ reaction. One possible explanation for this result is that none of the isotopic versions of the reaction display significant tunnelling at 300K. This possibility is supported by the Lyman- α fluorescence Mu:H:D rate constant ratios which

are very close to the classical mass factor ratios. This apparent classical behaviour can be understood in terms of the experimental indications of a relatively low quasiclassical threshold energy. Although there is no simple analytic relationship between activation energies and quasiclassical threshold energies, in the absence of strong dynamical contributions, such as tunnelling or the bottleneck effect, the activation energy is very nearly equal to the quasiclassical threshold energy [Levine (74)]. Thus, a threshold energy of about 1.4 kcal/mole is indicated for the $Y + Cl_2$ reactions, which may be compared with the value of 2 kcal/mole for the $Y + F_2$ reactions and with $k_B T(300K) = 0.6$ kcal/mole. Clearly, the $Y + Cl_2$ reactions are much more capable of reacting classically at 300K than the $Y + F_2$ reactions, thereby minimizing the importance of tunnelling.

Indeed, the above hypothesis is confirmed by recent preliminary QCT calculations, performed on a newly optimized LEPS surface, which gives quasiclassical threshold energies for the collinear Mu and H reactions with $Cl_2(v=0)$ of 1.2 and 1.4 kcal/mole respectively [Laganà (79)]. Preliminary quantum calculations indicate a large reduction in tunnelling for the $Y + Cl_2$ reactions compared with the $Y + F_2$ reactions at 300K [Laganà (79)]. Topologically, the $Y + Cl_2$ LEPS surface used in these calculations closely resembles the $Y + F_2$ LEPS surface of Jonathan (72) with their saddle points placed in almost exactly the same relative positions. Of course, the $Y + Cl_2$ surface has a deeper reactant valley and a shallower product valley (see Table V) than the $Y + F_2$ reaction. The most

significant difference between these $Y + Cl_2$ and $Y + F_2$ surfaces is their classical barrier heights: ~ 1.5 kcal/mole for the $Y + Cl_2$ surface compared with 2.35 kcal/mole for the $Y + F_2$ surface [Jakubetz 1-(78)]. Again, the reduced tunnelling enhancement for the $Y + Cl_2$ reactions at 300K is consistent with this low reaction barrier which allows a large fraction of trajectories to proceed to reaction classically. It should be noted that this smaller $Y + Cl_2$ barrier also explains the observation that the $Y + Cl_2$ reactions proceed faster than the corresponding $Y + F_2$ reactions.

The preliminary calculations of Laganà (79) also indicate that the onset of non-reactive back reflection of the representative points off the product valley wall occurs at $E_{trans}^{QC} < 2.0$ kcal/mole for the $Mu + Cl_2 (v=0)$ reaction, whereas for the other H isotopes it occurs at $E_{trans}^{QC} \gg 3.5$ kcal/mole. This is an interesting contrast to the $Y + F_2 (v=0)$ reaction where this phenomenon does not occur until $E_{trans}^{QC} = 7$ and 40 kcal/mole for Mu and H respectively - collision energies which are certainly unimportant even at 1000K. The effect of wall reflection is to reduce the reaction probability, P_s^t , from unity. Calculations are presently being undertaken to determine how much the $Mu + Cl_2$ reaction rate is reduced due to wall reflection [Laganà (79)]. Qualitatively, it is clear that for this reaction, wall reflection will tend to offset tunnelling more and more with increasing temperature. Thus, it appears that the value of k_{Mu}/k_H at 300K is less for the Cl_2 reaction than for the F_2 reaction, not only because of the reduced importance of tunnelling due to the smaller reaction barrier, but also

because some of the tunnelling that does occur is cancelled due to classical wall reflection. There are other interesting consequences of this wall reflection phenomenon. As the temperature is raised and the centroid of the Boltzmann distribution shifts toward energies where wall reflection dominates, the rate of increase in $k(\text{Mu} + \text{Cl}_2)$ will fall and eventually, at sufficiently high temperatures (perhaps 1000K), $k(\text{Mu} + \text{Cl}_2)$ itself will actually decrease. One might therefore expect the activation energy of this reaction to pass through a maximum as it passes from the low temperature tunnelling-dominated region to the high temperature wall reflection-dominated region.

It is interesting to speculate on the reason for the dramatic reduction in the minimum collision energy for the onset of wall reflection in going from F_2 to Cl_2 . According to the Connor mass weighting scheme (p 73), changing the mass of X_2 from F_2 to Cl_2 further contracts the product valley by about 26% for each H isotope. While this greater contraction in the $\text{Y} + \text{Cl}_2$ product valley undoubtedly enhances wall reflection quite significantly, it seems unlikely that this alone accounts for the reduction in the wall reflection "threshold", from 7 kcal/mole for $\text{Mu} + \text{F}_2$ to 2 kcal/mole for $\text{Mu} + \text{Cl}_2$, for example. It is likely that the exothermicity of the reactions also plays an important role. For the $\text{Y} + \text{F}_2$ reaction, the bottom of the product valley lies about 106 kcal/mole below the classical barrier, whereas for the $\text{Y} + \text{Cl}_2$ reaction the product valley is only about 50 kcal/mole below the classical barrier. Since the saddle points for the two reactions lie

at about the same positions relative to the reactant and product valleys, it is clear that the force tending to make the representative point "round the corner" and "bobsled" down the product valley is greater on the steeper $Y + F_2$ surface than on the more gently sloped $Y + Cl_2$ surface. Finally, since the angle of reflection is equal to the angle of incidence, it is likely that the fact that the skewing angle for the mass weighted $Mu + Cl_2$ surface is about 1 degree more than for the $Y + F_2$ surface also makes a minor contribution in reducing the $Mu + Cl_2$ wall reflection threshold.

Before closing this Section, it should be remarked that the role played by the experimental Mu reaction rate measurements in the development of the theoretical calculations of Connor et al. is quite different for the F_2 and Cl_2 reactions. In the former case, the reasonably accurate potential energy surface due to Jonathan (72), optimized for the $H + F_2$ reaction, existed before calculations were performed for the $Mu + F_2$ reaction. Thus, in this case, the experimental Mu reaction rate data provided a test of the quality of the theoretical predictions based on this surface. The first calculations, which were collinear QMT calculations, gave two main results: (1) the $Mu + F_2$ reaction is dominated by quantum tunnelling, and (2) despite the facts that the $Mu + F_2$ reaction rates were calculated using a "line of no return" method (p 139) and the calculations were only collinear, the QMT results seemed to predict the ratio k_{Mu}/k_H and the activation energies quite accurately. Next, QCT calculations showed that (1) the classical (high temperature) $Y + F_2$ reaction rates are governed

by the bottleneck effect and (2) wall reflection is unimportant up to 1000K, thereby explaining the success of the "line of no return" method. Finally, it was discovered that simple Eckart tunnelling corrected VA-TST worked well for the $Y + F_2$ reactions, and, more importantly, the success of this method could be understood in terms of the very early reaction barrier and the favored collinear geometry.

The natural next theoretical step was to make similar calculations for the $Y + Cl_2$ reactions to determine if the conclusions previously drawn could be generalized for light-heavy-heavy atom reactions with early barriers. Unfortunately, unlike the Jonathan surface for the $Y + F_2$ reactions, no accurate experimentally optimized potential energy surface existed for the $Y + Cl_2$ reactions. Two very similar LEPS surfaces due to Kuntz et al. (66) and Baer (74) have been used in several investigations of the $H + Cl_2$ reaction (eg. [Wilkins (75), [Essén (76)], [Truhlar (78)]), but the primary aim of these studies has been to compare computational methods [Truhlar (79)], such as TST versus QMT, rather than to model experimental results. Jakubetz (79) used the Kuntz surface to test if tunnelling corrected VA-TST gives comparable estimates for the QMT calculations for the $H + Cl_2$ reaction and for the $H + F_2$ reaction, or if there are some unforeseen kinematic effects due to the change in X_2 mass from F_2 to Cl_2 . Arrhenius plots of the tunnelling corrected VA-TST rate constants for the $Y + Cl_2$ reaction, calculated on the Kuntz surface, are compared with those for the $Y + F_2$ reaction, calculated on the Jonathan surface, in Figure 31. As expected for the $H + Cl_2$ reaction,

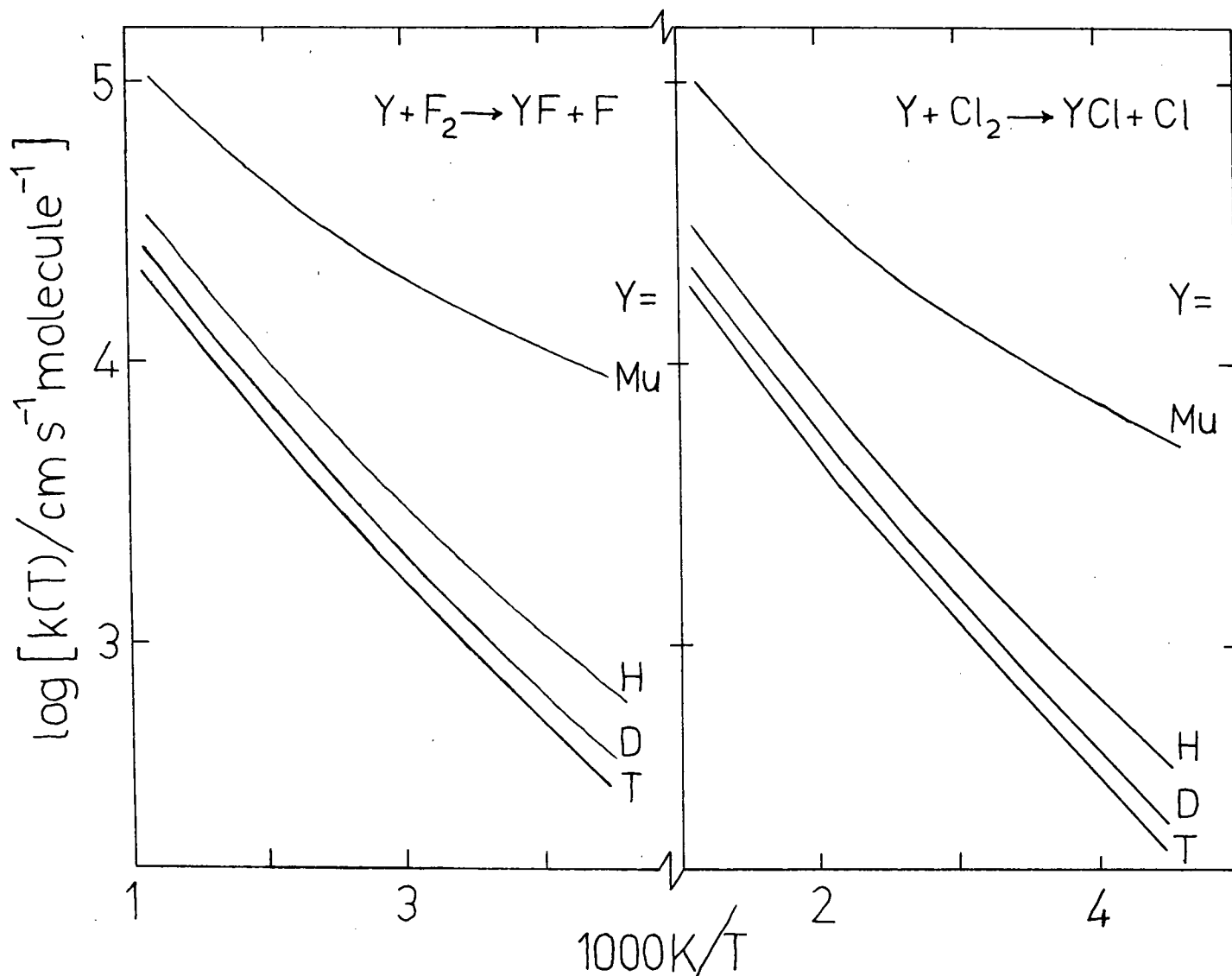


FIGURE 31: Arrhenius plots for collinear $Y + F_2$ and $Y + Cl_2$, for Boltzmann distributed reactants, calculated by tunnelling²corrected Eckart barrier VA-TST, adapted from Jakubetz (79). LEPS surface due to Jonathan (72) used for $Y + F_2$, LEPS surface due to Kuntz (66) used for $Y + Cl_2$.

tunnelling corrected VA-TST is as good as QMT. However, these calculations do rather poorly in reproducing the experimental results. For example, the predicted rate constant ratio, $k_{\text{Mu}+\text{Cl}_2}/k_{\text{H}+\text{Cl}_2}$, is 7.7 compared with the experimental value of 4.3 ± 0.4 at 300K. Furthermore, at 300K the $\text{Mu} + \text{Cl}_2$ and $\text{H} + \text{Cl}_2$ activation energies are calculated to be 1.4 and 2.4 kcal/mole respectively, compared with the experimental values of about 1.4 kcal/mole for both. In fact, these predictions are quite similar to those for the $\text{Y} + \text{F}_2$ reaction. This result is not unexpected since the Kuntz surface, which is known to be inaccurate, is very similar to the Jonathan surface, with classical barriers of 2.42 and 2.35 kcal/mole for the Kuntz and Jonathan surfaces respectively. Besides underlining the deficiency of the Kuntz surface, the calculations of Jakubetz suggest that tunnelling corrected VA-TST is also essentially applicable to the $\text{Y} + \text{Cl}_2$ reactions, where $\text{Y} = \text{H}, \text{D},$ and T ; for $\text{Y} = \text{Mu}$, this inference could not be made since no quantum calculations were available for comparison.

From this point, the calculations on the $\text{Y} + \text{Cl}_2$ reactions have been proceeding in the reverse order to the $\text{Y} + \text{F}_2$ reactions. First, Jakubetz used tunnelling corrected VA-TST to "tune" the calculation of an optimized $\text{Y} + \text{Cl}_2$ surface. Jakubetz found that by reducing the barrier height from 2.4 to 1.5 kcal/mole, the rate constant ratio, $k_{\text{Mu}}/k_{\text{H}}$, at 300K became 4.1, in good agreement with the experimental result. It has been noted by Connor 1-(78), that a much stronger constraint is placed on the choice of a potential energy surface by the $k_{\text{Mu}}/k_{\text{H}}$ ratio than by the activation energies.

The details of the newly optimized Y + Cl₂ surface are currently in press [Connor 3-(79)]. In this way, the experimental rate constant measurements of the Mu + Cl₂ reaction have been used to optimize the Y + Cl₂ surface, rather than to test the quality of the theoretical predictions. Consequently, it is inappropriate to call any of the subsequently calculated values of the Mu + Cl₂ reaction rates "predictions." However, as this Section has shown, theoretical calculations using this new surface are able to explain the origins of the experimental results by such effects as the reduction in tunnelling and increase in wall reflection. It may be noted that the preliminary results discussed in this Section on wall reflection suggest that the "line of no return" method may not be applicable to the Mu + Cl₂ reaction. Since TST implicitly also makes use of a "line of no return" (the so-called "dividing surface"), TST may also fail for muonium at high temperatures.

C Mu + Br₂ → MuBr + Br

The MSR relaxation rates at various Br₂ concentrations, measured in argon moderator at 295K, are listed in Table XIII and plotted in Figure 32. The bimolecular rate constant at 295K, determined by χ^2 minimum fits of the relaxation rate data to equation II(3), is [Fleming (76), 2-(77)]

$$k(295K) = (2.4 \pm 0.3) \times 10^{11} \text{ l/mole-s.} \quad (1\sigma)$$

Details of this Mu reaction rate measurement, which was conducted at LBL, are given in Fleming (76). As shown in the Figure and Table, two of the MSR relaxation rates are anomalously large; these points were taken during a time of known

TABLE XIII: MSR RELAXATION RATES FOR THE REACTION $\text{Mu} + \text{Br}_2 \rightarrow \text{MuBr} + \text{Br}$ [§]

$[\text{Br}_2]$ (10^{-6}M)	Relaxation Rate λ (μs^{-1}) [†]
0.0	0.19 ± 0.03
0.0	0.17 ± 0.04
1.74 ± 0.23	0.72 ± 0.12
2.19 ± 0.24	0.71 ± 0.06
2.95 ± 0.32	0.98 ± 0.10
3.45 ± 0.44	1.21 ± 0.15
4.13 ± 0.45	1.11 ± 0.10
5.75 ± 0.61	1.43 ± 0.16
7.73 ± 0.81	2.22 ± 0.25
1.02 ± 0.09	1.46 ± 0.20 [*]
4.25 ± 0.55	3.47 ± 0.58 [*]

[§] data from [Fleming (76)].

[†] relaxation rates reported are weighted averages of the left and right positron telescope histograms.

^{*} points taken with poor magnetic field regulation (see text)

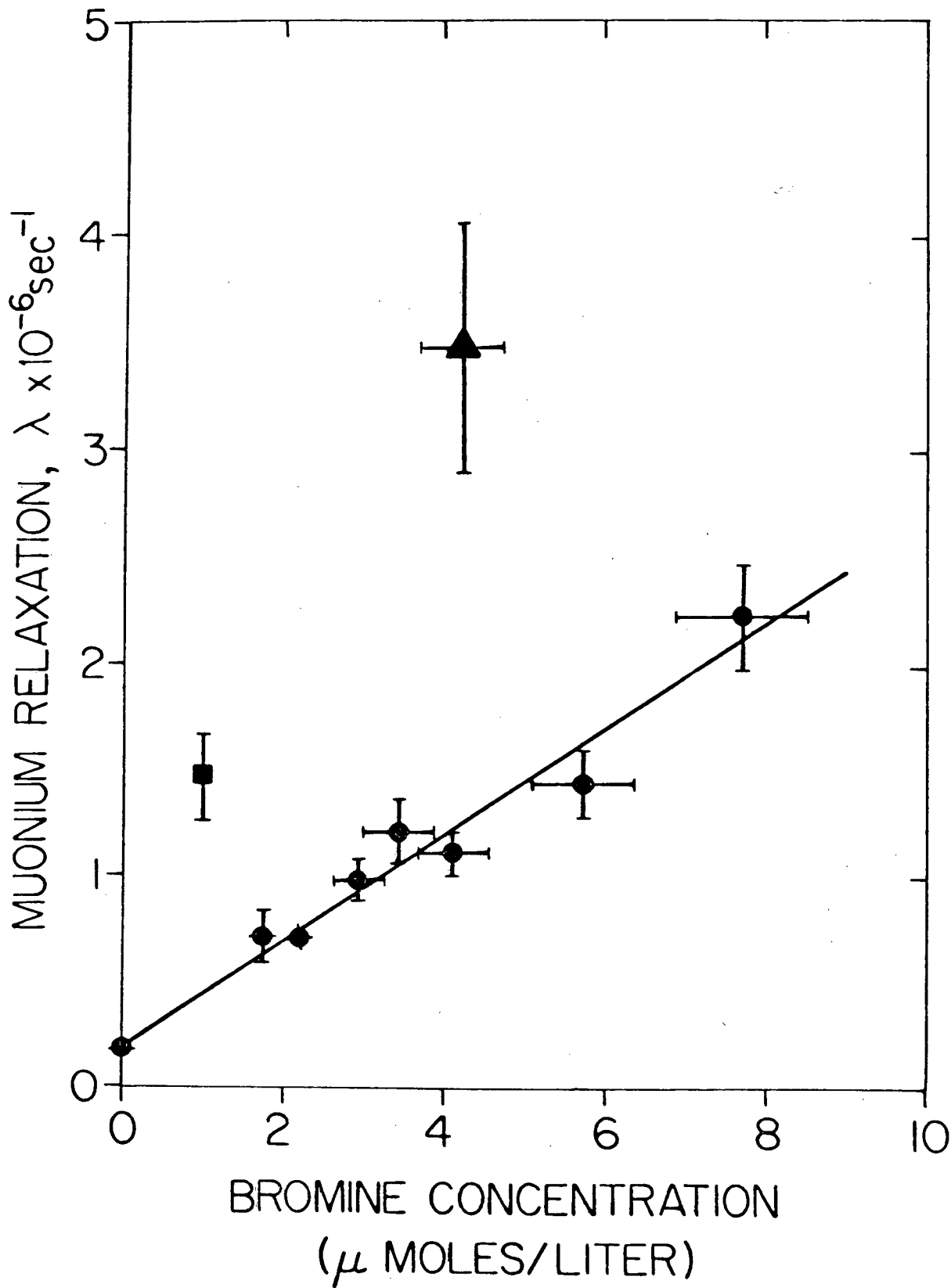


FIGURE 32: MSR relaxation rates as a function of Br_2 concentration in argon moderator at 295K; data taken at LBL during 1975 [Fleming (76)]. The high points are discussed in the text.

poor magnetic field regulation due to an unstable power supply. This serves to illustrate the fact that magnetic field inhomogeneities contribute to the background relaxation rate, λ_0 , in pure inert moderator gas. To ensure that such effects do not interfere with the Mu reaction rate measurements, λ_0 is periodically checked during the experiments. It is also noted that the Br_2 concentrations are not as precisely determined as the concentrations of the other gases studied in this thesis; these were determined from $\text{Br}_2(1)$ vapour pressures, for which reported values vary by up to 30% [Nesmeinov (63)].

Insofar as it is known, the bimolecular thermal rate constant for the $\text{H} + \text{Br}_2$ reaction has never been directly measured, although it is currently being investigated with Lyman- α fluorescence [Clyne (79)]. From a literature survey [Fleming (76)], it has been estimated that $k_{\text{H}}(295) = (2.2 \pm 1.5) \times 10^{10}$ l/mole-s and $k_{\text{D}}(295) = (6.1 \pm 3.2) \times 10^9$ l/mole-s, which gives rate constant ratios at 295K of Mu:H:D = 11 \pm 8: 1.0: 0.3 \pm 0.2. Perhaps more reliable estimates of these reaction rate constants can be obtained by combining recent direct ESR measurements of the rate constants for $\text{H} + \text{HBr} \rightarrow \text{H}_2 + \text{Br}$ and $\text{D} + \text{DBr} \rightarrow \text{D}_2 + \text{Br}$ [Endo (76), Takacs (73)] with earlier photolysis measurements of the ratios of these rate constants to those for the $\text{H} + \text{Br}_2$ and $\text{D} + \text{Br}_2$ reactions [Fass (70), (72)]. For H at 295K, $k(\text{H} + \text{HBr}) = (2.2 \pm 0.2) \times 10^9$ l/mole-s [Endo (76)] and $k(\text{H} + \text{Br}_2)/k(\text{H} + \text{HBr}) = 22.7 \pm 2.3$ [Fass(70)], which gives $k(\text{H} + \text{Br}_2) = (5.1 \pm 0.6) \times 10^{10}$ l/mole-s. For D at 295K, $k(\text{D} + \text{DBr}) = (8.0 \pm 1.0) \times 10^8$ l/mole-s [Endo (76)] and $k(\text{D} + \text{Br}_2)/k(\text{D} + \text{DBr}) = 58 \pm 1.7$

[Fass (72)] which gives $k(D + Br_2) = (4.6 \pm 0.6) \times 10^{10}$ l/mole-s. Using these results, the rate constant ratios at 295K are $Mu:H:D = 4.7 \pm 0.8:1.0:0.9 \pm 0.2$ compared with the temperature independent values of 2.9:1.0:0.72.

Like the rate constants, the activation energies for the $H + Br_2$ and $D + Br_2$ reactions are not well-known, though they are known to be small [Blais (74)]. Again, the direct ESR measurements of Endo may be combined with the photolysis results of Fass to give estimates of the $H + Br_2$ and $D + Br_2$ activation energies. For H, $E_a(H + HBr) = 2.6 \pm 0.1$ kcal/mole [Endo (76)] and $E_a(H + HBr) - E_a(H + Br_2) = 0.8 \pm 0.3$ kcal/mole [Fass (70)] which gives $E_a(H + Br_2) = 1.8 \pm 0.4$ kcal/mole. Similarly for D, $E_a(D + DBr) = 1.7 \pm 0.1$ kcal/mole [Endo (76)] and $E_a(D + DBr) - E_a(D + Br_2) = 0.9 \pm 0.2$ kcal/mole [Fass (72)], which gives $E_a(D + Br_2) = 0.8 \pm 0.3$ kcal/mole. However, recent molecular beam results of Hepburn et al. (78) suggest $E_a \leq 1$ kcal/mole for both the H and D reactions with Br_2 .

Without directly determined rate parameters for the $H + Br_2$ and $D + Br_2$ reactions and an activation energy measurement for the $Mu + Br_2$ reaction, it is difficult to speculate on isotope effects in this reaction family. From the estimated D:H rate constant ratio of 0.9 ± 0.2 , which is 1.3 ± 0.3 times the temperature independent mass factor of 0.72, there appears to be an "inverse" isotope effect at room temperature, if, in fact, there is any difference at all. At collision energies greater than the classical barrier height (estimated to be about 1 kcal/mole [Hepburn (78)]), this effect seems to be well-established in the reaction cross section measurements

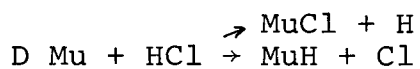
of Hepburn et al. (78) and in the trajectory calculations of Malcolme-Lawes (78) and White (73). This has been explained classically [White (73), Hepburn (78)] in terms of non-reactive back reflection of the representative points off the repulsive wall of the contracted product valley, which has been discussed for the Mu reactions with F_2 and Cl_2 . An equivalent way of picturing this effect without explicitly referring to potential surfaces, is to note that chemical reaction requires momentum transfer between the light attacking atom and the heavy parting product molecule; but in the case of $H + Br_2$ this has little time to occur because the H atom moves much faster than the heavy Br atoms. At a given value of E_{trans} , the $H - Br_2$ collision is about $\sqrt{2}$ faster than the $D - Br_2$ collision, and thus $H + Br_2$ has a lower reaction cross section. Indeed, Hepburn et al. (78) found that for $E_{trans} \geq 1$ kcal/mole, the $H + Br_2$ and $D + Br_2$ cross sections are coincident when plotted as a function of relative collision velocity rather than energy.

As discussed in the preceding Section, the reduction in the wall reflection threshold for the H - halogen reaction, from 40 to ≈ 1 kcal/mole as X_2 changes from F_2 to Br_2 , can probably be attributed to three factors: (1) according to the Connor mass weighting scheme, the product valleys for the $Y + Br_2$ reactions are about 50% narrower than for the $Y + F_2$ reactions, (2) the "down hill" part of the potential surface is about 106 kcal/mole for $Y + F_2$ compared with about 45 kcal/mole for $Y + Br_2$, and (3) the skewing angle for $H + Br_2$ is 85° compared with 81° for the $H + F_2$ reaction. Also, if the Mok-Polanyi relationship holds (p 76), then the $H + Br_2$ barrier

is earlier than the $Y + F_2$ and $Y + Cl_2$ barriers, and thus the slope of the down hill part of the surface at the corner is probably less than it would be if the barrier were later (i.e. the $H + Br_2$ surface is more attractive, p 81); thus, there is even less of a tendency for the representative point to "round the corner."

Certainly, extrapolation of the theoretical predictions of the wall reflection thresholds for $Mu + F_2$ and $Mu + Cl_2$ to $Mu + Br_2$ predicts that this effect will dominate the reaction rate for the latter system. In fact, one might expect the $Mu + Br_2$ reaction to be slower than the $H + Br_2$ reaction at 300K and that the estimated ratio: $k_{Mu}/k_H(300K)$ is in error. However, it must be cautioned that when the Boltzmann distribution is taken into account, the reaction cross sections at collision energies less than 1 kcal/mole (where there may be no wall reflection) have a strong influence on the thermally averaged reaction rates at room temperature. While these low energy cross sections for $Y + Br_2$ are as yet unknown, they should be much larger than for the F_2 or Cl_2 reactions because of the very low classical barrier and the fact that the collinear reaction geometry does not dominate this reaction [Baybutt (78), Bauer 1-(78), Blais (74)]. On the other hand, it cannot be expected that quantum tunnelling greatly enhances the $Mu + Br_2$ reaction rate at 300K since the barrier is so low. As discussed for the $Mu + Cl_2$ reaction, one might predict that the $Y + Br_2$ reaction apparent activation energies pass through a maximum as they change from the low temperature tunnelling region (if one exists) to the high temperature wall reflection region.

If it turns out that the apparent activation energy for the $\text{Mu} + \text{Br}_2$ reaction is less than that for $\text{H} + \text{Br}_2$ at 300K, then this would not necessarily indicate tunnelling, unlike the case of the F_2 reaction.



In Chapter III, p 98, it is noted that it is not yet possible to determine the individual reaction rate constants for the exchange and abstraction reaction channels for the $\text{Mu} + \text{HX}$ reactions by the MSR method - only the total reaction rate constants are measured. The MSR relaxation rates at various HCl concentrations, measured in N_2 moderator at 295K, are listed in Table XIV and illustrated in Figure 33. A χ^2 minimum fit of the relaxation rate data to equation II(3) yields a bimolecular rate constant

$$k(295\text{K}) \leq (3.41 \pm 0.46) \times 10^5 \text{ l/mole-s} \quad (1\sigma)$$

The rate constant for this very slow reaction is written as an inequality to emphasize the fact that it only represents an upper limit. There are two reasons why this experiment only gives an upper limit to the rate constant. (1) MSR relaxation rates are known for only two HCl concentrations, one of which is pure HCl at one atmosphere. Moreover, because of the reduced MSR signal amplitude (Table XIV and Figure 34) for these data and their small MSR relaxation rates, any systematic errors introduced to the measurements could easily exceed the statistical error in the rate constants. Thus, the data is both sparse and inherently unreliable. (2) More importantly, a known, estimable systematic error can account for half of

TABLE XIV: MSR RELAXATION RATES FOR THE TOTAL Mu + HCl
REACTION AT 295K

[HCl] (10 ⁻² M)	Relaxation Rate [†]		Total [§]	
	λ (μs^{-1})	A _{Mu} (%)	A _{μ} (%)	(%)
0.0	0.40 \pm 0.04	12.2 \pm 0.4	4.0 \pm 0.4	28.4 \pm 1.2
2.92 \pm 0.11	1.66 \pm 0.39	8.9 \pm 1.3	7.0 \pm 0.7	24.8 \pm 3.3
4.33 \pm 0.12	1.79 \pm 0.26	5.9 \pm 0.6	9.7 \pm 0.3	21.5 \pm 1.4

[†] relaxation rates reported are weighted averages of the left and right positron telescope histograms.

[§] total asymmetry = $2A_{\text{Mu}} + A_{\mu}$ (see Appendix II)

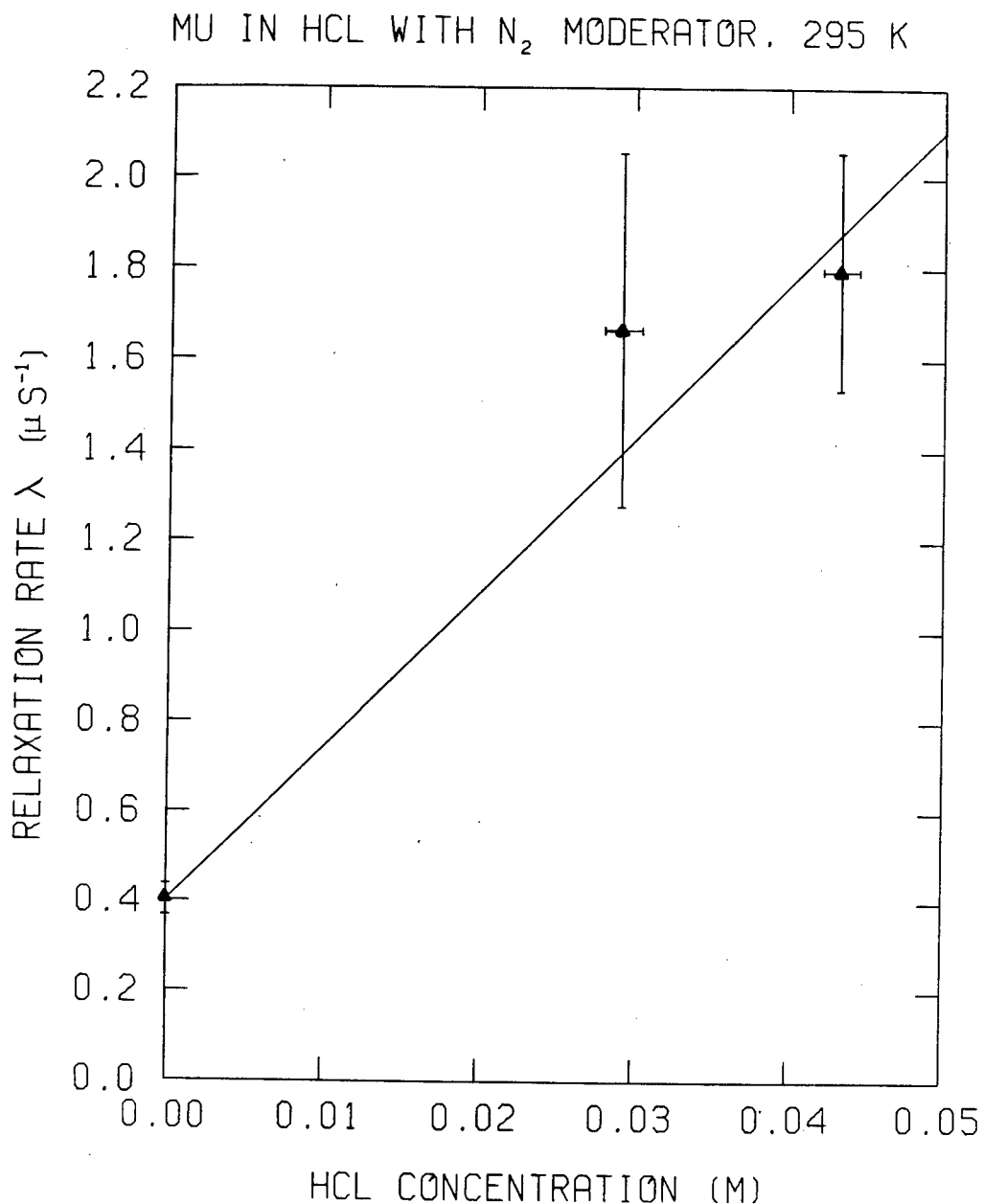


FIGURE 33: MSR relaxation rates as a function of HCl concentration in N₂ at 295K. The high concentration point represents 1 atmosphere of pure HCl. The line is a χ^2 minimum fit of the data yielding $k(295K) \leq (3.41 + 0.46) \times 10^5$ M⁻¹ s⁻¹. These data represent only an upper limit, as described in the text.

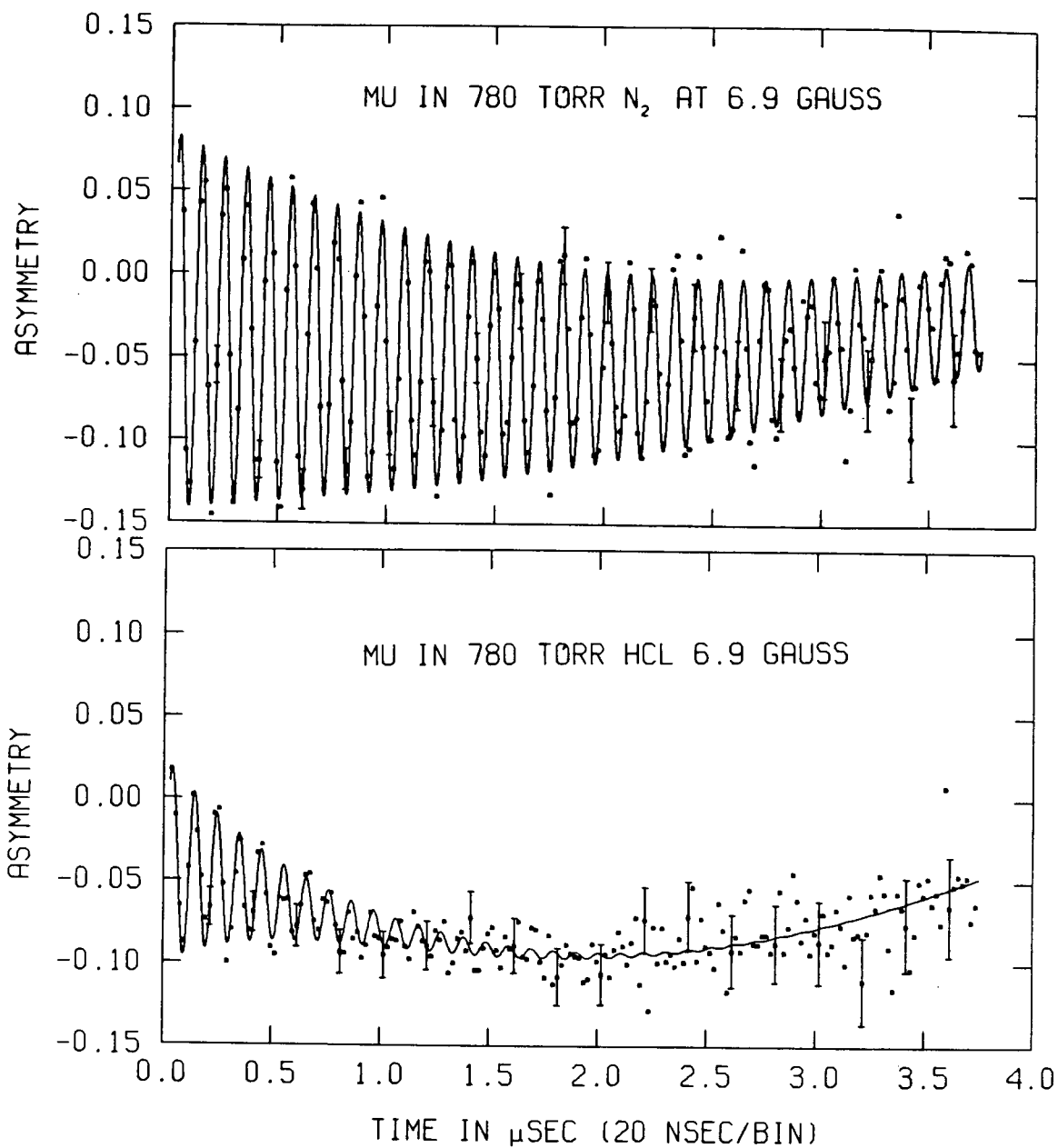


FIGURE 34: The MSR signals in pure N₂ versus pure HCl. Both spectra represent about 10⁶ events. The lines are χ^2 minimum fits to equation (8). For N₂, $A_{\text{Mu}} = 12.2\%$, $A_{\mu} = 4.0\%$, $\lambda = 0.4 \mu\text{s}^{-1}$; for HCl, $A_{\text{Mu}} = 5.9\%$, $A_{\mu} = 9.7\%$, and $\lambda = 1.8 \mu\text{s}^{-1}$.

the observed MSR relaxation. The anhydrous HCl reagent used in this experiment, obtained from Canadian Liquid Air Ltd., has a typical O₂ impurity of <100 ppm. Mu undergoes spin exchange with paramagnetic oxygen which relaxes the MSR signal with a bimolecular rate constant of $(1.6 \pm 0.1) \times 10^{11}$ l/mole-s in the gas phase [Fleming (79), Marshall (78)]. An O₂ concentration of 100 ppm in one atmosphere of HCl gives a spin exchange MSR relaxation rate of about $0.7 \mu\text{s}^{-1}$, half of the observed effect. The experiment must be repeated with electronic grade HCl which has an O₂ concentration of <4 ppm. It is important to emphasize that a similar systematic error due to O₂-contaminated reagents does not arise in the other systems studied in this thesis. In the first place, the O₂ contamination of the other gases used is <10 ppm and, secondly, all of the other reaction rate constants are within two orders of magnitude of the O₂ spin exchange rate constant. Consequently, the systematic error due to O₂ contamination in the X₂ and HX gases (other than HCl) is less than 0.1%.

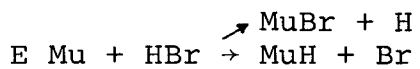
It may be noted that in addition to providing an estimate of the thermal Mu + HCl reaction rate constant, this experiment possibly gives some information about the muonium formation process or the role played by "hot" atom reactions of Mu. As illustrated in Figure 34, the muonium signal amplitude in pure HCl is about half of that in pure N₂ under identical conditions. As shown in the data of Table XIV, the reduction in the muonium signal with increasing HCl concentration is accompanied by an increase in the background "free" μ^+ signal amplitude. These data may be explained in two ways: (1) Mu may undergo fast

hot atom reactions with HCl before the muon spin has time to precess significantly, thereby placing muons into diamagnetic product molecules where they precess coherently like "free" μ^+ ions (see Appendix II), or (2) the high energy charge exchange cross sections of Mu with HCl may be such that a large fraction of the muons thermalize as free μ^+ ions, rather than as Mu atoms. The total signal amplitude, given by $2A_{\text{Mu}} + A_{\mu^+}$, appears to decrease with increasing HCl concentration; unfortunately, these data cannot be treated quantitatively, since the "free" μ^+ signal amplitudes result from fits of data covering only about one period of the slow μ^+ precession at 6.9 gauss. Again, further experiments are required to clearly interpret these effects. In principle, it is possible to distinguish the hot atom process from the charge exchange process by the use of the residual polarization method (Appendix II, and [Brewer (72)]). It must be emphasized that the limiting rate constant for Mu + HCl reported in this Section is for the thermal reaction, not the hot atom reaction. Hot atom reaction processes take place during the first several nanoseconds of the muon's entry into the target, whereas the MSR signal relaxation is measured over several microseconds.

As discussed in Chapter III, the experimental and theoretical situation with respect to the H + HCl abstraction and exchange reactions is rather confused. An excellent review of these reactions has recently been prepared by Weston (79). For the $\text{H} + \text{HCl} \rightarrow \text{H}_2 + \text{Cl}$ reaction, Weston (79) recommends values of $E_a = 3.18 \pm 0.17$ kcal/mole, $\log_{10} A(1/\text{mole-s}) = 9.87 \pm 0.11$ and $k(295\text{K}) = (2.1 \pm 0.2) \times 10^7$ 1/mole-s.

Although most experimental evidence indicates that the abstraction reaction is faster than the exchange reaction, this question remains unresolved [Weston (79)]. Bott and Heidner (76) measured the total reaction rate for $H + HCl$ directly by laser induced fluorescence and found $k(295K) = (9 \pm 4) \times 10^7$ l/mole-s. Since the rate constant reported here for the $Mu + HCl$ reaction is also a total rate constant, the Bott and Heidner H atom rate constant provides the most useful comparison giving k_{Mu}/k_H at 295K $\leq 0.004 \pm 0.002$. Even with the very large uncertainties in the H and Mu data, it is certain that the total Mu reaction rate with HCl is at least 100 times slower than the corresponding H atom rate! It is unnecessary to turn to fancy detailed theoretical calculations to explain this result. From Table V, it is seen that both reaction channels for Mu with HCl are endothermic: $\Delta H_0^0 = +6.2$ and $+7.9$ kcal/mole for abstraction and exchange respectively. In contrast, the $H + HCl$ reactions give $\Delta H_0^0 = -1.1$ and 0 kcal/mole for abstraction and exchange respectively. The classical barriers for these reactions, though poorly known, are thought to be ~ 4 kcal/mole for the abstraction reaction [Thompson (75)] and even more for the exchange reaction [Weston (79)]. However, even if the classical barriers were zero, Mu must overcome an enormous zero point energy barrier of at least 6.2 kcal/mole in order to react with HCl ; a barrier which is at least 6.2 kcal/mole greater than the reaction barrier for $H + HCl$. In the absence of reliable experimental data or theoretical calculations, it is impossible to check the general predictions on the $Y + Cl_2$

reactions given in Chapter III, p 97-109.



The MSR relaxation rates at various HBr concentrations, measured in Ar moderator at 295K, are listed in Table XV and illustrated in Figure II-2 (Appendix II). A χ^2 minimum fit of these relaxation rate data to equation II(3) yields a total bimolecular rate constant for the exchange plus abstraction reactions of

$$k(295\text{K}) = (9.09 \pm 0.97) \times 10^9 \text{ l/mole-s} \quad (1\sigma)$$

Insofar as it is known, Endo et al. (76) and Takacs et al. (73) have made the only direct measurements of the analogous H reaction rate using ESR detection of H atoms in a flow system. Their measurements, summarized in Table XVI, gave the rate parameters for the sum of the exchange plus abstraction channels for the four H and D variations of the Y + Y'Br reaction between 230 and 318K, as well as the rate constants for the H + DBr and D + HBr reactions at 295K from which the abstraction:exchange branching ratios are obtained. These measurements clearly show that for H and D, the abstraction reaction channels are much faster than the exchange reaction channels at room temperature. From the measured abstraction reaction activation energies and the estimated exchange reaction activation energy, it can be inferred that the classical barrier to abstraction is about 1.5-3 kcal/mole whereas the barrier to exchange is about 5 kcal/mole. In drawing this inference it must be cautioned that activation energies are approximately equal to the classical barrier heights only in

TABLE XV: MSR RELAXATION RATES FOR THE TOTAL Mu + HBr
REACTION AT 295K

[HBr] (10^{-4} M)	Relaxation Rate λ (μs^{-1}) [†]
0.00	0.27 \pm 0.04
0.77 \pm 0.07	0.92 \pm 0.09
1.50 \pm 0.03	1.60 \pm 0.26
2.85 \pm 0.08	2.56 \pm 0.71
4.49 \pm 0.10	4.76 \pm 0.94
5.92 \pm 0.13	6.66 \pm 1.20

[†] relaxation rates reported are weighted averages of the left and right positron telescope histograms.

TABLE XVI: EXPERIMENTAL RATE PARAMETERS FOR THE REACTIONS: $Y + Y'Br \rightleftharpoons YY' + Br$, $Y = Mu, H, D$; $Y' = H, D$

Reaction	E_a^\dagger (kcal/mole)	$\log_{10} A (M^{-1} s^{-1})$	$k(295K)$ (10^9 l/mole-s)	$\frac{k_{Y+HBr}}{k_{H+HBr}}(295K)$	ΔH_0^0 [type] (kcal/mole)
Mu+HBr \rightarrow products	_____	_____	9.09 ± 0.97	4.4 ± 0.6	-9.4 [abs] +7.1 [exc]
H+HBr \rightarrow products	2.57 ± 0.11	11.22 ± 0.05	2.08 ± 0.16	1.0	-16.7 [abs] 0 [exc]
D+HBr \rightarrow products	2.13 ± 0.08	10.59 ± 0.03	1.02 ± 0.05	0.49 ± 0.04	-17.5 [abs] -1.1 [exc]
				$\frac{k_{Y+DBr}}{k_{H+DBr}}(295K)$	
H+DBr \rightarrow products	2.19 ± 0.11	10.82 ± 0.04	1.57 ± 0.18	1.0	-16.4 [abs] +1.1 [exc]
D+DBr \rightarrow products	1.69 ± 0.13	10.14 ± 0.03	0.78 ± 0.11	0.50 ± 0.09	-17.4 [abs] 0 [exc]
				$\frac{k_{abs}}{k_{exc}}(295K)$	
D+HBr \rightarrow DBr+H	5.2^*	10^*	0.0078 ± 0.0024	137_{-32}^{+60}	
H+DBr \rightarrow HBr+D	_____	_____	≤ 0.023	>69	

† between 230 and 318K

* estimates based on the measured rate constant at 295K and high temperature molecular beam and photolysis data [Endo (76) and references therein].

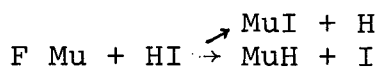
the absence of strong dynamical effects; as discussed on p 109, it is possible that the activation energies are governed by rotational screening of the H isotope. In fact, from the Table it appears that at 295K, the abstraction:exchange branching ratio for D + HBr is greater than for H + DBr. This is consistent with the rotational screening hypothesis since the D atom approaches the more quickly rotating HBr about $\sqrt{2}$ times slower than the H atom approaches the more slowly rotating DBr. As remarked on p 109, if rotational screening is important, it is expected that for Mu, the abstraction:exchange branching ratio will be smaller than for the other H isotopes at 295K due to the greater mean velocity of the lighter muonium atoms. On the other hand, it can be argued that the exchange channel for Mu + HBr should be very much suppressed because $\Delta H_0^0 = +7.1$ kcal/mole; this is the minimum exchange barrier for Mu + HBr. If the barrier heights estimated from the activation energies are correct, then the effective Mu + HBr exchange barrier is at least twice as large as the abstraction barrier; therefore, it seems reasonable to assume that the measured value of k for Mu + HBr essentially corresponds to the abstraction reaction channel only.

Table XVI gives the rate constant ratios Mu:H:D at 300K of $4.4 \pm 0.6:1.0:0.49 \pm 0.04$, which exceeds the temperature independent mass ratios by 1.52 ± 0.21 and 1.47 ± 0.12 for Mu:H and H:D respectively. Truhlar (79) has pointed out that tunnelling is expected to be more important for a given H + HX abstraction reaction than for the corresponding H + X₂ reactions, because the imaginary frequency of the unbound normal

mode vibration of the transition state tends to be much larger for the H + HX systems than for the H + X₂ systems (see Figure 18; in this Figure, the α parameter is inversely proportional to the imaginary frequency [Johnston (61)]). This is equivalent to saying that H + HX barriers tend to be narrower than the H + X₂ barriers. Assuming that the rate constant ratios reported above do correspond to abstraction, then they may be interpreted as an indication of tunnelling in this reaction. Since the barrier height for abstraction appears to be comparable to the H + F₂ barrier (~2 kcal/mole), by analogy it may also be expected that tunnelling will be important at 300K. Although the degree of tunnelling cannot be inferred from a set of rate constant ratios at one temperature, it appears that Mu and H tunnel comparable amounts when reacting with HBr at 295K. This is consistent with the discussion on p 105 where it is suggested that "corner cutting" might equalize the tunnelling advantage of the various isotopes due to the mass weighted coordinate skewing angles of 72°, 45°, 36°, and 31° for Mu, H, D and T respectively.

Table XVI shows the activation energies for the H reactions with HBr and DBr to be larger than those for D by about 25-30%. This result may be explained in terms of the vibrationally adiabatic barriers which should be considerably larger for the lighter H isotopes (see p 104 and Table V). On the other hand, this seems to contradict the tunnelling hypothesis just discussed, since, despite corner cutting, H is expected to tunnel more than D, thereby predicting smaller activation energies for H + HBr than for D + HBr. Of course,

the possibility always exists that the experimental data are in error. If it is assumed that these data are correct, then, in order to rationalize the two seemingly contradictory observations that even though H + HBr has a larger activation energy than D + HBr, H + HBr still reacts faster at 295K, it seems necessary to postulate that these systems have unusual excitation functions (i.e. cross section versus collision energy curves). It will be interesting to see if Mu + HBr also follows this trend by having a larger activation energy than H + HBr.



The MSR relaxation rates at various HI concentrations, measured in both argon and N₂ moderator gases at 295K, are listed in Table XVII and illustrated in Figure 35. A χ^2 minimum fit of these relaxation rate data to equation II(3) yields a total bimolecular rate constant for the exchange plus abstraction reactions of

$$k(295\text{K}) = (2.53 \pm 0.12) \times 10^{10} \text{ l/mole-s} \quad (1\sigma)$$

Insofar as it is known, the analogous H atom reaction rate has never been directly measured, and the indirect measurements that have been made are sparse and unreliable [Bauer 2-(78)]. For the abstraction reaction, Jones et al. (73) report $E_a = 0.7 \pm 0.25$ kcal/mole, $\log_{10} A$ (l/mole-s) = 10.7, and $k(295\text{K}) = (1.5 \pm 0.5) \times 10^{10}$ l/mole-s, based on the H₂/I₂ thermal reaction experiments of Sullivan (62) between 667 and 800K, which gives $k_{\text{Mu}}/k_{\text{H}} = 1.7 \pm 0.6$ when extrapolated to 295K. However, this estimate must represent some type of re-analysis of

TABLE XVII: MSR RELAXATION RATES FOR THE TOTAL Mu + HI REACTION AT 295K

[HI] (10^{-4} M)	Relaxation Rate $\lambda - \lambda_0$ (μs^{-1}) [†]
0.00	0.00 [*]
0.36 \pm 0.01	0.96 \pm 0.13 [*]
1.03 \pm 0.03	2.35 \pm 0.20 [*]
1.39 \pm 0.04	4.19 \pm 0.55 [*]
2.03 \pm 0.06	5.11 \pm 0.67 [*]
0.00	0.00 [§]
0.46 \pm 0.02	1.29 \pm 0.42 [§]
0.98 \pm 0.03	3.58 \pm 0.63 [§]
1.25 \pm 0.03	3.84 \pm 0.52 [§]

[†] relaxation rates reported are weighted averages of the left and right telescope histograms, given as $\lambda - \lambda_0$ to account for the slightly different background relaxation rates in argon and N₂.

[§] argon moderator

^{*} N₂ moderator

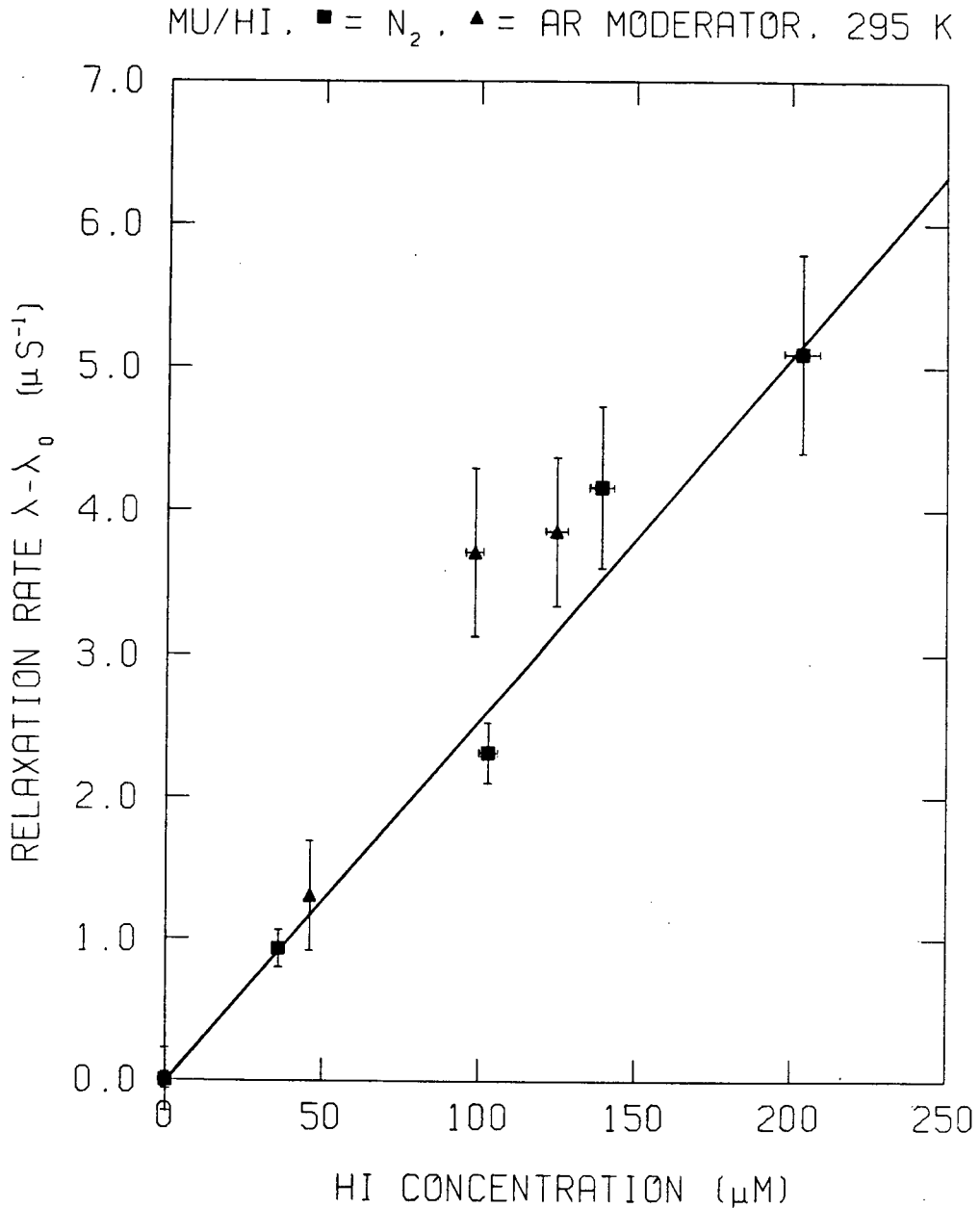


FIGURE 35: MSR relaxation rates as a function of HI concentration in argon (diamonds) and N₂ (squares). The data are plotted as $\lambda - \lambda_0$ to account for the small differences in λ_0 for each moderator gas. The line is a χ^2 minimum fit of the data yielding $k(295K) = (2.5 \pm 0.1) \times 10^{10} \text{ M}^{-1} \text{ s}^{-1}$.

Sullivan's data since the paper referenced reports $E_a = 0.0 \pm 0.25$ kcal/mole, $\log_{10} A(1/\text{mole-s}) = 9.05 \pm 0.07$ and $k(295\text{K}) = (1.1 \pm 0.2) \times 10^9$ 1/mole-s which gives $k_{\text{Mu}}/k_{\text{H}} = 23 \pm 4$ when extrapolated to 295K. Photolysis experiments of Persky and Kuppermann (74) give abstraction fractions ($k_{\text{abs}}/[k_{\text{abs}} + k_{\text{ex}}]$) = 0.95 ± 0.04 and 0.88 ± 0.08 for H + DI and D + HI respectively, which again, indicates that abstraction is much faster than exchange for these H-HX reactions. However, it should be cautioned that in an analogous experiment with HBr, the abstraction fractions indirectly obtained by Persky and Kuppermann (74) have the opposite ordering to the direct measurements of Endo (76).

Given the terrible experimental situation with these reactions, little can be said about the Mu + HI reaction and isotope effects. It appears that the reaction barrier for abstraction is very small, which explains why the Mu + HI rate constant is larger than the Mu + HBr rate constant. It also appears that $k_{\text{Mu}}/k_{\text{H}}$ at 295K for this reaction is greater than one, as expected, though this estimate is based on an extrapolation of very questionable data. Finally, based on the experimental results of Persky and Kupperman and invoking the endothermicity arguments of the previous Sections, it seems reasonable to again suggest that the abstraction reaction channel dominates the Mu + HI reaction at 300K. A measurement of the activation energy of Mu + HI at 300K would certainly represent a substantial increase in the available data on the Y + HI system.

CHAPTER V - SUMMARY AND CONCLUSIONS

A Summary

This thesis describes, in considerable detail, the present experimental and theoretical state of the study of gas phase muonium reaction kinetics. On the experimental side, it outlines most of the significant practical problems encountered in this study, details the currently implemented solutions to these problems, and makes some specific suggestions for further improvements. Particular attention is paid to coping with the data acquisition problems that arise in handling the high current beams produced by meson factories. On the theoretical side, the remarkably large body of calculations, mainly due to Connor, Jakubetz, Manz, and Laganà, provide detailed interpretations of the experimental results and establish the relevance of gas phase muonium reaction kinetics to the more conventional and more general fields of chemical kinetics and molecular reaction dynamics. Two main contentions are made: (1) that muonium provides an unusually useful tool with which to investigate hydrogen isotope effects, specifically in terms of the dynamics of the $Y + X_2$ and $Y + HX$ reactions, and (2) that the peculiar property of the MSR technique - that it literally examines one atom at a time - blesses it with some distinct advantages over conventional H atom studies. Thanks to the theoretical work of Connor et al., the experimental study of gas phase muonium reactions seems to have sparked progress in both the understanding of the $Y + F_2$ and $Y + Cl_2$ reactions and in the development of useful computational tools for dealing with them. However, more experimental data on the reactions of Mu and H are re-

quired in order to firmly establish the MSR method.

B. Past Perspective

Chapter I includes a brief historical summary that sketches the development of muonium chemistry in gases up to 1975; the discussion then takes a quantum leap by describing the present status of the subject. In many ways, this creates a distorted perspective which this Section shall attempt to correct. The work in this thesis took place during a time when the use of muons as probes of physical phenomena matured from seed to seedling - from well-demonstrated possibility to a serious, albeit still-developing, study. This is particularly true in the case of muonium chemistry which, in 1975, was rather neglected compared with the application of μ^+ SR to solid state physics. Indications of the maturation of gas phase muonium chemistry from 1975 to the present are many; Figure 36 provides a graphic example of its experimental development. The Figure is a reproduction of typical MSR signals obtained during the study of the $\text{Mu} + \text{Br}_2$ reaction at the Lawrence Berkeley Laboratory in 1975 [Fleming (76)]. With an average muon stopping rate of $2 \times 10^3 \text{ s}^{-1}$, these were necessarily low statistics runs of typically 1.5×10^5 events. Figure 36 may be compared with the TRIUMF spectra illustrated in Figure II-1, taken under much less primitive conditions. The early MSR experiments were characterized by an almost total preoccupation with gadgets and gizmos required to obtain muons and ultimately to obtain data

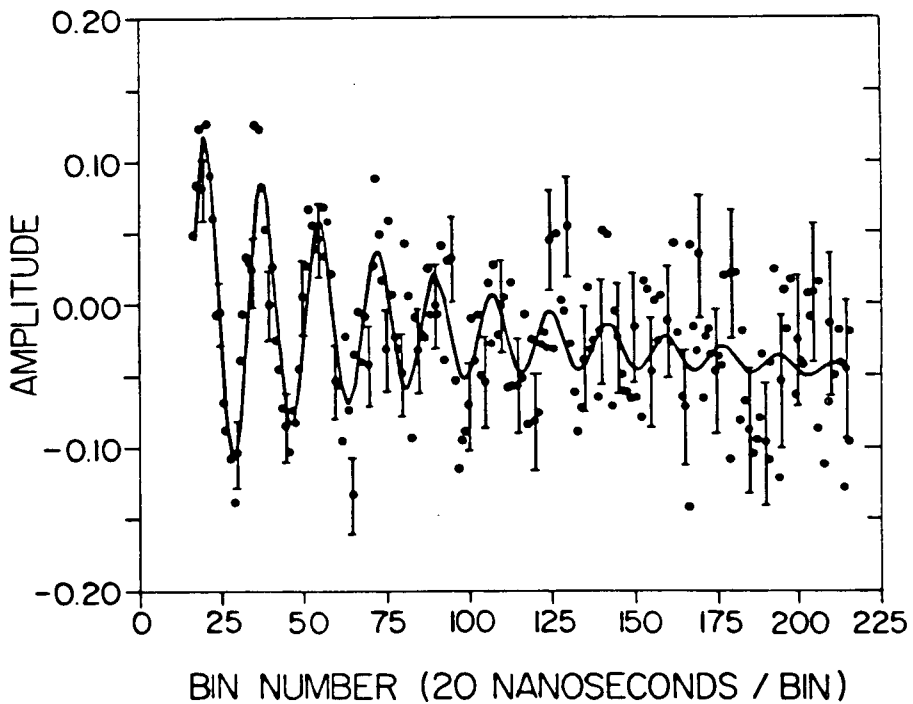
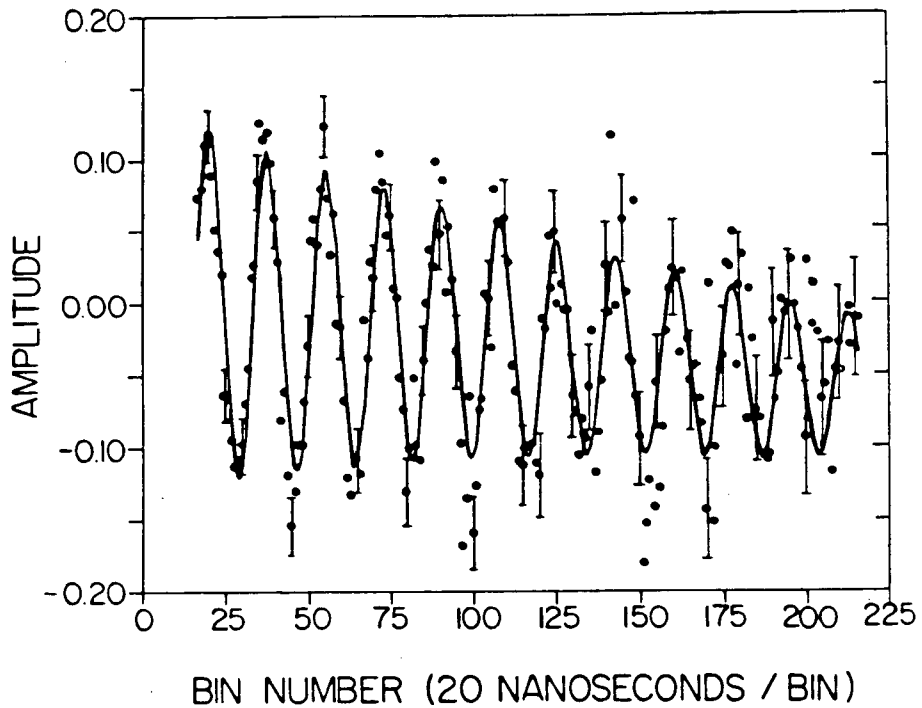


FIGURE 36: Gas phase MSR signals in a magnetic field of 1.8 gauss obtained at LBL in 1975. The target contained pure Ar (top) and Ar with ~ 10 ppm Br_2 (bottom) at 295K and one atmosphere pressure. The error bars are due to counting statistics only. Each histogram contains about 150×10^3 events. The line is a χ^2 minimum fit to an approximation of equation (8) [Fleming (76)].

from them; "doing physics"¹ seemed to play a subordinate role. At times it appeared that the possibility of having the cyclotron, beam lines, counters, electronics, and data acquisition computers all functioning simultaneously was little more than a fanciful dream. Today, the priorities are usually reversed. Getting muons and taking data are more-or-less routine; equipment breakdowns are less frequent and tend to be irritations rather than catastrophes. The bulk of the experimental effort now goes into designing more sophisticated targets with which to explore new and often more subtle phenomena.

This thesis work leaned heavily on the theoretical work of Connor et al., not only in order to explain the results, but also as a guide with which to formulate an experimental strategy. This happy symbiosis of theory and experiment came about by a fortunate chain of circumstance. The first publication of a low pressure gas phase reaction rate constant, for the $\text{Mu} + \text{Br}_2$ reaction [Fleming (76)], set forth the basis of the MSR technique and optimistically offered an experimentalist's view of its prospectus. Connor et al., who had just completed a theoretical QMT study of the collinear $\text{H} + \text{F}_2$ reaction [Connor 2-(76)], picked up on this Mu paper, decided to extend their calculations to include the Mu, H, D, and T reactions, and suggested that an experimental study of the $\text{Mu} + \text{F}_2$ reaction be carried out. Although experimental work was in progress on the other reactions reported in this thesis, there was reason to

¹ Around cyclotron facilities, one speaks of "doing physics" - saying "doing chemistry" invariably has an unsettling effect on the listener. "Scientists have odious manners, except when you prop up their theory; then you can borrow money from them."

Mark Twain, What is a Man and Other Essays, p 283.

believe that the $\text{Mu} + \text{F}_2$ reaction would be immeasurably slow, and, besides, the use of F_2 with the thin-windowed target apparatus would create formidable (probably insurmountable) problems. Fortunately, the theorists' judgement prevailed, and the experiment proved to be feasible. The preliminary theoretical calculations on the $\text{Mu} + \text{F}_2$ reaction [Connor 1-(77)] were completed a few months before the experiment [Garner (78)]. As discussed in Chapter IV, the theoretical calculations have since been revised and supplemented. Subsequently, the experimental and theoretical work has proceeded in parallel. Experimental results on the $\text{Mu} + \text{Cl}_2$ reaction [Fleming (79)] have been followed by TST calculations of Jakubetz (79), while QMT and QCT calculations are presently underway [Connor 2-(78)].

C Future Perspective

The experimental interest in gas phase muonium is by no means confined to the study of its thermal chemical reactions. At TRIUMF, programmes are in progress to examine the muonium formation process (μ^+ charge exchange) in various gases [R.J. Mikula and D.G. Fleming], muonium spin exchange with paramagnetic species [D.G. Fleming, R.J. Mikula, and D.M. Garner], and the production of thermal muonium in vacuum through the use of fine powdered insulators as a stopping medium [G.M. Marshall, R. Kiefel, and J.B. Warren]. It is highly likely that both the understanding of these phenomena and the development of experimental techniques with which to study them will have a mutual impact on the future studies of Mu chemical reaction rates.

It seems that the immediate objective of future gas phase

Mu reaction rate experiments ought to be to complete the present study. In particular, it is desirable to develop a new target reaction vessel that provides an operational temperature range of from about 200 - 600K, if possible, and to extend the rate measurements of the reactions studied in this thesis to span that temperature range. In conjunction with the analogous H atom reaction rate data, this would provide a very complete set of isotopic rate parameters for two dynamically different classes of elementary chemical reactions. For the $Y + X_2$ reactions (if possible, X should be extended to include I), this temperature range should be sufficient to check the predicted Arrhenius plot curvature, thereby placing a firmer experimental handle on the reaction dynamics. In changing X from F to I, the reaction dynamics should gradually shift from collinear domination to the full three dimensional reaction which may dramatically affect the H isotope effects. As already described, the $Y + HX$ reactions are dynamically much more complicated than the $Y + X_2$ reactions, and, in fact, the $Mu + HX$ reactions may be quite different from the $H + HX$ reactions. In Chapter III, p.98, it is described how it may be possible to determine the exchange:abstraction branching ratios for $Mu + HX$ reactions by simply obtaining Arrhenius data over a wide temperature range. Chapter III, p. 102, also describes how low temperature rate data on these reactions might provide information about the presence or absence of wells in the $Mu + HX$ potential surfaces. It seems probable that this temperature range extension of the present experiments will provide new dynamical information on these important elementary reactions.

For many years, the ultimate reactions for experimental kinetics study have been the isotopic variations of the H + H₂ reactions, mainly because they have been the subject of exhaustive theoretical investigation. Preliminary data on the Mu + H₂ reaction [Mikula (79)] indicates that at room temperature, the rate is at or near the lower limit of the MSR method ($\approx 10^5$ l mole⁻¹ s⁻¹). However, this reaction, which has a high activation energy (≥ 7 kcal/mole [Jones (73)]), may be measurable between 400 - 600K where it is at least from 20 - 350 times faster than at 300K. Certainly, the experimental investigation of this reaction should have a high priority in the immediate future.

Looking deeper into the crystal ball, where should gas phase Mu reaction kinetics go after the programme outlined above is completed? This may depend strongly on the prevailing technology and theory at the time. One direction that it could certainly take, is simply to measure the reaction rates of muonium with other molecules. The desirability of such a programme will depend largely on the understanding of Mu isotope effects. If the differences and similarities between Mu and H reaction rates could be predicted with confidence, then the MSR method may provide a more accurate means of measuring H atom reaction rates. More importantly, MSR may also be applied to chemical systems where direct measurements of the H atom reaction rates are not experimentally possible.

One very interesting direction gas phase muonium kinetics might take is to venture into the realm of state-to-state chemistry. Unfortunately, the experimental obstacles to such

a study presently appear to be prohibitive. In the first place, muonium atomic beams do not exist; only very high energy muon ion beams do. Some progress has been made in producing thermal muonium in vacuum [Marshall (78)]; however, even if an ideal "muon to muonium converter" existed, the use of such an atomic beam would be severely restricted due to the muon lifetime of 2.2 μ s. At 300K, a Mu atom travels about one inch during its lifetime. Associated with the lifetime problem is the intrinsic beam intensity problem. State-to-state experiments would likely not be MSR experiments, but would employ some other detection technique such as infrared chemiluminescence. Even at meson factories, the most intense muon beam ideally available would deliver no more than $10^8 \mu^+ s^{-1}$ over a 1 cm^2 area. According to Appendix III, the average number of muons in a target at any time, given a 100% duty cycle beam, is $\mathcal{N}\tau_\mu$, where \mathcal{N} is the beam current; with $\mathcal{N} = 10^8 s^{-1}$, the target would have no more than 200 muons in it at a time. This may be improved by using a low duty cycle accelerator which could deliver bursts of $10^4 - 10^5$ muons at any instant. Still, one is faced with the formidable problem of measuring an observable at such intensities on the time scale of the muon lifetime. For example, it appears that Mu infrared chemiluminescence experiments would require infrared, energy selective, single photon counters - the infrared analogue of such gamma ray detectors as sodium iodide crystals.

D Concluding Remarks

"He is not a liar, but he will become one if he keeps on."
Mark Twain, Following the Equator, p. 291

Two aspects of this thesis work have, I think, given me an

unusual and unique view of gas phase chemical kinetics in general, and muonium chemistry in particular: (1) the inherent interdisciplinary nature of a subject which exploits particle physics as a chemical tool, and (2) the timing of my involvement in the programme, which spanned the twilight days of the 184" Cyclotron at Berkeley to the early stages of the operation of the TRIUMF meson factory. On the first point, I will simply state that I began in a state of innocence - as I recall, the first question I ever asked my research supervisor was, "What is a muon?" To this day, my wife, an art historian, still questions (quite sensibly, I think) the sanity of people who claim to study unseen particles that last for two millionths of a second.

As for my involvement in the infant research project, this gave me a range of experience in MSR that will not ordinarily be available to future MSR workers. As an oldtimer, I have helped build the cyclotron and beamlines (which are now buried in radiation shielding, and seldom accessible); I was involved in beam line tuning and the design and implementation of data acquisition and analysis systems. Of course, I did not always cherish this experience which seemed at many times to be frustrating drudgery. Nonetheless, I think this ground floor experience has provided me with a reasonable understanding of most of the experimental paraphernalia, and, in some cases, a fairly intimate understanding, which de-mystifies the many black boxes of MSR, thereby affording greater control over the experiments.

Literature Cited - Chapter I

- Anderson (37) C.C. Anderson and S.H. Neddermeyer, *Phys. Rev.* 51 (1937) 884.
- Babaev (66) A.I. Babaev, M. Ya. Balats, G.G. Myasishcheva, Yu.V. Obukhov, V.S. Roganov, and V.G. Firsov, *Sov. Phys. JETP* 23 (1966) 583.
- Bjorken (64) J.D. Bjorken and S.D. Drell, *Relativistic Quantum Mechanics*, McGraw-Hill, New York, (1964).
- Brewer (72) J.H. Brewer, Ph.D. Thesis, Lawrence Berkeley Laboratory Report LBL-950, (1972).
- Brewer (73) J.H. Brewer, F.N. Gygax, and D.G. Fleming, *Phys. Rev.* A8 (1973) 77.
- Brewer (75) J.H. Brewer, K.M. Crowe, F.N. Gygax, and A. Schenck, in *Muon Physics*, Vol. III, Eds. C.S. Wu and V.W. Hughes, Academic Press, New York, (1975), Chapter 7.
- Bucci (78) C. Bucci, G. Guidi, G.M. de'Munari, M. Manfredi, P. Podini, R. Tedeschi, P.R. Crippa, and A. Vecchi, *Chem. Phys. Letters* 57 (1978) 634.
- Connor 1-(77) J.N.L. Connor, W. Jakubetz, and J. Manz, *Chem. Phys. Letters* 45 (1977) 265.
- Firsov (65) V.G. Firsov and V.M. Byakov, *Sov. Phys. JETP* 20 (1965) 719.
- Fleming (76) D.G. Fleming, J.H. Brewer, D.M. Garner, A.E. Pifer, T. Bowen, D.A. Delise, and K.M. Crowe, *J. Chem. Phys.* 64 (1976) 1281.
- Fleming 1-(77) D.G. Fleming, D.M. Garner, J.H. Brewer, J.B. Warren, G.M. Marshall, G. Clark, A.E. Pifer, and T. Bowen, *Chem. Phys. Letters* 48 (1977) 393.
- Fleming (79) D.G. Fleming, D.M. Garner, L.C. Vaz, D.C. Walker, J.H. Brewer, and K.M. Crowe, in *Positronium and Muonium Chemistry*, Ed. H.J. Ache, American Chemical Society Advances in Chemistry Series, in press.
- Garwin (57) R.L. Garwin, L.M. Lederman, and M. Weinrich, *Phys. Rev.* 105 (1957) 1415.
- Gold (78) V. Gold and M.E. McAdam, *Accounts of Chemical Res.* 11 (1978) 36.

Literature Cited - Chapter I (Cont'd.)

- Goldanskii (71) V.I. Goldanskii and V.G. Firsov, *Ann. Rev. Phys. Chem.* 22 (1971) 209.
- Grebinnik (76) V.G. Grebinnik, I.I. Gurevich, V.A. Zhukov, I.G. Ivanter, A.P. Manych, B.A. Nikol'skii, V.I. Selivanov, and V.A. Suetin, *Sov. Phys. JETP Letters* 23 (1976) 8.
- Hague (70) J.F. Hague, J.E. Rothberg, A. Schenck, D.L. Williams, R.W. Williams, K.K. Young, and K.M. Crowe, *Phys. Rev. Letters* 25 (1970) 628
- Hughes (66) V.W. Hughes, *Ann. Rev. Nucl. Sci.* 16 (1966) 445.
- Ivanter (68) I.G. Ivanter and V.P. Smilga, *Sov. Phys. JETP* 27 (1968) 301.
- Ivanter (69) I.G. Ivanter and V.P. Smilga, *Sov. Phys. JETP* 28 (1969) 796.
- Jean (78) Y.C. Jean, J.H. Brewer, D.G. Fleming, D.M. Garner, R.J. Mikula, L.C. Vaz, and D.C. Walker, *Chem. Phys. Letters* 57 (1978) 293.
- Kent (77) M. Kent, M.Sc. Thesis, University of British Columbia, (1977), unpublished.
- Lederman (77) L.M. Lederman, *Comments on Nucl. and Part. Phys.* VII (1977) 89.
- Mobley (66) R.M. Mobley, J.M. Bailey, W.E. Cleland, V.W. Hughes, and J.E. Rothberg, *J. Chem. Phys.* 44 (1966) 4354.
- Mobley 1-(67) R.M. Mobley, J.J. Amato, V.W. Hughes, J.E. Rothberg, and P.A. Thompson, *J. Chem. Phys.* 47 (1967) 3074.
- Mobley 2-(67) R.M. Mobley, Ph.D. Thesis, Yale University, (1967), unpublished.
- Nishida (77) N. Nishida, R.S. Hayano, K. Nagamine, T. Yamazaki, J.H. Brewer, D.M. Garner, D.G. Fleming, T. Takeuchi, and Y. Ishikawa, *Solid State Comm.* 22 (1977) 235.
- Nosov (63) V.G. Nosov and I.V. Yakovleva, *Sov. Phys. JETP* 16 (1963) 1236.
- Percival 1-(76) P.W. Percival and H. Fischer, *Chem. Phys.* 16 (1976) 89.

Literature Cited - Chapter I (Cont'd)

- Percival 2-(76) P.W. Percival, H. Fischer, M. Camani, F.N. Gygax, W. Ruegg, A. Schenck, H. Schilling, and H. Graf, Chem. Phys. Letters 39 (1976) 333.
- Percival (77) P.W. Percival, E. Roduner, H. Fischer, M. Camani, F.N. Gygax, and A. Schenck, Chem. Phys. Letters 47 (1977) 11.
- Percival (78) P.W. Percival, μ SR Newsletter 16 (1978) 409.
- Pifer (76) A.E. Pifer, T. Bowen, and K.R. Kendall, Nucl. Instr. Methods 135 (1976) 39.
- Roduner 1-(78) E. Roduner, P.W. Percival, D.G. Fleming, J. Hochmann, and H. Fischer, Chem. Phys. Letters 57 (1978) 37.
- Roduner 2-(78) E. Roduner, μ SR Newsletter 16 (1978) 407.
- Sachs (75) A.M. Sachs and A. Sirlin, in Muon Physics, Vol. II, Eds. C.S. Wu and V.W. Hughes, Academic Press, New York, (1975).
- Schenck (76) A. Schenck, in Nuclear and Particle Physics at Intermediate Energies, Ed. J.B. Warren, Plenum, New York, (1976) 159.
- Stambaugh (74) R.D. Stambaugh, D.E. Casperson, T.W. Crane, V.W. Hughes, H.F. Kaspar, P. Souder, P.A. Thompson, H. Orth, G. zu Pulitz, and A.B. Dennison, Phys. Rev. Letters 33 (1974) 568.
- Street (37) J.C. Street and E.C. Stevenson, Phys. Rev. 52 (1937) 1003.
- Swanson (58) R.A. Swanson, Phys. Rev. 112 (1958) 580.
- Weissenberg (67) A.O. Weissenberg, Muons, North-Holland, Amsterdam, (1967), published in Russian in 1964.

Literature Cited - Chapter II

- Cvetanovic (77) R.J. Cvetanovic and D.L. Singleton, *Int. J. Chem. Kinet.* IX (1977) 481; *ibid*, IX (1977) 1007.
- Davidon (68) W.C. Davidon, *Computer Journal* 10 (1968) 406.
- Fleming (76) D.G. Fleming, J.H. Brewer, D.M. Garner, A.E. Pifer, T. Bowen, D.A. Delise, and K.M. Crowe, *J. Chem. Phys.* 64 (1976) 1281.
- Fleming 1-(77) D.G. Fleming, D.M. Garner, J.H. Brewer, J.B. Warren, G.M. Marshall, G. Clark, A.E. Pifer, and T. Bowen, *Chem. Phys. Letters* 48 (1977) 393.
- Frost (61) A.A. Frost and R.G. Pearson, Kinetics and Mechanism, 2nd Edition, Wiley, New York, (1961).
- Hague (70) J.F. Hague, J.E. Rothberg, A. Schenck, D.L. Williams, K.K. Young, and K.M. Crowe, *Phys. Rev. Letters* 25 (1970) 628.
- Hayano 1-(76) R.S. Hayano, University of Tokyo Nuclear Physics Report UTPN-61, (1976).
- Hayano 2-(76) R.S. Hayano, University of Tokyo Nuclear Physics Report UTPN-64, M.Sc. Thesis, (1976).
- James (71) F. James and M. Roos, MINUIT, CERN Computer 7600 Interim Programme Library, (1971).
- Marshall (76) G.M. Marshall, M.Sc. Thesis, University of British Columbia, (1976), unpublished.
- Mobley 2-(67) R.M. Mobley, Ph.D. Thesis, Yale University, (1967), unpublished.
- Nelder (67) J.A. Nelder and R. Mead, *Computer Journal* 7 (1967) 308.
- Pifer (76) A.E. Pifer, T. Bowen, and K.R. Kendall, *Nucl. Instr. Methods* 135 (1976) 39.
- Sachs (75) A.M. Sachs and A. Sirlin, in Muon Physics, Vol. II, Eds. C.S. Wu and V.W. Hughes, Academic Press, New York, (1975).
- Schenck (76) A. Schenck, in Nuclear and Particle Physics at Intermediate Energies, Ed. J.B. Warren, Plenum, New York, (1976), 159.
- Stambaugh (74) R.D. Stambaugh, D.E. Casperson, T.W. Crane, V.W. Hughes, H.F. Kaspar, P. Souder, P.A. Thompson, H. Orth, G. zu Pulitz and A.B. Dennison, *Phys. Rev. Letters* 33 (1974) 568.

Literature Cited - Chapter III

- Anlauf (72) K.G. Anlauf, D.S. Horne, R.G. MacDonald, J.C. Polanyi, and K.B. Woodall, J. Chem. Phys. 57 (1972) 1561.
- Arnoldi (76) D. Arnoldi and J. Wolfrum, Ber. Bunsenges. physik. Chem. 80 (1976) 892.
- Baer (76) M. Baer, J. Chem. Phys. 65 (1976) 493.
- Bardo (78) R.D. Bardo and M. Wolfsberg, J. Chem. Phys. 68 (1978) 2686.
- Bauer 1-(78) W. Bauer, K. Shobatake, J.P. Toennies, and K. Walaschewski, J. Chem. Phys. 68 (1978) 3413.
- Bauer 2-(78) W. Bauer, L.Y. Rusin, and J.P. Toennies, J. Chem. Phys. 68 (1978) 4490.
- Baybutt (78) P. Baybutt, F.W. Bobrowicz, L.R. Kahn, and D.G. Truhlar, J. Chem. Phys. 68 (1978) 4809.
- Blais (74) N.C. Blais and D.G. Truhlar, J. Chem. Phys. 61 (1974) 4186; *ibid* 65 (1976) 3303.
- Bondybey (71) V. Bondybey, G.C. Pimentel, and P.N. Noble, J. Chem. Phys. 55 (1971) 540.
- Botschwina (77) P. Botschwina and W. Meyer, J. Chem. Phys. 67 (1977) 2390.
- Clyne (66) M.A.A. Clyne and D.H. Stedman, J. Chem Soc. Faraday Trans. 62 (1966) 2164.
- Connor (75) J.N.L. Connor, W. Jakubetz, and J. Manz, Mol. Phys. 29 (1975) 347.
- Connor 1-(76) J.N.L. Connor, Chem. Soc. Rev. 5 (1976) 125.
- Connor 1-(77) J.N.L. Connor, W. Jakubetz, and J. Manz, Chem. Phys. Letters, 45 (1977) 265.
- Connor 2-(77) J.N.L. Connor, private communication, (1977).
- Connor 1-(78) J.N.L. Connor, W. Jakubetz, and J. Manz, Chem. Phys. 28 (1978) 219.
- Connor 2-(78) J.N.L. Connor, private communication, (1978).
- Connor 1-(79) J.N.L. Connor, W. Jakubetz, and A. Laganà, J. Phys. Chem. 83 (1979) 73.
- Douglas (76) D.J. Douglas, J.C. Polanyi, and J.J. Sloan, Chem. Phys. 13 (1976) 15.

Literature Cited - Chapter III (Cont'd)

- Dunning (77) T.H. Dunning, J. Chem. Phys. 66 (1977) 2752.
- Eliason (59) M.A. Eliason and J.O. Hirschfelder, J. Chem. Phys. 30 (1959) 1426.
- Endo (76) H. Endo and G.P. Glass, Chem. Phys. Letters 44 (1976) 180.
- Fischer 1-(77) S. Fischer and G. Venzl, J. Chem. Phys. 67 (1977) 1335.
- Fischer 2-(77) S. Fischer, Ber. Bunsenges. physik. Chem. 81 (1977) 197.
- Fleming (76) D.G. Fleming, J.H. Brewer, D.M. Garner, A.E. Pifer, T. Bowen, D.A. Delise, and K.M. Crowe, J. Chem. Phys. 64 (1976) 1281.
- Fleming 1-(77) D.G. Fleming, D.M. Garner, J.H. Brewer, J.B. Warren, G.M. Marshall, G. Clark, A.E. Pifer, and T. Bowen, Chem. Phys. Letters 48 (1977) 393.
- Frost (61) A.A. Frost and R.G. Pearson, Kinetics and Mechanism, 2nd Edition, Wiley, New York, (1961).
- Gatz (66) C.R. Gatz, J. Chem. Phys. 44 (1966) 1861.
- Heidner (76) R.F. Heidner and J.F. Bott, J. Chem. Phys. 64 (1976) 2267.
- Hirschfelder (76) J.O. Hirschfelder and K.T. Tang, J. Chem. Phys. 64 (1976) 760.
- Jakubetz 1-(78) W. Jakubetz, "Gas Phase Muonium Chemistry, Isotope Effects, and Collision Theory: Theoretical Investigations of the $\mu + F_2$ and $\mu + Cl_2$ Reactions and their Isotopic Counterparts," pre-print submitted to Hyperfine Interactions, from Proceedings of the First International Conference on μ SR, Rorshack, Switzerland, September, (1978).
- Jakubetz (79) W. Jakubetz, J. Am. Chem. Soc. 101 (1979) 298.
- Johnston (61) H.S. Johnston and D.L. Rapp, J. Am. Chem. Soc. 83 (1961) 1.
- Johnston (66) H.S. Johnston, Gas Phase Reaction Rate Theory, Ronald, New York, (1966).
- Jonathan (72) N. Jonathan, S. Okuda, and D. Timlin, Mol. Phys. 24 (1972) 1143.

Literature Cited - Chapter III (Cont'd)

- Karplus (70) M. Karplus and R.N. Porter, Atoms and Molecules, Benjamin, New York, (1970).
- Klein (78) F.S. Klein and I. Veltman, J. Chem. Soc. Faraday II 74 (1978) 17.
- Korsch (78) H.J. Korsch, Chem. Phys. 33 (1978) 313.
- Kuntz (66) P.J. Kuntz, E.M. Nemeth, J.C. Polanyi, S.D. Rosner, and C.E. Young, J. Chem. Phys. 44 (1966) 1168.
- Kuppermann (79) A. Kuppermann, J. Phys. Chem. 83 (1979) 171.
- Laidler (65) K.J. Laidler and J.C. Polanyi, Progress in Reaction Kinetics, Vol. 3, Ed. G. Porter, Pergamon, New York (1965), 1.
- Levine (74) R.D. Levine and R.B. Bernstein, Molecular Reaction Dynamics, Oxford University Press, (1974).
- Liu (78) B. Liu and P. Siegbahn, J. Chem. Phys. 68 (1978) 2457.
- Manz (74) J. Manz, Mol. Phys. 28 (1974) 399.
- Manz (75) J. Manz, Mol. Phys. 30 (1975) 899.
- Manz (76) J. Manz, private communication, (1976).
- Marcus (77) R.A. Marcus and M.E. Coltin, J. Chem. Phys. 67 (1977) 2609.
- McDonald (75) J.D. McDonald and D.R. Herschbach, J. Chem. Phys. 62 (1975) 4740.
- Messiah (58) A. Messiah, Quantum Mechanics, Vol. I, translated by G.M. Temmer, North-Holland, Amsterdam, (1958).
- Mok (69) M.H. Mok and J.C. Polanyi, J. Chem. Phys. 51 (1969) 1451.
- Nikitin (74) E.E. Nikitin, Theory of Elementary Atomic and Molecular Processes in Gases, M.J. Kearsley, translator, Clarendon, Oxford, (1974).
- Noble (68) P.N. Noble and G.C. Pimentel, J. Chem. Phys. 49 (1968) 3165.
- Noble (72) P.N. Noble, J. Chem. Phys. 56 (1972) 2088.
- Pattengill (76) M.D. Pattengill, J.C. Polanyi, and J.L. Schreiber, J. Chem. Soc. Faraday II 72 (1976) 897.

Literature Cited - Chapter III (Cont'd)

- Persky (77) A. Persky, J. Chem. Phys. 66 (1977) 2932.
- Persky (78) A. Persky, J. Chem. Phys. 68 (1978) 2411.
- Polanyi (69) J.C. Polanyi and W.H. Wong, J. Chem. Phys. 51 (1969) 1439.
- Polanyi (72) J.C. Polanyi, Accounts of Chem. Res. 5 (1972) 161.
- Polanyi (75) J.C. Polanyi, J.L. Schreiber, and J.J. Sloan, Chem. Phys. 9 (1975) 403.
- Polanyi (78) J.C. Polanyi and N. Sathyamurthy Chem. Phys. 33 (1978) 287.
- Porter (73) R.N. Porter, L.B. Sims, D.L. Thompson, and L.M. Raff, J. Chem. Phys. 58 (1973) 2855.
- Sato (55) S. Sato, J. Chem. Phys. 23 (1955) 2465.
- Schatz (77) G.C. Schatz and J. Ross, J. Chem. Phys. 66 (1977) 1021.
- Smith (77) I.W.M. Smith, in Gas Kinetics and Energy Transfer, Vol. 2, Ed. P.G. Ashmore and R.J. Donovan, Billings, London, (1977).
- Thompson (75) D.L. Thompson, H.H. Suzukawa, and L.M. Raff, J. Chem. Phys. 62 (1975) 4727.
- Thompson (76) D.L. Thompson, Accounts of Chem. Res. 9 (1976) 338.
- Tolman (27) R.C. Tolman, Statistical Mechanics With Applications to Physics and Chemistry, Chem. Catalog, New York, (1927), 260.
- Truhlar (69) D.G. Truhlar and A. Kuppermann, J. Phys. Chem. 73 (1969) 1722.
- Valencich (77) T. Valencich, J. Hsieh, J. Kwan, T. Stewart, and T. Lenhardt, Ber. Bunsenges. physik. Chem. 81 (1977) 131.
- Van Hook (70) W.A. Van Hook, in Isotope Effects in Chemical Reactions, ACS Monograph, C.J. Collins and N.S. Bowman, Eds., Van Nostrand Reinhold, Toronto, (1970), 1.
- Weston (72) R.E. Weston and H.A. Schwarz, Chemical Kinetics, Prentice Hall, Toronto, (1972).
- Weston (79) R.E. Weston, J. Phys. Chem. 83 (1979) 61.

Literature Cited - Chapter III (Cont'd)

- White (73) J.M. White, J. Chem. Phys. 58 (1973) 4482.
- Wilkins (75) R.L. Wilkins, J. Chem. Phys. 63 (1975) 2963.
- Wolfrum (77) J. Wolfrum, Ber. Bunsenges. physik. Chem. 81 (1977) 114.

Literature Cited - Chapter IV

- Albright (69) R.G. Albright, A.F. Dodonov, G.K. Lavrovskaya, I.I. Morosov, and V.L. Tal'roze, J. Chem. Phys. 50 (1969) 3632.
- Ambidge (76) P.F. Ambidge, J.N. Bradley and D.A. Whytock, J. Chem. Soc. Faraday I 72 (1976) 1157.
- Baer (74) M. Baer, J. Chem. Phys. 60 (1974) 1057.
- Bauer 1-(78) W. Bauer, K. Shobatake, J.P. Toennies, and K. Walaschewski, J. Chem. Phys. 68 (1978) 3413.
- Bauer 2-(78) W. Bauer, L.Y. Rusin, and J.P. Toennies, J. Chem. Phys. 68 (1978) 4490.
- Baybutt (78) P. Baybutt, I.W. Bobrowicz, L.R. Kahn, and D.G. Truhlar, J. Chem. Phys. 68 (1978) 4809.
- Bemand (77) P.P. Bemand and M.A.A. Clyne, J. Chem. Soc. Faraday II 73 (1977) 394.
- Benson (60) S.W. Benson, The Foundations of Chemical Kinetics, McGraw-Hill, New York, (1960).
- Blais (74) N.C. Blais and D.G. Truhlar, J. Chem. Phys., 61 (1974) 4186; *ibid* 65 (1976) 3303.
- Brewer (72) J.H. Brewer, Ph.D Thesis, Lawrence Berkeley Laboratory Report LBL-950, (1972).
- Clyne (79) M.A.A. Clyne, private communication, (1979).
- Connor 1-(77) J.N.L. Connor, W. Jakubetz, and J. Manz, Chem. Phys. Letters 45 (1977) 265.
- Connor 1-(78) J.N.L. Connor, W. Jakubetz, and J. Manz, Chem. Phys. 28 (1978) 219.
- Connor 2-(78) J.N.L. Connor, private communication, (1978).
- Connor 1-(79) J.N.L. Connor, W. Jakubetz, and A. Laganà, J. Phys. Chem. 83 (1979) 73.
- Connor 2-(79) J.N.L. Connor and A. Laganà, "Quasiclassical dynamics of light heavy heavy atom reactions: The reaction $X + F_2 \rightarrow XF + F$, $X = (Mu, H, D, T)$ ", preprint, (1979).
- Connor 3-(79) J.N.L. Connor, W. Jakubetz, J. Manz, and J.C. Whitehead, "The reaction $X + Cl_2 \rightarrow XCl + Cl$ ($X = H, D$). I. A new inversion procedure for obtaining potential energy surfaces from experimental rate coefficient data," to be published, (1979).

Literature Cited - Chapter IV (Cont'd)

- Dodonov (70) A.F. Dodonov, G.K. Lavrovskaya, I.I. Morosov, R.G. Albright, V.L. Tal'roze, and A.K. Lyubimova, *Kinetica i Kataliz*, 11 (1970); english translation: *Kinetics and Catalysis* 11 (1970) 677.
- Endo (76) H. Endo and G.P. Glass, *J. Phys. Chem.* 80 (1976) 1519.
- Essén (76) H. Essén, G.D. Billing, and M. Baer, *Chem. Phys.* 17 (1976) 443.
- Fass (70) R.A. Fass, *J. Phys. Chem.* 74 (1970) 984.
- Fass (72) R.A. Fass, J.W. Hoover, and L.M. Simpson, *J. Phys. Chem.* 76 (1972) 2801.
- Fleming (76) D.G. Fleming, J.H. Brewer, D.M. Garner, A.E. Pifer, T. Bowen, D.A. Delise and K.M. Crowe, *J. Chem. Phys.* 64 (1976) 1281.
- Fleming 1-(77) D.G. Fleming, D.M. Garner, J.H. Brewer, J.B. Warren, G.M. Marshall, G. Clark, A.E. Pifer, and T. Bowen, *Chem. Phys. Letters* 48 (1977) 393.
- Fleming 2-(77) D.G. Fleming, J.H. Brewer, and D.M. Garner, *Ber. Bunsenges. physik. Chem.* 81 (1977) 159.
- Fleming (79) D.G. Fleming, D.M. Garner, L.C. Vaz, D.C. Walker, J.H. Brewer, and K.M. Crowe, in Positronium and Muonium Chemistry, Ed. H.J. Ache, *American Chemical Society Advances in Chemistry Series*, in press.
- Foon (75) R. Foon and K. Kaufman, Progress in Reaction Kinetics, Vol. 8, Ed. G. Porter, Pergamon, New York, (1975) 85.
- Garner (78) D.M. Garner, D.G. Fleming, and J.H. Brewer, *Chem. Phys. Letters*, 55 (1978) 163.
- Hepburn (78) J.W. Hepburn, D. Klimek, K. Liu, J.C. Polanyi, and S.C. Wallace, *J. Chem. Phys.* 69 (1978) 4311.
- Homann (77) K.H. Homann, H. Schweinfurth, and J. Warnatz, *Ber. Bunsenges. physik. Chem.* 81 (1977) 724.
- Jakubetz 1-(78) W. Jakubetz, "Gas phase muonium chemistry, isotope effects, and collision theory: theoretical investigations of the $\text{Mu} + \text{F}_2$ and $\text{Mu} + \text{Cl}_2$ reactions and their isotopic counterparts", preprint submitted to Hyperfine Interactions, from proceedings of the First

Literature Cited - Chapter IV (Cont'd)

- Jakubetz 1-(78) International Conference on μ SR, Rorshack, Switzerland, September, 1978.
(Cont'd)
- Jakubetz 2-(78) W. Jakubetz, J. Chem Phys. 69 (1978) 1783.
- Jakubetz (79) W. Jakubetz, J. Am. Chem. Soc. 101 (1979) 298.
- Johnston (61) H.S. Johnston and D.L. Rapp, J. Am. Chem. Soc. 83 (1961) 1.
- Jonathan (72) N. Jonathan, S. Okuda, and D. Timlin, Mol. Phys. 24 (1972) 1143.
- Jones (73) W.E. Jones, S.D. MacKnight, and L. Teng, Chem. Rev. 73 (1973) 407.
- Korsch (78) H.J. Korsch, Chem. Phys. 33 (1978) 313.
- Kuntz (66) P.J. Kuntz, E.M. Nemeth, J.C. Polanyi, S.D. Rosner, and C.E. Young, J. Chem. Phys. 44 (1966) 1168
- Laganà (79) A. Laganà, private communication, (1979).
- Laidler (65) K.J. Laidler and J.C. Polanyi, Progress in Reaction Kinetics, Vol. 3, Ed. G. Porter, Pergamon, New York, (1965) 1.
- Levine (74) R.D. Levine and R.B. Bernstein, Molecular Reaction Dynamics, Oxford University Press, (1974).
- Levy (68) J.B. Levy and B.K. Copeland, J. Phys. Chem., 72 (1968) 3168.
- Malcolme-
Lawes (78) D.J. Malcolme-Lawes, J. Chem. Soc. Faraday II 74 (1978) 182
- Marshall (78) G.M. Marshall, J.B. Warren, D.M. Garner, G.S. Clark, J.H. Brewer, and D.G. Fleming, Phys. Letters 65A (1978) 351.
- Nesmeinov (63) A.N. Nesmeinov, in Vapor Pressure of the Chemical Elements, Ed. R. Gary, Elsevier, New York, (1963).
- Persky (74) A. Persky and A. Kuppermann, J. Chem. Phys. 61 (1974) 5035.
- Polanyi (72) J.C. Polanyi and J.J. Sloan, J. Chem. Phys. 57 (1972) 4988.
- Polanyi (75) J.C. Polanyi, J.L. Schreiber, and J.J. Sloan, Chem. Phys. 9 (1975) 403.

Literature Cited - Chapter IV (Cont'd)

- Rabideau (72) S.W. Rabideau, H.G. Hecht, and W.B. Lewis, J. Magn. Reson. 6 (1972) 384.
- Stedman (70) D.H. Stedman, D. Steffeson, and H. Niki, Chem. Phys. Letters 7 (1970) 173.
- Sullivan (62) J.H. Sullivan, J. Chem Phys. 36 (1962) 1925.
- Takacs (73) G.A. Takacs and G.P. Glass, J. Phys. Chem. 77 (1973) 1060.
- Thompson (75) D.L. Thompson, H.H. Suzukawa, and L.M. Raff, J. Chem. Phys. 62 (1975) 4727.
- Truhlar (78) D.G. Truhlar and J.C. Gray, Chem. Phys. Letters 57 (1978) 93.
- Truhlar (79) D.G. Truhlar, J. Phys. Chem. 83 (1979) 188.
- Venzl (78) G. Venzl and S.F. Fischer, Chem. Phys. 33 (1978) 305.
- Wagner (76) H. Gg. Wagner, U. Welzbacker, and R. Zellner, Ber. Bunsenges. physik. Chem. 80 (1976) 902.
- Weston (79) R.E. Weston, J. Phys. 83 (1979) 61.
- White (73) J.M. White, J. Chem. Phys. 58 (1973) 4482.
- Wilkins (75) R.L. Wilkins, J. Chem. Phys. 63 (1975) 2963.

Literature Cited - Chapter V

- Connor 2-(76) J.N.L. Connor, W. Jakubetz, and J. Manz, Chem. Phys. 17 (1976) 501.
- Connor 1-(77) J.N.L. Connor, W. Jakubetz, and J. Manz, Chem. Phys. Letters 45 (1977) 265.
- Connor 2-(78) J.N.L. Connor, private communication, (1978).
- Fleming (76) D.G. Fleming, J.H. Brewer, D.M. Garner, A.E. Pifer, T. Bowen, D.A. Delise, and K.M. Crowe, J. Chem. Phys. 64 (1976) 1281.
- Fleming (79) D.G. Fleming, D.M. Garner, L.C. Vaz, D.C. Walker, J.H. Brewer, and K.M. Crowe, in Positronium and Muonium Chemistry, Ed. H.J. Ache, American Chemical Society Advances in Chemistry Series, in press.
- Garner (78) D.M. Garner, D.G. Fleming, and J.H. Brewer, Chem. Phys. Letters 55 (1978) 163.
- Jakubetz (79) W. Jakubetz, J. Am. Chem. Soc., 101 (1979) 298.
- Jones (73) W.E. Jones, S.D. MacKnight, and L. Teng, Chem. Rev. 73 (1973) 407.
- Marshall (78) G.M. Marshall, J.B. Warren, D.M. Garner, G.S. Clark, J.H. Brewer, and D.G. Fleming, Phys. Letters 65A (1978) 351.
- Mikula (79) R.J. Mikula, private communication, (1979).

Literature Cited - Appendix I

- Breit (31) G. Breit and I. Rabi, Phys. Rev. 38 (1931) 2082.
- Brewer (75) J.H. Brewer, K.M. Crowe, F.N. Gygax, and A. Schenck, in Muon Physics, Vol. III, Eds., C.S. Wu and V.W. Hughes, Academic Press, New York, (1975), Chapter 7.
- Carrington (67) A. Carrington and A.D. McLachlan, Introduction to Magnetic Resonance, Harper and Row, New York, (1967), 14.
- Fleming (79) D.G. Fleming, D.M. Garner, L.C. Vaz, D.C. Walker, J.H. Brewer, and K.M. Crowe, in Positronium and Muonium Chemistry, H.J. Ache, Ed., American Chemical Society Advances in Chemistry Series, in press.
- Gurevich (71) I.I. Gurevich, I.G. Ivanter, E.A. Meleshko, B.A. Nikol'skii, V.S. Roganov, V.I. Selivanov, V.P. Smilga, B.V. Sokolov, and V.D. Shestakov, Sov. Phys. JETP 33 (1971) 253.
- Percival 1-(76) P.W. Percival and H. Fischer, Chem. Phys. 16 (1976) 89.
- Schenck (76) A. Schenck, in Nuclear and Particle Physics at Intermediate Energies, Ed. J.B. Warren, Plenum, New York, (1976) 159.
- Tinkham (64) M. Tinkham, Group Theory and Quantum Mechanics, McGraw-Hill, New York, (1964), Chapter 5.

Literature Cited - Appendix II

- Arnold (68) V.I. Arnold and A. Avez, Ergodic Problems in Quantum Mechanics, Benjamin, New York, (1968) 16.
- Brewer (72) J.H. Brewer, Ph.D. Thesis, Lawrence Berkeley Laboratory Report, LBL-950, (1972).
- Brewer (75) J.H. Brewer, K.M. Crowe, F.N. Gygax, and A. Schenck, in Muon Physics, Vol. III, Eds., C.S. Wu and V.W. Hughes, Academic Press, New York, (1975), Chapter 7.
- Fleming (79) D.G. Fleming, D.M. Garner, L.C. Vaz, D.C. Walker, J.H. Brewer, and K.M. Crowe, in Positronium and Muonium Chemistry, Ed., H.J. Ache, American Chemical Society Advances in Chemistry Series, in press.
- Schenck (71) A. Schenck and K.M. Crowe, Phys. Rev. Letters 26 (1971) 57.

Literature Cited - Appendix III

- Biswell (73) L.R. Biswell and R.E. Rajala, Los Alamos Scientific Laboratory Report LA-5144, (1973).
- Feller (50) W. Feller, An Introduction to Probability Theory and its Applications, Wiley, London, (1950), 337.
- Shlaer (74) S. Shlaer, Los Alamos Scientific Laboratory Report LA-511-MS, (1974).
- Thomas (73) R.F. Thomas, Los Alamos Scientific Laboratory Report LA-5404-MS, (1973).

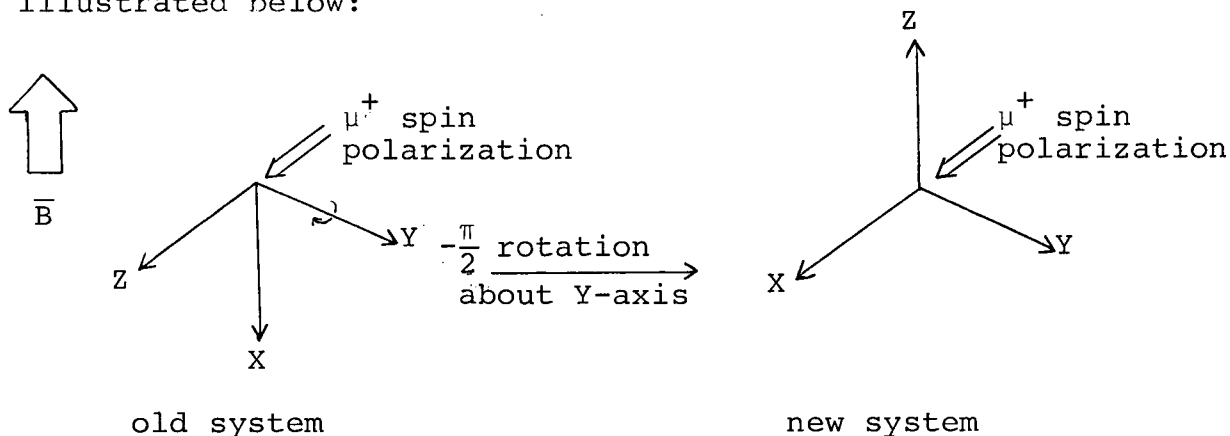
Appendix I - The Time Evolution of the μ^+ Spin Polarization in Muonium in a Transverse Magnetic Field.

Solutions to the problem treated in this Appendix may be found in several references which use the density matrix formalism [Gurevich (71), Brewer (75), Schenck (76), Percival (76)] . In this Appendix, the approach to the problem follows that of Fleming (79) which is, perhaps, more physically transparent than the density matrix approach.

A. State Vectors

The initial states of the system are most easily described using the μ^+ spin polarization direction as the quantization axis. Since all of the muons are polarized while the electrons captured to form Mu are unpolarized, the initial states are $\psi_A(0) = |\alpha\alpha\rangle_{\perp}$ and $\psi_B(0) = |\alpha\beta\rangle_{\perp}$ using the standard convention in which the first α or β refers to μ^+ spin and the second refers to e^- spin. The subscripts \perp indicate that the quantization axis is perpendicular to the applied magnetic field. The application of a magnetic field transverse to the initial muon polarization direction defines a new quantization axis and it is the task of this section to show the appropriate transformation of the initial Mu state functions into this new coordinate system.

The required transformation of state vectors is illustrated below:



The rotation is most easily applied to spin states labeled with respect to the total Mu spin angular momenta, $|JM\rangle_{\perp}$, where J is the total Mu spin and M is its projection on the original quantization axis, as usual. The initial spin states can be expressed in this way by the appropriate manipulation of Wigner or Clebsch-Gordon coefficients [Tinkham (64)],

$$\psi_M^J = \sum_m C_{mM-m}^{j_1 j_2 J} \phi_m^{j_1} \phi_{M-m}^{j_2}$$

from which one obtains:

$$\begin{aligned} |1,1\rangle_{\perp} &= |\alpha\alpha\rangle_{\perp} \\ |1,-1\rangle_{\perp} &= |\beta\beta\rangle_{\perp} \\ |1,0\rangle_{\perp} &= \frac{1}{\sqrt{2}} (|\alpha\beta\rangle_{\perp} + |\beta\alpha\rangle_{\perp}) \\ |0,0\rangle_{\perp} &= \frac{1}{\sqrt{2}} (|\alpha\beta\rangle_{\perp} - |\beta\alpha\rangle_{\perp}) \end{aligned} \tag{1}$$

Thus,

$$\begin{aligned} \psi_A(0) &= |\alpha\alpha\rangle_{\perp} = |1,1\rangle_{\perp} \\ \psi_B(0) &= |\alpha\beta\rangle_{\perp} = \frac{1}{\sqrt{2}} (|1,0\rangle_{\perp} + |0,0\rangle_{\perp}) \end{aligned}$$

A rotation of a state function which is a linear combination of basis vectors,

$$\psi = \sum_m \phi_m^j c_m = \underline{\phi}^j \underline{c}$$

about Eulerian angles α, β , and γ , is accomplished with the application of the rotation operator [Tinkham (64)]

$$\hat{R}(\alpha, \beta, \gamma)\psi = \sum_{m' m} \phi_{m'}^j [\underline{D}^{(j)}(\alpha, \beta, \gamma)\underline{c}]_m$$

Following the Condon and Shortley phase convention given in Tinkham, the required rotation is $\alpha=0$, $\beta=-\frac{\pi}{2}$, $\gamma=0$, where β is negative since it would advance a right handed screw in the negative y-direction. The $\underline{D}^{(j)}$ matrix elements are defined as:

$$D^{(j)}(\alpha, \beta, \gamma)_{m' m} = e^{-im'\alpha} e^{-im\gamma} \sum_{\kappa} \frac{(-1)^{\kappa} \sqrt{(j+m)!(j-m)!(j+m')!(j-m')!}}{\kappa! (j+m-\kappa)! (j-m'-\kappa)! (\kappa+m'-m)!} \\ \cdot (\cos\frac{\beta}{2})^{2j-2\kappa-m'+m} (-\sin\frac{\beta}{2})^{2\kappa+m'-m}$$

Since we are rotating the coordinate system (basis vectors) rather than functions, for which the above expression for $\underline{D}^{(j)}$ was calculated, the required rotation corresponds to $\underline{D}^{(j)}(-\gamma, -\beta, -\alpha)$. The required matrix is, then,

$$\underline{D}^1(0, \frac{\pi}{2}, 0) = \begin{pmatrix} \frac{1}{2} & -\frac{1}{\sqrt{2}} & \frac{1}{2} \\ \frac{1}{\sqrt{2}} & 0 & -\frac{1}{\sqrt{2}} \\ \frac{1}{2} & \frac{1}{\sqrt{2}} & \frac{1}{2} \end{pmatrix}$$

Thus

$$\hat{R}(0, \frac{\pi}{2}, 0)\psi_A(0) = \frac{1}{2}|1, 1\rangle_{\parallel} + \frac{1}{\sqrt{2}}|1, 0\rangle_{\parallel} + \frac{1}{2}|1, -1\rangle_{\parallel}$$

and
$$\hat{R}(0, \frac{\pi}{2}, 0)\psi_B(0) = -\frac{1}{2}|1, 1\rangle_{\parallel} + \frac{1}{2}|1, -1\rangle_{\parallel} + \frac{1}{\sqrt{2}}|0, 0\rangle_{\parallel}$$

where the subscripts \parallel indicate that the states are quantized with respect to the magnetic field and where it is noted that the totally symmetric basis function $|0, 0\rangle_{\parallel}$ is unaffected by the rotation. Using I(1) to transform back into uncoupled spin

states, $|m_{\mu} m_e\rangle$, we obtain:

$$\begin{aligned} \psi_A(0) &= \frac{1}{2} (|\alpha\alpha\rangle_{\parallel} + |\beta\beta\rangle_{\parallel} + |\alpha\beta\rangle_{\parallel} + |\beta\alpha\rangle_{\parallel}) \\ \psi_B(0) &= \frac{1}{2} (-|\alpha\alpha\rangle_{\parallel} + |\beta\beta\rangle_{\parallel} + |\alpha\beta\rangle_{\parallel} - |\beta\alpha\rangle_{\parallel}) \end{aligned} \quad \text{I(2)}$$

B Time Evolution of the Mu States

In order to find the expectation value of the μ^+ polarization in the Schrödinger picture, it is necessary to determine the time evolution of the Mu spin states. These are simply given by $\psi(t) = \hat{U}(t)\psi(0)$ where $\hat{U}(t)$ is the time evolution operator: $\hat{U}(t) = e^{-i\hat{\mathcal{K}}t/\hbar}$ where $\frac{\partial \hat{\mathcal{K}}}{\partial t} = 0$ and $\psi(0)$ are the eigenvectors of $\hat{\mathcal{K}}$. The Hamiltonian is the sum of the μ^+ and e^- Zeeman terms and the μ^+e^- hyperfine interaction:

$$\hat{\mathcal{K}} = g\beta_e \hat{B} \hat{S}_z - g\beta_{\mu} \hat{B} \hat{I}_z + a\bar{S} \cdot \bar{I}$$

where g is the electron or muon g -factor (which are essentially the same), β_e and β_{μ} are the e and μ magnetons, \bar{S} and \bar{I} are the e and μ spin operators, and 'a' is the Fermi contact constant. The electron and muon magnetons are equal to $\frac{e\hbar}{2mc}$ where m is the corresponding electron or muon mass. The 'a' term has been calculated to be [see, for example, Carrington (67)]

$$a = \frac{8\pi}{3} g\beta_e g\beta_{\mu} |\psi(0)|^2$$

where $|\psi(0)|^2$ is the probability density of the electron at the muon. For the $1s$ electron orbital

$$\psi(r) = \frac{1}{\sqrt{\pi a_0^3}} e^{-r/a_0}$$

with

$$a_0 = \hbar^2 / \mu e^2$$

which is the first Bohr radius; here μ represents the reduced mass of the electron and muon.

The eigenvalues of this Hamiltonian are most easily determined by re-expressing the spin vector operators of the hyperfine term in their vector components:

$$\hat{\mathcal{H}} = g\beta_e B \hat{S}_z - g\beta_\mu B \hat{I}_z + a(\hat{S}_x \hat{I}_x + \hat{S}_y \hat{I}_y + \hat{S}_z \hat{I}_z) \quad \text{I(3)}$$

Defining the raising and lowering operators in the usual way

$$\hat{S}^+ = \hat{S}_x + i\hat{S}_y$$

and
$$\hat{S}^- = \hat{S}_x - i\hat{S}_y$$

it is readily shown that

$$\hat{S}_x \hat{I}_y + \hat{S}_y \hat{I}_x = \frac{1}{2}(\hat{S}^+ \hat{I}^- + \hat{S}^- \hat{I}^+)$$

Substitution of this expression into I(3) gives

$$\hat{\mathcal{H}} = g\beta_e B \hat{S}_z - g\beta_\mu B \hat{I}_z + a\left\{\frac{1}{2}(\hat{S}^+ \hat{I}^- + \hat{S}^- \hat{I}^+) + \hat{S}_z \hat{I}_z\right\}$$

The matrix representation of $\hat{\mathcal{H}}$ given by $H_{ij} = \langle \phi_i | \hat{\mathcal{H}} | \phi_j \rangle$ with

respect to the basis set $|m_\mu m_e\rangle$ is:

$$\underline{\underline{H}} = \hbar \begin{pmatrix} \omega_- + \frac{\omega_0}{4} & 0 & 0 & 0 \\ 0 & \omega_+ - \frac{\omega_0}{4} & \frac{\omega_0}{2} & 0 \\ 0 & \frac{\omega_0}{2} & -\omega_+ - \frac{\omega_0}{4} & 0 \\ 0 & 0 & 0 & -\omega_- + \frac{\omega_0}{4} \end{pmatrix}$$

where $\omega_{\pm} = \frac{1}{2}(g\beta_e B/\hbar \pm g\beta_{\mu} B/\hbar)$ and $\omega_0 = \frac{a}{\hbar}$ is the hyperfine frequency. The eigenvalues of the Hamiltonian are:

$$E_1/\hbar = \omega_- + \frac{\omega_0}{4}$$

$$E_2/\hbar = -\frac{\omega_0}{4} + \left(\omega_+^2 + \frac{\omega_0^2}{4}\right)^{\frac{1}{2}} \quad \text{I (4)}$$

$$E_3/\hbar = -\omega_- + \frac{\omega_0}{4}$$

$$E_4/\hbar = -\frac{\omega_0}{4} - \left(\omega_+^2 + \frac{\omega_0^2}{4}\right)^{\frac{1}{2}}$$

The eigenvectors of \hat{H} may be obtained by inspection for the 1x1 submatrices and by a tedious but straightforward calculation for the 2x2 submatrix:

$$\begin{aligned} |1\rangle &= |\alpha\alpha\rangle \\ |2\rangle &= s|\alpha\beta\rangle + c|\beta\alpha\rangle \\ |3\rangle &= |\beta\beta\rangle \\ |4\rangle &= c|\alpha\beta\rangle - s|\beta\alpha\rangle \end{aligned} \quad \text{I (5)}$$

where

$$c = \frac{1}{\sqrt{2}} \left(1 + \sqrt{\frac{2\omega_+}{\omega_0^2 + 4\omega_+^2}}\right)^{\frac{1}{2}} = \frac{1}{\sqrt{2}} \left(1 + \sqrt{\frac{x}{1+x^2}}\right)^{\frac{1}{2}}$$

and

$$s = \frac{1}{\sqrt{2}} \left(1 - \sqrt{\frac{2\omega_+}{\omega_0^2 + 4\omega_+^2}}\right)^{\frac{1}{2}} = \frac{1}{\sqrt{2}} \left(1 - \sqrt{\frac{x}{1+x^2}}\right)^{\frac{1}{2}}$$

with $x = \frac{2\omega_+}{\omega_0}$. It should be noted that $c^2 + s^2 = 1$.

The above results are illustrated in the familiar Breit-Rabi diagram in Figure I-1 [Breit (31)]. The zero field

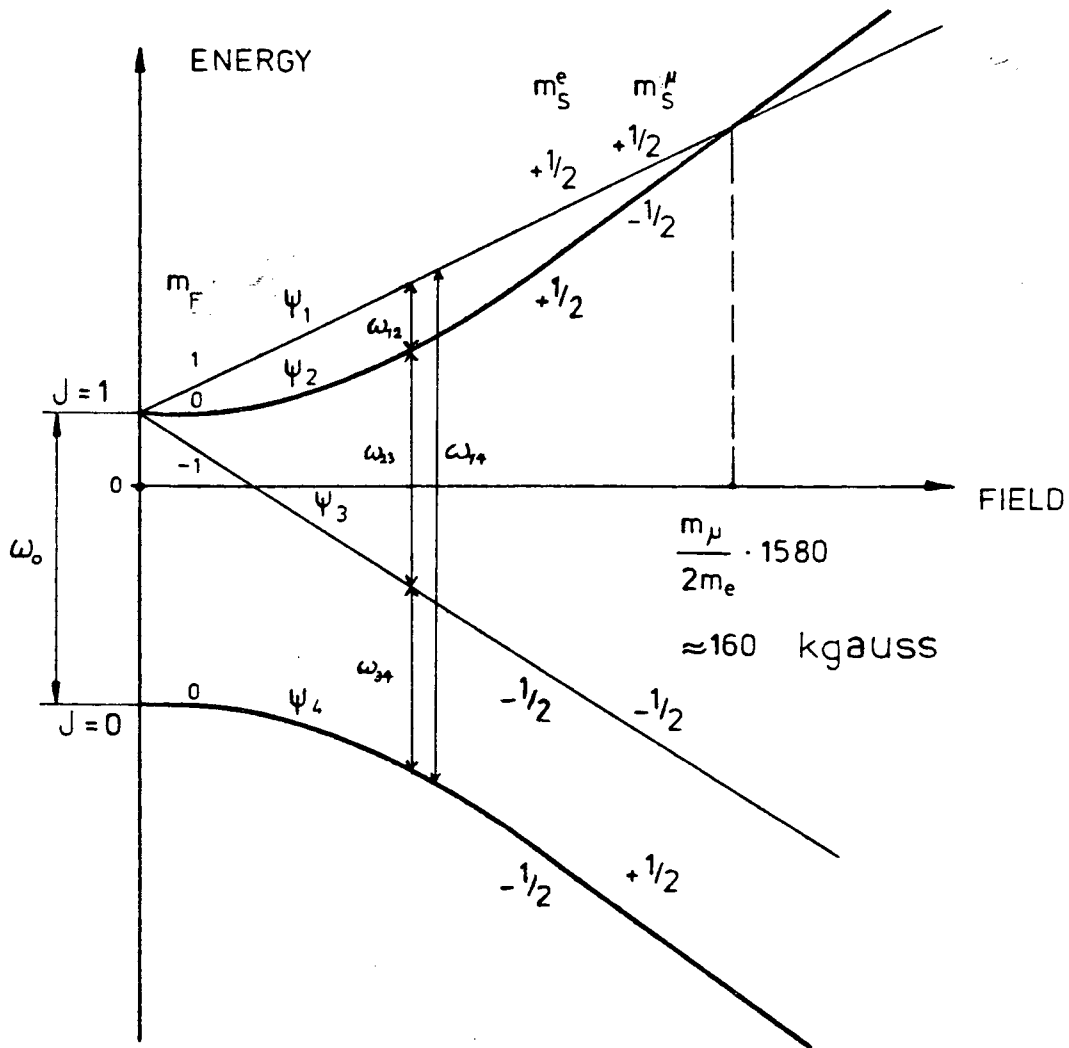


FIGURE I-1: Breit-Rabi diagram of the energy eigenstates of muonium in an external magnetic field. The four allowed transitions ($\Delta m = \pm 1$) are indicated. In weak fields ($B \leq 10$ gauss), the transitions, ω_{12} and ω_{23} , are degenerate and provide the characteristic muonium frequency, $\omega_{\text{Mu}} = 8.76 \times 10^6 \cdot B \text{ rad s}^{-1}$.

splitting or hyperfine frequency, ω_0 , for Mu is 2.8×10^{10} rad s^{-1} . The cross-over of ω_1 and ω_2 may be calculated by setting

$$\frac{\omega_0}{4} + \omega_- = -\frac{\omega_0}{4} + \left(\frac{\omega_0^2}{4} + \omega_+^2\right)^{\frac{1}{2}}$$

Denoting $\Delta_e = g\beta_e/\hbar$ and $\Delta_\mu = g\beta_\mu/\hbar$ and recalling the definitions of ω_+ and ω_- , this cross-over is found to be at

$$B = \frac{\Delta_e - \Delta_\mu}{2\Delta_e \Delta_\mu} \omega_0 \approx \frac{1}{2\Delta_\mu} \omega_0 = \frac{m_\mu \hbar}{2gm_e \beta_e} \omega_0$$

which corresponds to about 160 kgauss.

It is now possible to express the initial state vectors I(2) in terms of the eigenvectors of the Hamiltonian I(5):

$$\psi_A(0) = \frac{1}{2}|1\rangle + p|2\rangle + \frac{1}{2}|3\rangle - q|4\rangle$$

and
$$\psi_B(0) = -\frac{1}{2}|1\rangle + q|2\rangle + \frac{1}{2}|3\rangle + p|4\rangle$$

where $p = \frac{s+c}{2}$ and $q = \frac{s-c}{2}$. The time dependent Mu states are computed from the eigenvalues I(4):

$$\psi_A(t) = \frac{1}{2}e^{-i\omega_1 t}|1\rangle + pe^{-i\omega_2 t}|2\rangle + \frac{1}{2}e^{-i\omega_3 t}|3\rangle - pe^{-i\omega_4 t}|4\rangle \tag{I(6)}$$

and

$$\psi_B(t) = -\frac{1}{2}e^{-i\omega_1 t}|1\rangle + qe^{-i\omega_2 t}|2\rangle + \frac{1}{2}e^{-i\omega_3 t}|3\rangle + pe^{-i\omega_4 t}|4\rangle$$

where $\omega_i = E_i/\hbar$

Since the calculation of the time evolution of the μ^+ spin polarization will require computation of the expectation value of the muon spin operator, the calculation is most easily done in the basis $|m_\mu m_e\rangle$. In this basis, equations I(6) become:

$$\begin{aligned} \psi_A(t) = & \frac{1}{2}e^{-i\omega_1 t}|\alpha\alpha\rangle + (pse^{-i\omega_2 t} - qce^{-i\omega_4 t})|\alpha\beta\rangle \\ & + \frac{1}{2}e^{-i\omega_3 t}|\beta\beta\rangle + (pce^{-i\omega_2 t} + qse^{-i\omega_4 t})|\beta\alpha\rangle \end{aligned} \quad I(7)$$

$$\begin{aligned} \text{and } \psi_B(t) = & -\frac{1}{2}e^{-i\omega_1 t}|\alpha\alpha\rangle + (qse^{-i\omega_2 t} + pce^{-i\omega_4 t})|\alpha\beta\rangle \\ & + \frac{1}{2}e^{-i\omega_3 t}|\beta\beta\rangle + (qce^{-i\omega_2 t} - pse^{-i\omega_4 t})|\beta\alpha\rangle \end{aligned}$$

C Time Evolution of the μ^+ Spin Polarization in Mu

In an MSR experiment in transverse magnetic field, we are interested in the muon polarization in the x-y plane. For this, we define the "complex muon polarization" operator

$$\hat{P}_\mu = \sigma_\mu^X + i\sigma_\mu^Y$$

where σ^X and σ^Y are the familiar Pauli spin matrices:

$$\sigma^X = \begin{pmatrix} 0 & 1 \\ 1 & 0 \end{pmatrix} \quad \sigma^Y = \begin{pmatrix} 0 & -i \\ i & 0 \end{pmatrix}$$

Thus \hat{P}_μ is a form of the muon spin raising operator:

$$\hat{P}_\mu = \begin{pmatrix} 0 & 2 \\ 0 & 0 \end{pmatrix} = 2\hat{I}^+$$

This operator only acts on the muon spin part of the $|m_\mu m_e\rangle$ spin states in the usual way:

$$\text{eg. } \hat{P}_\mu|\alpha\beta\rangle = 0, \hat{P}_\mu|\beta\alpha\rangle = 2|\alpha\alpha\rangle, \text{ etc.}$$

The object of this section, then, is to calculate $\langle \hat{P}_\mu(t) \rangle$:

$$\langle \hat{P}_\mu(t) \rangle = f \langle \psi_A(t) | \hat{P}_\mu | \psi_A(t) \rangle + (1-f) \langle \psi_B(t) | \hat{P}_\mu | \psi_B(t) \rangle$$

where $0 \leq f \leq 1$ is the fraction of μ^+ that initially form Mu state $\psi_A(0)$ and $(1-f)$ is the fraction in $\psi_B(0)$. Normally, it is assumed $f = \frac{1}{2}$ [Fleming (79)] since the electrons are unpolarized. However, the more general case is derived here

since it does not greatly complicate the calculation and it may have physical applicability in certain ordered systems such as chiral molecules. After substituting $p = \frac{s + c}{2}$ and $q = \frac{s - c}{2}$ and rearranging, the calculation yields:

$$\begin{aligned} \langle \hat{P}_\mu(t) \rangle = & \frac{1}{2} \{ [(2f-1)sc+c^2] e^{i\omega_{12}t} - [(2f-1)sc-s^2] e^{i\omega_{14}t} \\ & + [(2f-1)sc+s^2] e^{i\omega_{23}t} - [(2f-1)sc-c^2] e^{-i\omega_{34}t} \} \end{aligned} \quad \text{I(8)}$$

where $\omega_{ij} = \omega_i - \omega_j$ which are explicitly given below from equations I(4):

$$\begin{aligned} \omega_{12} &= \omega_- + \frac{\omega_0}{2} - \left(\omega_+^2 + \frac{\omega_0^2}{4} \right)^{\frac{1}{2}} \\ \omega_{14} &= \omega_- + \frac{\omega_0}{2} + \left(\omega_+^2 + \frac{\omega_0^2}{4} \right)^{\frac{1}{2}} \\ \omega_{23} &= \omega_- - \frac{\omega_0}{2} + \left(\omega_+^2 + \frac{\omega_0^2}{4} \right)^{\frac{1}{2}} \\ \omega_{34} &= -\omega_- + \frac{\omega_0}{2} + \left(\omega_+^2 + \frac{\omega_0^2}{4} \right)^{\frac{1}{2}} \end{aligned} \quad \text{I(9)}$$

$$\text{Defining } \Omega = \frac{1}{2}(\omega_{23} - \omega_{12}) = \left(\omega_+^2 + \frac{\omega_0^2}{4} \right)^{\frac{1}{2}} - \frac{\omega_0}{2} = \frac{\omega_0}{2} [(1+x^2)^{\frac{1}{2}} - 1]$$

where it is recalled that $x = \frac{2\omega_+}{\omega_0}$, equations I(9) become:

$$\begin{aligned} \omega_{12} &= \omega_- - \Omega & \omega_{34} &= -\omega_- + \omega_0 + \Omega \\ \omega_{14} &= \omega_- + \omega_0 + \Omega & \omega_{23} &= \omega_- + \Omega \end{aligned} \quad \text{I(10)}$$

Substituting equations I(10) into I(8) and expanding exponentials, $e^{ikt} = \cos kt + i \sin kt$, yields:

$$\begin{aligned} \langle \hat{P}_\mu(t) \rangle = e^{i\omega_0 t} \left\{ \cos \frac{\omega_0 t}{2} \left[\cos \left(\Omega + \frac{\omega_0}{2} \right) t - i v \sin \left(\Omega + \frac{\omega_0}{2} \right) t \right] \right. \\ \left. + 2(2f - 1) s c \sin \frac{\omega_0 t}{2} \sin \left(\Omega + \frac{\omega_0}{2} \right) t \right\} \end{aligned} \quad \text{I(11)}$$

where it is noted $c^2 + s^2 = 1$ and $c^2 - s^2 = v = \frac{x}{\sqrt{1+x^2}}$.

Noting that $sc = \frac{1}{2} \left(\frac{1}{1+x^2} \right)^{1/2}$ and manipulating trigonometric identities gives the general expression:

$$\begin{aligned} \langle \hat{P}_\mu(t) \rangle = \frac{1}{2} e^{i\omega_0 t} \left\{ \left[1 + \left(\frac{1}{1+x^2} \right)^{1/2} (2f - 1) \right] \cos \Omega t \right. \\ \left. + \left[1 - \left(\frac{1}{1+x^2} \right)^{1/2} (2f - 1) \right] \cos (\omega_0 + \Omega) t \right. \\ \left. - i \frac{x}{\sqrt{1+x^2}} [\sin (\omega_0 + \Omega) t + \sin \Omega t] \right\} \end{aligned} \quad \text{I(12)}$$

This equation is general for all magnitudes of magnetic fields.

D Experimental Implications of $\langle \hat{P}_\mu(t) \rangle$

It is the task of this section to simplify the complex general expression for $\langle \hat{P}_\mu(t) \rangle$ (equation I(12)) in terms of practical experimental considerations. Two experimental constraints must be borne in mind throughout this section:

(1) the practical timing resolution of conventional counting and timing technology is about 1 ns, and (2) the lifetime of μ^+ is 2.2 μ s which limits the maximum experimental time range to, at most, about 10 μ s. The hyperfine frequency, ω_0 is 2.8×10^{10}

rad s⁻¹ which corresponds to a period of about 0.225 ns and is not, therefore, experimentally observable. At the other limit, frequencies slower than 1.2 x 10⁵ rad s⁻¹ which have periods of greater than 50 μs are not observable with the μ⁺ 10 μs time range.

$\langle \hat{P}_\mu(t) \rangle$ is related to the experimental MSR "signal"

$$S(\phi, t) = A(t) \langle \hat{P}_\mu(\phi, t) \rangle$$

where A(t) is the time dependent empirical asymmetry, and φ is the angle between the positron counter and initial muon polarization. S(t) in equation(8) of Chapter I is a particular example of an MSR signal. The signal appears in the exponential histogram:

$$N(\phi, t) = N_0 e^{-t/\tau_\mu} [1 + S(\phi, t)] + Bg \quad I(13)$$

which is analogous to equations (4) and (6) in Chapter I. Hence, the signal is the oscillatory muon function which remains when the exponential muon lifetime and background are removed from the time histogram. Chemical reactions and other relaxation effects are not included in S(φ, t) here; these effects are incorporated into the formalism in Appendix II.

Table I-1 lists values of the magnetic field dependent variables of equation I(12) for a number of practically available magnetic field strengths ranging from 1 gauss to 10 kgauss. This section examines $\langle \hat{P}_\mu(t) \rangle$ for three magnetic field regimes.

(i) Very Weak Fields (<10gauss) - the Standard MSR Signal

From Table I-1, it is seen that for B < 10 gauss,

$x = 0$, $\left(\frac{1}{1+x^2} \right)^{\frac{1}{2}} = 1$, and $v = 0$ to better than 1%. Furthermore,

TABLE I-1: VALUES OF MAGNETIC FIELD DEPENDENT VARIABLES IN EQUATIONS I(8) AND I(12)[†]

Field (gauss)	x	v	c ²	s ²	2sc	ω_+ (10 ⁶)	ω_- (10 ⁶)	Ω (10 ⁷)	ω_{12} (10 ¹⁰)	ω_{23} (10 ¹⁰)	ω_{14} (10 ¹⁰)	ω_{34} (10 ¹⁰)
1	0.001	0.001	0.500	0.500	1.000	8.847	8.761	0.000	0.001	0.001	2.805	2.804
3	0.002	0.002	0.501	0.499	1.000	26.54	26.28	0.003	0.003	0.003	2.807	2.802
5	0.003	0.003	0.502	0.498	1.000	44.24	43.81	0.007	0.004	0.004	2.809	2.800
7	0.004	0.004	0.502	0.498	1.000	61.93	61.33	0.013	0.006	0.006	2.811	2.798
10	0.006	0.006	0.503	0.497	1.000	88.47	87.61	0.028	0.009	0.009	2.813	2.796
20	0.013	0.013	0.506	0.494	1.000	177.0	175.2	0.111	0.017	0.018	2.822	2.787
30	0.019	0.019	0.509	0.491	1.000	265.4	262.8	0.250	0.026	0.027	2.831	2.778
50	0.032	0.032	0.516	0.484	1.000	442.4	438.1	0.697	0.043	0.045	2.849	2.761
75	0.047	0.047	0.524	0.476	0.999	663.6	657.1	1.569	0.064	0.067	2.872	2.740
100	0.063	0.063	0.531	0.469	0.998	884.7	876.1	2.788	0.085	0.090	2.895	2.720
150	0.095	0.094	0.547	0.453	0.996	1327.	1314.	6.266	0.125	0.138	2.942	2.679
200	0.126	0.125	0.563	0.437	0.992	1770.	1752.	11.12	0.164	0.186	2.991	2.640
300	0.189	0.186	0.593	0.407	0.983	2654.	2628.	24.90	0.238	0.288	3.092	2.566
500	0.315	0.301	0.650	0.350	0.954	4424.	4381.	68.13	0.370	0.506	3.310	2.435
1000	0.631	0.534	0.767	0.233	0.846	8847.	8761.	255.8	0.620	1.132	3.936	2.184
2000	1.262	0.784	0.892	0.108	0.621	17695	17522	855.5	0.897	2.608	5.412	1.908
3000	1.893	0.884	0.942	0.058	0.467	26542	26283	1600.	1.029	4.228	7.032	1.776
5000	3.155	0.953	0.977	0.023	0.302	44237	43805	3238.	1.142	7.619	10.42	1.662
10000	6.310	0.988	0.994	0.006	0.153	88474	87610	7556.	1.205	16.32	19.12	1.599

[†] frequencies are given in units of rad s⁻¹

for small x , $(1 + x^2)^{\frac{1}{2}} \approx 1 + \frac{1}{2}x^2$; thus

$$\Omega = \frac{\omega_0}{2} [(1 + x^2)^{\frac{1}{2}} - 1] \approx \frac{\omega_0}{2} (1 + \frac{1}{2}x^2 - 1) = \frac{\omega_0^2}{\omega_0}$$

In this limit, equation I(12) becomes:

$$\langle \hat{P}_\mu(t) \rangle_{B \leq 10 \text{ gauss}} = e^{i\omega_- t} [f \cos \Omega t + (1-f) \cos(\omega_0 + \Omega)t] \quad \text{I(14)}$$

The real part of the muon polarization is (including the counter phase dependence):

$$\begin{aligned} \text{Re} \langle \hat{P}_\mu(\phi, t) \rangle_{B \leq 10 \text{ gauss}} &= f \cos(\omega_- t + \phi) \cos \Omega t \\ &+ (1-f) \cos(\omega_- t + \phi) \cos(\omega_0 + \Omega)t \end{aligned} \quad \text{I(15)}$$

where $\omega_- = \frac{1}{2}(g\beta_e B/\hbar - g\beta_\mu B/\hbar) = 103\omega_\mu$ corresponds to the

characteristic muonium precession frequency. Notice that the counter phase dependence is added only to the Larmor precession parts of each term in I(15). By construction, the real part of $\langle \hat{P}_\mu(t) \rangle$ corresponds to the μ^+ polarization in the x direction and the imaginary part corresponds to the μ^+ polarization in the y direction. Introduction of the counter phase to either the real or imaginary parts generalizes $\langle \hat{P}_\mu(t) \rangle$ to correspond to any direction in the x-y plane. For example, $\text{Re} \langle \hat{P}_\mu(0, t) \rangle = \text{Im} \langle \hat{P}_\mu(\frac{\pi}{2}, t) \rangle$. Since the hyperfine frequency is too fast to be experimentally resolvable, the second term in I(15) averages to zero and this fraction (1-f) of the μ^+ appears to be unpolarized. The remaining term shows the muonium precession, ω_- , modulated by the slower beat frequency $\Omega \leq 2.8 \times 10^5 \text{ rad s}^{-1}$ which corresponds to a period $\geq 22.5 \text{ } \mu\text{s}$ for $B \leq 10 \text{ gauss}$. This beat frequency is slow enough that it may be ignored in fields of less than 10 gauss

except, possibly, in experiments which attempt highly precise measurements of very slow Mu relaxation rates ($\lambda \leq 0.2 \mu\text{s}^{-1}$). The net observable signal in this weak field regime thus reduces to the very simple expression:

$$\langle \hat{P}_\mu(\phi, t) \rangle = f \cos(\omega_- t + \phi). \quad \text{I(16)}$$

Experiments of this type which monitor a single characteristic Mu frequency, $\omega_- \equiv \omega_{\text{Mu}} = 103 \omega_\mu$, are called MSR experiments as defined in Chapter I. In most cases, f is assumed to be $\frac{1}{2}$. Generally, for reasons cited in Chapter I, the experimental asymmetry is treated empirically so that this fraction is indeterminable.

Figure I-2 illustrates the time evolution of μ^+ given by I(15) assuming $f = \frac{1}{2}$ and perfect experimental time resolution. Although Figure I-2 was calculated for a 100g field, equation I(15) is valid at early times (a few ns) since $\left(\frac{1}{1+x^2}\right)^{\frac{1}{2}} = 1$ at 100 gauss to better than 1%. The effects of Ω are unobservable at early times at this field. The figure shows the fast hyperfine oscillation in the envelope of the slower muonium precession. In practice, the fast oscillation is averaged over, leaving an observable muonium envelope of reduced amplitude.

(ii) Intermediate Fields ($10 \leq B \leq 150$ gauss) - Two Frequency Muonium

At magnetic fields less than 150 gauss, Table I-1 shows

$\left(\frac{1}{1+x^2}\right)^{\frac{1}{2}} = 1$ and $v \leq 0.1$. In these fields, the real part of equation I(12) is

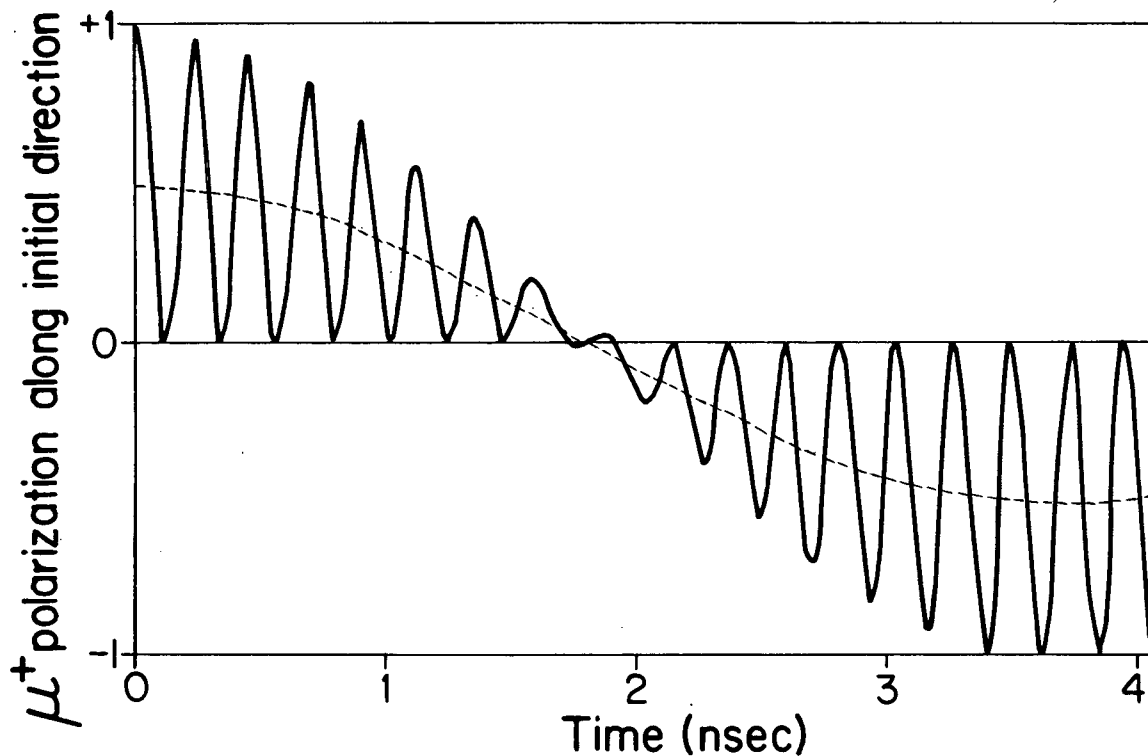


FIGURE I-2: The time evolution of the μ^+ spin polarization in a 100 gauss transverse magnetic field from equation I(15), assuming $f=\frac{1}{2}$, $\phi=0$. The fast oscillations are essentially at the hyperfine frequency, $\omega_0 = 2.80 \times 10^{10}$ rad s⁻¹ and the envelope is at the muonium frequency, $\omega_{\text{Mu}}(100 \text{ gauss}) = 8.76 \times 10^8$ rad s⁻¹. The beat frequency, $\Omega = 2.8 \times 10^7$ rad s⁻¹ at 100 gauss, is too slow to be observed on this time scale. Experimentally, the fast hyperfine oscillation is averaged over, leaving an observable ω_{Mu} envelope of reduced amplitude, indicated by the broken line.

$$\begin{aligned} \text{Re} \left\langle \hat{P}_\mu(\phi, t) \right\rangle_{10 \leq B \leq 150 \text{ gauss}} &= f \cos(\omega_- t + \phi) \cos \Omega t \\ &+ (1-f) \cos(\omega_- t + \phi) \cos(\omega_0 + \Omega)t \\ &+ \frac{V}{2} \sin(\omega_- t + \phi) [\sin(\omega_0 + \Omega)t + \sin \Omega t] \end{aligned}$$

As before, the hyperfine frequency is unobservably fast so that the effective expression for $\text{Re} \langle \hat{P}_\mu(\phi, t) \rangle$ becomes:

$$\begin{aligned} \text{Re} \left\langle \hat{P}_\mu(\phi, t) \right\rangle_{10 \leq B \leq 150 \text{ gauss}} &= f \cos(\omega_- t + \phi) \cos \Omega t \\ &+ \frac{V}{2} \sin(\omega_- t + \phi) \sin \Omega t \end{aligned}$$

Generally this expression is re-written by manipulation of trigonometric identities:

$$\begin{aligned} \text{Re} \left\langle \hat{P}_\mu(\phi, t) \right\rangle_{10 \leq B \leq 150 \text{ gauss}} &= \frac{1}{2} \left\{ \left(f - \frac{V}{2}\right) \cos[(\omega_- + \Omega)t + \phi] \right. \\ &\left. + \left(f + \frac{V}{2}\right) \cos[(\omega_- - \Omega)t + \phi] \right\} \end{aligned} \tag{17}$$

At 150 gauss, $\omega_- = 1.3 \times 10^9 \text{ rad s}^{-1}$ corresponding to a period of $\sim 5 \text{ ns}$ which is just observable with a time resolution of 1 ns. The resultant signal is a fast muonium oscillation beating at the slower frequency Ω . This was first observed experimentally by Gurevich (71) in quartz at 95 gauss; the data are shown in Figure I-3. This is referred to as the "two frequency precession" of the muon in muonium.

(iii) High Fields (>150 gauss)

At these fields, the characteristic muonium frequency, $\omega_- \equiv \omega_{\text{Mu}}$, becomes immeasurably large. With an experimental time resolution of about 1 ns, an observable

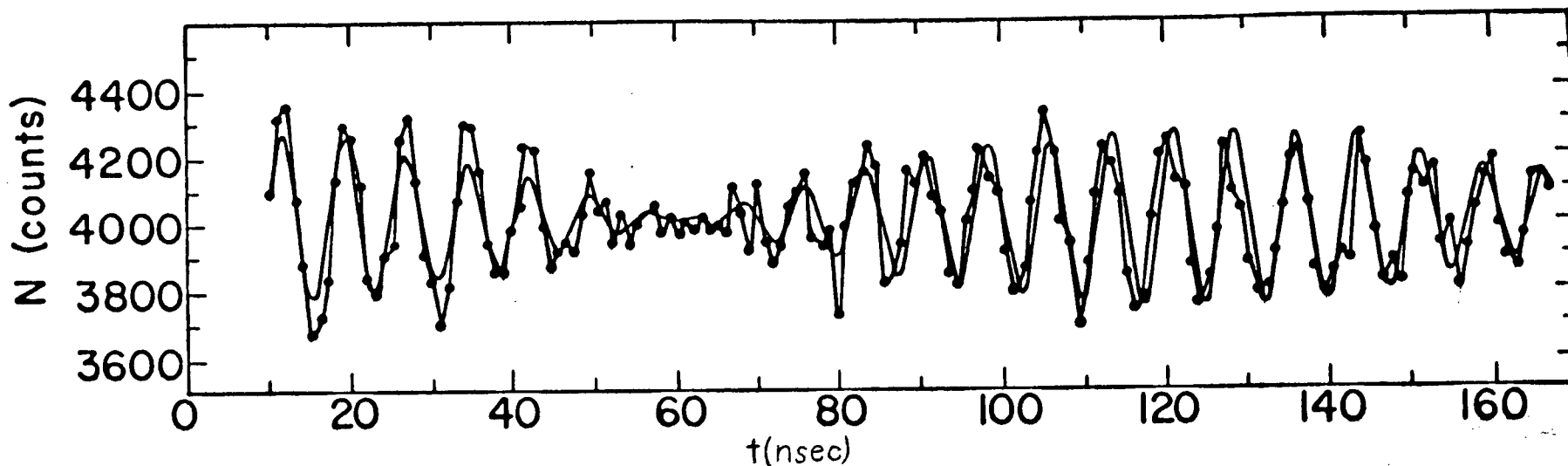


FIGURE I-3: "Two frequency precession" of the muon in muonium in fused quartz at 95 gauss [from Gurevich(71)]. The smooth line is a theoretical fit to the data. The fast oscillations at the characteristic muonium frequency, $\omega_{\text{Mu}}(95 \text{ gauss}) = 8.7 \times 10^{10} \text{ rad s}^{-1}$, are modulated by the slower beat frequency, $\Omega(95 \text{ gauss}) = 2.7 \times 10^7 \text{ rad s}^{-1}$.

signal in the time domain must have a period of 5 ns or more, corresponding to a frequency of $\leq 0.13 \times 10^{10}$ rad s⁻¹. Table I-1 shows that none of the Breit-Rabi transitions have such a frequency between 150 gauss and 10 kgauss. At much higher fields (≥ 100 kgauss), ω_{12} will once more become resolvable, but such fields are not experimentally available. If the experimental time resolution could be improved by a factor of 10, it would be possible to observe ω_{12} up to 10 kgauss and ω_{23} up to 1 kgauss. This illustrates an essential difference between μ^+ SR and MSR: while the former may be performed in magnetic fields of up to 15 kgauss, the latter is constrained to fields of less than a few hundred gauss.

Appendix II - The Effect of Chemical Reaction on the Muon Polarization

A. General

This Appendix will examine the muon spin polarization in a muonium ensemble which is undergoing chemical reaction in weak magnetic field ($B \leq 10$ gauss). Excluding the effects of chemical reaction, the muon polarization is characterized by equation I(16) of Appendix I:

$$\hat{P}_\mu(\phi, t) = f \cos(\omega_- t + \phi)$$

When a muonium atom reacts chemically, its electron forms a chemical bond and becomes paired with another electron breaking the hyperfine interaction between the Mu electron and muon (in general, intermediate muonic radicals are expected to be formed - this situation is not considered here since the lifetimes of any such radicals formed in the simple gas phase reactions studied in this thesis are surely shorter than one hyperfine period of 0.225 ns). Such a muon finds itself in a diamagnetic environment where it precesses at essentially the "free" muon frequency $\omega_\mu = \frac{1}{103} \omega_-$. Since $\omega_- = \frac{1}{2} (g\beta_e B/\hbar - g\beta_\mu B/\hbar)$ is dominated by the electron magnetic moment, the sense of ω_- precession is opposite to that of ω_μ . The correction between the free muon frequency and the diamagnetic muon frequency due to electron shielding (the so-called "chemical shift") is at the part per million level which is not resolvable with present MSR technology. The stronger dipolar coupling between diamagnetic muons and protons in water molecules (MuHO) has been resolved for crystalline gypsum ($\text{CaSO}_4 \cdot 2\text{H}_2\text{O}$) [Schenck (71)]. In fluids,

however, this effect appears as a broadening which does not fundamentally effect the approximation that the diamagnetic μ^+ frequency is ω_μ .

To zeroth order, because muonium atoms react at statistically distributed times, the coherently precessing Mu ensemble becomes an incoherently precessing μ^+ ensemble as the reaction proceeds. The net result is a relaxation of the Mu signal. The Mu signal, then, becomes a measure of the time-dependent probability of a Mu atom surviving without chemical reaction. Hence, the relaxation of the Mu signal has a simple exponential decay as given by equation (8) in Chapter I

$$S(\phi, t) = A_{\text{Mu}} e^{-\lambda t} \cos(\omega_{\text{Mu}} t + \phi) + A_\mu \cos(\omega_\mu t - \phi) \quad \text{II(1)}$$

where it is noted that $\omega_{\text{Mu}} \equiv \omega_-$ (see Figure II-1).

From the viewpoint of chemical kinetics, the rate equation for a bimolecular reaction of Mu with reagent X is given by the standard second order expression:

$$\frac{d[\text{Mu}]}{dt} = -k[X][\text{Mu}] \quad \text{II(2)}$$

where k is the bimolecular rate constant, [X] is the concentration of reagent X, and [Mu] is the muonium "concentration." Here, of course, the concept of a Mu concentration invokes the ergodic principle: an ensemble in time is formally the same as an ensemble in space [Arnold (68)]. Since the total number of Mu atoms involved in a reaction is minute compared with the number of reagent molecules ($\sim 10^7$ compared with $\sim 10^{19}$), equation II(2) may be

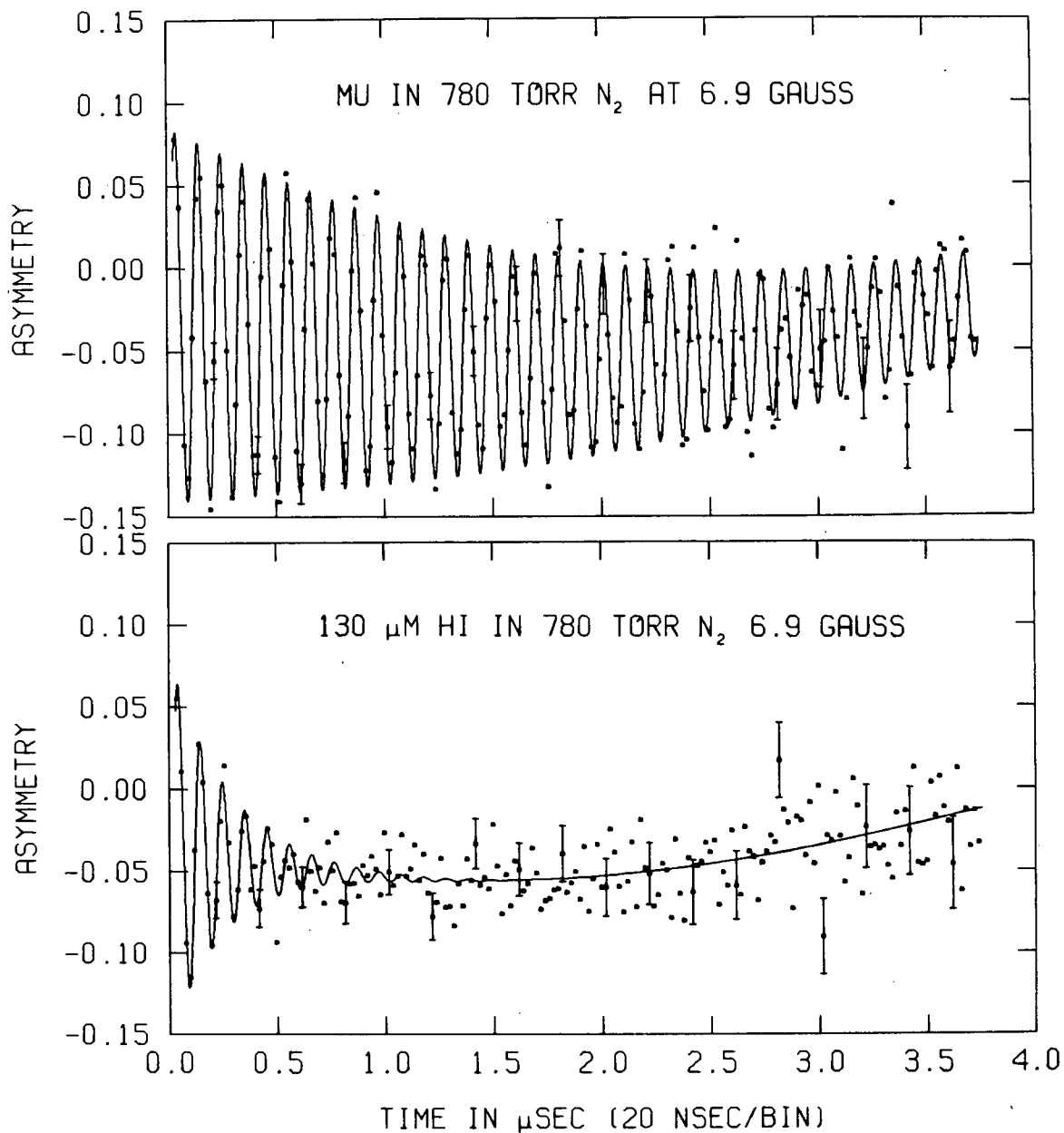


FIGURE II-1: The effect of chemical reaction on the muonium signal, $S(\phi, t)$ (equation II(1)). The upper figure shows the slow background relaxation rate of μ^+ muonium in pure N₂ giving $\lambda_0 = 0.34 \pm 0.02 \mu\text{s}^{-1}$ (equation II(3)). In the presence of HI reagent (lower figure), the exponential decay of the muonium signal due to removal of muonium atoms by chemical reaction is pronounced, giving a relaxation rate, $\lambda = 3.75 \pm 0.38 \mu\text{s}^{-1}$. Each histogram contains about 10^6 events and the lines are χ^2 -minimum fits to equation II(1).

rigorously re-written as a pseudo-first order rate, following the conventions of chemical kinetics:

$$\frac{d [\text{Mu}]}{dt} = -\lambda [\text{Mu}]$$

which identifies the Mu relaxation rate (equation II(1)) as the pseudo-first order rate constant, λ , as given by the linear relation (see Figure II-2):

$$\lambda = k[\text{X}] + \lambda_0 \quad \text{II(3)}$$

The intercept, λ_0 , is introduced to account for "background" relaxation of the Mu signal due to effects other than the chemical reaction of interest, such as magnetic field inhomogeneity, pressure broadening from the reaction medium, or background reactions with chemical impurities in the moderator gas. Thus, a bimolecular rate constant is simply determined from equation II(3) by the direct observation of the relaxation rate of a Mu signal as a function of concentration of the reacting molecules, [X].

B Generation of a Coherent Diamagnetic Muon Background:

$$\lambda \rightarrow 15 \mu\text{s}^{-1}, B \leq 10 \text{ gauss}$$

In practice, Mu relaxation rates are extracted from time histograms by the sort of fitting procedures described in Chapter II; consequently, it is important that the functional form of the muonium signal be properly described. Complications to equation II(1) arise under the conditions:

$$\omega_{\text{Mu}} \lesssim \lambda \ll \omega_0 \quad \text{II(4)}$$

because a significant fraction of muons in Mu are placed into diamagnetic environments by fast thermal chemical reactions

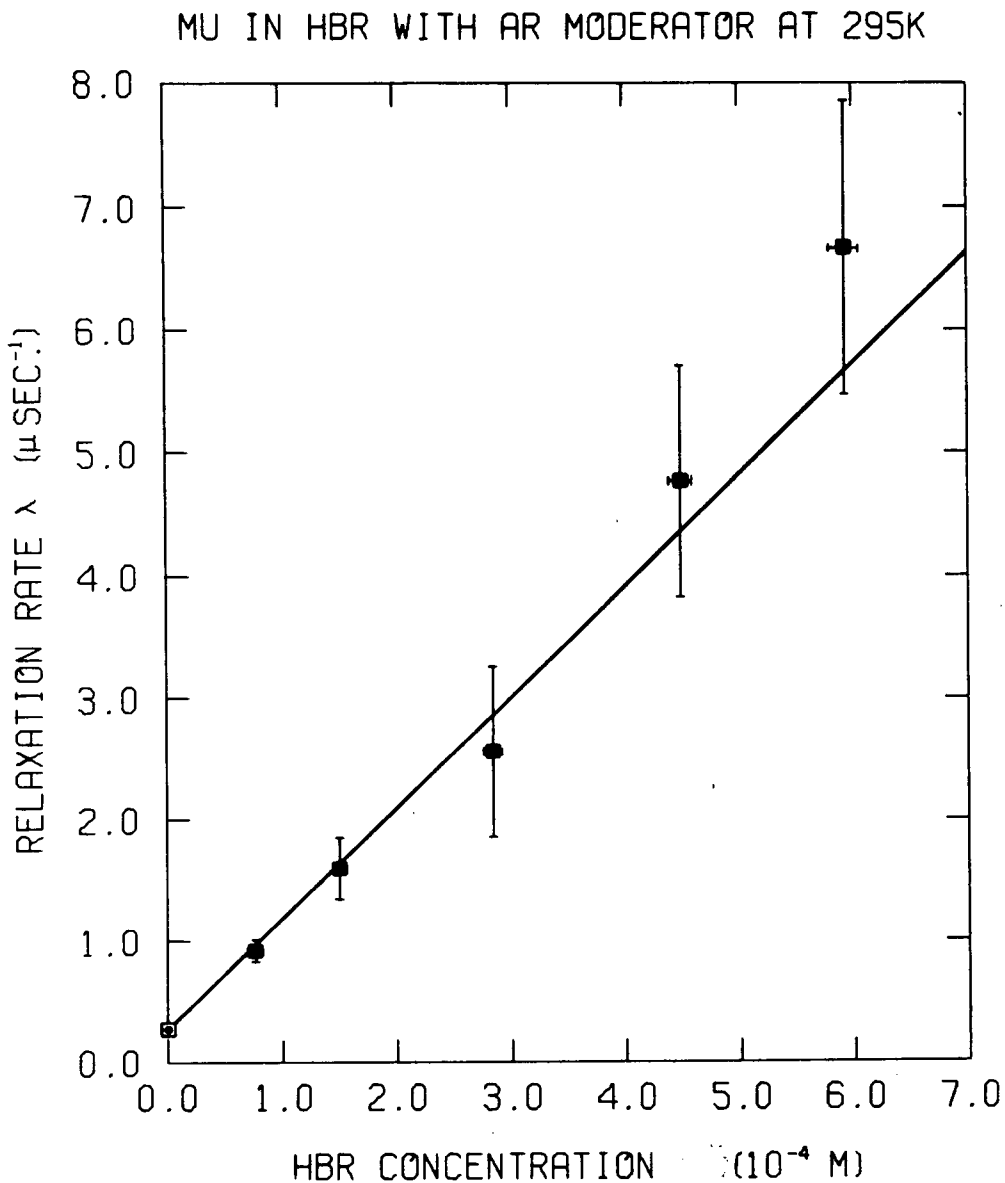


FIGURE II-2: The linear dependence of the relaxation rate of the muonium signal on reagent concentration (equation II(3)). The data points are weighted averages of λ 's extracted from left and right histograms, and the error bars represent 1σ . The line is a χ^2 -minimum fit giving a bimolecular rate constant, $k(295\text{K}) = (9.1 \pm 1.0) \times 10^7 \text{ l mole}^{-1} \text{ s}^{-1}$ and $\lambda_0 = 0.26 \pm 0.06 \mu\text{s}^{-1}$.

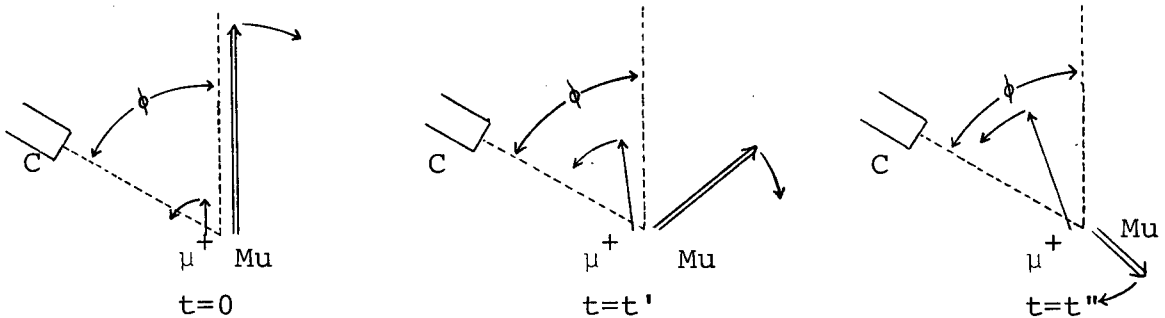
before the phase coherence is lost due to the rapid ω_{Mu} oscillation. That such a reaction is thermal is clear when it is recalled from Chapter I that thermalization of μ^+ takes place in ~ 1 ns and condition II(4) corresponds to reaction times much longer than 0.2 ns, the hyperfine period. Indeed, for experimental reasons cited in Chapter II, a detectable MSR signal is not observed for times less than 10 ns and, as described below, a signal must last for at least 300 ns to be measurable. The diamagnetic μ^+ ensemble generated under condition II(4) does not precess incoherently as assumed in Section A above, but, in fact, may give rise to a significant diamagnetic μ^+ signal. It is the task of this section to evaluate the functional form for $S(\phi, t)$ under such conditions. The condition in II(4) that $\lambda \ll \omega_0$ ensures that the fast hyperfine term in equation I(15) of Appendix I may still be ignored.

The maximum relaxation rate which is practical to measure directly is typically about $15 \mu\text{s}^{-1}$ which corresponds to a Mu signal lasting for about 300-400 ns. (limited by counting statistics). The magnetic field range, $1 \leq B \leq 10$ gauss, corresponds to $9 \mu\text{s}^{-1} \leq \omega_{\text{Mu}} \leq 89 \mu\text{s}^{-1}$; thus, for $\lambda = 15 \mu\text{s}^{-1}$, condition II(4) is reasonably well satisfied.

The calculation below invokes the following assumptions: (1) the muon lifetime is independent of the μ^+ environment; (2) the field is weak enough that beating may be ignored (Ω in equation I(15) of Appendix I) and λ is small enough that the hyperfine oscillation may be ignored (terms

containing ω_0 in equation I(15) of Appendix I), (3) the chemical process that places a single μ^+ from Mu into a diamagnetic environment occurs instantaneously over statistically distributed times, (4) diamagnetic μ^+ precess at the same frequency as "free" μ^+ ions, (5) while it is not required that all μ^+ entering the target initially form Mu (allowing for μ^+ to thermalize as free μ^+ ions or to be placed into diamagnetic environments by fast epithermal reactions that occur before one hyperfine oscillation), it is assumed that these fates are arbitrated at essentially $t=0$, (6) the initial phases of μ^+ in Mu and free μ^+ are the same, (7) thermal free μ^+ do not relax by, say, forming Mu after $t=0$. For convenience, both free μ^+ ions and diamagnetic μ^+ will be referred to as "free" μ^+ .

A geometrical formulation of the problem is schematically given by:



Here, C is a counter placed at an angle ϕ to the initial μ^+ polarization, \Uparrow represents the Mu spin polarization and \Uparrow represents the free μ^+ polarization. The lengths of the arrows represent the magnitudes of the Mu and free μ^+ polarizations in arbitrary units. By inspection, the total μ^+ signal is given by:

$$S_{\text{total}}(\phi, t) = A_{\text{Mu}}(t) \cos(\omega_{\text{Mu}} t + \phi) + A_{\mu}(t) \cos(\omega_{\mu} t - \phi)$$

where $A_{Mu}(t)$ and $A_{\mu}(t)$ are the asymmetries of muons in Mu and free μ^+ ensembles respectively. $A_{Mu}(t)$ is given by equation (7) in Chapter I and $A_{\mu}(t)$ is:

$$A_{\mu}(t) = A_{\mu} + A_{Mu} \int_0^t e^{-\lambda t'} \cos \omega_p t' dt' \quad \text{II(5)}$$

where A_{μ} and A_{Mu} are the amplitudes of the free μ^+ and Mu ensembles at $t=0$, and $\omega_p = (\omega_{Mu} + \omega_{\mu})$ is the relative angular velocity of the two ensemble spin vectors precessing in opposite directions. Performing the integration in II(5), the total signal becomes:

$$S_{total}(\phi, t) = A_{Mu} e^{-\lambda t} \cos(\omega_{Mu} t + \phi) + A_{\mu} \cos(\omega_{\mu} t - \phi) \\ + \frac{A_{Mu} \lambda}{\lambda^2 + \omega_p^2} [\omega_p e^{-\lambda t} \sin \omega_p t - \lambda e^{-\lambda t} \cos \omega_p t + \lambda] \cos(\omega_{\mu} t - \phi) \quad \text{II(6)}$$

The correction calculated above is illustrated in Figure II-3 which plots equation II(1) (lower lines asymptotically approaching an asymmetry of zero at long times) and equation II(6) (upper lines) for a series of fields ranging from 2 to 10 gauss with $\phi = 1$ radian, $A_{Mu} = 0.1$, $A_{\mu} = 0.0$, and $\lambda = 15 \mu\text{s}^{-1}$. The ω_{μ} oscillation in the upper curves is not obvious because of its low frequency at these fields. Clearly, at 10 gauss, equation II(1) is a very good approximation to $S_{total}(\phi, t)$ while at 2 gauss, the coherent diamagnetic μ^+ signal requires description by equation II(6).

In Figure II-4, equations II(1) and II(6) are again plotted for a series of λ 's ranging from $15 \mu\text{s}^{-1}$ to $300 \mu\text{s}^{-1}$ at a fixed field of 7.5 gauss with $A_{Mu} = 0.1$, $A_{\mu} = 0.0$, and $\phi = 1$ radian. Although the Mu signal in the plots where $\lambda > 15 \mu\text{s}^{-1}$ is not

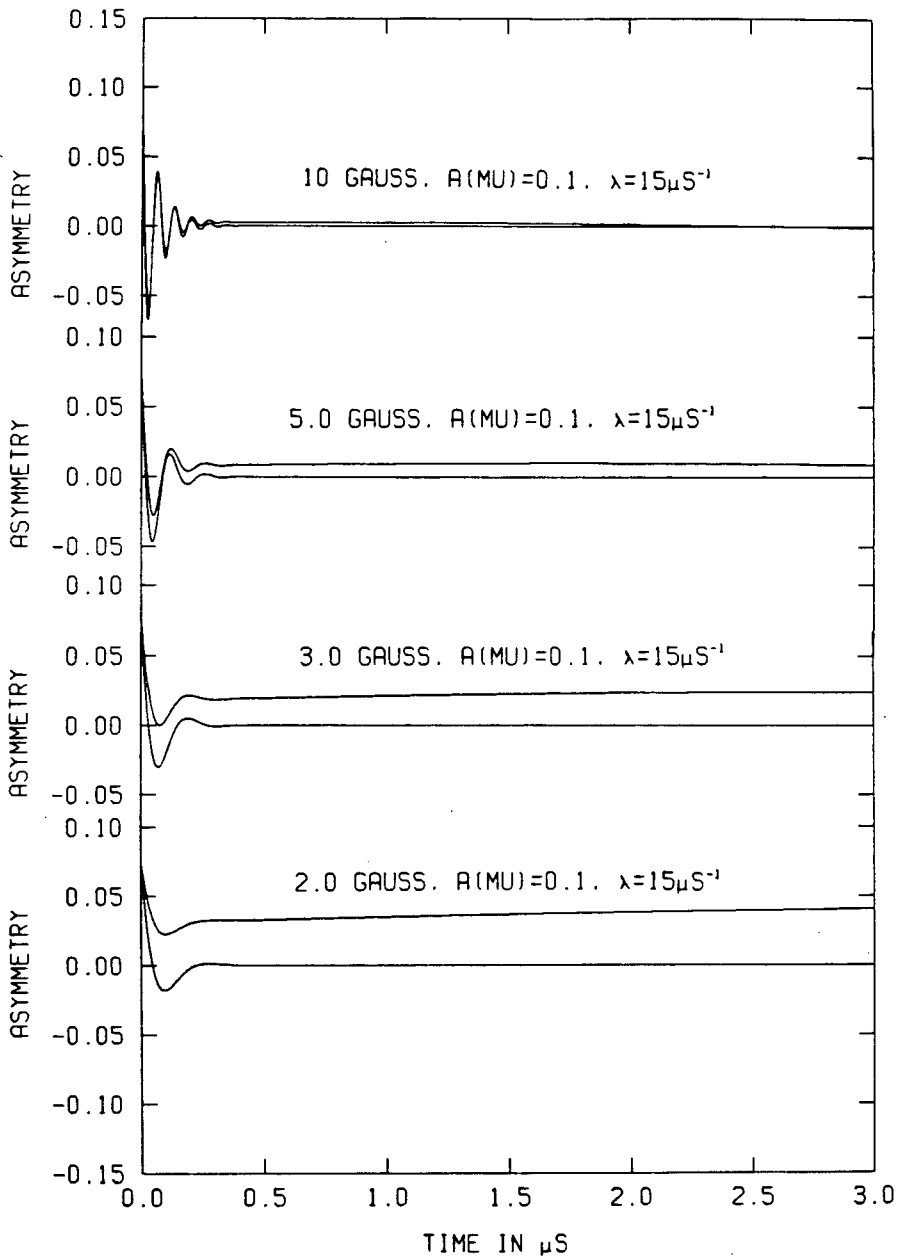


FIGURE II-3: The generation of a coherent diamagnetic muon background signal by fast chemical reactions of muonium. The lines are theoretical muonium signals with pseudo first order rate constants, $\lambda = 15 \mu\text{s}^{-1}$, in various weak magnetic fields for counters placed at 1 radian to the muon beam. The initial muonium amplitude is 10% and the initial free muon amplitude is 0%. The lower curves correspond to equation II(1) and assume complete loss of muon phase coherence during chemical reaction; the upper curves correspond to equation II(6) and show that if $\lambda \geq \omega_{\text{Mu}}$, the muon phase coherence is not lost during chemical reaction, but may give rise to a significant "residual muon polarization" signal.

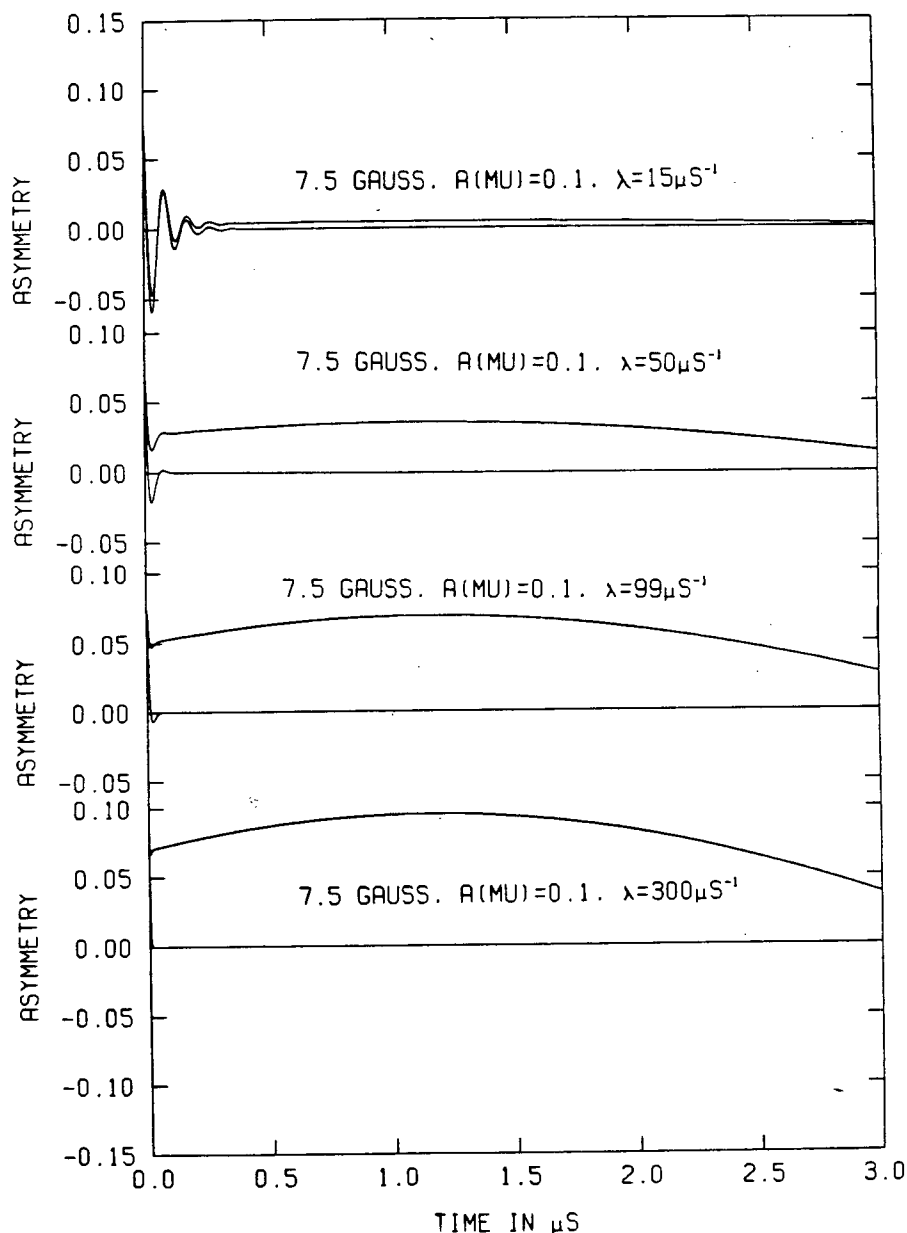


FIGURE II-4: The dependence of the amplitude of the "residual muon polarization" on muonium reaction rate at 7.5 gauss. As in Figure II-3, the lower curves correspond to equation II(1) and the upper curves to equation II(6). Early determinations of muonium reaction rates [Brewer (72)] were made by the residual polarization method by measuring the amplitude and phase of the diamagnetic muon signal by μ^+ SR and relating these to the fast muonium relaxation rates. In the present work, muonium reaction rates are measured directly by MSR.

of long enough duration to allow useful fitting of the data, these plots do illustrate the effect known as the "residual muon polarization" [Brewer (75), Fleming (79)] in which large values of λ manifest themselves as larger values of the "free" muon polarization. When λ becomes sufficiently large that the condition

$$\omega_- \ll \omega_0 \lesssim \lambda \quad \text{II(7)}$$

is fulfilled, the expression for $S_{\text{total}}(\phi, t)$ must include an integration analogous to II(5) over the hyperfine terms of equation I(15) in Appendix I. The upshot of the calculation is that fast Mu relaxations not only express themselves as large values of the residual polarization, but also with rate dependent values of the phase of the residual polarization. Previously, these facts have been exploited to measure the rates of fast reactions of Mu in liquids by this indirect method mentioned in Chapter I [Brewer (72)].

Appendix III - Data Acquisition with High Current Muon Beams:
Theory and Practice

In Chapter II, Section C, a qualitative assessment of the problem of muon pile-up is presented; in the first two Sections of this Appendix, the absolute magnitude of various multiple muon events and their effects on the resultant MSR time spectra are calculated. The last Section of this Appendix details the existing MSR data acquisition system at TRIUMF which deals with high muon beam currents.

A The Optimal Good Event Rate

It is the task of this Section to calculate the optimal "good" (see Chapter II, Section C) event rate for an experiment with a data acquisition system that discards the ambiguous multiple muon events. The first calculation is for "post- μ_i " second muons arriving during the observation time T after the entry of the initial clock-starting muon, μ_i , into the target. For this and subsequent calculations, it is assumed that the arrival of beam muons obeys a Poisson time distribution; this assumption is valid over time intervals much larger than the microscopic beam structure at the cyclotron radio frequency - 23 MHz at TRIUMF. The Poisson distribution function is:

$$P_p(n, \mathcal{N}, t) = \frac{(\mathcal{N}t)^n}{n!} e^{-\mathcal{N}t} \quad \text{III(1)}$$

where P is the probability of n events occurring in a time t, given an average event rate \mathcal{N} . If a valid event is defined as one where no other muons appear during a time T after the first

muon, then the probability of an event being valid is given by

$$P_p(0, \mathcal{N}, T) = e^{-\mathcal{N}T}$$

and the average valid event rate, \mathcal{N}_g , is

$$\mathcal{N}_g = \mathcal{N}e^{-\mathcal{N}T} \quad \text{III(2)}$$

Since $\mathcal{N}_g = 0$ when $\mathcal{N} = 0$ or $\mathcal{N} = \infty$, it is clear that this positive function of \mathcal{N} has a maximum for constant T as shown in Figure III-1; this point is also intuitively obvious since at low muon beam currents pile-up is negligible, while at high beam currents valid events are rare. The optimum beam rate occurs under the condition

$$\frac{d\mathcal{N}_g}{d\mathcal{N}} = e^{-\mathcal{N}T} - \mathcal{N}Te^{-\mathcal{N}T} = 0$$

or
$$\mathcal{N}_{\text{Max}} = \frac{1}{T} \quad \text{III(3)}$$

This important result implies that under optimal conditions, 37% of the muons are free of pile-up and 63% must be rejected. For $T = 4\tau_\mu$ in the example of Chapter II, the optimal beam current is $1.1 \times 10^5 \text{ s}^{-1}$. It may be noted that function III(2) is asymmetrically peaked with respect to \mathcal{N} , rising rapidly to a maximum and tapering off slowly at large \mathcal{N} . This becomes a practical consideration since muon beam currents are generally lowered incrementally by collimation rather than by fine adjustment of the proton beam itself. Since it is unlikely that any collimator will provide exactly the optimal effective beam current, it is advantageous to bias it toward a larger-than-optimal value rather than a smaller one.

How can the above calculation be extended to include

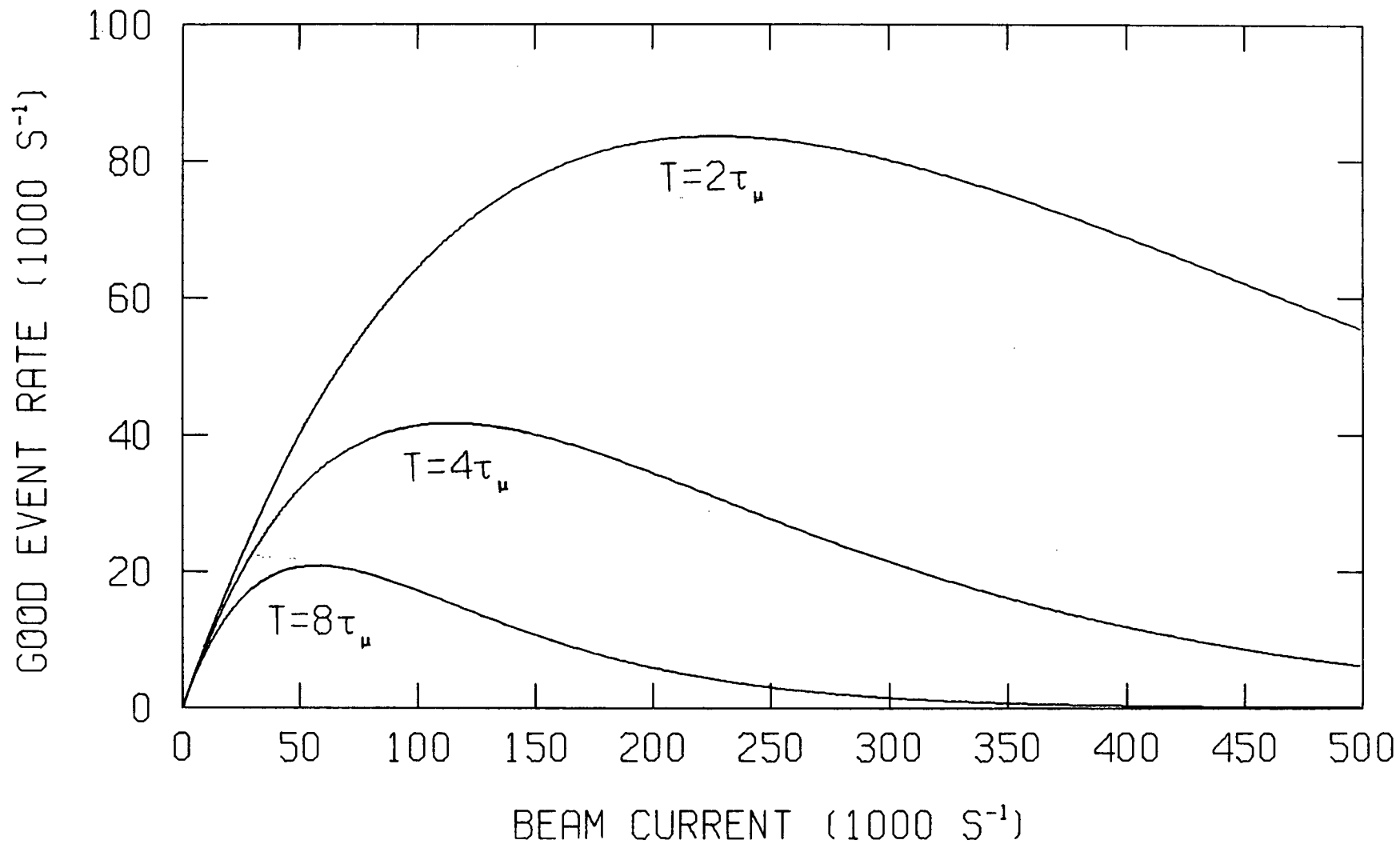


FIGURE III-1: The net good event rate (without pile-up) as a function of beam current for various muon decay gates. The good event rate is given by equation III(2).

rejection of "pre- μ_i " second muons arriving during a time T before the entry of μ_i , the clock-starting muon? The answer is simply to apply the above arguments backwards in time. While intuitively correct, this is also a recognition of the fact that the arrival of muons is a Markov process (a random process in which the future is completely determined by the present and independent of the way in which the present evolved) and that a Markov process is also Markov in reverse (see for example [Feller (50)]). The net result for both post- μ_i and pre- μ_i event rejection is that the rate of valid events is given by:

$$\mathcal{N}_g = \mathcal{N}(e^{-\mathcal{N}T} \cdot e^{-\mathcal{N}T}) = \mathcal{N}e^{-2\mathcal{N}T}$$

which is optimal when

$$\mathcal{N}_{\text{Max}} = \frac{1}{2T} \quad \text{III (4)}$$

that is, when the beam rate is the inverse of twice the muon gate width. Thus, for $T = 4\tau_\mu$, $\mathcal{N}_{\text{Max}} = 5.7 \times 10^4 \text{ s}^{-1}$ which, again, corresponds to an event acceptance rate of 37%.

B Spectral Distortions due to Muon Pile-up

In the preceding Section, it was shown that pre- and post- μ_i multiple muon events reduce the good event rate by the same amount, given pre- and post- μ_i T -gates of the same width. However, this does not imply that the spectral distortions due to pre- and post- μ_i multiple muon events are of either the same magnitude or character; rather, it is shown in this Section

that post- μ_i events are much more devastating than pre- μ_i events.

The effects of muon pile-up upon the time histogram are calculated separately for the pre- and post- μ_i cases in three stages: firstly, the pile-up effects on the apparent muon lifetime (ignoring the μ SR or MSR signal) are calculated assuming 100% efficiency for decay positron detection (i.e. 4π steradians solid angle, 100% counter efficiency); secondly, this calculation is extended (again, ignoring the μ SR or MSR signal) to allow for imperfect decay positron detection efficiency, $0 \leq \epsilon \leq 1$, $\epsilon = \text{counter solid angle} \times \text{counter efficiency}$; finally, the muon pile-up effects on the μ SR or MSR signal are calculated for the case of imperfect decay positron detection.

In the following discussion, two concepts must not be confused: (1) The function, e^{-t/τ_μ} , sometimes called a "decay" curve, is really a "survival" curve giving the probability that a muon will survive until time t . The probability that a muon will decay before time t is $(1 - e^{-t/\tau_\mu})$.

(2) Given that a muon has survived until t , the probability that it will decay during the next interval dt is the same for all muons; that is, a 10 μ s old muon has the same probability of decaying during the next ps as a 1 ns old muon. What is the probability that a muon will decay during the interval t and $t + dt$? This is just the product of the probability that it has survived until t (that is, e^{-t/τ_μ})

and the probability of it decaying during the next dt , which is a constant independent of t . Therefore, the probability of a muon decaying between t and $t + dt$ is proportional to e^{-t/τ_μ} , and in this sense e^{-t/τ_μ} may be thought of as a "decay" curve. It is this probability that is identified with an experimental time histogram.

At first glance, it might appear that pile-up events cannot introduce distortions in the measured lifetime of the muon since the probability of decay per unit time is the same for all muons. Lifetime distortions are introduced as experimental artifacts, however, because in a pile-up situation the experiment cannot identify which muon decays; consequently, it is the first detected decay that stops the clock. This effect may be understood by considering the following gedanken experiment: imagine a magic beamline that delivers exactly two muons at intervals of T , the muon gate width, and imagine 100% decay detection efficiency. Obviously, one muon will generally decay before the other. Since it is the first muon decay that stops the clock, an accumulated histogram will be strongly biased toward early times, thereby reducing the apparent muon lifetime. For a given pair of muons entering the target at $t = 0$, what is the probability that the clock will not be stopped before some later time t ? Denoting the probability that the n th muon will survive until t as

$$P(s_n) = e^{-t/\tau_\mu} \quad \text{III(5)}$$

and recognizing that the decay or survival of individual muons are statistically independent events, the required probability is

$$P(s_1 \cdot s_2) = P(s_1)P(s_2) = e^{-2t/\tau_\mu} \quad \text{III(6)}$$

That is, the probability that the clock will not be stopped by t is just the probability that both muons survive (at least) until t . Similarly, denoting the probability that the n th muon will decay before t as

$$P(d_n) = 1 - e^{-t/\tau_\mu} \quad \text{III(7)}$$

it is seen that the probability that the clock will be stopped before t :

$$\begin{aligned} P(d_1+d_2) &= P(d_1) + P(d_2) - P(d_1 \cdot d_2) \\ &= P(d_1) + P(d_2) - P(d_1)P(d_2) \\ &= 2(1 - e^{-t/\tau_\mu}) - (1 - e^{-t/\tau_\mu})^2 \quad \text{III(8)} \\ &= 1 - e^{-2t/\tau_\mu} \end{aligned}$$

It may be noted that $P(s_1 \cdot s_2) + P(d_1+d_2) = 1$, as it should. As discussed in the previous paragraph, an experimental time histogram corresponds to the probability that the clock is not stopped before t , but does stop between t and $t + dt$ and that this is proportional to the probability that the clock is not stopped before time t . Since there are two muons resident in the target at t in this example, the probability of some muon decaying between t and $t + dt$ is doubled, and the experimental histogram has the form

$$N(t) = 2e^{-2t/\tau_\mu}$$

In this gedanken experiment, then, the measured muon lifetime

is $\frac{1}{2}\tau_\mu$. The last expression must be normalized by dividing by 2 making it correspond to one muon at $t = 0$ so that it may be compared with the theoretical non-distorted histogram ($N(t) = e^{-t/\tau_\mu}$), giving:

$$N_0(t) = e^{-2t/\tau_\mu}$$

In this example, the normalization is trivial and it makes the argument that led to the extra factor of 2 in the first place seem superfluous. However, when the procedure used in this example is applied to more complex cases below, the normalizations that result are non-trivial.

(i) Pre- μ_i Muons and τ_μ : 100% Decay Positron Detection Efficiency

Equation III(6) may be extended to give the probability that the clock will not be stopped before t if n muons enter the target at $t = 0$:

$$P(s_1 \cdot s_2 \cdot \dots \cdot s_n) = e^{-nt/\tau_\mu} \quad \text{III(9)}$$

where $P(s_1) = P(s_2) = \dots = P(s_n)$; and equation III(8) may be extended to give the probability that the clock will be stopped before t if n muons enter the target at $t = 0$:

$$\begin{aligned} P(d_1 + d_2 + \dots + d_n) &= \sum_{k=1}^n (-1)^{k-1} \binom{n}{k} P(d_k)^k \\ &= 1 - e^{-nt/\tau_\mu} \end{aligned} \quad \text{III(10)}$$

where $P(d_1) = P(d_2) = \dots = P(d_n)$.

Pre- μ_i muons arrive in the target before $t = 0$ (when μ_i arrives) but may not be resident in the target at $t = 0$ because they have already decayed. What, then, is the

probability of there being n muons in the target at $t = 0$ (not counting the μ_i muon)? Consider an arbitrary time interval γ before $t = 0$ (it will be shown eventually that the following calculation is independent of γ for sufficiently large γ and that $\gamma = T$, the muon gate width, fulfills this condition). The probability of n muons entering the target during γ for an average beam rate of λ muons per unit time is given by the Poisson distribution, equation III(1). Since, on average, the probability of a muon arriving in the target during any subinterval $\Delta\gamma$ of γ is the same for all $\Delta\gamma$, the average probability that a muon arriving during γ survives until $t = 0$ is:

$$\bar{P}(s(\gamma)) = \frac{\int_0^\gamma e^{-t/\tau_\mu} dt}{\int_0^\gamma dt} = \frac{\tau_\mu}{\gamma}(1 - e^{-\gamma/\tau_\mu}) \quad \text{III(11)}$$

where \bar{P} denotes the average probability. The subscripts used in equation III(5) have been dropped since this probability is the same for all muons; also, γ has been included as an argument of $\bar{P}(s)$. It may be noted that equation III(11) goes to the proper limits of γ :

$$\lim_{\gamma \rightarrow 0} \frac{\tau_\mu}{\gamma}(1 - e^{-\gamma/\tau_\mu}) = 1$$

and
$$\lim_{\gamma \rightarrow \infty} \frac{\tau_\mu}{\gamma}(1 - e^{-\gamma/\tau_\mu}) = 0$$

Similarly, the average probability that a muon entering the target during γ has decayed by $t = 0$ is:

$$\bar{P}(d(\gamma)) = 1 - \bar{P}(s(\gamma)) \quad \text{III(12)}$$

Assuming that there are no muons in the target at $t = 0 - \gamma$, the probability of there being n muons in the target at $t = 0$ is the probability that:

n arrive during $\gamma \times$ the prob. that all last until $t=0$
 $+ n+1$ arrive during $\gamma \times$ the prob. that all but 1 last until $t=0$
 $+ n+2$ arrive during $\gamma \times$ the prob. that all but 2 last until $t=0$
 $+ \dots$

This may be expressed symbolically by combining equations III(11) and III(12) with the Poisson distribution:

$$\sum_{k=n}^{\infty} \binom{k}{n} P_p(k, \mathcal{N}, \gamma) \bar{P}(s(\gamma))^n \bar{P}(d(\gamma))^{k-n} \quad \text{III(13)}$$

Combining this expression with equation III(9) multiplied by the number of muons in the target gives the unnormalized histogram:

$$N(t, \mathcal{N}, \gamma) = \sum_{n=0}^{\infty} \left[\sum_{k=n}^{\infty} \binom{k}{n} P_p(k, \mathcal{N}, \gamma) \bar{P}(s(\gamma))^n [1 - \bar{P}(s(\gamma))]^{k-n} \right] \cdot (n+1) e^{-(n+1)t/\tau_{\mu}} \quad \text{III(14)}$$

where $n+1$ refers to n pre- μ_i muons plus the μ_i muon.

It must now be verified that equation III(14) is not a function of γ for sufficiently large γ . Since the last term of equation III(14) is not a function of γ (but only a function of $t \geq 0$), it may be set to 1 (i.e. $t = 0$) and the equation re-written by expanding the Poisson term:

$$N(0, \mathcal{N}, \gamma) = \sum_{n=0}^{\infty} (n+1) \bar{P}(s(\gamma))^n e^{-\mathcal{N}\gamma} \sum_{k=n}^{\infty} \binom{k}{n} \frac{(\mathcal{N}\gamma)^k}{k!} [1 - \bar{P}(s(\gamma))]^{k-n}$$

Changing the index of the second summation yields:

$$N(0, \mathcal{N}, \gamma) = \sum_{n=0}^{\infty} (n+1) \bar{P}(s(\gamma))^n e^{-\mathcal{N}\gamma} \frac{(\mathcal{N}\gamma)^n}{n!} \sum_{m=0}^{\infty} \frac{(\mathcal{N}\gamma)^m}{m!} [1 - \bar{P}(s(\gamma))]^m$$

Substituting equation III(11) for $\bar{P}(s(\gamma))$ and $e^x = \sum_{n=0}^{\infty} \frac{x^n}{n!}$

yields:

$$\begin{aligned} N(0, \mathcal{N}, \gamma) &= \sum_{n=0}^{\infty} (n+1) \bar{P}(s(\gamma))^n \frac{(\mathcal{N}\gamma)^n}{n!} e^{-\mathcal{N}\gamma} e^{\mathcal{N}\gamma} e^{-\mathcal{N}\gamma \bar{P}(s(\gamma))} \\ &= \sum_{n=0}^{\infty} \frac{(n+1)}{n!} [\mathcal{N}\tau_{\mu} (1 - e^{-\gamma/\tau_{\mu}})]^n e^{-\mathcal{N}\tau_{\mu}} e^{\mathcal{N}\tau_{\mu}} (e^{-\gamma/\tau_{\mu}}) \end{aligned}$$

Taking the limit of this expression as $\gamma \rightarrow \infty$ gives:

$$\lim_{\gamma \rightarrow \infty} N(0, \mathcal{N}, \gamma) = \sum_{n=0}^{\infty} \frac{(n+1)}{n!} (\mathcal{N}\tau_{\mu})^n e^{-\mathcal{N}\tau_{\mu}}$$

$$\begin{aligned} \text{or } N(0, \mathcal{N}) &= e^{-\mathcal{N}\tau_{\mu}} \left\{ \mathcal{N}\tau_{\mu} \sum_{m=0}^{\infty} \frac{(\mathcal{N}\tau_{\mu})^m}{m!} + \sum_{n=0}^{\infty} \frac{(\mathcal{N}\tau_{\mu})^n}{n!} \right\} \\ &= 1 + \mathcal{N}\tau_{\mu} \end{aligned} \tag{III(15)}$$

As a check, one may arrive at this result by answering the question, "What is the average number of muons in the target at any time?" The answer is simply the integral of the product of the beam current and the muon survival probability:

$$\begin{aligned} \int_0^{\infty} \mathcal{N} e^{-t/\tau_{\mu}} dt &= \mathcal{N}\tau_{\mu} (e^0 - e^{-\infty/\tau_{\mu}}) \\ &= \mathcal{N}\tau_{\mu} \end{aligned}$$

where the lower integration limit refers to the time the beam is turned on and the upper integration limit refers to some very much later time. Thus, when the μ_i muon enters the target at $t = 0$, there are, on average, already $\mathcal{N}\tau_{\mu}$ pre- μ_i muons in the target for a total of $1 + \mathcal{N}\tau_{\mu}$ muons. It is easily verified that equation III(14) is reasonably independent of γ for $\gamma \geq T$, a typical muon decay gate. For example, if the

upper integration limit of the last expression is set to $\mathcal{T} = T \neq 4\tau_\mu$, say, the result is accurate to better than 2%.

Equation III(15) provides the normalization for equation III(14):

$$N_0(t, \mathcal{N}) = \frac{\sum_{n=0}^{\infty} \left(\sum_{k=n}^{\infty} \binom{k}{n} P_p(k, \mathcal{N}, T) \bar{P}(s(T))^n [1 - \bar{P}(s(T))]^{k-n} \right)}{1 + \mathcal{N}\tau_\mu} \cdot (n+1)e^{-(n+1)t/\tau_\mu} \quad \text{III(16)}$$

The true muon survival curve, e^{-t/τ_μ} , is compared with equation III(16) for various beam currents in Figures III-2 and III-3. As expected, the effect of pre- μ_i muons is pronounced at early times but diminishes to insignificance at late times, as evidenced by the fact that the logarithmic curves are parallel at late times. This is because, by definition, a pre- μ_i muon is older than the μ_i muon, and so its chance of surviving until $t = 4\mu\text{s}$, say, is much less than that of the μ_i muon. The apparent muon lifetimes obtained by fitting the histogram to e^{-t/τ_μ} over a $4\mu\text{s}$ time range would be (from Figure III-3) 2.0, 1.85, and 1.7 μs for beam currents of 50, 100, and $150 \times 10^3 \text{ s}^{-1}$ respectively.

(ii) Pre- μ_i Muons and τ_μ ; ϵ Decay Positron Detection Efficiency

The provision of a decay positron detection efficiency means that there are two possible outcomes of a muon decay: either it is detected or it is not. Using the notation of the previous Section, the probability that a muon decays and is detected is

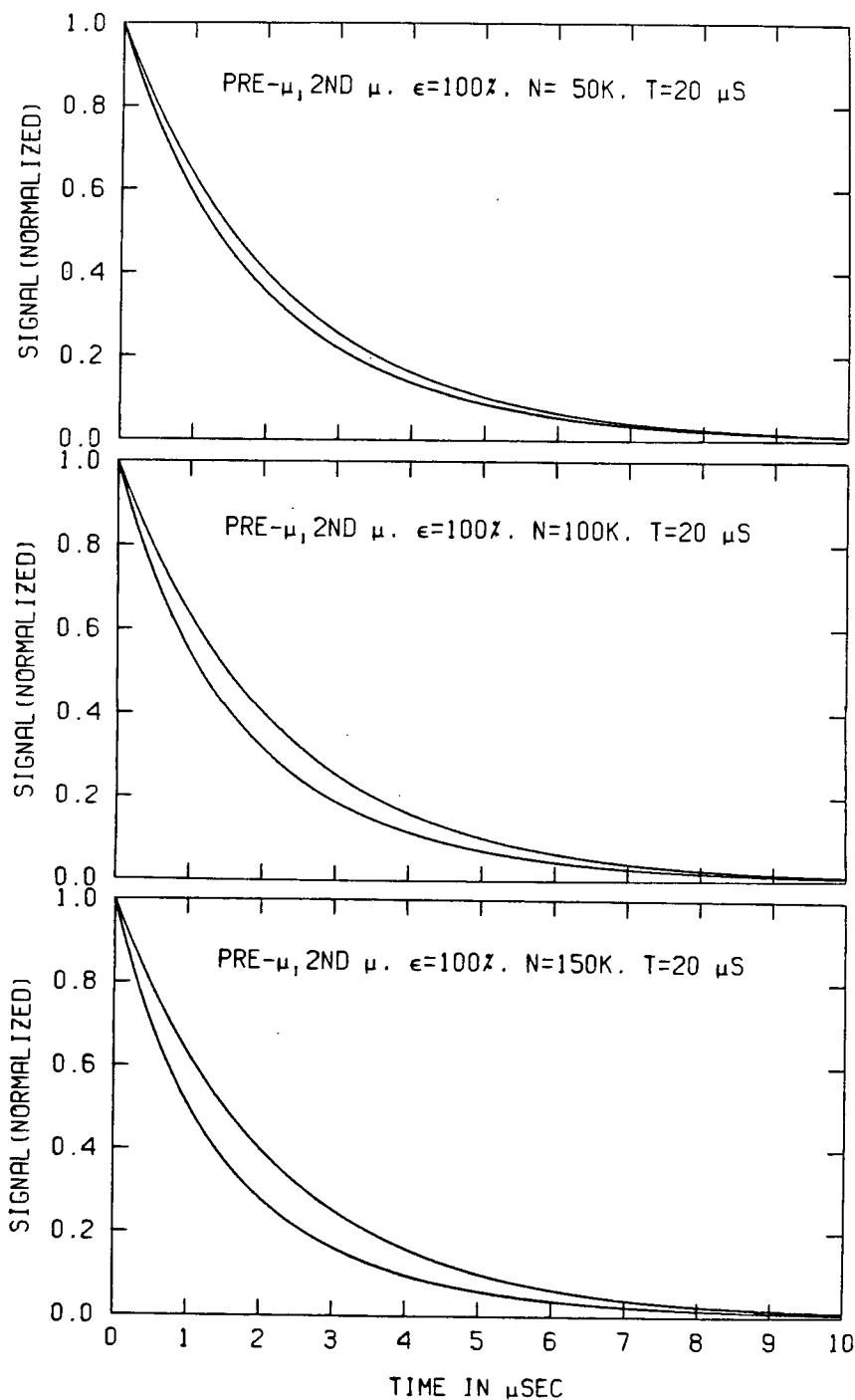


FIGURE III-2: The effect of pre- μ_i muons on the apparent muon lifetime, with $\epsilon = 100\%$ positron counting efficiency. The upper curves in each plot show the "true" histogram, e^{-t/τ_μ} , while the lower curves show equation III(16) for beam currents of 50, 100, and 150 $\times 10^3 \text{ s}^{-1}$. With the muon decay gate $T = 20 \mu\text{s}$, this calculation is accurate to about 1 ppm.

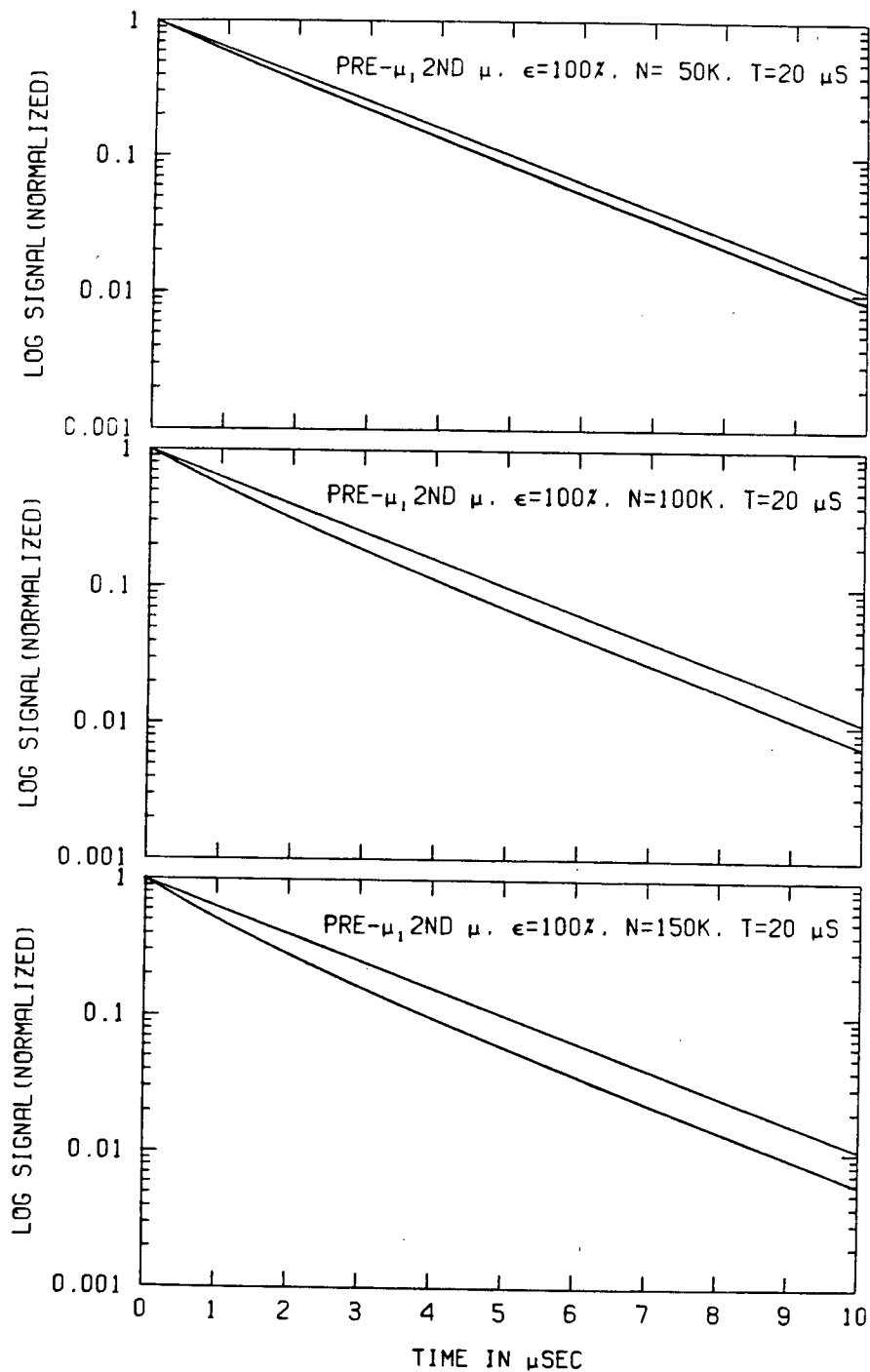


FIGURE III-3: Logarithmic plots of Figure III-2. At late times, the lower, pre- μ_1 curves are parallel to the true muon lifetime curves, showing that the effect of pre- μ_1 muons on the measured muon lifetime is only important at early times.

$$P(d) = \epsilon(1-e^{-t/\tau_\mu})$$

Similarly, the probability that a muon decays and is not detected is

$$P(\hat{d}) = (1-\epsilon)(1-e^{-t/\tau_\mu})$$

Proceeding as in the previous Section, an equation analogous to equation III(6) may be written to give the probability that the clock will not be stopped before t if two muons enter the target at $t = 0$:

$$\begin{aligned} & P(s_1 \cdot s_2) + P(s_1 \cdot \hat{d}_2) + P(\hat{d}_1 \cdot s_2) + P(\hat{d}_1 \cdot \hat{d}_2) \\ & = (e^{-t/\tau_\mu})^2 + 2(1-\epsilon)e^{-t/\tau_\mu}(1-e^{-t/\tau_\mu}) + (1-\epsilon)^2(1-e^{-t/\tau_\mu})^2 \end{aligned} \quad \text{III(17)}$$

The first term is identical to equation III(6), the second term corresponds to one muon surviving and the other decaying undetected, and the last term corresponds to both muons decaying without detection. Similarly, the probability that the clock will be stopped before t may be written (analogous to equation III(8)):

$$P(d_1+d_2) = 2\epsilon(1-e^{-t/\tau_\mu}) - \epsilon^2(1-e^{-t/\tau_\mu})^2 \quad \text{III(18)}$$

that is, it corresponds to the probability of either muon decaying with detection. Again, it is readily checked that the sum of equations III(17) and III(18) is one. Equation III(17) may be generalized to correspond to the case of n muons entering the target at $t = 0$:

$$P_{\text{not stopped}} = \sum_{k=0}^n \binom{n}{k} (1-\epsilon)^k (e^{-t/\tau_\mu})^{n-k} (1-e^{-t/\tau_\mu})^k \quad \text{III(19)}$$

and equation III(18) may be generalized in like manner:

$$P_{\text{stopped}} = \sum_{k=1}^n (-1)^{k-1} \binom{n}{k} \epsilon^k (1-e^{-t/\tau_{\mu}})^k \quad \text{III(20)}$$

The experimental histogram corresponds to the probability that the clock has not stopped before t but does stop between t and $t + dt$. When each term in equation III(19) is multiplied by the number of muons still in the target at t , the desired result is obtained:

$$N(t) = \sum_{k=0}^n \binom{n}{k} (1-\epsilon)^k (e^{-t/\tau_{\mu}})^{n-k} (1-e^{-t/\tau_{\mu}})^k (n-k) \quad \text{III(21)}$$

Notice that the factor of $(n-k)$ eliminates the last term in equation III(21) corresponding to the situation in which all muons decay undetected before t . One can now write the experimental histogram analogous to equation III(14) corresponding to pre- μ_i muons with a counting efficiency ϵ by combining equation III(21) with expression III(13) yielding:

$$N(t, \mathcal{N}) = \sum_{n=0}^{\infty} \left[\sum_{k=n}^{\infty} \binom{n}{k} P_P(k, \mathcal{N}, T) \bar{P}(s(T))^n [1-\bar{P}(s(T))]^{k-n} \right] \cdot \left[\sum_{\ell=0}^{m=n+1} \binom{m}{\ell} (1-\epsilon)^{\ell} (e^{-t/\tau_{\mu}})^{m-\ell} (1-e^{-t/\tau_{\mu}})^{\ell} \right] \quad \text{III(22)}$$

where $m = n+1$ corresponds to n pre- μ_i muons plus the μ_i muon. Since the introduction of a positron counting efficiency does not alter the derivation of expression III(13), equation III(21) is written as being independent of \mathcal{V} for $\mathcal{V} = T$ as discussed previously. Noting that

$$\sum_{\ell=0}^{m=n+1} \binom{m}{\ell} (1-\epsilon)^{\ell} (e^{-t/\tau_{\mu}})^{m-\ell} (1-e^{-t/\tau_{\mu}})^{\ell}$$

$$\begin{aligned}
 &= \sum_{\ell=0}^{n+1} (n+1-\ell) \frac{(n+1)!}{\ell!(n+1-\ell)!} (e^{-t/\tau_{\mu}})^{n+1-\ell} (1-\epsilon - e^{-t/\tau_{\mu}} + \epsilon e^{-t/\tau_{\mu}})^{\ell} \\
 &= (n+1)e^{-t/\tau_{\mu}} \sum_{\ell=0}^n \binom{n}{\ell} (e^{-t/\tau_{\mu}})^{n-\ell} (1-\epsilon - e^{-t/\tau_{\mu}} + \epsilon e^{-t/\tau_{\mu}})^{\ell} \\
 &= (n+1)e^{-t/\tau_{\mu}} [(1-\epsilon) + \epsilon e^{-t/\tau_{\mu}}]^n
 \end{aligned}
 \tag{III(23)}$$

where the last step applies the binomial theorem, $(a+b)^n =$

$$\sum_{\ell=0}^n \binom{n}{\ell} a^{n-\ell} b^{\ell}, \text{ equation III(22) becomes:}$$

$$\begin{aligned}
 N_0(t, \mathcal{N}) &= \frac{\sum_{n=0}^{\infty} \left(\sum_{k=n}^{\infty} \binom{k}{n} P_p(k, \mathcal{N}, T) \bar{P}(s(T))^n [1 - \bar{P}(s(T))]^{k-n} \right)}{1 + \mathcal{N}\tau_{\mu}} \\
 &\cdot \left[(n+1)e^{-t/\tau_{\mu}} [(1-\epsilon) + \epsilon e^{-t/\tau_{\mu}}]^n \right]
 \end{aligned}
 \tag{III(24)}$$

This equation is identical with equation III(14) except for the factor of $[(1-\epsilon) + \epsilon e^{-t/\tau_{\mu}}]^n$ which is simply the binomial distribution of success or failure in pile-up muon decay detection. Notice that as $\epsilon \rightarrow 1$, equation III(24) becomes identical to equation III(14), as it should. Furthermore, in the limit of $\mathcal{N} \rightarrow 0$ (no pile-up), the histogram becomes simply $N(t) = e^{-t/\tau_{\mu}}$ as it should since

$$\begin{aligned}
 \lim_{\mathcal{N} \rightarrow 0^+} (\mathcal{N}t)^k &= 1 \quad \text{if } k = 0 \\
 &= 0 \quad \text{if } k \geq 1
 \end{aligned}$$

Equation III(24) is compared with $e^{-t/\tau_{\mu}}$ for various muon beam currents in Figures III-4 and III-5 with a positron detection efficiency of 10%. Clearly, the low decay positron detection efficiency dramatically decreases the effect of pre- μ_i muons by decreasing their opportunity for interference.

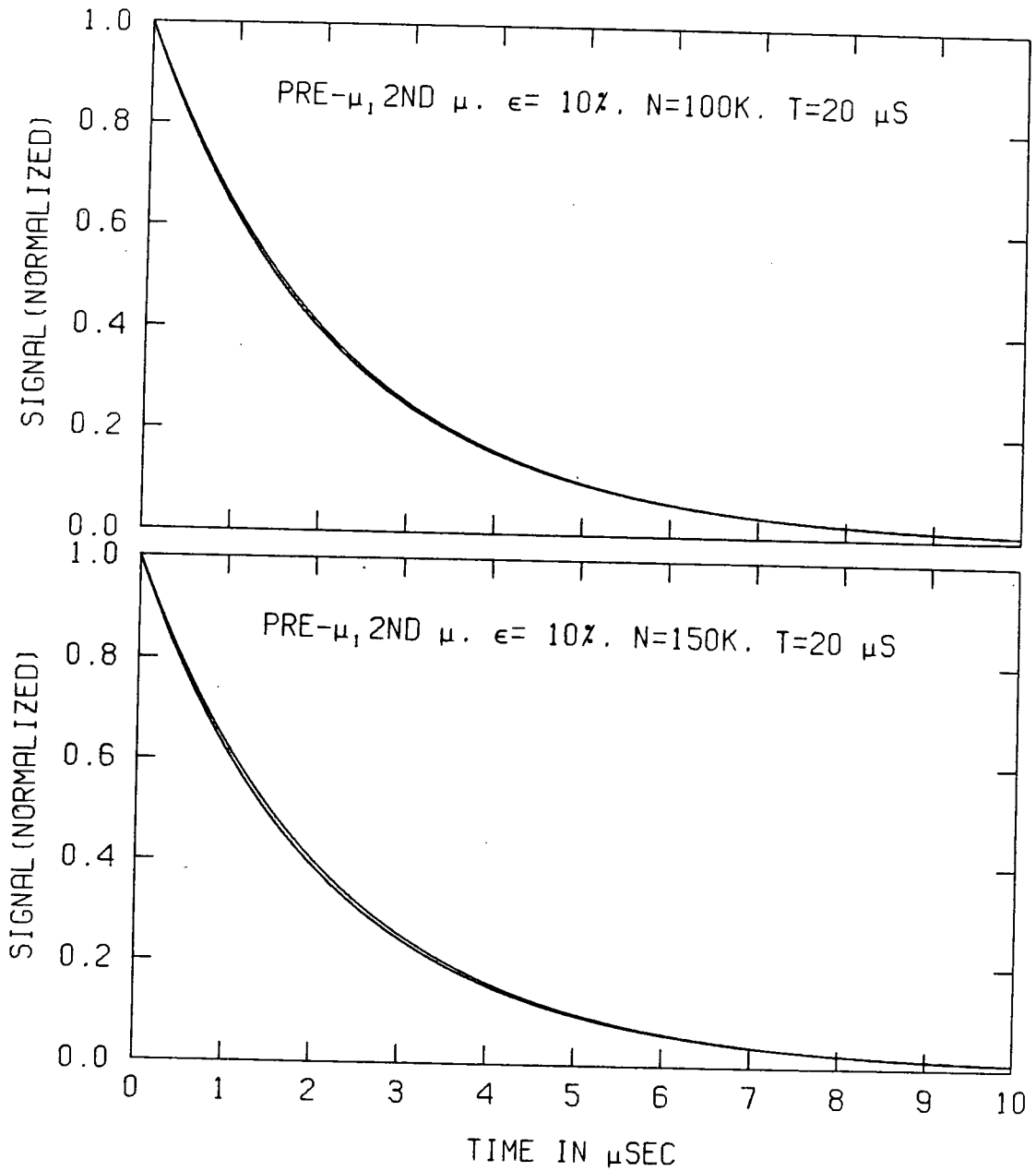


FIGURE III-4: The effect of pre- μ_i muons on the apparent muon lifetime with $\epsilon = 10\%$. Comparison with Figure III-2 shows that the introduction of a positron counting efficiency dramatically reduces the distortion due to pile-up since the pre- μ_i muons have less chance to interfere with the measurement.

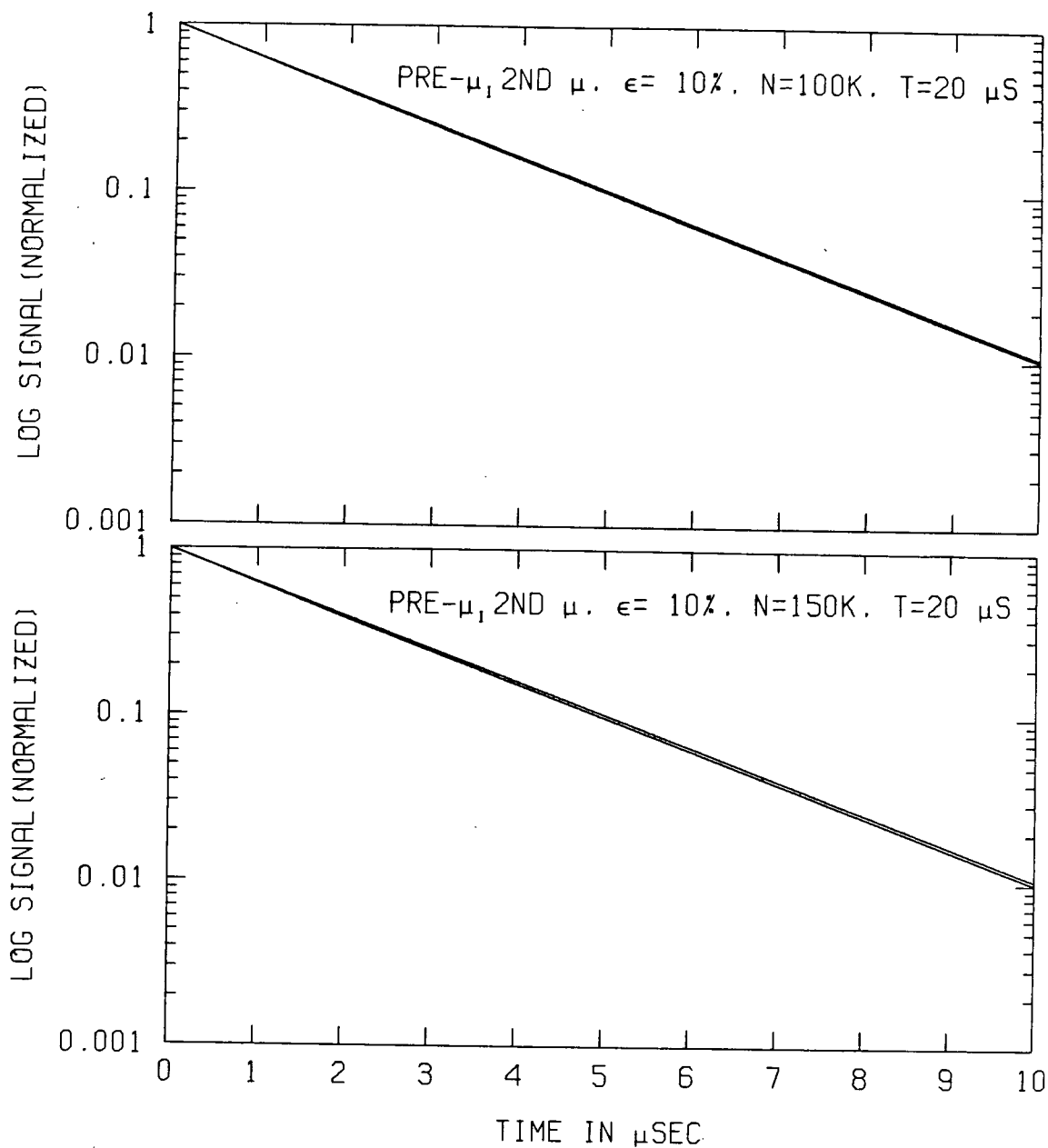


FIGURE III-5: Logarithmic plots of Figure III-4. In the top plot, the effect of pre- μ_1 muons is so small that the distorted curve is almost coincident with the true curve on this scale.

The dependence of the apparent muon lifetime on the decay positron detection efficiency indicates that any muon lifetime measurements using more than one positron telescope may not give the same result, even though the telescopes look at the same target. The apparent muon lifetimes obtained by fitting the histogram to e^{-t/τ_μ} over a $4\mu\text{s}$ time range would be (from Figure III-5) 2.16 and 2.13 μs for beam currents of 100 and $150 \times 10^3 \text{ s}^{-1}$ respectively.

(iii) Pre- μ_i Muons and the MSR Signal; ϵ Decay Positron Detection Efficiency

In the following calculation, it is assumed that the muon precession frequency (either in muonium or as "free" muons) is sufficiently large that all pre- μ_i muons are out of phase with the precession of the μ_i muon and therefore do not contribute to the precession signal. This assumption, valid in almost all experimental situations, naturally partitions equation III(21) into two sets of terms: those due to detection of μ_i decay which manifest a muon precession signal; and those due to detection of pre- μ_i decay without a muon precession signal.

Consider the general situation when n muons are in the target at $t = 0$, not counting the μ_i muon. The probability that the clock has not been stopped before t , but will be stopped by the μ_i muon between t and $t + dt$ is

$$P_{\mu_i} = e^{-(n+1)t/\tau_\mu} + ne^{-nt/\tau_\mu}(1-\epsilon)(1-e^{-t/\tau_\mu}) + \binom{n}{2} e^{-(n-1)t/\tau_\mu} \\ \cdot (1-\epsilon)^2(1-e^{-t/\tau_\mu})^2 + \dots + e^{-t/\tau_\mu}(1-e^{-t/\tau_\mu})^n(1-\epsilon)^n$$

where the first term represents the case where all (n+1) muons survive until t, the second term corresponds to the n permutations in which one of the pre- μ_i muons decay undetected before t, and so on, until the last term representing the case where all n pre- μ_i muons decay before t. Re-writing this expression and applying the binomial theorem as in the derivation of equation III(23) above, one obtains:

$$P_{\mu_i} = \sum_{\ell=0}^n \binom{n}{\ell} (1-\epsilon)^\ell (e^{-t/\tau_\mu})^{n+1-\ell} (1-e^{-t/\tau_\mu})^\ell \\ = e^{-t/\tau_\mu} \sum_{\ell=0}^n \binom{n}{\ell} (e^{-t/\tau_\mu})^{n-\ell} (1-\epsilon-e^{-t/\tau_\mu} + \epsilon e^{-t/\tau_\mu})^\ell \\ = e^{-t/\tau_\mu} [(1-\epsilon) + \epsilon e^{-t/\tau_\mu}]^n \tag{III(25)}$$

Similarly, the probability that the clock has not stopped before t, but will be stopped by a pre- μ_i muon decay during t and t + dt is:

$$P_{\text{pre-}\mu_i} = ne^{-nt/\tau_\mu}(1-\epsilon)(1-e^{-t/\tau_\mu}) + (n-1)ne^{-(n-1)t/\tau_\mu} \\ \cdot (1-\epsilon)^2(1-e^{-t/\tau_\mu})^2 + (n-2) \binom{n}{2} e^{-(n-2)t/\tau_\mu} \\ \cdot (1-\epsilon)^3(1-e^{-t/\tau_\mu})^3 + \dots + ne^{-t/\tau_\mu}(1-\epsilon)^n \\ \cdot (1-e^{-t/\tau_\mu})^n + ne^{-(n+1)t/\tau_\mu} + n(n-1)e^{-nt/\tau_\mu} \\ \cdot (1-\epsilon)(1-e^{-t/\tau_\mu}) + \binom{n}{2} (n-2)e^{-(n-1)t/\tau_\mu}(1-\epsilon)^2 \\ \cdot (1-e^{-t/\tau_\mu})^2 + \dots + ne^{-2t/\tau_\mu}(1-\epsilon)^{n-1} \\ \cdot (1-e^{-t/\tau_\mu})^{n-1} \tag{III(26)}$$

where the first n terms correspond to the cases where the μ_i muon is among the muons that decayed undetected before t and the last n terms correspond to the cases where the μ_i muon is among the survivors at t . In particular, the first term corresponds to the case where the μ_i muon has decayed undetected before t , leaving n surviving pre- μ_i muons which may decay between t and $t + dt$; the second term corresponds to the case where the μ_i muon and any one of the n pre- μ_i muons have decayed undetected before t leaving any of $n-1$ surviving pre- μ_i muons which may decay between t and $t + dt$; and so on until the n th term corresponding to the case where the μ_i muon and all but one of the n pre- μ_i muons have decayed undetected before t , leaving one surviving pre- μ_i muon that may decay during t and $t + dt$. The $(n+1)$ th term corresponds to the case where all muons have survived until t leaving n pre- μ_i muons that may decay between t and $t + dt$ (decay of the μ_i muon belongs to equation III(25)); the $(n+2)$ term corresponds to the case where any one of n pre- μ_i muons has decayed before t leaving $(n-1)$ pre- μ_i muons that may decay between t and $t + dt$; and so on. In the last n terms, μ_i survives both t and $t + dt$. Proceeding as before, equation III(26) becomes

$$\begin{aligned}
 P_{\text{pre-}\mu_i} &= \sum_{\ell=0}^n n \binom{n}{\ell} (1-\epsilon)^\ell (e^{-t/\tau_\mu})^{n+1-\ell} (1-e^{-t/\tau_\mu})^\ell \\
 &= ne^{-t/\tau_\mu} \sum_{\ell=0}^n \binom{n}{\ell} (e^{-t/\tau_\mu})^{n-\ell} (1-\epsilon-e^{-t/\tau_\mu} + \epsilon e^{-t/\tau_\mu})^\ell \\
 &= ne^{-t/\tau_\mu} [(1-\epsilon) + \epsilon e^{-t/\tau_\mu}]^n
 \end{aligned}
 \tag{III(27)}$$

Clearly, the sum of equations III(25) and III(27) is equal to equation III(23) as expected.

Denoting the MSR signal as $S(t)$ as defined in Appendix I and Chapter I, and combining equations III(25) and III(27) with III(24), the normalized histogram becomes:

$$N_o(t, \mathcal{N}) = \frac{\sum_{n=0}^{\infty} \left[\sum_{k=n}^{\infty} \binom{k}{n} P_p(k, \mathcal{N}, T) \bar{P}(s(T))^n [1 - \bar{P}(s(T))]^{k-n} \right]}{1 + \mathcal{N}\tau_{\mu}} \cdot \left\{ ne^{-t/\tau_{\mu}} [(1-\epsilon) + \epsilon e^{-t/\tau_{\mu}}]^n + e^{-t/\tau_{\mu}} \right. \quad \text{III(28)}$$

$$\left. \cdot [(1-\epsilon) + \epsilon e^{-t/\tau_{\mu}}]^n (1 + S(t)) \right\}$$

It may be noted that when $\mathcal{N} = 0$ (no pile-up), this reduces to $e^{-t/\tau_{\mu}}(1 + S(t))$ as expected.

This calculation shows that pre- μ_1 muons not only distort the apparent muon lifetime upon which the MSR signal is superimposed, but they also generate an exponential background containing no MSR signal. Figures III-6 and III-7 illustrate the result of this calculation at various beam currents and a 10% decay positron counting efficiency, for the very simple MSR signal: $S(t) = A_{\text{Mu}} \cos \omega_{\text{Mu}} t$ at 5 gauss. Four functions are plotted in each Figure:

- (1) the upper muon precession curve is the "true" histogram:

$$N(t) = e^{-t/\tau_{\mu}} (1 + A_{\text{Mu}} \cos \omega_{\text{Mu}} t)$$

- (2) the apparent histogram given by equation III(28) is almost superimposed on the true histogram (see the detailed plot in Figure III-7).

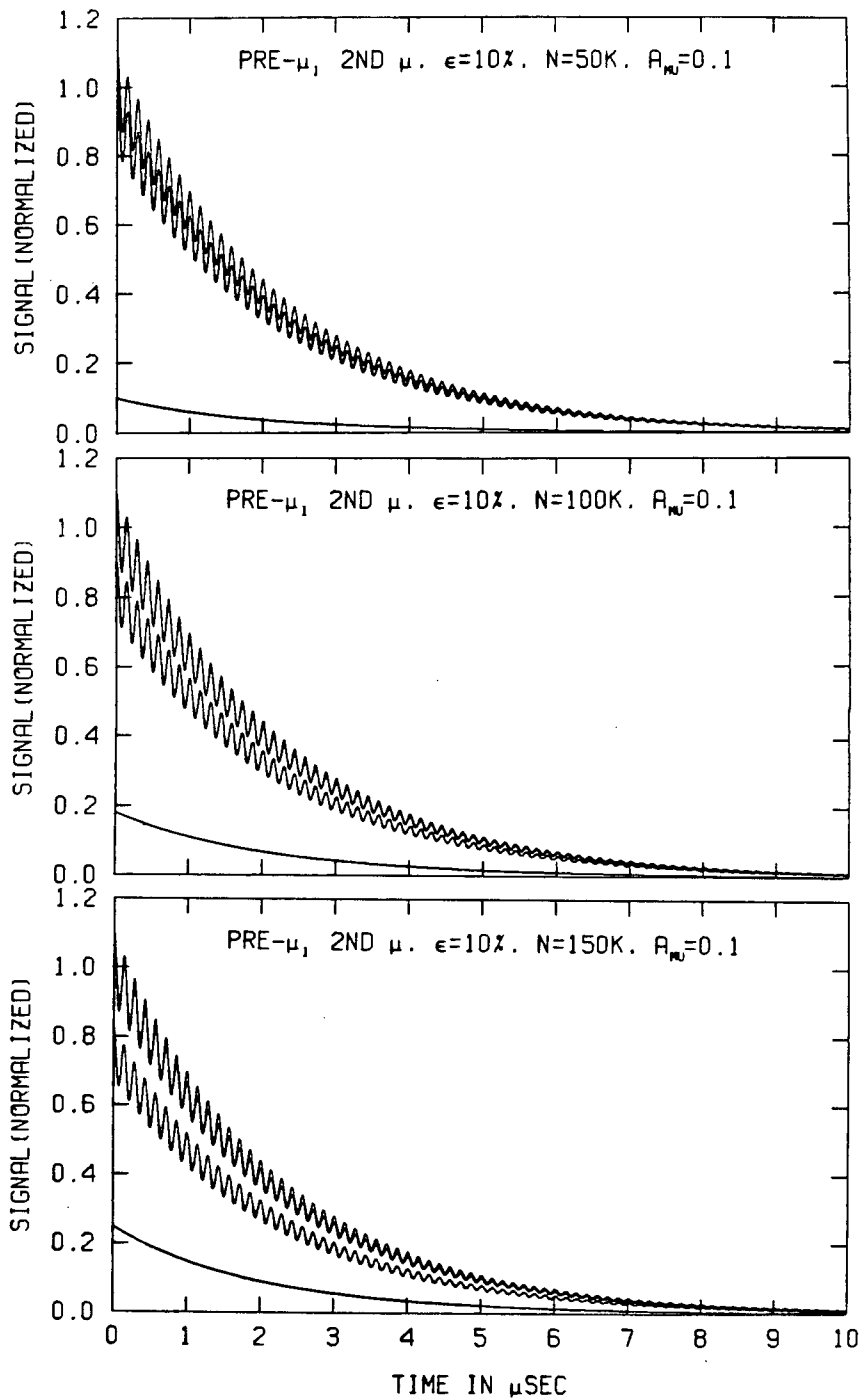
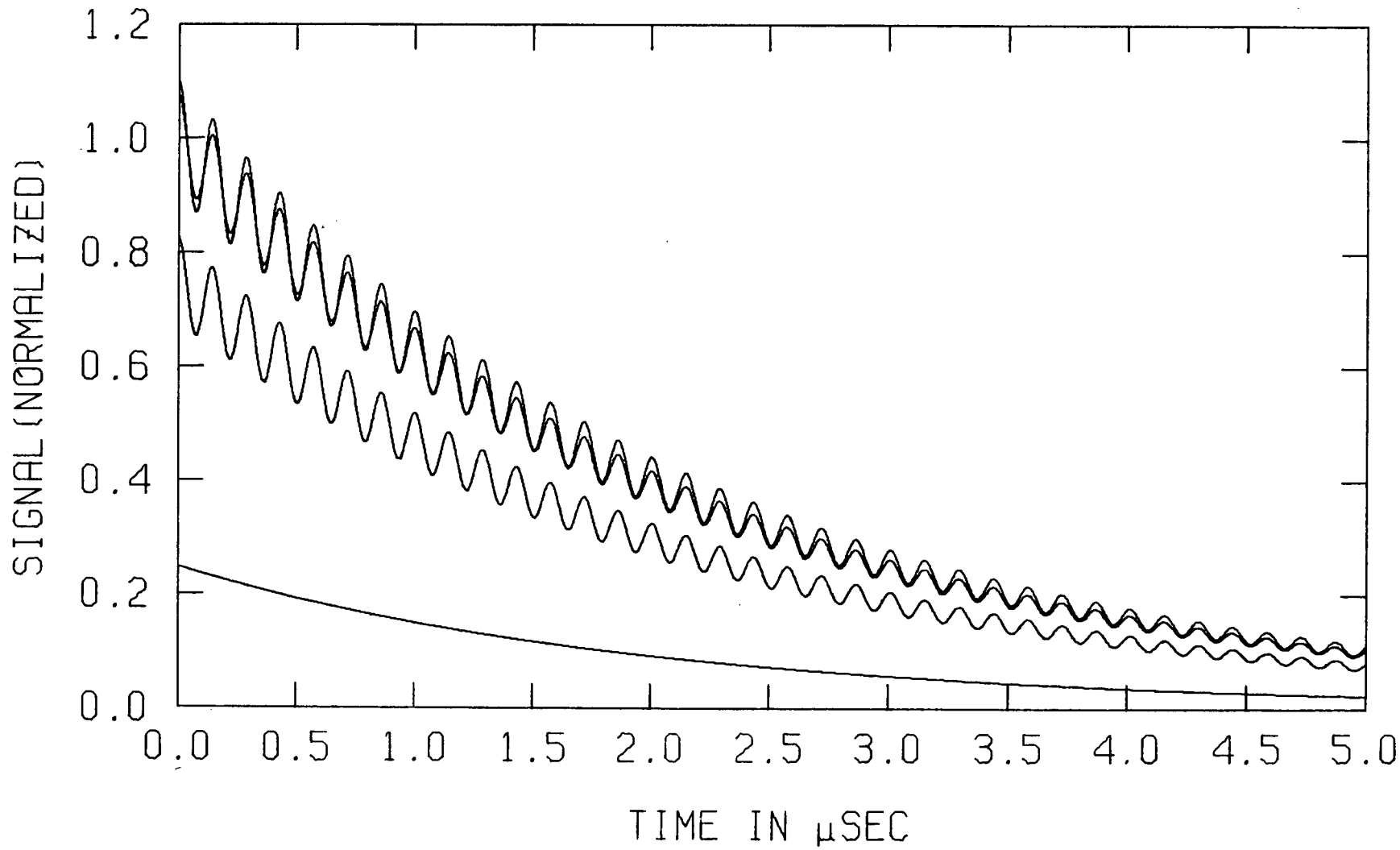


FIGURE III-6: The effect of pre- μ_i muons on the MSR signal with $\epsilon = 10\%$. The top two curves in each plot are almost coincident, but can be distinguished in Figure III-7. The measured signal, which is almost identical with the true signal in each plot, is made up of a signal-bearing curve (the lowest sinusoidal curve in each plot), and an approximately exponential curve without a signal which is due to pre- μ_i muon decay detection.

PRE- μ_1 2ND μ . $\epsilon=10\%$, $N=150K$, $A_{\mu}=0.1$



-274-

FIGURE III-7: The effect of pre- μ_1 muons on the MSR signal. (detail). Of the top two curves, the one with the largest amplitude is the true signal, while the apparent signal has a distorted exponential and an amplitude reduced by $1 + \mathcal{N}\tau_{\mu}$.

(3) the lower sinusoidal exponential corresponds to

$$N_o(t, \mathcal{N}) = \frac{\sum_{n=0}^{\infty} \left[\sum_{k=n}^{\infty} \binom{k}{n} P_p(k, \mathcal{N}, T) \bar{P}(s(T))^n [1 - \bar{P}(s(T))]^{k-n} \right]}{1 + \mathcal{N}\tau_{\mu}} \quad \text{III(29)}$$

$$\cdot e^{-t/\tau_{\mu}} [(1-\epsilon) + \epsilon e^{-t/\tau_{\mu}}]^n (1 + S(t))$$

(4) the lower exponential corresponds to

$$N_o(t, \mathcal{N}) = \frac{\sum_{n=0}^{\infty} \left[\sum_{k=n}^{\infty} \binom{k}{n} P_p(k, \mathcal{N}, T) \bar{P}(s(t))^n [1 - \bar{P}(s(T))]^{k-n} \right]}{1 + \mathcal{N}\tau_{\mu}} \quad \text{III(30)}$$

$$\cdot n e^{-t/\tau_{\mu}} [(1-\epsilon) + \epsilon e^{-t/\tau_{\mu}}]^n$$

Curve (2) is the sum of curves (3) and (4). As illustrated in Figure III-7, pre- μ_i muons reduce the effective MSR asymmetry, A_{Mu} , by exactly the factor $(1 + \mathcal{N}\tau_{\mu})$. In order to illustrate the origins of the muon lifetime distortions in the histogram, Figure III-8 shows the four curves in logarithmic plots in which the asymmetry has been set to zero (no MSR signal). The upper two curves in each plot are exactly those illustrated in Figure III-5.

Figure III-9 shows an experimental μ^+ SR histogram taken by G.M. Marshall of U.B.C. using the electronic logic described in Section C of this Appendix at a beam current of about $50 \times 10^3 \text{ s}^{-1}$. The logic discards post- μ_i muon events, but not pre- μ_i events. Both plots are of the "normalized residuals" of the experimental data; that is, the experimental data has been divided by the best fit to a model in order to expose any deficiencies in the model - if the model faith-

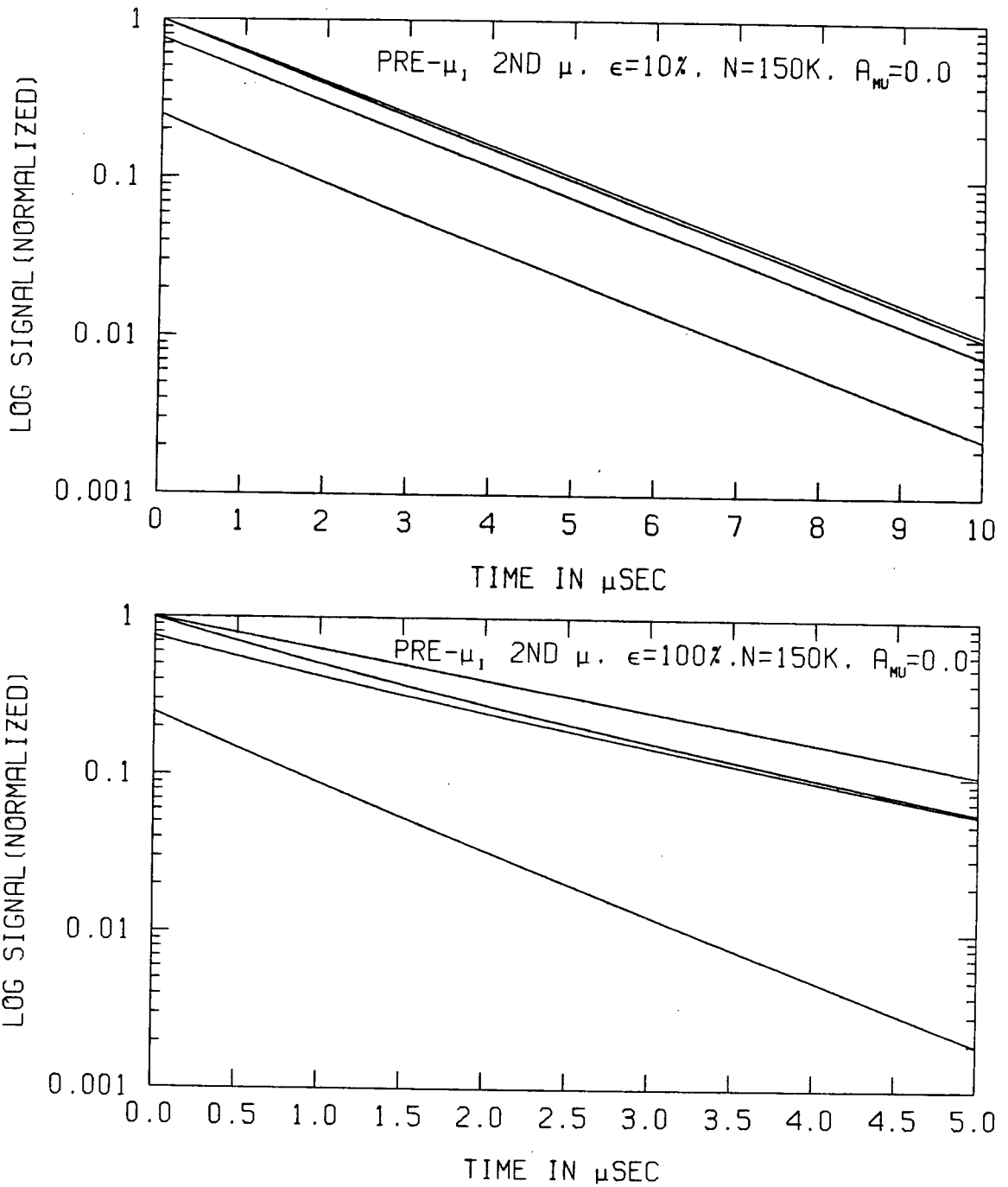


FIGURE III-8: The origins of the lifetime distortions due to pre- μ_1 muons. The top two curves of each plot are the same as the lower plots of Figures III-3 and III-5. The top curve in each plot is the true lifetime and the second curve, showing the net effect of pre- μ_1 muons, is the sum of the third curve due to decay detection of the μ_1 muon, and the fourth curve due to decay detection of pre- μ_1 muons.

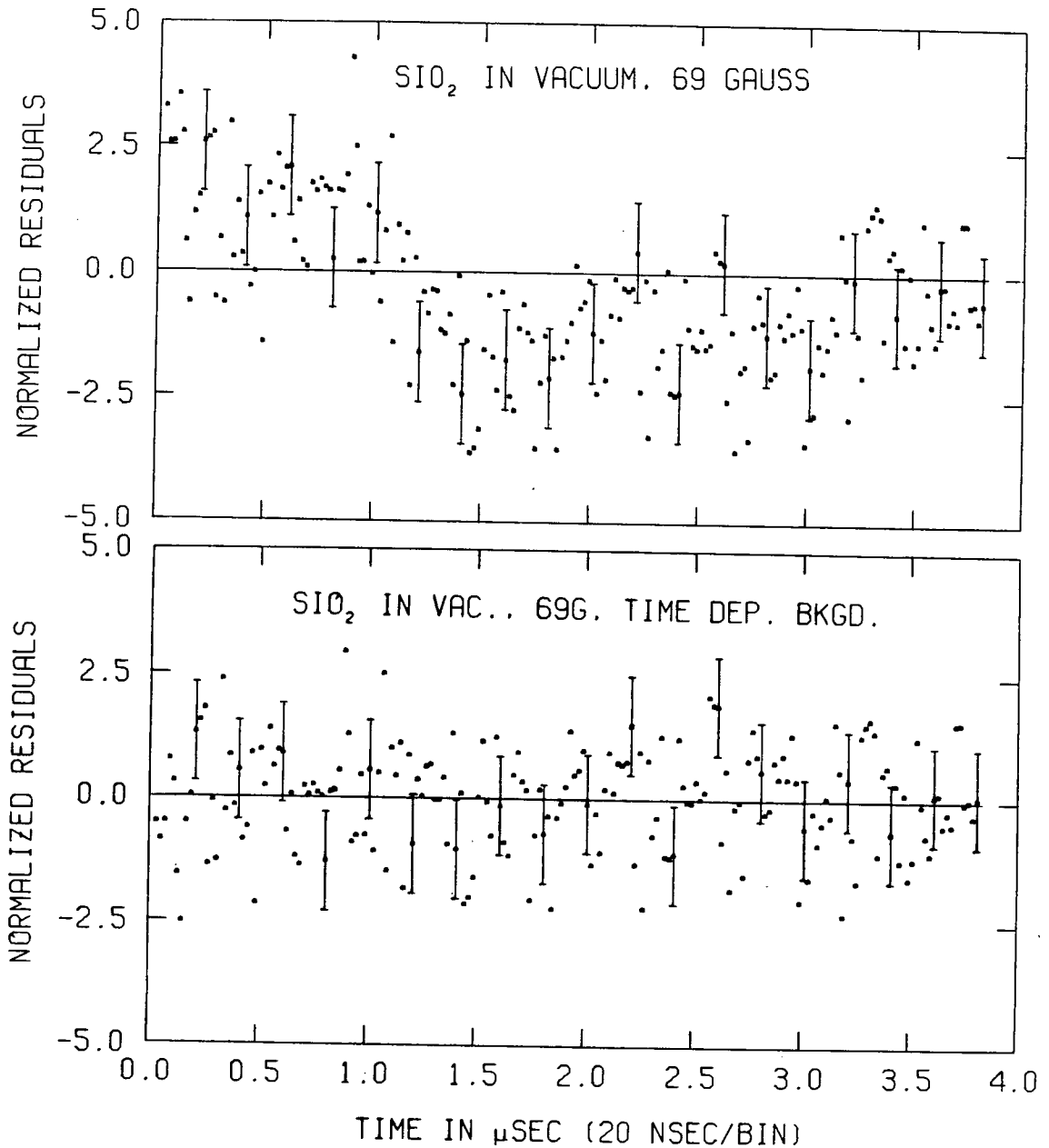


FIGURE III-9: A possible experimental example of the effect of pre- μ_1 muons (due to G.M. Marshall). The normalized residuals (see text) should be randomly scattered about zero if the model used to describe the data is correct. The top plot clearly reveals the inadequacy of the standard μ SR model; inclusion of an exponential background with a lifetime shorter than τ_μ provides a more credible description of the data (bottom). This is consistent with the effects of pre- μ_1 muons.

fully describes the data, the plot of residuals should be randomly scattered about zero. In the top plot of the Figure, the data were fitted to the standard μ^+ SR model (equation (4), Chapter I):

$$N(t) = N_0 e^{-t/\tau_\mu} (1 + A_\mu e^{-\lambda t} \cos(\omega_\mu t + \phi)) + Bg.$$

The result is a poor fit as evidenced by the obvious drift in the Figure and by the χ^2 per degree of freedom of 2.8.

Modifying the model to

$$N(t) = N_0 e^{-t/\tau_\mu} (1 + A_\mu e^{-\lambda t} \cos(\omega_\mu t + \phi)) + Bg + N_1 e^{-t/T_1}$$

results in a much better fit as evidenced by the lower plot of the Figure and by the χ^2 per degree of freedom of 1.1. The second fit gives $T_1 = 1.42 \mu\text{s}$ and $N_0 = 3N_1$. The qualitative behavior of these data is consistent with the foregoing calculations of the effects of pre- μ_i muons. Unfortunately, it is not possible to make a quantitative comparison of these data with the calculations because of the rejection of post- μ_i muons and the deadtime characteristics of the electronic logic system. Thus, it cannot be stated unequivocally that the apparent distortion of this spectrum is due to pre- μ_i muons.

(iv) Post- μ_i Muons and τ_μ : 100% Decay Positron Detection Efficiency

The probability of n post- μ_i muons arriving in the target between $t = 0$ and t is again given by the Poisson distribution, $P_p(n, \mathcal{N}, t)$. As in the calculation of equation III(11), the probability of a post- μ_i muon arriving during any

subinterval Δt of t is the same for all Δt . Consequently, the average probability that a muon arriving between $t = 0$ and t survives until t is:

$$\bar{P}(s(t)) = \frac{\tau_\mu}{t} (1 - e^{-t/\tau_\mu}) \quad \text{III(31)}$$

The unnormalized experimental histogram has the very simple form:

$$N(t, \mathcal{N}) = \sum_{n=0}^{\infty} P_p(n, \mathcal{N}, t) \bar{P}(s(t))^n (n+1) e^{-t/\tau_\mu} \quad \text{III(32)}$$

where $(n+1)$ refers to n post- μ_i muons plus the μ_i muon, any of which may decay between t and $t + dt$, e^{-t/τ_μ} is the survival probability of the μ_i muon, and $P_p(n, \mathcal{N}, t) \bar{P}(s(t))^n$ is the entry and survival probability of n post- μ_i muons.

The normalization of post- μ_i histograms is somewhat more complicated than for pre- μ_i histograms. In the present case, there is only one muon in the target at $t = 0$. However, by t , another muon may have entered the target such that if the total muon survival probability at t is extrapolated back to $t = 0$, it will not correspond to one. For example, if a post- μ_i muon enters the target at t , this corresponds to a muon population of $\frac{1}{e^{-t/\tau_\mu}} + 1$ at $t = 0$, where the factor of one is due to μ_i . Consequently, this time-dependent normalization must be applied to ensure that the total muon survival probability at any time extrapolated back to $t = 0$ corresponds to one. The required normalization is:

$$1 + \frac{\sum_{n=0}^{\infty} P_p(n, \mathcal{N}, t) n \bar{P}(s(t))}{e^{-t/\tau_\mu}} \quad \text{III(33)}$$

that is, $nP_p(n, \mathcal{N}, t) \bar{P}(s(t))$ gives the post- μ_i muon population at t and the factor e^{-t/τ_μ} extrapolates this population back to $t = 0$. The normalized histogram is:

$$N_o(t, \mathcal{N}) = \frac{\sum_{n=0}^{\infty} P_p(n, \mathcal{N}, t) \bar{P}(s(t))^{n(n+1)} e^{-t/\tau_\mu}}{1 + \sum_{n=0}^{\infty} P_p(n, \mathcal{N}, t) \frac{n \bar{P}(s(t))}{e^{-t/\tau_\mu}}} \quad \text{III(34)}$$

Figures III-10 and III-11 compare equation III(34) with the true histogram, e^{-t/τ_μ} , for various beam currents. As expected, the effects of post- μ_i muons are felt at late times because of the increased opportunity for such a muon to enter the target (see Figure III-11). The apparent muon lifetimes obtained by fitting the histogram to e^{-t/τ_μ} over a 4 μ s time range would be (from Figure III-11) 1.9, 1.6 and 1.5 μ s for beam currents of 50, 100, and 150 $\times 10^3 \text{ s}^{-1}$ respectively.

(v) Post- μ_i Muons and τ_μ ; ϵ Decay Positron Detection Efficiency

The introduction of a positron counting efficiency greatly complicates the calculation of the post- μ_i histogram. As before, we must compute the probability that the clock is not stopped before t but will be stopped between t and $t + dt$. The possibility of an undetected muon decay leads to the generation of two kinds of terms: those in which μ_i is a survivor at t and those in which μ_i has decayed before t . As in the derivation of equation III(13), the probability of there being n muons (not counting the μ_i muon) in the target at time t without the clock stopping is:

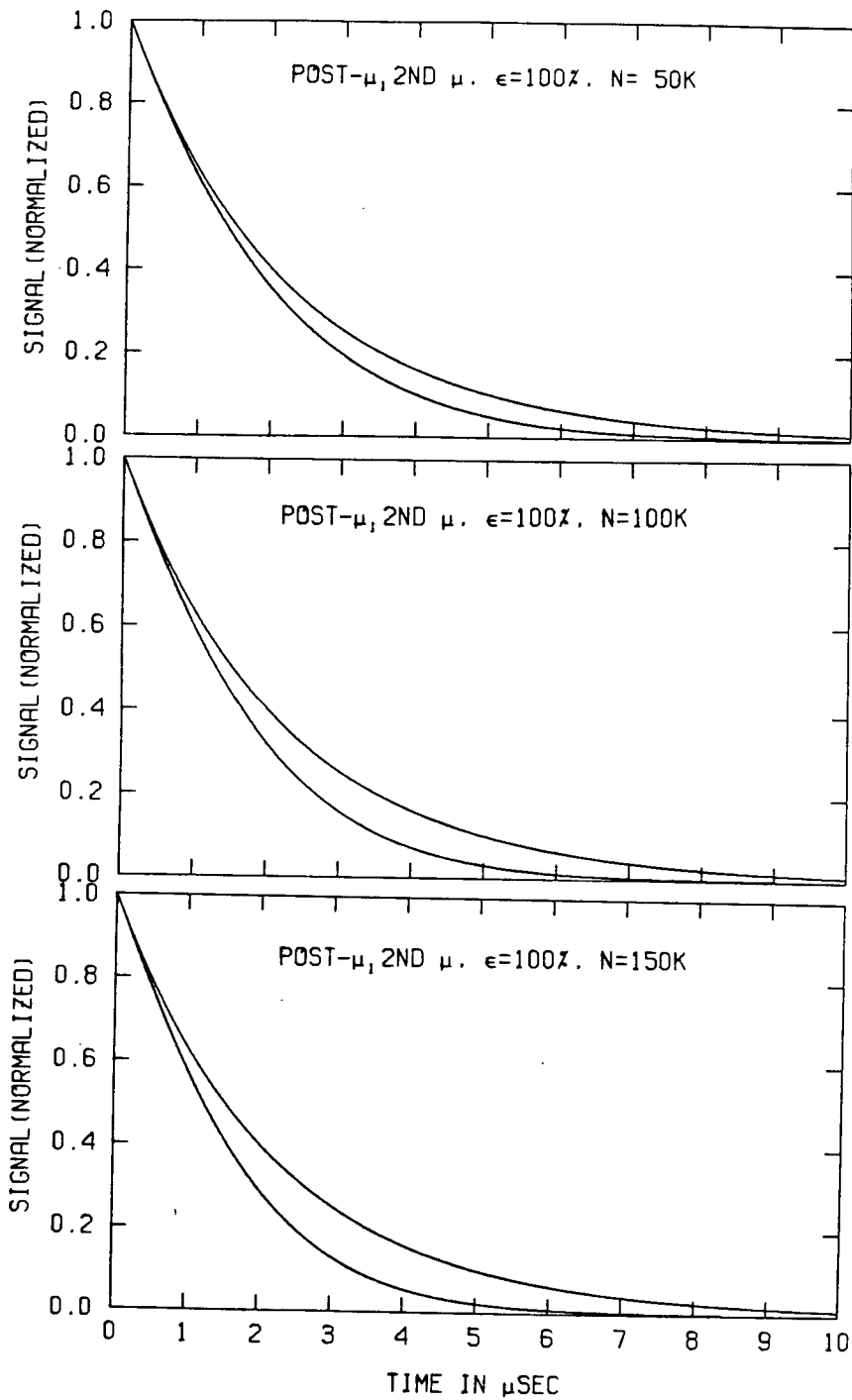


FIGURE III-10: The effect of post- μ_1 muons on the apparent muon lifetime with $\epsilon = 100\%$.

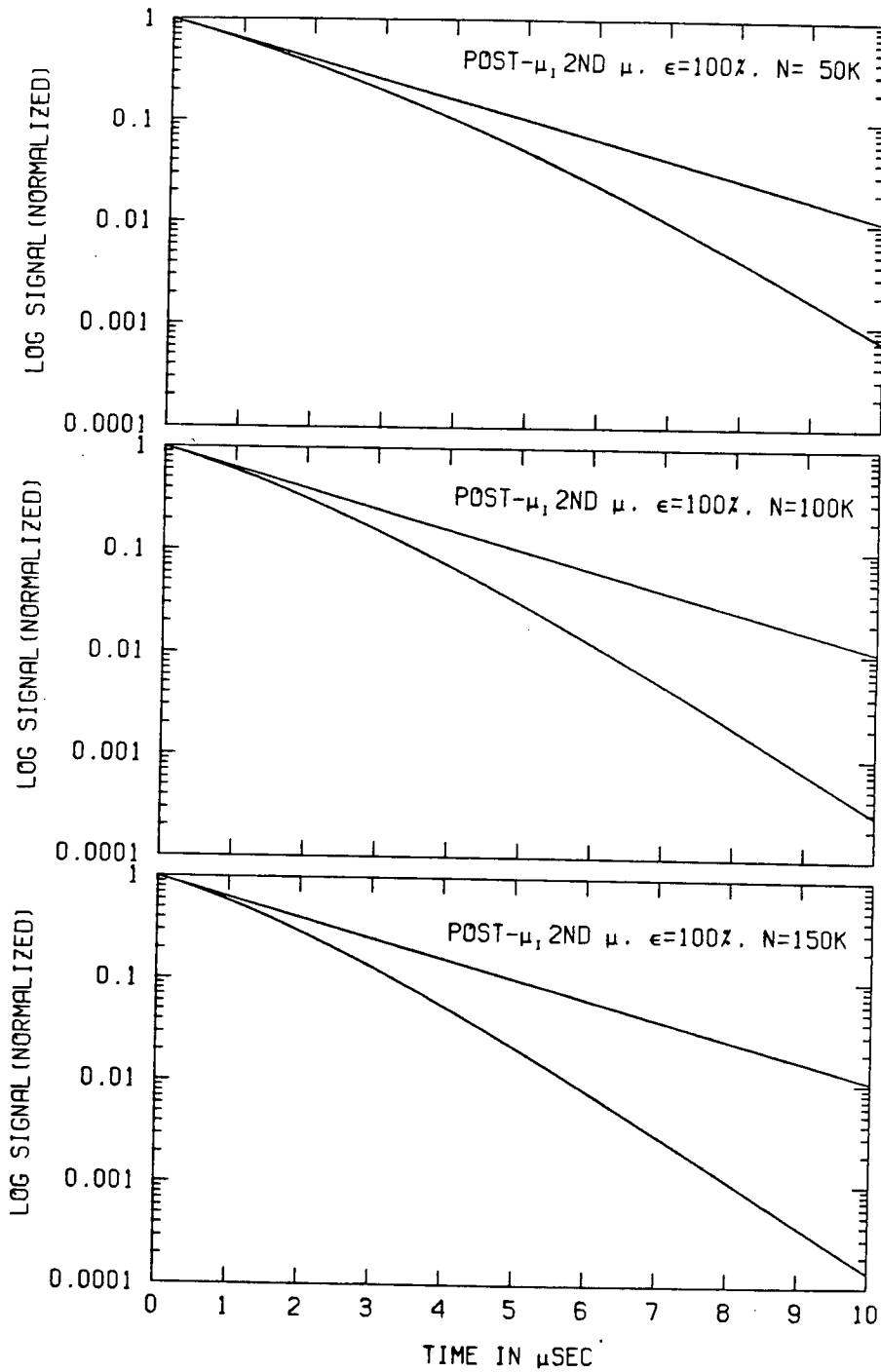


FIGURE III-11: Logarithmic plots of Figure III-10. Clearly, the effects of post- μ_i muons are important at late times, in contrast to the case of pre- μ_i muons.

the probability of n muons arriving during t x the probability that all survive until t
 + the probability of $n+1$ muons arriving during t x the probability that one decays undetected before t
 + the probability of $n+2$ muons arrive during t x the probability that two decay undetected before t
 + ...

This may be written symbolically as:

$$\begin{aligned}
 & P_p(n, \mathcal{N}, t) \bar{P}(s(t))^n + P_p(n+1, \mathcal{N}, t) (1-\epsilon) \left\{ \binom{n+1}{n} [1-\bar{P}(s(t))] \right. \\
 & \quad \left. \cdot \bar{P}(s(t))^n e^{-t/\tau_\mu} + \left(\frac{1}{n+1}\right) \binom{n+1}{n} \bar{P}(s(t))^{n+1} (1-e^{-t/\tau_\mu}) \right\} \\
 & + P_p(n+2, \mathcal{N}, t) (1-\epsilon)^2 \left\{ \binom{n+2}{n} [1-\bar{P}(s(t))]^2 \bar{P}(s(t))^n e^{-t/\tau_\mu} \right. \\
 & \quad \left. + \left(\frac{2}{n+1}\right) \binom{n+2}{2} \bar{P}(s(t))^{n+1} (1-e^{-t/\tau_\mu}) [1-\bar{P}(s(t))] \right\} \\
 & + P_p(n+3, \mathcal{N}, t) (1-\epsilon)^3 \left\{ \binom{n+3}{n} [1-\bar{P}(s(t))]^3 \bar{P}(s(t))^n e^{-t/\tau_\mu} \right. \\
 & \quad \left. + \left(\frac{3}{n+1}\right) \binom{n+2}{n} \bar{P}(s(t))^{n+1} (1-e^{-t/\tau_\mu}) [1-\bar{P}(s(t))]^2 \right\} + \dots
 \end{aligned}$$

where the first term in the large brackets corresponds to the case where n post- μ_i muons plus the μ_i muon survive until t and all other post- μ_i muons decay undetected before t ; the second term in large brackets corresponds to the case where $(n+1)$ post- μ_i muons survive until t and the μ_i muon plus all other post- μ_i muons decay undetected before t . Since the muon population at any time is independent of the features of the positron counters, the normalization calculated in the preceding Section remains valid and the normalized histogram is given by:

$$N_0(t, \mathcal{N}) = \frac{\sum_{n=0}^{\infty} (n+1) \bar{P}(s(t))^n \sum_{k=n}^{\infty} P_p(k, \mathcal{N}, t) (1-\epsilon)^{k-n} \binom{k}{n}}{1 + \frac{\sum_{n=0}^{\infty} P_p(n, \mathcal{N}, t) n \bar{P}(s(t))}{e^{-t/\tau_\mu}}}$$

$$\cdot [1 - \bar{P}(s(t))]^{k-n-1} \left\{ [1 - \bar{P}(s(t))] e^{-t/\tau_\mu} \right. \quad \text{III (35)}$$

$$\left. + \binom{k-n}{n+1} \bar{P}(s(t)) (1 - e^{-t/\tau_\mu}) \right\}$$

Noting that

$$\lim_{\epsilon \rightarrow 1} (1-\epsilon)^{k-n} = 1 \quad \text{if } k-n = 0$$

$$= 0 \quad \text{if } k-n \geq 1$$

it is seen that equation III(35) reduces to equation III(34) as it should. Equation III(35) is compared with e^{-t/τ_μ} for various beam currents in Figures III-12 and III-13 with a positron detection efficiency of 10%. As in the case of pre- μ_i muons, the introduction of a positron counter efficiency dramatically decreases the effect of the pile-up. The apparent muon lifetimes obtained by fitting the histogram to e^{-t/τ_μ} over a time range of $4\mu\text{s}$ would be (from Figure III-13) 2.15, 2.12, and 2.07 μs for beam currents of 50, 100, and 150 $\times 10^3 \text{ s}^{-1}$ respectively.

(vi) Post- μ_i Muons and the MSR Signal; ϵ Decay Positron Detection Efficiency

As in the case of pre- μ_i muons, the following calculation assumes that the muon precession frequency (in both muonium and as "free" muons) is sufficiently large that all

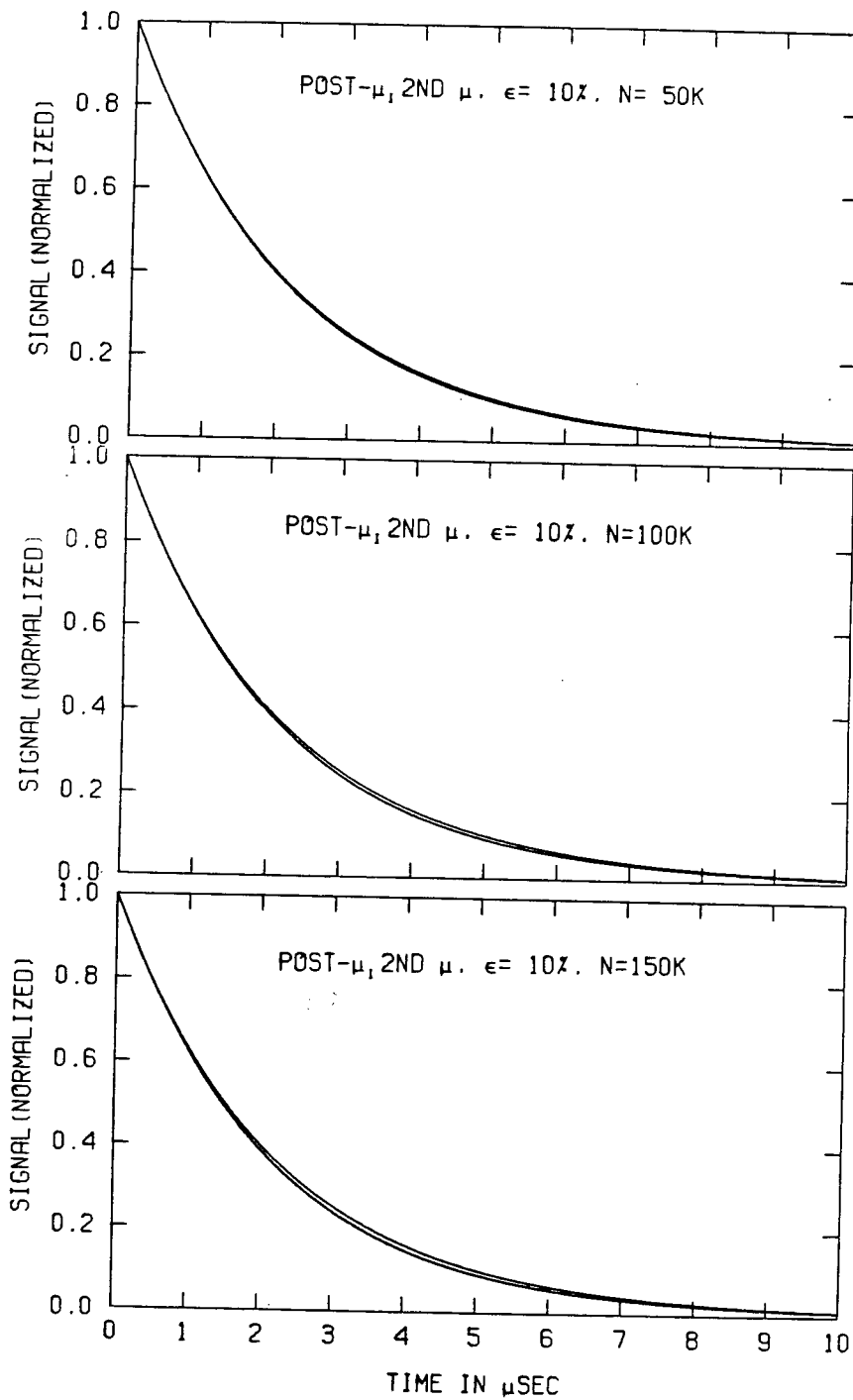


Figure III-12: The effects of post- μ_i muons on the apparent muon lifetime with $\epsilon = 10\%$. As in the case of pre- μ_i muons, the introduction of a positron counting efficiency greatly reduces the distortion due to pile-up, though not as much.

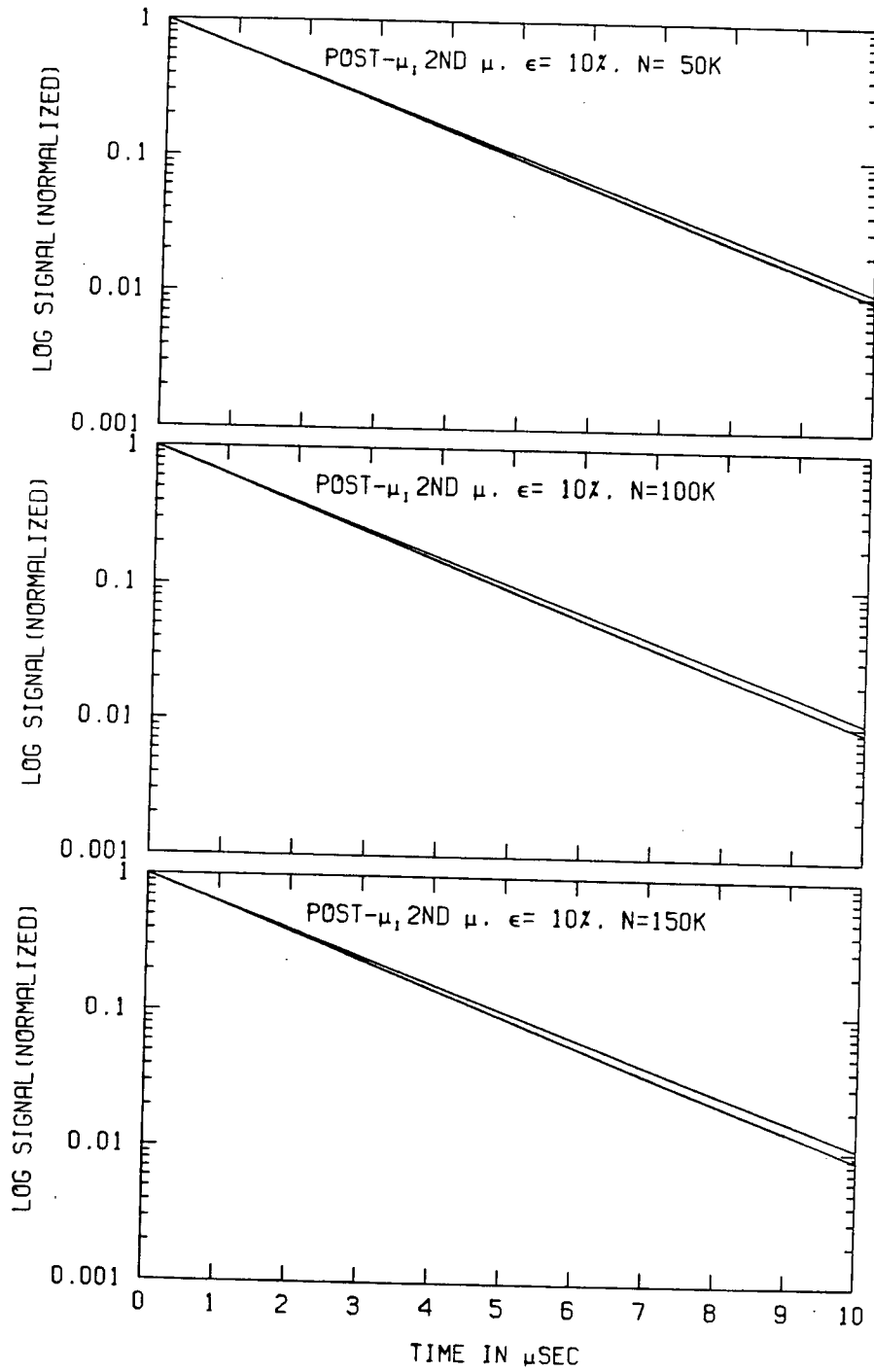


FIGURE III-13: Logarithmic plots of Figure III-12.

post- μ_i muons are out of phase with the precession of the μ_i muon and therefore do not contribute to the precession signal. The calculation of the preceding Section has already partitioned the histogram into terms in which the μ_i muon has survived until t and those in which it has decayed undetected before t . The only terms which carry a MSR signal are those where μ_i survives until t but decays between t and $t + dt$. Following the arguments leading to the derivation of equation III(28), it is easily seen that of the terms corresponding to μ_i survival until t ,

$$(n+1) [1-\bar{P}(s(t))] e^{-t/\tau_\mu}$$

the MSR signal-bearing terms are

$$[1-\bar{P}(s(t))] e^{-t/\tau_\mu}$$

and the remaining terms:

$$n[1-\bar{P}(s(t))] e^{-t/\tau_\mu}$$

correspond to μ_i survival until $t + dt$ (at least). Denoting the MSR signal as $S(t)$, the histogram has the form:

$$N_o(t, \mathcal{N}) = \frac{\sum_{n=0}^{\infty} \bar{P}(s(t))^n \sum_{k=n}^{\infty} P_p(k, \mathcal{N}, t) (1-\epsilon)^{k-n} [1-\bar{P}(s(t))]^{k-n-1}}{1 + \frac{\sum_{n=0}^{\infty} P_p(n, \mathcal{N}, t) n \bar{P}(s(t))}{e^{-t/\tau_\mu}}} \quad \text{III(36)}$$

$$\cdot \binom{k}{n} \left\{ [1-\bar{P}(s(t))] e^{-t/\tau_\mu} [1 + S(t)] + n[1-\bar{P}(s(t))] e^{-t/\tau_\mu} + (k-n)\bar{P}(s(t)) (1-e^{-t/\tau_\mu}) \right\}$$

The effects of post- μ_i muons are illustrated in Figures III-14 and III-15 at various beam currents and a 10%

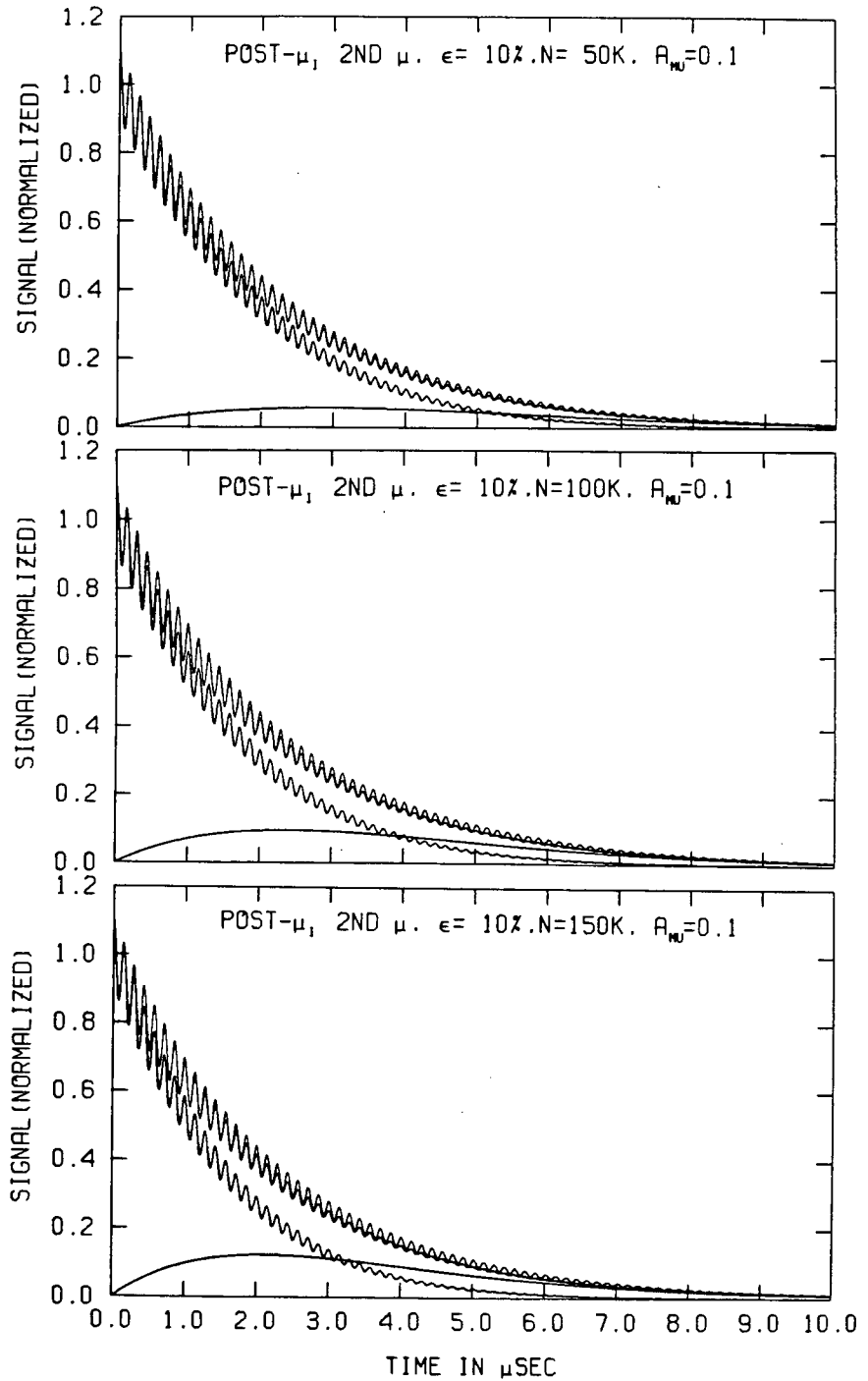


FIGURE III-14: The effect of post- μ_1 muons on the MSR signal with $\epsilon = 10\%$. The top two curves in each plot are more distinguishable in Figure III-15. The equations of each curve are given in the text.

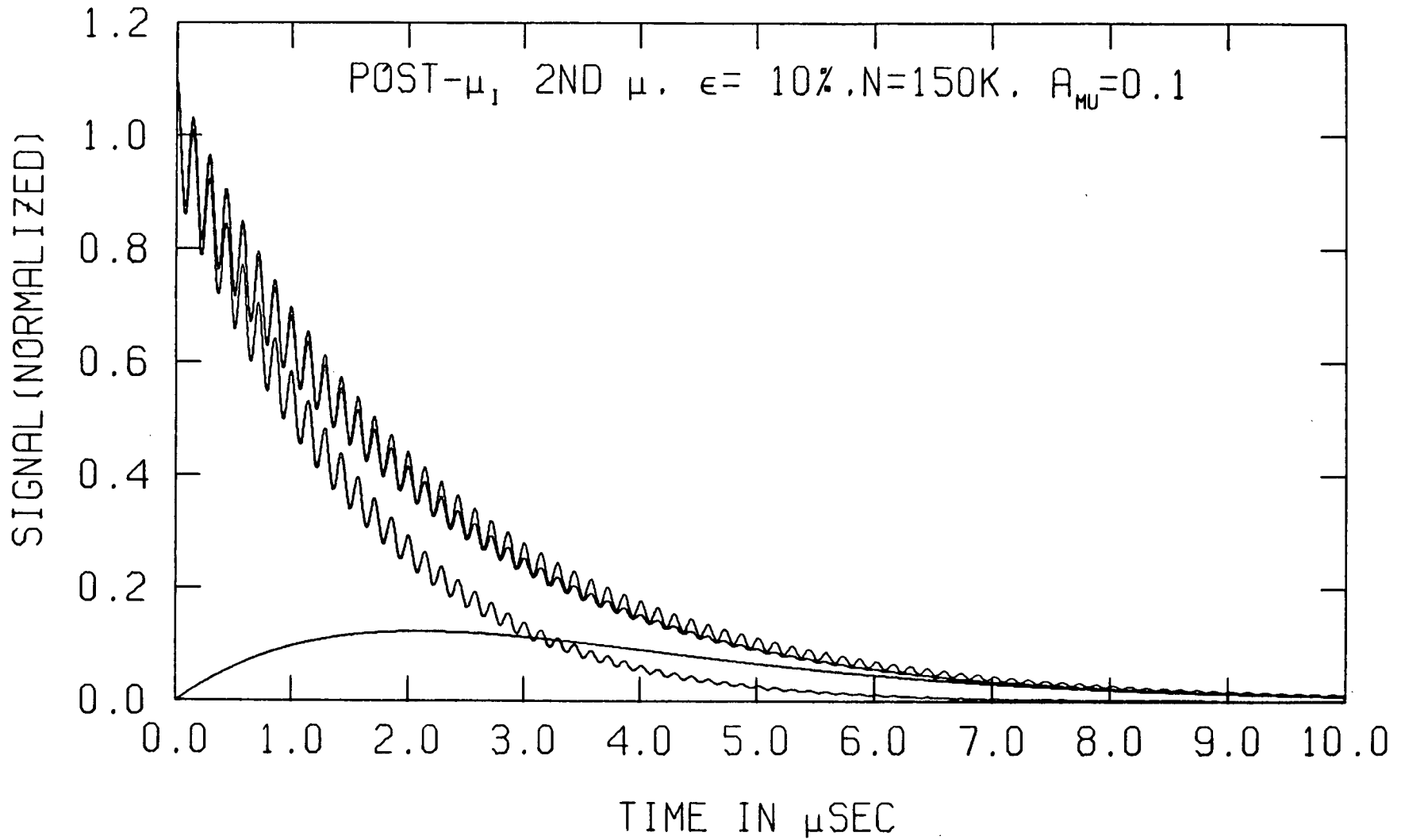


FIGURE III-15: The effect of post- μ_1 muons on the MSR signal (detail). The top curve is the true signal and the second curve is the effective pile-up signal. At late times, the damping of the pile-up signal is clearly evident.

positron detection efficiency for the very simple MSR signal:
 $S(t) = A_{\text{Mu}} \cos \omega_{\text{Mu}} t$ at 5 gauss. Four functions are plotted in each Figure:

- (1) The upper curve is the "true" histogram: $N(t) = e^{-t/\tau_{\mu}} \cdot (1 + A_{\text{Mu}} \cos \omega_{\text{Mu}} t)$. This is the curve with the longest-lived MSR signal.
- (2) The apparent histogram given by equation III(36) is almost superimposed on the true histogram (see the detailed plot of Figure III-15). The MSR signal in this function is much shorter-lived than for the "true" histogram.
- (3) The lower sinusoidal exponential corresponds to:

$$N_o(t, \mathcal{N}) = \frac{\sum_{n=0}^{\infty} \bar{P}(s(t))^n \sum_{k=n}^{\infty} P_p(k, \mathcal{N}, t) (1-\epsilon)^{k-n} [1-\bar{P}(s(t))]^{k-n-1}}{1 + \frac{\sum_{n=0}^{\infty} P_p(n, \mathcal{N}, t) n \bar{P}(s(t))}{e^{-t/\tau_{\mu}}}} \quad \text{III(37)}$$

$$\cdot \binom{k}{n} [1-\bar{P}(s(t))] e^{-t/\tau_{\mu}} [1 + S(t)]$$

- (4) The bottom, non-sinusoidal curve corresponds to:

$$N_o(t, \mathcal{N}) = \frac{\sum_{n=0}^{\infty} \bar{P}(s(t))^n \sum_{k=n}^{\infty} P_p(k, \mathcal{N}, t) (1-\epsilon)^{k-n} [1-\bar{P}(s(t))]^{k-n-1}}{1 + \frac{\sum_{n=0}^{\infty} P_p(n, \mathcal{N}, t) n \bar{P}(s(t))}{e^{-t/\tau_{\mu}}}} \quad \text{III(38)}$$

$$\cdot \binom{k}{n} \left\{ n [1-\bar{P}(s(t))] e^{-t/\tau_{\mu}} + (k-n) \bar{P}(s(t)) (1-e^{-t/\tau_{\mu}}) \right\}$$

Curve (2) is the sum of curves (3) and (4). Besides

confirming the fact that the muon lifetime distortion due to post- μ_i muons is the most dominant at late times, these plots illustrate the very important fact that post- μ_i muons introduce a "bogus" relaxation into the MSR signal. The details of the muon lifetime distortions are illustrated in Figure III-16 which plots the four curves on a logarithmic scale while suppressing the MSR signal ($A_{\text{Mu}} = 0$). The top two curves on each plot are identical to those shown in Figure III-13.

The effects of muon pile-up on the relaxation of the MSR signal are illustrated in Figure III-17 for both pre- and post- μ_i muons. The pre- μ_i asymmetry plot is of the function:

$$A(t) = \frac{[\text{equation III(28)}]}{e^{-t/\tau_\mu}} - 1 \quad \text{III(39)}$$

and the post- μ_i asymmetry plot is of the function:

$$A(t) = \frac{[\text{equation III(36)}]}{e^{-t/\tau_\mu}} - 1 \quad \text{III(40)}$$

with $S(t) = A_{\text{Mu}} \cos \omega_{\text{Mu}} t$ in both cases. Clearly, there is no relaxation of the MSR signal in the case of pre- μ_i muons.

The curving envelope of the precession signal is simply due to the muon lifetime distortions detailed earlier. However, the post- μ_i curve shows a distinct damping of the MSR signal with an approximately Gaussian shape. Again, the downward drifting envelope of the precession curve is due to muon lifetime distortions detailed above.

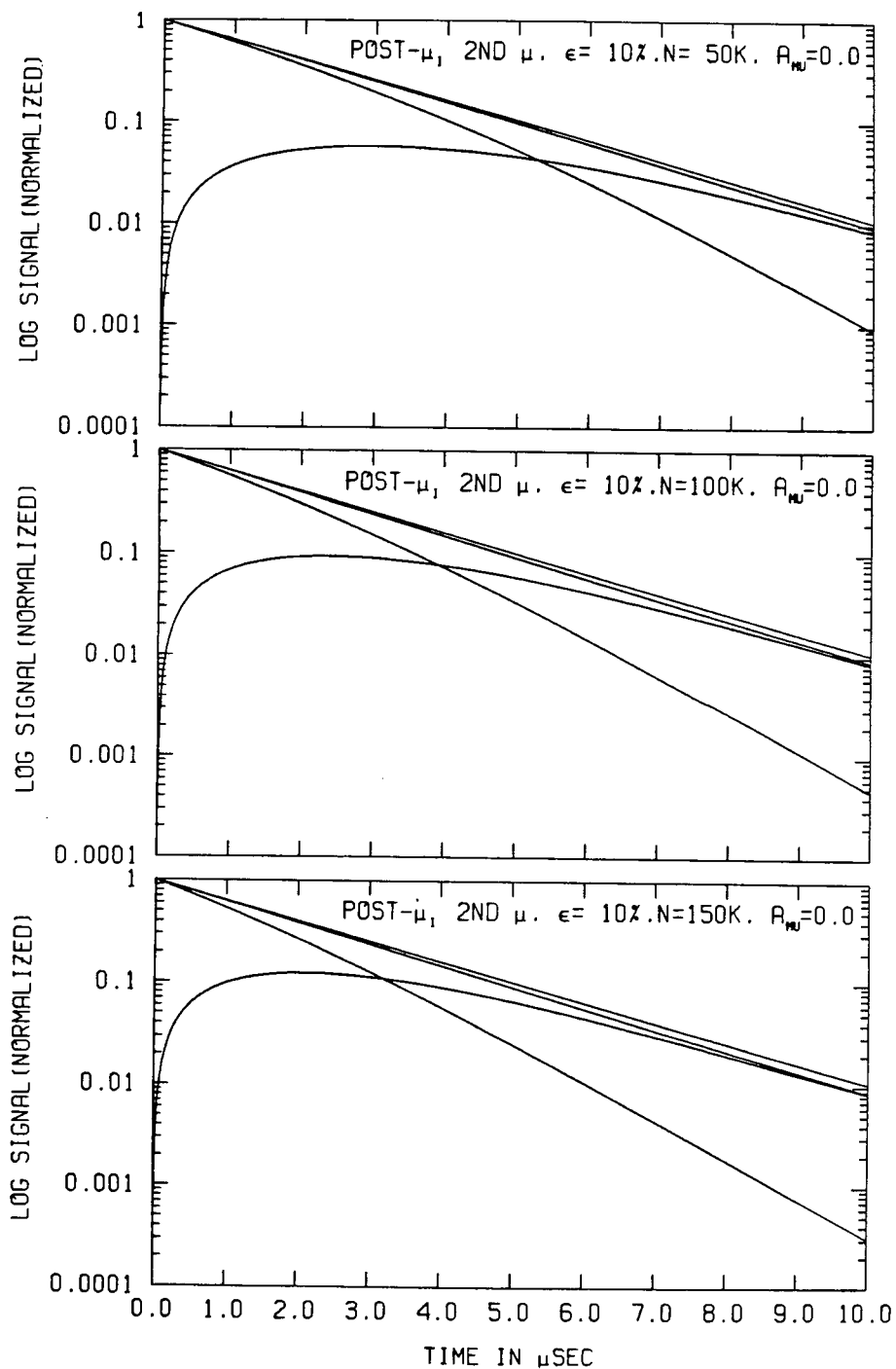


FIGURE III-16: The origins of the lifetime distortions due to post- μ_i muons. The top two curves in each plot are identical to those in Figure III-13. The monotonically decreasing curve with the greatest curvature is due to μ_i decay detection, and the lower curve which rises and falls is due to post- μ_i decay detection.

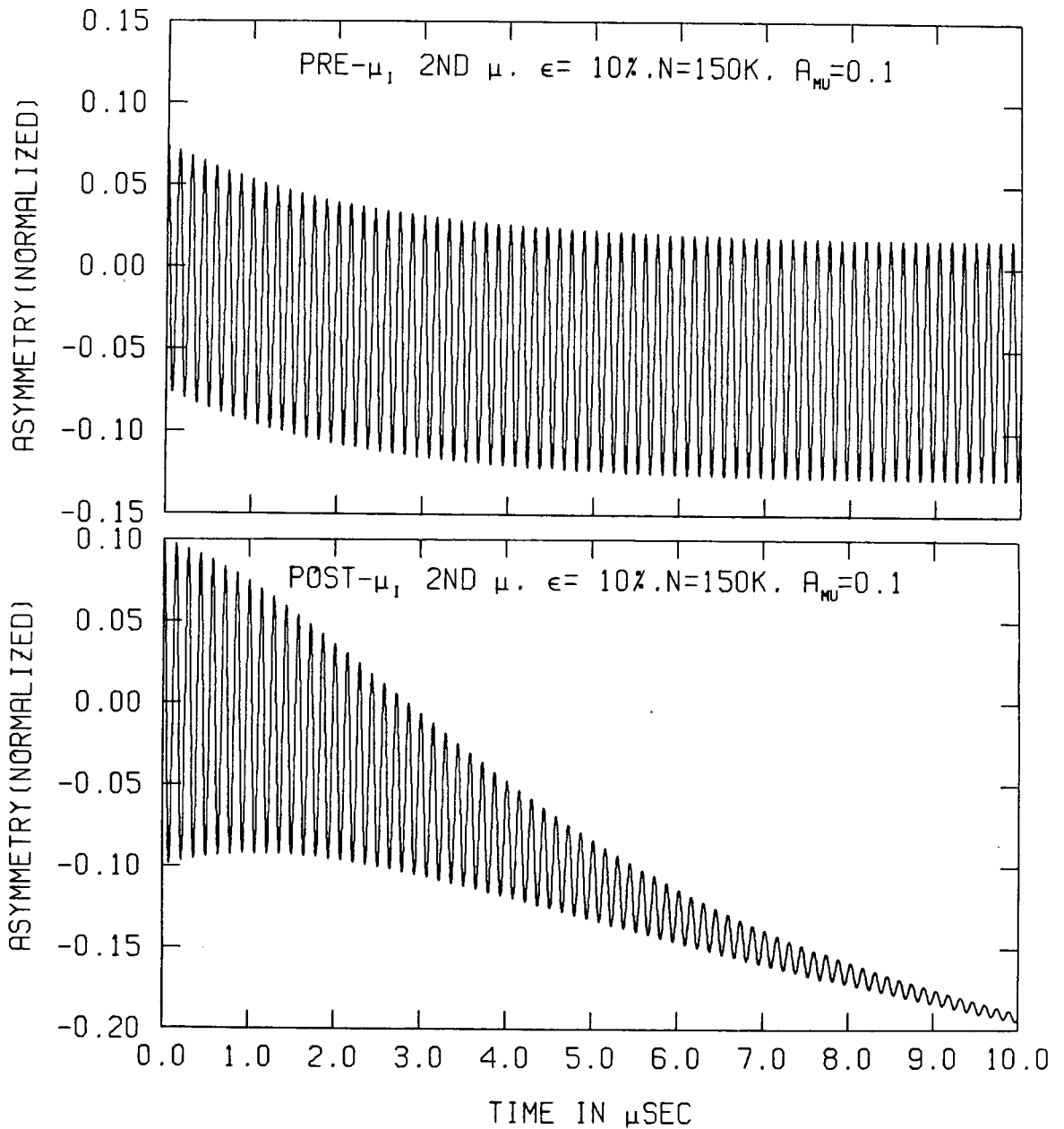


FIGURE III-17: Relaxation effects in the MSR signal due to muon pile-up. The top plot of pre- μ_1 muons shows no relaxation in the MSR signal, but it does show that the amplitude of the signal is reduced by $1 + 2\tau_{\mu}$. The bottom plot of post- μ_1 muons shows no such reduction in the initial amplitude of the signal, but it does show a strong relaxation of the signal with a Gaussian shape. The curving envelopes of both signals are due to muon lifetime distortions.

C The MSR Data Acquisition System

This Section presents a detailed description of the data acquisition system that was briefly sketched in Chapter II. The electronic logic is designed to discard post- μ_i and second e^+ events, but not pre- μ_i events; however, modifications to the logic to incorporate pre- μ_i event rejection are presently being implemented. The first part of this Section describes the electronic logic including CAMAC modules, while the second part explains the role of the MBD. The main computer, a PDP 11/40, is discussed only with respect to its interaction with the MBD.

(i) The Electronic Logic

A schematic diagram of the pre-CAMAC electronic logic is given in Figure III-18. The operation of the TDC-100 and CAMAC pattern recognition unit (a strobed coincidence unit), naturally leads to separate rejection of early and late second muon events (see Chapter II, Section C). Early second muons may be rejected in hardware by inhibiting the positron logic thereby preventing the setting of a bit pattern in the CAMAC coincidence unit and forcing the TDC-100 to "time-out" and reset. Late second muons, however, are detected after the CAMAC coincidence unit has been set and after the TDC-100 has begun its time digitization; these events are rejected in software by the MBD.

File-up conditions are monitored by three LRS 222 Dual Gate Generators designated g1, g2, and g3. All three

90°/270° or "Arizona" data acquisition mode logic diagram

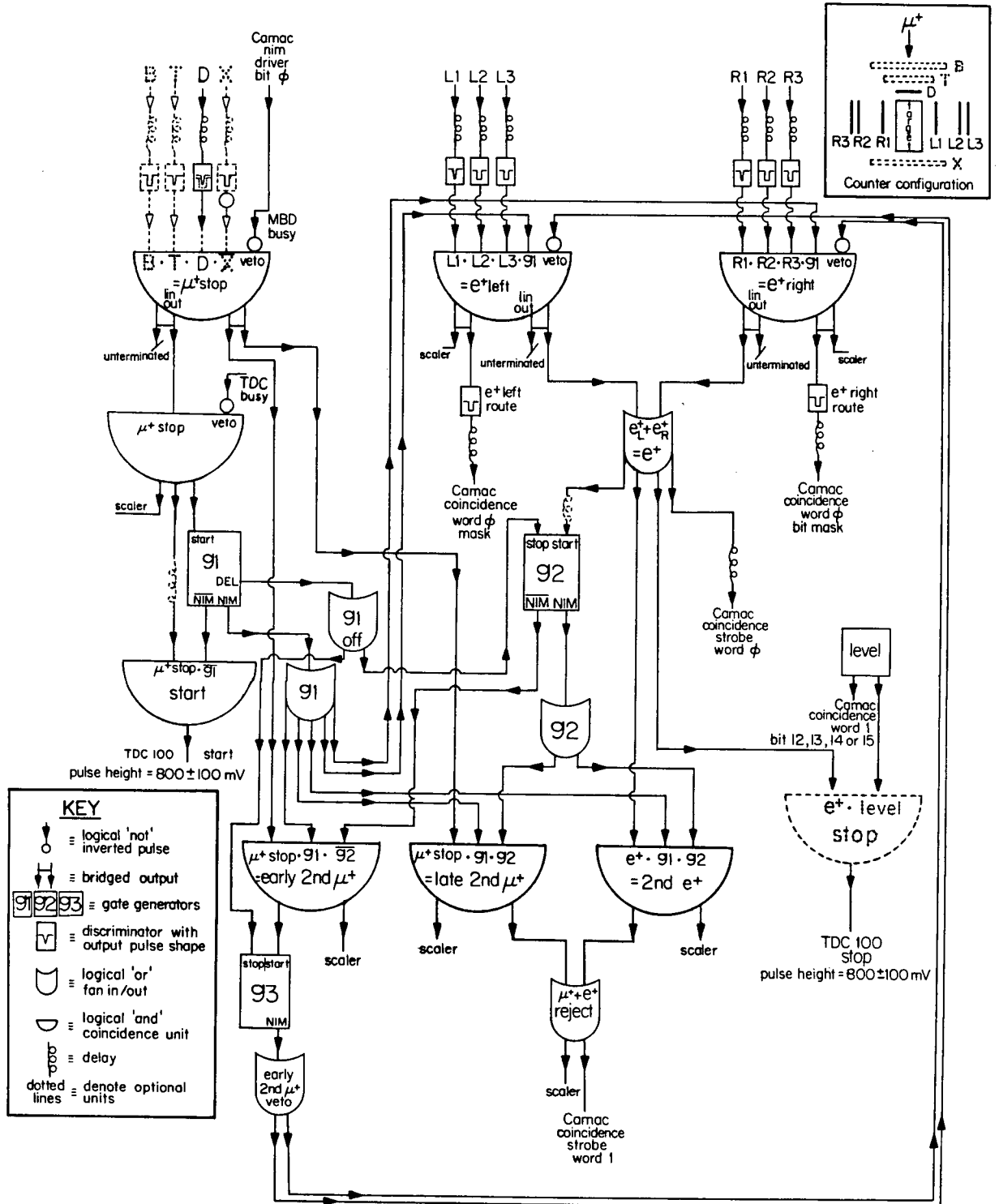


FIGURE III-18: The TRIUMF MSR data acquisition logic (detail). This logic rejects post- μ_i muon events and second e^+ events, but not pre- μ_i muon events.

gates are set to a width equal to the muon decay gate, T , of several muon lifetimes ($T = 4\tau_{\mu}$ in previous examples). A schematic diagram of the various accepted and rejected event sequences is given in Figure III-19. The pile-up monitor, g_1 , is opened by μ_i , the muon that starts the clock, under the condition $\mu_{\text{stop}} \cdot g_1$. g_2 , used to distinguish early from late second muons, is opened by an accepted decay positron signal (an accepted TDC stop pulse). An early second muon, defined by the condition $\mu_{\text{stop}} \cdot g_1 \cdot \overline{g_2}$, opens the third gate, g_3 , which serves to inhibit the positron logic. Late second μ^+ , defined as $\mu_{\text{stop}} \cdot g_1 \cdot g_2$, or second e^+ , defined as $e^+ \cdot g_1 \cdot g_2$, set a veto bit in the CAMAC coincidence unit, causing subsequent rejection of the event by the MBD. A delayed pulse, fired by the closing of g_1 , serves to close g_2 and g_3 . Accepted decay positrons, defined as $e^+ \cdot g_1 \cdot \overline{g_2}$, serve to stop the TDC-100, open g_2 and set the appropriate telescope "routing" bits of the CAMAC coincidence unit. The TDC-100 ignores multiple start and stop pulses.

Upon completion of time digitization, taking $2.5 \mu\text{s}$ from the receipt of a stop pulse on average, the TDC-100 sends the digitized time to the CAMAC EG&G RI 224 Input Register by the "handshake" method. The CAMAC input register sends a LAM signal to the MBD indicating the presence of data. Two types of inhibit signals are used to prevent multiple firing of the CAMAC coincidence unit during the slow ($20\text{-}30 \mu\text{s}$) MBD data handling operation. The primary inhibit is generated by the MBD through a CAMAC EG&G ND 027 Output Register or NIM driver which serves to inhibit the μ_{stop} logic, thereby preventing

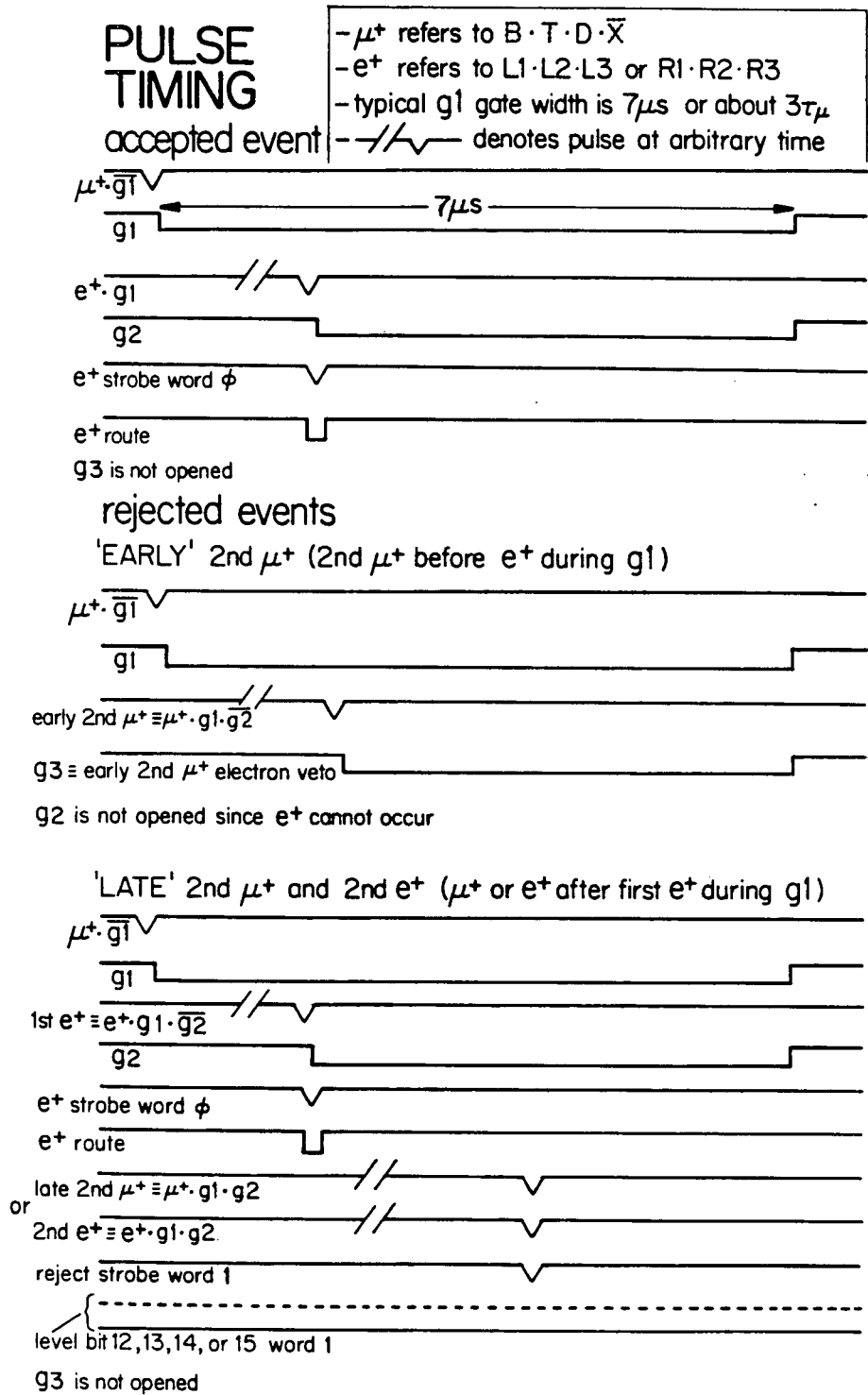


FIGURE III-19: Pulse timing and event identification for the logic of Figure III-18.

re-opening of the g1 gate which, in turn, suppresses the positron logic. To protect any time interval between the closing of g1 and the generation of the NIM driver inhibit, a clock "busy" pulse from the TDC also serves to veto the g1 starting logic. The TDC busy goes up with the acceptance of a start pulse and remains on until the CAMAC input register is cleared by the MBD.

Some details in Figure III-18, such as pulse height specifications and the designation of unterminated bridged outputs on some coincidence units, are hardware-specific for the electronic modules used at TRIUMF and have no fundamental logical function.

A general simplification of the electronic logic and its extension to reject pre- μ_1 muons are presently being implemented with the use of pile-up rejectors which have recently become available.

(ii) The Microprogrammed Branch Driver

The first part of this Section provides a general operational description of the MBD and the second part gives a detailed description of the general TRIUMF MSR data acquisition programme. A number of references are available on the MBD: Biswell(73), Thomas(73), and Shlaer(74).

The MBD-11 is an interface between the PDP-11 computer and CAMAC systems. It is a microprocessor controlled, multiple channel, direct memory access (DMA) branch driver that looks like a PDP-11 peripheral. In normal operation, the MBD runs like a small stored-programme computer with the programmes

contained in 16-bit word, 256-word page memory. The MBD is organized into 8 "channels" which, in some sense correspond to programmes, each of which has a priority with channel 7 the highest and channel 0 the lowest priority. Each channel has a dedicated set of 14 programmable 16-bit registers in which data is processed. In addition, there are a number of registers common to all channels: UNIBUS registers which are used to transfer data to and from PDP memory, CAMAC registers which are used to transfer data to and from CAMAC, and a number of miscellaneous registers. There are also a group of PDP-11 registers accessible to the PDP via its I/O page through which the PDP exercises ultimate control over the MBD. Some of these non-channel registers may only be used by the MBD either as sources or sinks. This elaborate register structure is designed with the intention that all data, whether it be data to be transferred between PDP and CAMAC or control data, be held in registers, while the MBD memory is used to hold programme instructions, constants, and buffers.

The MBD instruction set permits addition, subtraction, masking, shifting of 16 bit integers as well as testing of results, execution of CAMAC commands, and communication with the PDP. The execution cycle time is fast, typically 350 ns. Many instructions allow multiple operands thereby eliminating the need for intermediate storage registers. MBD programmes are assembled with the PDP-11 macroassembler and loaded into MBD memory.

MBD communication with the PDP is carried out usually

by NPR's (non-processor requests) through its DMA channel. This operation is asynchronous with the PDP processor and allows transfer of data to and from PDP memory without the necessity of intervention by the PDP processor. In addition, each channel of the MBD may have an interrupt vector assigned to it which points to the address of a PDP interrupt service routine. Thus, the MBD has the ability to force the PDP processor to intervene in data handling. Similarly, each MBD channel has a graded-L (GL) bit assigned to it for communication with CAMAC. If the MBD is to respond to LAM's from a CAMAC module, the CAMAC crate controller must have the appropriate GL jumper between the crate address of the LAM-generating module and the corresponding MBD channel. Data taking from several experiments at once could be accomplished by assigning different MBD channels to each experiment.

Each MBD channel to be used has a programme in MBD memory associated with it. In order that the PDP exercise ultimate control over the MBD, each channel must be started, at least once, by the PDP. In fact, this process assigns a particular MBD programme to a particular channel. At the completion of this channel initialization, the channel may "exit" or cease execution in one of four ways, determined by the programme: it may exit such that it cannot be restarted except by the PDP; it may exit such that it will be restarted when a LAM associated with it becomes active; it may exit from a LAM-started programme such that the PDP must restart it; and

it may exit such that it will restart itself the next time that channel has the highest priority. To retain PDP control over the MBD, there is a sub-priority hierarchy which gives the PDP-restarted channels higher priority than channels restarted by LAM's or by themselves. For example, PDP started channel 4 has higher priority than LAM restarted channel 6 which, in turn, has higher priority than self-started channel 5. Since channels cannot interrupt each other, channel priority arbitration only occurs after an executing channel has exited.

For most applications, data taking channels are initialized by the PDP, but they exit such that they are restarted by LAM's. The PDP initialization generally provides the MBD programme with control information such as histogram addresses in PDP memory, histogram sizes, data masks etc. This information is generated by the PDP data acquisition programme which solicits the initialization information from the experimenter. After the initialization process, the MBD runs in response to LAM's from CAMAC modules without intervention from the PDP. A typical MBD data handling programme performs such tasks as: reading data from CAMAC modules; checking data masks for good/bad event arbitration or histogram dispatching; adjusting data resolution by shift instructions; calculating the word address of the correct histogram bin in PDP memory; incrementing the histogram bin in PDP memory via an NPR; and, finally, resetting the appropriate CAMAC modules. One can exploit the asynchronous operation of the MBD to minimize both experimental and PDP deadtimes. For

example, the MBD can be involved in a data manipulation operation while data is being transferred to or from the PDP and to or from CAMAC.

The design of an MBD programme for general application to MSR at TRIUMF must have a number of features: it must allow simultaneous data acquisition for more than one experiment using either the same MBD channel or different ones; any experimenter must have the option of starting or stopping data acquisition for his experiment at any time without interfering with the data acquisition of other experiments simultaneously using the same system; the number, size and time resolution of histograms associated with each experiment must be completely flexible (within the physical constraints of computer memory size); it must be possible to associate a time "offset" with each histogram (that is, an experimenter may only want to histogram data corresponding to time ranges greater than some minimum "offset" value); there must be provision for software rejection of bad events; and there must not, obviously, be any "cross talk" between one histogram and another. In addition, the MBD programme should be efficient since its data processing is a major contributor to experimental deadtime.

While the time range of the TDC-100 is externally adjustable to some extent, its time resolution is not - it is fixed at 0.125 ns. The time range may be varied from 8 μ s to 34 ms in binary steps. Furthermore, the TDC-100 transfers its binary coded data into two words in the CAMAC input register. The first 16 bits of data (8 μ s) are stored in word 0 of the

input register and the high order 13 bits (for times $> 8 \mu\text{s}$) are stored in word 1 of the input register. Since both the PDP and MBD are organized into 16 bit registers and memory words, TDC-100 time measurements are constrained to 15 bits (the highest order bit is a sign bit). The MBD must adjust measured time resolutions by the execution of shift instructions and concatenate the two words of TDC-100 output into one word. This is accomplished in the following way: if the desired time resolution is 1 ns, say, $(0.125 \text{ ns} \times 2^3)$, the MBD logically shifts the data in word 0 three bits to the right, logically shifts the data in word 1 $(16-3 =)$ 13 bits to the left and merges (via an exclusive "or" instruction) the data into one 16 bit word. The desire to allow each histogram to have its own time resolution presents a problem to the MBD coding since it must have a different shift field for each histogram. This problem is solved by programming the MBD with self-modifying code that inserts the proper shift instructions as required.

The standard TRIUMF MBD data acquisition programme, which is LAM initiated on channel 6, supports up to 16 histograms and fulfills the requirements outlined above. When the data acquisition system is "boot-strapped", the MBD code is automatically loaded by the PDP. The MBD then executes a brief initialization sequence which removes the inhibit on the CAMAC crate 'A' controller, enables LAM generation by the TDC-100 CAMAC input register, enables the "branch demand" on the CAMAC crate controller (this allows the crate controller to send the LAM's generated by CAMAC modules along the branch).

highway to the MBD), and, finally, exits to await restarting by LAM's. Any LAM received by the MBD at this point causes the MBD to execute a dummy code which merely clears the CAMAC modules but does not communicate with the PDP. It is not until an experimenter actually orders the system to commence data acquisition, thereby modifying the MBD code via the PDP, that data acquisition commences.

To accomplish the data acquisition objectives outlined above, the MBD uses three sets of tables contained in its memory, two of which are written by the PDP (these may be modified at any time by the PDP). The first is a mask table, listing the valid histogram masks. These masks are simply bit patterns that identify which histogram a particular datum belongs to. With each event, the MBD reads a mask from the CAMAC coincidence unit and identifies which histogram the event belongs to by comparing it with the masks in the mask table. The mask table is written by the PDP on advice from the experimenter who selects a unique mask pattern for each histogram. Besides providing histogram identification, this mask table allows software event rejection since the MBD discards any events with masks not contained in its table. Thus, an experimenter can set a false mask to reject specific types of events.

By identifying a mask in its mask table, the MBD automatically finds a pointer in a "dispatch" table that gives the location in its memory of the "histogram" table that corresponds to that mask. These tables, which are written by the PDP, each contain six words of information about their

histogram. The first word tells the MBD if the histogram is currently active (that is, whether data acquisition for that experiment is currently off or on). This word is modified by the PDP whenever the associated experimenter decides to start or stop data acquisition, thereby allowing different experiments to start or stop independently. The second word in the table gives the address of the first word of the histogram (the "base" address) stored in PDP memory. The third word gives the size (number of bins) of that histogram. The MBD discards any data corresponding to time ranges greater than the histogram size. The fourth and fifth words contain shift left logical and shift right logical instructions respectively, corresponding to the histogram time resolution. The MBD dynamically inserts these instructions into its data handling code as required, thereby allowing different time resolutions for each histogram. The last word in the table contains the histogram offset which the MBD subtracts from the measured time interval. The MBD calculates the address of the word in PDP memory corresponding to the particular time bin of a histogram by adjusting the time resolution of a measurement, subtracting the offset, comparing the result with the histogram size, and, if it is not greater than the histogram size, adding the base address.

The MBD communicates with CAMAC via the branch highway and with the PDP via the UNIBUS. Relative to the 350 ns data manipulation operations of the MBD, communication with external devices is slow. MBD-CAMAC communication time depends on the physical length of the branch highway and takes about

2.7 μ s at TRIUMF for each operation. MBD-PDP communication by NPR's depends on the level of PDP activity since the MBD must compete for control of the UNIBUS with other devices such as the central processor etc. Each UNIBUS operation takes an average of 3.5 μ s when the PDP is moderately active. In order to realize the objective of minimizing MBD data processing time, it is desirable to execute data manipulation procedures such as checking masks while simultaneously communicating with CAMAC and the PDP. There is an inherent contradiction in this strategy, however, since the MBD has no data to manipulate until it completes several CAMAC read operations to obtain the data. In order to circumvent this problem, the MBD has been coded so that many of its data manipulation operations are one programme execution pass behind; that is, while the MBD is waiting for receipt of data from CAMAC corresponding to the present LAM, it processes the data from the previous LAM which was temporarily stored in its registers. By the time it completes execution of the current pass of its code, the MBD has finished with the previous data, either by writing it into the PDP, or rejecting it, and has stored the current data in its registers until it re-commences execution in response to the next LAM.

A flow diagram of the standard TRIUMF MBD code is given in Figure III-20.

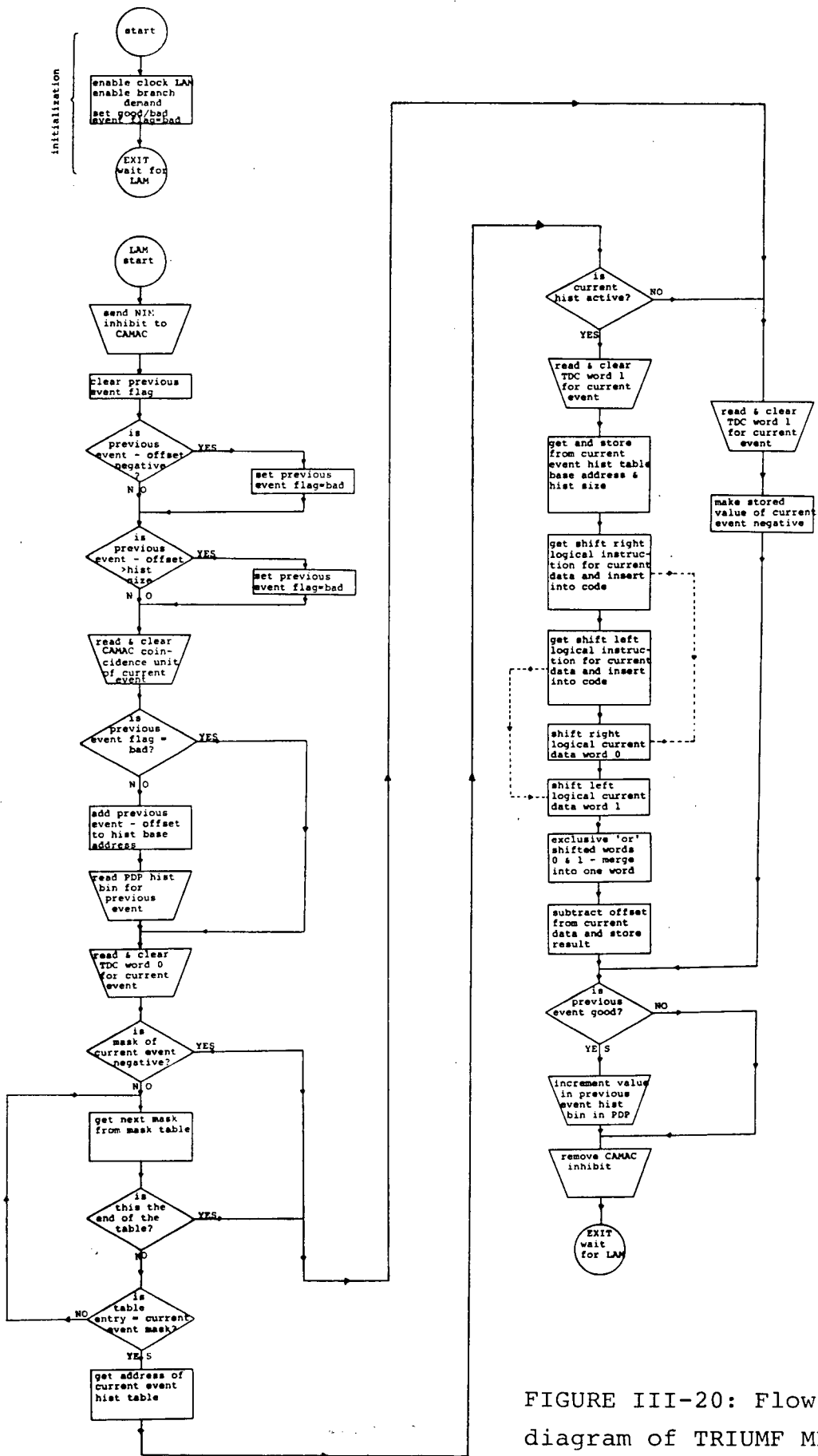


FIGURE III-20: Flow diagram of TRIUMF MBD programme.